Effect of Lime Addition Methods on Performance Related Properties of Asphalt Concrete Mixture

Assist. Prof. Dr. Amjad Hamd Khalil Albayati
University of Baghdad
Transportation Engineering
Amjad.Albayati@coeng.uobaghdad.edu.iq

Ahmad Mahir Mohammed
University of Baghdad
M.Sc. Transportation Engineering
Ahmed86ani@gmail.com

ABSTRACT

In the recent years, some of the newly constructed asphalt concrete pavements in Baghdad as well as other cities across Iraq showed premature failures with consequential negative impact on both roadway safety and economy. Frequently, load associated mode of failure (rutting and fatigue) as well as, occasionally, moisture damage in some poorly drained sections are the main failure types found in those newly constructed road.

In this research, hydrated lime was introduced into asphalt concrete mixtures of wearing course in two methods. The first one was the addition of dry lime on dry aggregate and the second one was the addition of dry lime on saturated surface dry aggregate moisturized by 2.0 to 3.0 percent of water. For each type of addition, five different percentages of lime as a partial replacement of ordinary limestone mineral filler were used; these were; 1.0, 1.5, 2.0, 2.5, and 3 percent by weight of aggregate besides a control mixture that did not contain lime. Marshall Mix design method was used and the performance properties of moisture damage, resilient modulus, permanent deformation and fatigue characteristics were evaluated using indirect tensile strength, uniaxial repeated loading and repeated flexural beam tests. Also, VESYS5W software was implemented to evaluate the pavements performance in terms of rut depth and fatigue area for a typical pavement structure. The main conclusion withdrawn from this research revealed that the use of 2.5 percent hydrated lime in dry addition method and wet addition method showed an improved fatigue and permanent deformation characteristics, lower moisture susceptibility and high resilient modulus.

Key Words: Asphalt, Hydrated Lime, Moisture Damage, Permanent Deformation, Fatigue, VESYS5W.

تأثير طرق اضافة النورة المطفئة على خصائص الاداء لخلطات الخرسانة الاسفلتية

لوحظ في السنوات الاخيرة في بعض رصفات الخلطات الاسفلتية في بغداد و مدن العراق الاخرى ظهور فشل مبكر و ما قد يترتب علية من اثار سلبية على الناحيتين الاقتصادية و الامان للطريق والتي غالباً ماتكون الاحمال المصحوبة بالفشل (التخدد و الكلل) و احياناً ما تكون مصحوبة بالدور المخرب للماء (الرطوبة) والتي هي احد الاسباب الرئيسية الموجودة في طبقات التبليط المرصوفة حديثاً. في هذا البحث تم اضافة مادة النورة المطفأة الى خلطات المزيج الاسفلتي والتي تمثل الطبقة السطحية من خلال اتباع طريقتين للاضافة , الاولى باضافة نورة جافة الى الركام الجاف و الثانية باضافة نورة جافة الى ركام رطب السطح (مشبع بنسبة 2.0-3.0%) بالماء وذلك بأستخدام خمس نسب مختلفة كنسب استبدال جزئية من المادة المالئة (الفلر) و هي 1.0,1.5,2.0,2.5,3.0 من وزن الركام الكلي , وكذلك تم عمل مزيج أعتيادي خالي من المادة المضافة النورة لغرض مقارنة النتائج . ولغرض تحقيق اهداف هذا البحث فقد تم استخدام طريقة مارشال في تصميم بالاضافة الى الخصائص التي من خلالها يتم تقييم الاداء و التي تشتمل على الضرر المصاحب للماء ,معامل المرونة الاستردادي , التشوهات الدائمية و عمر الكلل , حيث اشتمل البرنامج المختبري على تقييم هذه الخصائص من خلال استخدام فحص الشد غير المباشر , فحص الحمل المتكررللاسطوانة والعتبات الاسفلتية التي تم تهئيتها باشكال و ابعاد لتغطية البرنامج العملي لهذا البحث , اضافة الى ذلك تم استخدام برنامج VESYS 5W و الذي تم اختياره لتقييم الاداء للخلطات الاسفلتية من خلال احتساب عمق التخدد و مساحة التشققات للكلل لمنشأ تبليط اسفلتي تقليدي .النتائج و الاستنتاجات المترتبة على هذا البحث اظهرت بأن استخدام نسبة 2.5% بالطريقة الجافة و

الطريقة الرطبة يمكن ان تؤدي الى تحسين خصائص مقاومة الكلل و التشوهات الدائمية بالاضافة الى تقليل الحساسية تجاه الدور المخرب للماء واظهار قيم عالية لمعامل المرونة الاسترداي.

BACKGROUND

The related mechanisms and reactions involved in the change of the performance of lime-modified HMA mixtures are not totally understood. Nevertheless, when hydrated lime is added to HMA, a portion of the lime forms insoluble salts with the highly polar molecules of the asphalt, which could otherwise react in the mixtures to form water-soluble soaps that promote stripping (National Lime Association 2003). Dispersion of the tiny hydrated lime particles throughout the mixture makes it stiffer and tougher, reducing the likelihood that the bond between the asphalt cement (AC) binder and the aggregate will be broken mechanically. Furthermore, a portion of the hydrated lime can reduce the viscosity-building polar components in the AC binder and thus improve the long-term oxidative aging characteristics of HMA (Huang et al. 2002). The structure of hydrated lime consists of differently sized proportions. The smaller fraction of lime increases binder film thickness, enhances binder viscosity, and improves binder cohesion leading to increased adhesion between the aggregates and binder, which reduces mixture segregation (Mohammad et al 2000). The larger fraction performs as a filler to increase the indirect tensile strength and resilient modulus and improve (i.e., decrease) both the indirect tensile creep slope and the fatigue slope (with higher number of cycles to failure of HMA) (Kennedy and Ping 1991, Mohammad et al 2000, Sebaaly 2006). It has also been reported that the addition of lime to HMA improves its resistance to rutting (Little and Epps2001, Al-Suhaibani 1992, Shahrour and Saloukeh 1992). Hydrated lime replacement with lime stone or bag house fine dust or any other has gained a considerable recognition due to its efficient effect on both pavement and cost manifest and it benefits into decreasing maintenance and respire in current and newly constructed pavement section. The reasons why hydrated lime is so effective in asphalt mixtures lie in the strong interactions between the major components, i.e. aggregate and bitumen, and the combination of 4 effects, two on the aggregate and two on the bitumen. Hydrated lime modifies the surface properties of aggregate, allowing for the development of a surface composition (calcium ions) and roughness (precipitates) more favorable to bitumen adhesion. Then, hydrated lime can treat the existing clay particles adhering to the aggregate surface, inhibiting their detrimental effect on the mixture. Also, hydrated lime reacts chemically with the acids of the bitumen, which in turns slows down the age hardening kinetics and neutralizes the effect of the “bad” adhesion promoters originally present inside the bitumen, enhancing the moisture resistance of the mixture. Finally, the high porosity of hydrated lime explains its stiffening effect above room temperature. The temperature dependence and the kinetics of the stiffening effect might explain why hydrated lime is not always observed to stiffen asphalt mixtures and why it is more efficient in the high temperature region where rutting is the dominant distress (European Lime Association 2011). The various ways to add hydrated lime, i.e., into the drum, as mixed filler, dry to the damp aggregate, as lime slurry, with or without marination are described. No definitive evidence demonstrates that one method is more effective than the other, in general, contractors and (or) transportation departments have adopted one or more of three popular techniques in dry, wet, and slurry state. The three techniques along with a brief description of each and the major pros and cons of each are listed in Table 1 (Button and Epps 1983).

OBJECTIVE

1. To evaluate and compare the addition of hydrated lime in both wet and dry method on the laboratory performance-based properties of asphalt mixtures.

2. To determine the optimum content of hydrated lime for use in both methods to improve the performance of asphalt mixtures.
3. To compare the performance-based properties between hydrated lime modified asphalt mixture and control mixture.
4. To study the effectiveness of hydrated lime based on the long-term performance analysis by employing VESYS5W software.

MATERIAL CHARACTERIZATION

The materials used in this work, namely asphalt cement, aggregate, and fillers were characterized using routine type of tests and results were compared with state corporation for roads and bridges specifications (SCRB, R/9 2003).

ASPHALT CEMENT

The asphalt cement used in this work is of 40-50 penetration grades. It was obtained from the Dora refinery, south-west of Baghdad. The asphalt properties are shown in Table 2.

AGGREGATE

The aggregate used in this work was crushed quartz obtained from Amanat Baghdad asphalt concrete mix plant located in Taji, north of Baghdad, its source is Al-Nibaie quarry. This aggregate is widely used in Baghdad city for asphaltic mixes. The coarse and fine aggregates used in this work were sieved and recombined in the proper proportions to meet the wearing (W) course gradations as required by SCRB specification (SCRB, R/9 2003). Routine tests were performed on the aggregate to evaluate their physical properties. The results together with the specification limits as set by the SCRB are summarized in Table 3. Tests results show that the chosen aggregate met the SCRB specifications; while, gradation curve for the aggregate are shown in Figures 1 and Table 4.

MINERAL FILLER

The filler is a non-plastic material passing sieve No.200 (0.075mm). In this work, the control mixes were prepared using limestone dust as mineral filler at a content of 7 percent; this content represented the mid-range set by the SCRB specification for two types of mixes IIIA for wearing course. Hydrated lime has been known to be a promising potential material for pavements due to its unique physical/chemical/mechanical characteristic. The use of hydrated lime has been recommended by SRCB with a rate of 1.5% by weight of aggregates, as an anti-stripping additive for HMA pavements. This study used hydrated lime in two different forms (dry lime added to dry aggregates and dry lime added to wet aggregate) prior to asphalt mixing in five different content (1.0% , 1.5%, 2.0% 2.5% and 3.0%) by weight of aggregate as a limestone dust replacement. The limestone dust and hydrated lime were obtained from lime factory in Karbala governorate, south east of Baghdad. Tables 5 and 6 illustrate the basic physical and chemical properties of hydrated lime and limestone dust used for this study.

LIME ADDITION TECHNIQUES AND SPECIMEN FABRICATION

One of the main objectives of this research is to study the effect of lime addition method on a mixture's mechanical properties, noticing that hydrated lime was added by the weight of aggregate as a mineral filler replacement. For the lime modified mixes, two methods were performed in terms of introducing lime into the aggregate. For the first method, called "dry method", dry hydrated lime by total aggregate weight is added following the normal procedure for adding mineral filler into the mixture. The second method, "wet method", introduces the hydrated lime to wet aggregate at a moisture content of 2–3% over SSD condition. Five different content of hydrated lime (1, 1.5, 2.0, 2.5 and 3.0) % was added with both methods by weight of aggregate as the amount of filler reduced; 20 of the 22 mix designs were modified using hydrated lime aggregates treatment method. Each mix was designed with the same blend of aggregates to avoid variability due to physical and mineralogical characteristics of the aggregates. The dry method follows the normal procedure for preparing the general mix after consideration of the variability in hydrated lime and mineral filler content. Wet hydrated lime method involves spreading hydrated lime onto the aggregate that has been wet to approximately 2 to 3% over its SSD. Dry aggregate blends were moisturized with an addition of 3.0% water by weight of total aggregates. Dry hydrated lime at a different rate (from 1.0% to 3.0%) by the total dry weight of aggregate was then mixed with the wet aggregates for 10 minutes to produce evenly distributed lime-water films on the aggregate surfaces. The lime-treated aggregates were then oven dried for four hours to eliminate all water before the addition of the asphalt binder. The mixtures replaced with hydrated lime in the form of wet method were not marinated for 48hours. This procedure was elaborated based on a study by McCann and Sebaaly (2003). They evaluated behavior of different lime application methods such as with and without 48 hours marinating process of lime-aggregate mixtures and found no statistical difference behind the marination process. In fact, a 48 hour marination time was used to allow for any pozzolanic reaction that might occur between the aggregates and lime. The steps for wet hydrated lime addition method are shown in Figures (2, 3,4and 5).

Consequential, in order to determine the optimum percent of bitumen in asphaltic specimens a triplicate number of specimens for each asphalt content by Marshall design method (ASTM D6926-2010a) were prepared for 10 mix of 11 treated with hydrated lime by aggregate treatment. The specimen prepared for this study, have the diameter of 100mm and height of 63 mm for Marshall and tensile strength ratio (ASTM- D-4867-96), Table 7 list Marshall for lime modified and control mixes. Specimens were compacted using Marshall standard compaction with 75 blows per each face, only for tensile strength the blows was less in order to produce HMA with targeted air voids between 6-8% to accelerate the potential damage of moisture in specimen and simulate the actual filed. Superpave Gyratory Compactor (AASHTO 2004) was used to fabricate HMA specimens with 50 gyrations of sample 101.1 mm diameter and 203.3mm height to quantify the effect of hydrated lime on rutting potential. Also compacted rectangular prismatic beams 76 mm (3 in) x 76 mm (3 in) x 381 mm (15 in) were produced by means of static compaction using a "double plunger" arrangement, using compressive machine device, and pressed in compressive machine under the gradual application of a static load for 2 minutes according to (ASTM-D1074-96), to promote homogeneity, the mixture is generally "rodded" or "spaded" prior to compaction, and the mold is made "free floating" by using a "double plunger" arrangement.

INDIRECT TENSILE TEST

The moisture susceptibility of the asphalt concrete mixtures was evaluated according to (ASTM- D-4867-96). The result of this test is the indirect tensile strength (ITS) and tensile strength ratio (TSR). In this test, a set of specimens were prepared for each mix according to Marshall procedure and compacted to 7±1 % air voids using different numbers of blows per face that varies from (34 to 49) according to the hydrated lime replacement rate. The set consisted of six specimens and divided into two subsets, one set (control) was tested at 25°C and the other set (conditioned) was subjected to one cycle of freezing and thawing then tested at 25°C. The test is shown below in figure 6. Involved loading the specimens with compressive load at a rate of (50.8mm/min) was acting parallel to and along the vertical diametrical plane through 0.5 in. wide steel strips which are curved at the interface with specimens. These specimens failed by splitting along the vertical diameter. The indirect tensile strength which is calculated according to (Eq.1) of the conditioned specimens (ITS_c) is divided by the control specimens (ITS_d), which gives the tensile strength ratio (TSR) as the following (Eq.2).

$$ITS = \frac{2P}{\pi t D} \tag{1}$$

$$TSR = \frac{ITS_c}{ITS_d} \tag{2}$$

where
ITS= Indirect tensile strength
P = Ultimate applied load
t = Thickness of specimen
D = Diameter of specimen other parameters are defined previously

UNIAXAIL REPEATED LOADING TEST

The uniaxial repeated loading tests were conducted for cylindrical specimens, 101.6 mm (4 inch) in diameter and 203.2 mm (8 inch) in height, using the pneumatic repeated load system (Albayati 2006), shown below in fig. (7). In this test, repetitive compressive loading with a stress level of 20 psi was applied in the form of rectangular wave with a constant loading frequency of 1 Hz (0.1 sec. load duration and 0.9 sec. rest period) and the axial permanent deformation was measured under the different loading repetitions. All the uniaxial repeated loading tests were conducted at 20°C, 40°C and 60°C as shown in figure (8). The permanent strain (ε_p) is calculated by applying the following equation:

$$\varepsilon_p = \frac{p_d \times 10^6}{h} \tag{3}$$

where
εp= axial permanent microstrain, pd= axial permanent deformation
h= specimen height

Also, throughout this test the resilient deflection is measured at the load repetition of 50 to 100, and the resilient strain (εr) and resilient modulus (Mr) are calculated as follows (Huang 2004):

$$\varepsilon_r = \frac{r_d \times 10^6}{h} \tag{4}$$

$$M_r = \frac{\sigma}{\varepsilon_r} \tag{5}$$

where
εr= axial resilient microstrain
rd= axial resilient deflection
h= specimen height
Mr= Resilient modulus
σ = repeated axial stress
εr= axial resilient strain

The permanent deformation test results for this study are represented by the linear log-log relationship between the number of load repetitions and the permanent microstrain with the form shown in Eq.6 below which is originally suggested by Monismith et. al., (1975) and Barksdale (1971).

$$\varepsilon_p = aN^b \tag{6}$$

where
εp= permanent strain
N=number of stress applications
a= intercept coefficient
b= slope coefficient

FLEXURAL BEAM FATIGUE TEST

Within this study, third-point flexural fatigue bending test was adopted to evaluate the fatigue performance of asphalt concrete mixtures using the pneumatic repeated load system, this test was performed in stress controlled mode with flexural stress level varying from 5 to 30 percent of ultimate indirect tensile strength applied at the frequency of 2 Hz with 0.1 s loading and 0.4 s unloading times and in rectangular waveform shape. All tests were conducted as specified in SHRP standards at 20°C (68°F) on beam specimens 76 mm (3 in) x 76 mm (3 in) x 381 mm (15 in) as shown in figure (9) prepared according to the (ASTM-D1074-96). In the fatigue test, the initial tensile strain of each test has been determined at the 50th repetition by using (Eq.7) shown below and the initial strain was plotted versus the number of repetition to failure on log scales, collapse of the beam was defined as failure, the plot can be approximated by a straight line and has the form shown below in (Eq. 8).

$$\varepsilon_t = \frac{\sigma}{Es} = \frac{12h\Delta}{3L^2 - 4a^2} \tag{7}$$

$$N_f = k_1(\varepsilon_t)^{-k2} \tag{8}$$

where
ε_t = Initial tensile strain
σ =Extreme flexural stress
Es =Stiffness modulus based on center deflection.
h =Height of the beam
Δ =Dynamic deflection at the center of the beam.
L = Length of span between supports.
a =Distance from support to the load point (L/3)
N_f = Number of repetitions to failure
k_1 = fatigue constant, value of Nf when = 1
k_2 = inverse slope of the straight line in the logarithmic relationship

TEST RESULTS AND DISCUSSION

EFFECTS OF HYDRATED LIME ON MOISTURE SUSCEPTIBILITY

Based on the data shown in Figure 10, it appears that the examined hydrated lime contents and addition method have influence on the moisture susceptibility of the asphalt concrete mixes. The figure clearly demonstrates that both hydrated lime addition methods contributed to an increase in TSR and the general observation shows that wet method seems to be more effective than dry methods. TSR has gained a considerable increasing by 4.2%, 5.9%, 10.9%, 12% and 9% by dry method with respect to ascending amount of lime replacement as compared to the control mix. While, it took a similar manner by acquiring a gain in TSR of wet method by 3.4%, 6%, 18.8%, 20.8% and 19.8%. These results indicated the affirmative data that confirm the role of hydrated lime as a superior anti striping agent. The improvement in increasing in TSR can be attributed to improve in the adhesion between aggregate and asphalt cement due to the presence of hydrated lime by interacting with carboxylic acids in the asphalt and forming insoluble salts that are readily adsorbed at the aggregate surface (Plancher et al. 1977; and Hicks 1991). Implementing of these phenomena on local Iraqi paving materials can be discussed as follow: the aggregate used in this study was brought form Al-Nibaie quarry, which is Quartzite and classified as acidic aggregate and the improvement showed by altering the surface chemistry of acidic aggregate, causes a basic coating, and develops a strong bond between aggregate and acidic asphalt binder. Such bonding developed between asphalt binder and aggregate results in mitigate moisture damage in the asphalt mixtures. The effect of wet method of hydrated lime replacement was significant and even more impressive when the mixes replaced with dry hydrated lime to wet aggregate, this could be explained by fact that wet replacement of hydrated lime on 3% SSD provides better coverage and allows for proper application as compared to that add dry hydrated lime to dry aggregate. These advantages are possible because moisture ionizes lime and helps distribute it on the surface of the aggregate. Also visual inspection for tested specimens show more broken aggregates on the split faces which reflect higher bonding strength of the binder.

EFFECTS OF HYDRATATED LIME ON PERMANANET DEFORMATION

Permanent deformation manifests itself as primary distress due to the hot climate of Iraqi hot summer season. In this study the effect of hydrated lime has been quantified at a range of three temperatures 20°C, 40°C and 60°C representing the actual climate variation during the year in Iraq. The analysis of permanent deformation potential affected by the addition of hydrated lime are shown in figure 11 to 16 which are based on the data presented in tables 8 and 9. Examinations of the presented data suggest that the permanent deformation parameters intercept and slope generally improved with the use of hydrated lime. At lower temperature 20°C, the trend line of permanent deformation shows a narrow corridor between control and lime treated mixture with different rates for both dry and wet hydrated lime method. In other words , hydrated lime seems insignificant in reducing slope and intercept values as shown in tables 8 and 9 This can be attributed to the fact that, hydrated lime had minor effect at lower temperature in reducing the permanent deformation parameter slope and intercept and this was expected and indicated throughout the study of (Little and Petersen 2005). At intermediate and higher temperatures, hydrated lime showed a significant effect in improving rutting resistance by decreasing slope value, using dry method the slope value decreased as the amount of hydrated increased at 40°C and 60°C, mixes replaced with dry method at 2.5% at 40°C and 60°C exhibits a lower slope value by 18.4 % and 8.1% respectively. The addition of more hydrated lime beyond this percent may not represent best scenario as the time to failure for the 3.0% case was not different, while the same scenario using wet method, mixture with 2.5% exhibited lower slope value with 21.3% and 11.5% respectively at 40°C and 60°C compared to the control mix. As a summery from the test result it also appears that the addition of more than

2.5% for dry and wet hydrated lime did not improve the performance, as the time to failure for the 3.0% case was very similar to the time to failure of the 2.5% case, expect at lower temperature 20°C where hydrated lime acts as inert filler and less chemically active. The addition-reduction trend in permanent deformations of specimens of asphalt by percentage reduction of hydrated lime content was more impressive. So, additional hydrated lime content will have less negative effect on permanent deformation parameter of asphalt specimens. On the other hand, wet method seems to be more effective in reducing the slope value. In general, hydrated lime show a significant effect when using with both method in HMA mixture as limestone dust replacement in increasing the resistance to permanent deformation potential. Therefore in dry and hot environments similar to that of Iraq, where rutting failure controls the selection of asphalt concrete mixture, the use of wet hydrated lime replacement confirms that the rutting mode of failure in asphalt concrete pavement which is enhanced at hot summer temperature can be reduced to large extent with the introduction of hydrated lime to asphalt concrete mixtures.

RESILIENT MODULUS

Table 10 as well as figure 17 exhibits the variation of the resilient modulus values with both hydrated lime addition methods. Higher values of Mr are found with 1%, 1.5%, 2.0%, and 2.5% with dry and wet hydrated lime replacement as compared to control mix at 20°C, 40°C and 60°C respectively. It is observed that as the percentage of dry hydrated lime is increased the moduli increase for both hydrated lime methods at all three temperatures, indicating the mix is becoming stiffer. Also the Mr values for wet method show decrease in their values with 3.0% at 40°C and 60°C respectively. Comparison of Mr between dry and wet hydrated indicated that, in case of wet method, up to 2.0% can increase the modulus value and above percentage it will decrease the modulus tremendously at 40°C and 60°C. While mixes with dry hydrated lime replacement show a trend of increase due to hydrated lime replacement increase in the mix at all three temperatures, may be attributed to production of dry mixes. Also, it should be noted that at lower temperature using both method the Mr value increases as hydrated lime replacement increases and this easily explained the mixture to become stiffer at lower temperature.

EFFECT OF HYDRATED LIME ON FATIGUE PERFORMANCE

The fatigue characteristic curves for all mixtures are presented in Figures 18 and 19. The fatigue parameters k_1 and k_2 are shown in Table 11 and 12. Values of k_1 and k_2 can be used as indicators of the effects of hydrated lime on the fatigue characteristics of a paving mixture. The flatter the slope of the fatigue curve, the larger the value of k_2. If two materials have the same k_1 value, then a large value of k_2 indicates a potential for longer fatigue life. On the other hand, a lower k_1 value represents a shorter fatigue life when the fatigue curves are parallel, that is, k_2 is constant.

From the figures listed previously, it is clearly shown that the dry method of replacement mixture with 2.5% show higher fatigue resistance accompanied by increasing in number of repetition and this clearly show by increasing in K2 than control mix value by 29% with respect to control mix. While a drastic reduction happened when the doze increase beyond threshold limits of 2.5% and result in decreasing k_2 value by 7% for 3.0%. This is due to the fact that the higher stiffness caused by increasing lime in the mix and supported by gradual increase in stiffness modulus effect. There is an indication that the k_2 value increases highly, and the k_1 values change correspondingly. It is worth noting here that all of the k_1 values ranging between 1.083303xE-8 to 7.7459xE-11is by using dry method. For wet method, the general trend was observed form figures and tables' results show synergistic effect to dry method by increasing the fatigue life to a point and then the extra amount will deteriorate the fatigue resistance. Mixture with 2.5% show longer fatigue resistance firstly by increasing in number of repetition and extending lower slope with flatter power trends and k_2 value for this mixture was increased by 31.4%. In comparing the effect of the two addition methods wet method extend the fatigue life better than dry methods, for the same percentage of lime content, the overall result for fatigue test showed that increasing trend in resistance to number of repetition as more hydrated lime was used, even if the better performance to fatigue damage was observed from the mixture with 2.5% for both dry and wet method. However, with more than 2.5% additional hydrated lime, no additional improvement in performance was observed.

PERFORMANCE ANALYSIS USING VESYS 5W SOFTWARE

Using **VESYS5W** software for analyzing pavement section consisted of a 150 mm asphalt concrete layer over a 400 mm base course layer with 10 million ESALs application during 20 years' service life, the present serviceability index trend line is abstracted from the output results of the software and the results are shown in figures 20 and 21. The figures clearly show that the pavement section which consists of asphalt concrete layer modified with 2.5 percent lime (wet application method) provide better performance as compared to the mixes with 2.5 percent lime (dry application method) or mix with 0 lime. The PSI values at the end of 20 years' service life are 11.8, 13.0and 6.6 for the pavement section with asphalt concrete layers containing 2.5 percent lime (wet), 2.5 percent lime (dry) and 0 lime, respectively. The PSI values in VESYS5W software reflect the effect of rutting and cracking for a pavement section during the design life.

CONCLUSIONS

The following conclusions and recommendations are based on the results of the laboratory tests and analysis presented in this study:

- The use of both hydrated addition methods exhibited a good resistance against the moisture damage, an increase in TSR is achieved by 4.2%, 5.3%, 5.9% 10.9%, 12% and 9.0% for dry hydrated lime replacement method and 3.4% , 6% , 18.8%, 20.8 and 19.8% for wet hydrated lime replacement method corresponding to 1.0, 1.5, 2.0 and 3.0 lime contents, respectively. This indicates that the wet addition method was more effective than the dry method in improving the resistance to moisture induced damage of asphalt concrete pavement modified with hydrated lime
- The permanent deformation parameters, slope and intercept, was significantly effected using dry and wet hydrated lime addition methods employing different percentages of hydrated lime and this effects is more pronounced at high testing temperatures. The lime modified mixed with 2.5 percent in dry method wet method result in a decrease in permanent deformation slope higher temperature of 40^{o}C and 60C as compared to control mixture with no lime.
- The dry addition method of hydrated lime as a filler substitute results in better elastic modulus as characterized by resilient modulus test in comparison with the wet addition method. The use

of 3 percent lime, respectively at 20°C, 40°C and 60°C test temperature improve the resilient modulus by 40.2, 35.2 and 21.9 percent in dry addition method whereas for wet addition method the corresponding values are 29.1, 29.8 and 22.4 percent as compared to control mixes with no lime.

- For both addition methods, the use of 2.5 percent hydrated lime as a filler substitute has improved the fatigue property of the asphalt concrete mixes as determined by flexural test, the k_2 value (inverse slope of fatigue line) for mixes with 2.5 percent hydrated in dry and wet addition methods was more than that of 0 percent hydrated lime by 29 and 31.4 percent, respectively.
- The use of 2.5 percent hydrated lime in wet addition method as replacement for limestone dust mineral filler has shown a significant improvement of asphalt concrete behavior and has added to the local knowledge the possibility of producing more durable mixtures with higher resistance to distresses.

Specimens Nomenclature

The mix designation or nomenclature is the layer and the amount of hydrated lime that were substitute to filler and addition method. The mix nomenclature is the first letter that refers to the layer wearing followed by the actual amount of hydrated lime and the last letter that refers to the method of adding hydrated lime to mix

REFRENCES

- AASHTO, 2004, *Evaluation of Superpave Gyratory Compactors (SGC's*), AASHTO Designation: PP-35, , American Association of State Highways and Transportation Officials, Washington, D.C.
- Albayati A.,H , Alani A,M., 2012 , *Laboratory investigation in the Hydrated Lime effect on asphalt concrete mixture*, preceding of The First National Conference for Engineering Sciences FNCES'12 , Baghdad , Iraq.
- Albayati, A.H., 2006, *Permanent Deformation Prediction of Asphalt Concrete Under Repeated Loading* Ph.D. Thesis, Baghdad University.
- Albayati,A. H., 2012, *Mechanistic Evaluation of Lime-Modified Asphalt Concrete Mixtures*, 7th RILEM International Conference on Cracking in Pavements RILEM Book series, 2012, Volume 4, PP .921-940.
- AlSuhaibani, A. R., Al-Mudaiheem, J., and Al-Fozan ,F. 1992 , *Effect of Filler Type and Content on Properties of Asphalt Concrete Mixes*. In Effects of Aggregates and Mineral Fillers on Asphalt Mixtures Performance, SPT 1147 (R. C. Meininger, ed.), ASTM, Philadelphia, Pa., pp. 107–130.
- Barksdale, R., 1971, *Compressive stress Pulse Times in flexible pavements for use in dynamic Testing*, No.345 , pp 32-44 ,Highway Research Record.
- Button, J.W., and Epps, J.A. 1983. *Evaluation of methods of mixing lime and asphalt paving mixtures*. Texas Hot Asphalt Pavement Association.

- European Lime Association / Asphalt Task Force, 2011, *Hydrated lime a Proven additives for Durable asphalt Pavement.*
- Hicks, R. G. 1991,: *Moisture Damage in Asphalt Concrete*, NCHRP Synthesis of Highway Practice 175,TRB, National Research Council, Washington, D.C.
- Huang ,Y. H., 2004, *Pavement Analysis and Design*, 2nd edition , Pearson Prentice Hall , Pearson Education, Inc . ,Upper Saddle River, NJ 0745 8.
- Huang, S.-C., J. C. Peterson, R. E. Robertson, and J. F. Branthaver. 2002, *Effect of Hydrated Lime on Long-Term Oxidative Aging Characteristics of Asphalt*. In Transportation Research Record: Journal of the Transportation Research Board, No. 1810, Transportation Research Board of the National Academies, Washington, D.C., pp. 17–24.
- Hydrated Lime, 2003, *More Than Just a Fille*r. National Lime Association, www.lime.org/HydratedLime.pdf.
- Kennedy, T. W., and Ping, W. V. 1991, *An Evaluation of Effectiveness of Antistripping Additives in Protecting Asphalt Mixtures from Moisture Damage*, Presented at Annual Meeting of the Association of Asphalt Paving Technologies.
- Little, D, and Epps, J. 2001,." *The Benefits of Hydrated Lime in Hot Mix Asphalt*. National Lime Association,. www.lime.org/ABenefit.pdf.
- Little, D.N. and Petersen, J.C. 2005. *Unique Effects of Hydrated Lime Filler on the Performance- Related Properties of Asphalt Cements: Physical and Chemical Interactions Revisited*. Journal of Materials in Civil Engineering, Volume 17, No. 2, pp.207-218.
- Mohammad, L. N., Abadie, C., Gokmen ,R., and Puppala, A. J., 2000 , *Mechanistic Evaluation of Hydrated Lime in Hot-Mix Asphalt Mixtures*. In Transportation Research Record: Journal of the Transportation Research Board, No. 1723, TRB, National Research Council, Washington, D.C.,pp. 26–36.
- Monismith, C., Ogawa, N. and Freeme, C. 1975. *Permanent Deformation Characteristics of Subgrade Soils due to Repeated Loadings*, TRR 537.
- Plancher, H., S. Dorrence, and J. C. Petersen. 1977. *Identification of Chemical Types in Asphalts Strongly Absorbed at the Asphalt–Aggregate Interface and Their Relative Displacement by Water*. Proc., Association of Asphalt Paving Technologists, Vol. 46, pp. 151–175.
- SCRB/R9 2003. *General Specification for Roads and Bridges*, Section R/9, Hot-Mix Asphalt Concrete Pavement, Revised Edition. State Corporation of Roads and Bridges, Ministry of Housing and Construction, Republic of Iraq.
- Sebaaly, P, E., 2006, *The Benefits of Hydrated Lime in Hot Mix Asphalt*, National Lime Association.

Table 1. Lime addition techniques with major positive and negative (Button and Epps 1983).

Method	Description	Major Positives	Major Negatives
Dry	- Simplest method - Lime and mineral filler introduced immediately after introduction of	- Least expensive method - Direct contact between aggregates and hydrated lime - Lime and mineral filler introduced immediately after introduction of	- Dusting and lime loss - Minimal mixing and coating of aggregates

	asphalt	asphalt	
Wet	- Lime metered into aggregate at a moisture content of 2-3% higher than SSD condition - Mixture processed in pug mill to ensure thorough mixing	- Proper coverage and application - Portion not mixing with aggregate will mix with asphalt, thus still aiding as anti-stripping agent	- Expensive due to extra fuel needed to dry aggregates before mix production
	- Aggregates kept in moist condition and marinated for up to 48 hours	- Moisture content slowly reduces over stockpiling period - Stockpiling can be separated from production, thus providing an economic advantage	- Aggregate handling effort is increased - Storage space needed for aggregate stockpiling - Concerns over carbonation of stockpiles with long stockpiling times
Slurry	-Slurry of lime and water applied to aggregates -Marinating optional	-Improved coverage of aggregates -Reduced dispersion and loss of lime -Improved stripping protection	-Increased water and fuel costs -Expensive, specialized equipment requirements

Table 2. Properties of asphalt cement

Property	ASTM designation	Penetration grade 40-50	
		Test results	SCRB specification
1-Penetration at 25C,100 gm,5 sec. (0.1mm)	D-5	45	40-50
2- Rotational viscosity at 135˚C (cP.s)	D4402	523	……
2- Softening Point. (˚C)	D-36	49	……
3-Ductility at 25 C, 5cm/min,(cm)	D-113	>100	>100
4-Flash Point, (˚C)	D-92	290	Min.232
5-Specific Gravity	D-70	1.041	……
6- Residue from thin film oven test	D-1754		
- Retained penetration,% of original	D-5	59.5	>55
- Ductility at 25 C, 5cm/min,(cm)	D-113	80	>25

Table 3. Physical properties for Alnibaie aggregate

Property	Alnibaie aggregate		
	Coarse Aggregate	Fine Aggregate	SCRB
Bulk Specific gravity (g/cm^3) (ASTMC127 and C128)	2.646	2.63	-----
Apparent Specific gravity (g/cm^3) (ASTM C127 and C128)	2.656	2.667	-----

Percent water absorption (ASTM C127 and C128)	0.14	0.523	-----
Percent wear (Los-Angeles Abrasion) (ASTM C131)	19.69		30 Max
Fractured pieces, %	98		90 Min
Sand Equivalent(ASTM D 2419)		55	45 Min*. Superpave (SP-2),
Soundness loss by sodium sulfate solution,% (C-88)	3.4	-------	12 Max

Table 4. Selected gradation for wearing and binder course

sieve size Inch	mm	Wearing course	
		Selected gradation	Specification limit (SCRB 2003/R9)
3/4	19.0mm	100	100
1/2	12.5mm	95	100-90
3/8	9.5mm	83	76-90
No.4	4.75mm	59	44-74
No.8	2.36mm	37	28-58
No.50	0.3 mm	13	5-21
No.200	0.075mm	7	4-10

Table 5. Physical properties of hydrated lime and limestone

Material property	Hydrated lime	Limestone dust
Specific gravity	2.41	2.78
Specific surface (m^2/Kg) *	398	244
-100 Mesh (150 µm) passing	100	100
-200 Mesh (75 µm) passing	90	85

*Tested by Blaine Air Permeability at material laboratory of civil engineering department according to ASTM C204

Table 6. Chemical composition and physical properties hydrated lime and limestone

Chemical composition	Hydrated lime	Limestone dust
% CaO	56.1	68.3
% SiO2	1.38	2.23
% Al2O3	0.72	-
% Fe2O3	0.12	-
% MgO	0.13	0.32
% SO3	0.21	1.2
% L. O. I.	40.65	27.3

Table 7. Marshall Design properties for wearing using dry and wet hydrated lime addition method

Mixture	OAC %	Density gm./cm^3	Stability kN	Flow mm	Air voids %	VMA %	VFA %
SCRB requirement			Min. 8.0 Kn	2-4	3-5	14 Min.	65-75
Control	4.9	2.338	11.67	4	4.018	14.07	70.4
W1H-d	4.9	2.337	12.12	3.75	4.01	13.93	70.2
W1.5H-d	5	2.331	12.47	3.5	4.08	14.08	72.4
W2H-d	5.2	2.328	14.37	3.5	4.14	14.33	72.1

W2.5H-d	5.2	2.316	13.77	3	4.30	14.41	71.1
W3H-d	5.3	2.309	12.01	2.75	4.09	14.57	71.2
W1H-w	4.9	2.328	12	3.75	4.17	14.06	74.6
W1.5H-w	4.9	2.326	13.79	3.75	4.12	14.09	72.4
W2H-w	5	2.317	12.02	4	4.21	14.17	73.5
W2.5H-w	5.2	2.311	11.51	4.25	4.12	14.31	70.6
W3H-w	5.2	2.296	10.22	4.75	4.32	14.34	70.7

Table 8. Effect of dry hydrated lime addition method on Intercept and slope Coefficient of permanent deformation

Mixture	20 C^0		40C^0		60C^0	
	a	b	a	b	a	b
Control	41.659	0.2761	115.3	0.3787	335.1	0.5675
W1H-d	39.717	0.2758	106.9	0.3576	311.6	0.5626
W1.5H-d	38.365	0.2682	98.8	0.3407	276.28	0.5332
W2H-d	34.225	0.2632	80.2	0.3203	240.5	0.5285
W2.5H-d	33.226	0.2628	71.9	0.3127	213.1	0.5225
W3H-d	31.389	0.2619	69.2	0.3005	200.83	0.511

Table 9. Effect of wet hydrated lime addition method on Intercept and slope Coefficient of permanent deformation

Mixture	20 C^0		40C^0		60C^0	
	a	b	a	b	a	b
W1H-w	41.004	0.2722	89.8	0.3551	289.8	0.5505
W1.5H-w	38.226	0.2681	78.9	0.3279	270.0	0.5359
W2H-w	37.412	0.267	61.1	0.3089	211.93	0.5169
W2.5H-w	35.129	0.259	60.0	0.3022	200.5	0.5082
W3H-w	33.356	0.2566	61.1	0.3372	205.48	0.5296

Table 10. Effect of dry and wet hydrated lime addition method on resilient modulus, Psi

Mixture	20C^0	Gains%	40C^0	Gains%	60C^0	Gains%
Control	179076	0	114814	0	79987	0
W1H-d	223220	19.7	127754	10.1	88059	9.16
W1.5H-d	247922	27.7	149119	23.0	93008	13.9
W2H-d	255959	30	157591	27.1	97943	18.3
W2.5H-d	278217	35.6	164636	30.2	100507	20.41
W3H-d	299952	40.2	177258	35.22	102547	21.9
W1H-w	199968	10.4	137754	16.65	85700	6.6
W1.5H-w	213299	16.04	159119	27.84	90126	11.24
W2H-w	234109	23.5	161210	28.77	117772	32.0
W2.5H-w	239962	25.3	164301	30.11	126629	36.8
W3H-w	252591	29.1	163350	29.71	103209	22.49

Mixture	Fatigue Equation	Number of repetition to fracture (N_f) Stress level(N)			
		222	489	311	400
Control	$N_f = 1.32484E\text{-}07 \varepsilon t^{-3.03}$	11285	7556	2332	1802
W1H-d	$N_f = 1.08303E\text{-}08 \varepsilon t^{-3.44}$	13542	8260	5427	2105
W1.5H-d	$N_f = 1.48877E\text{-}09 \varepsilon t^{-3.77}$	14531	9650	6321	3189
W2H-d	$N_f = 2.0395E\text{-}10 \varepsilon t^{-4.09}$	15780	13341	7443	4210

W2.5H-d	N_f = 7.74597E-11Ɛt $^{-4.27}$	16780	13123	8502	3277
W3H-d	N_f =7.47221E-10Ɛt $^{-3.93}$	13140	8420	5434	3780

Table 12. Fatigue life equation- wet hydrated lime.

Mixture	Fatigue Equation	Number of repetition to fracture (N_f) Stress level(N)			
		222	489	311	400
W1H-w	N_f =2.7558E-08Ɛt $^{-3.35}$	14537	10921	6258	3865
W1.5H-w	N_f =7.7565E-09Ɛt $^{-3.58}$	16482	11051	7320	5582
W2H-w	N_f =1.759E-10Ɛt $^{-4.18}$	22421	15237	11592	8872
W2.5H-w	N_f =3.745E-11Ɛt $^{-4.42}$	22532	17542	13542	6210
W3H-w	N_f =4.3598E-10Ɛt $^{-4.06}$	18218	13279	8421	5103

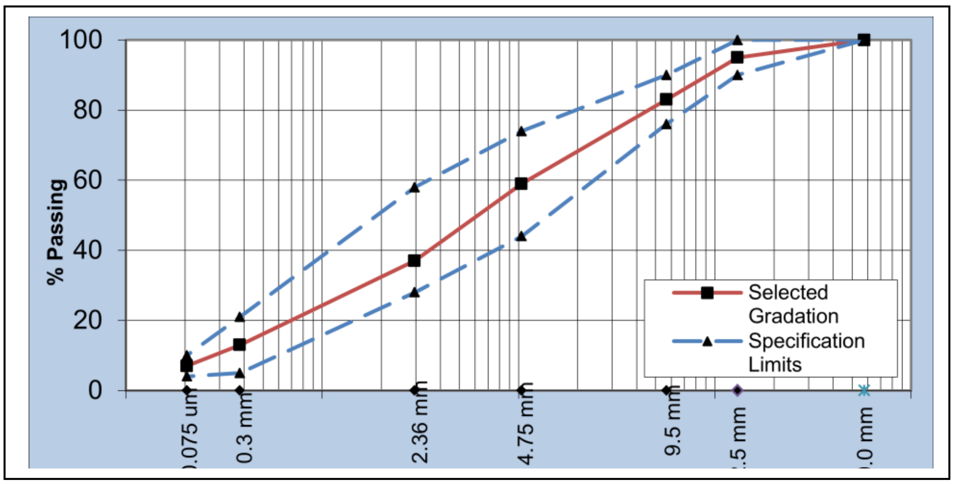

Figure 1. Wearing course gradation (W).

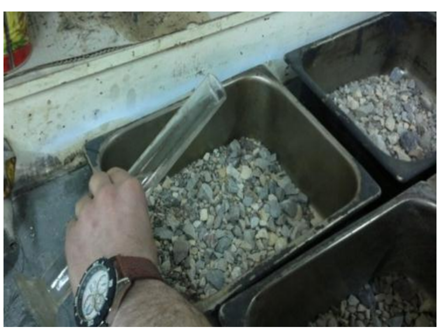

Figure 2. Adding water to the aggregates**.**

Figure 3. Mixing water with the aggregates.

Figure 4. Adding, Mixing hydrated lime to the wet Aggregate**.**

Figure 5. Oven dried Mix**.**

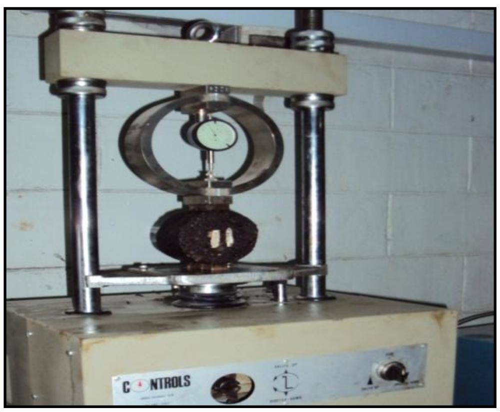

Figure 6. Photograph for ITS test**.**

Figure 7. Photograph for the PRLS**.**

Figure 8. Photograph for Permanent Deformation Specimen .

Figure 9. Photograph for Flexural Beam Specimen.

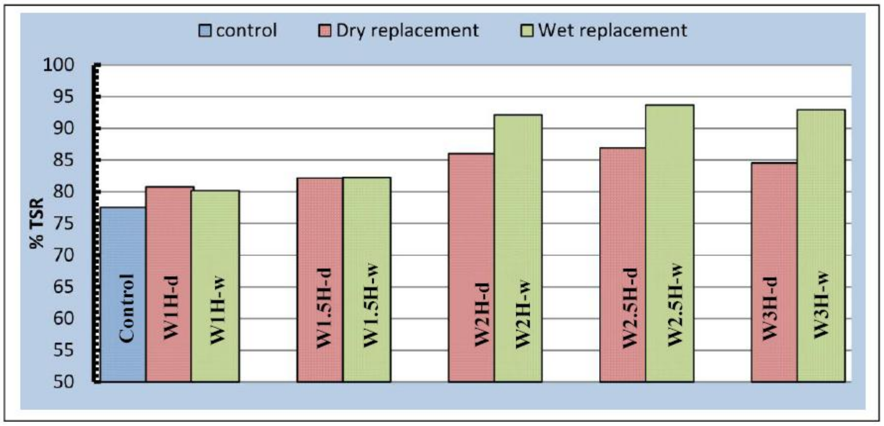

Figure 10. Effect of Dry and Wet hydrated lime addition method on TSR %.

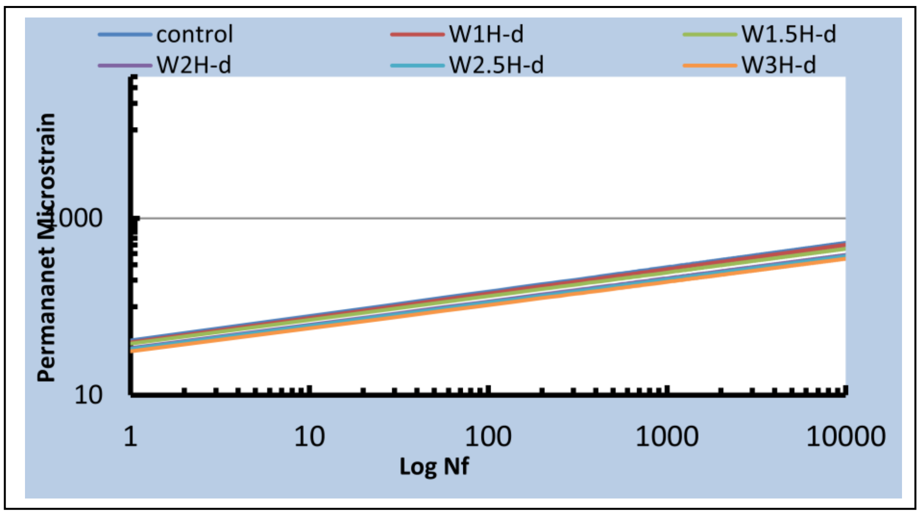

Figure 11. Effect of dry hydrated lime method on permanent deformation at 20^{o}C .

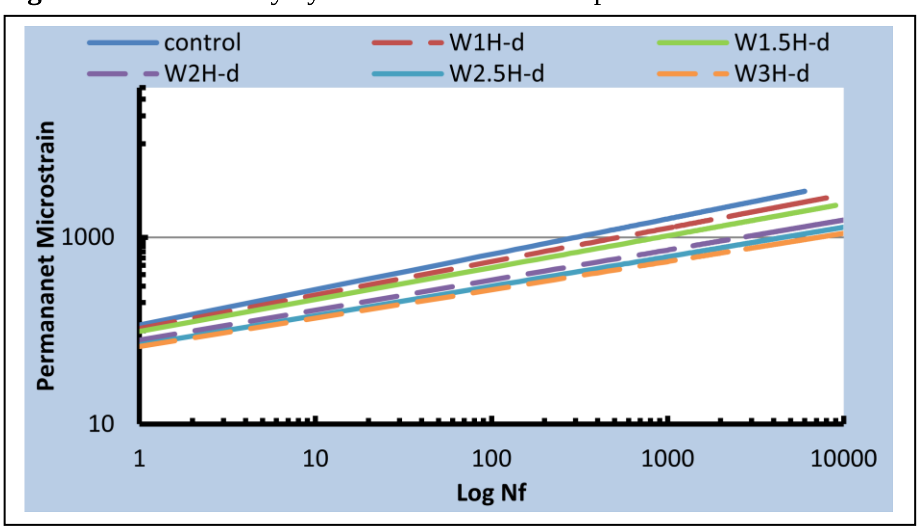

Figure 12. Effect of dry hydrated lime method on permanent deformation at 40^{o}C.

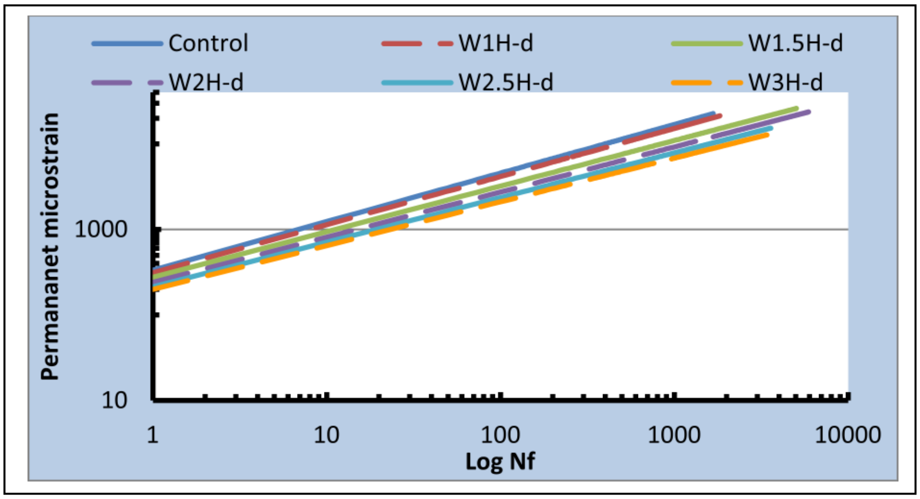

Figure 13. Effect of dry hydrated lime method on permanent deformation at 60°C.

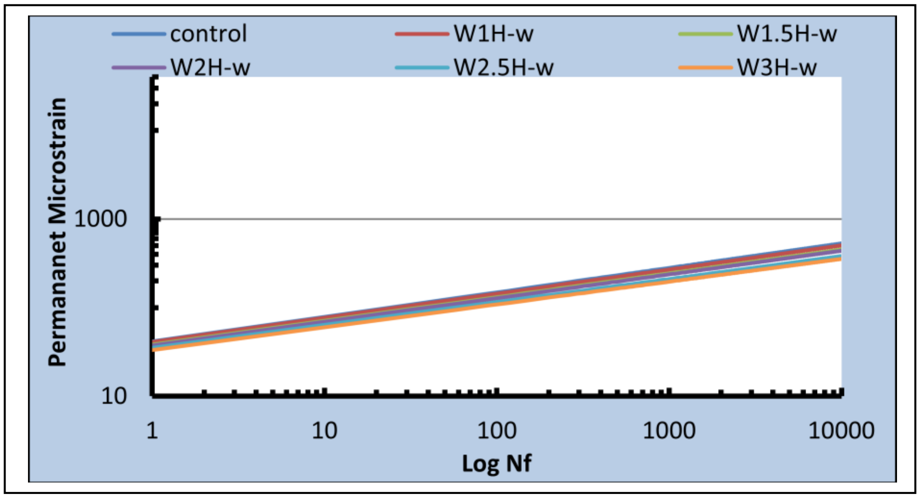

Figure 14. Effect of wet hydrated lime method on permanent deformation at 20°C .

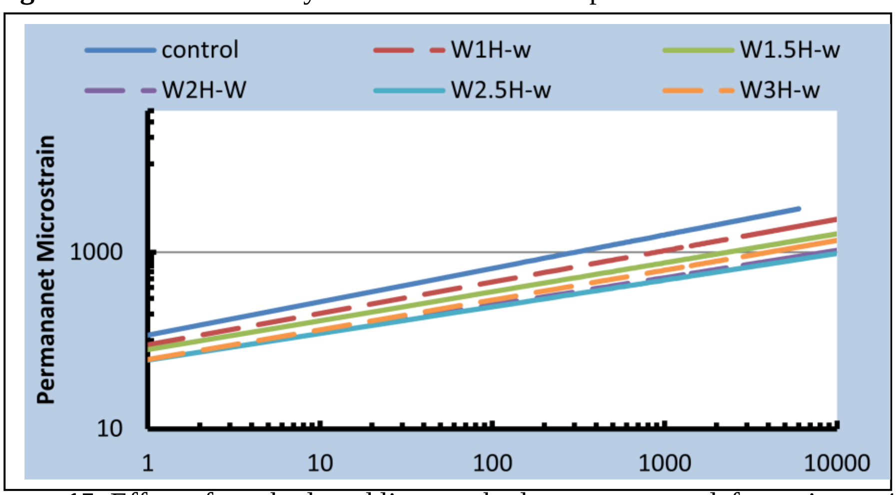

Figure 15. Effect of wet hydrated lime method on permanent deformation at 40°C.

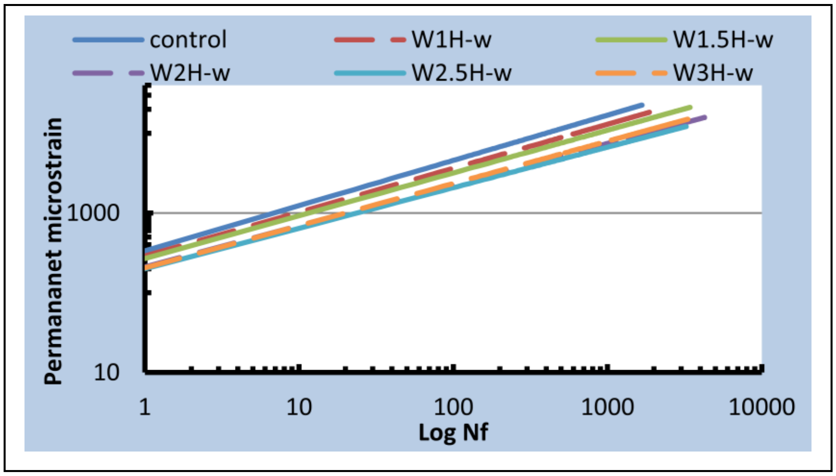

Figure 16. Effect of wet hydrated lime method on permanent deformation at 60^{o}C.

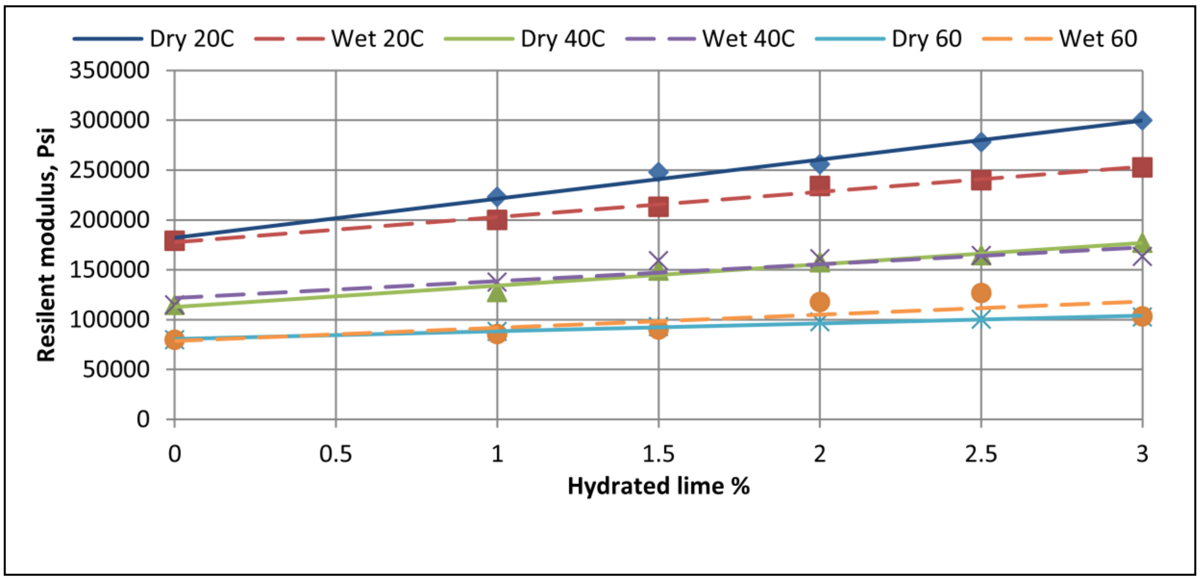

Figure 17. Effect of dry and wet hydrated lime addition method on Resilient Modulus.

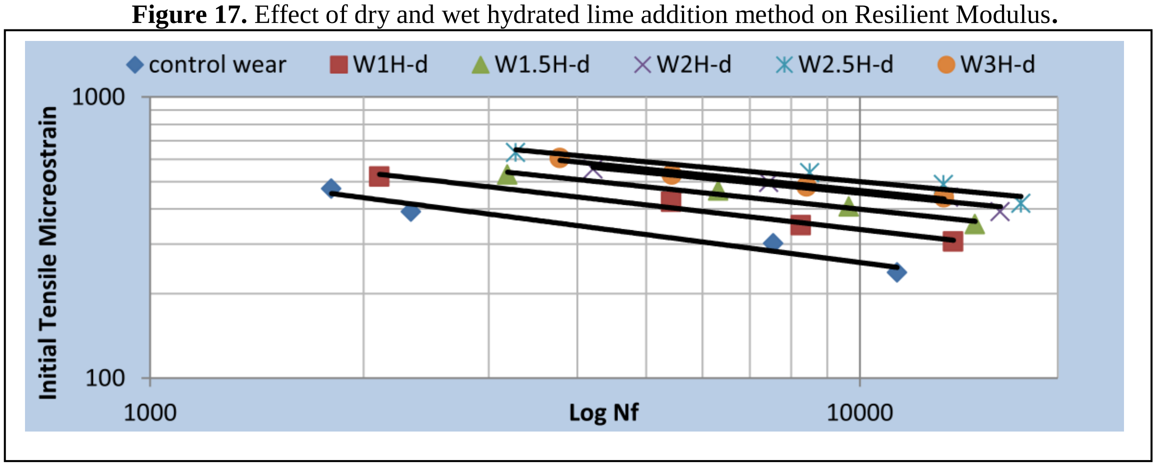

Figure 18. Effect of dry hydrated lime on fatigue cracking relationship.

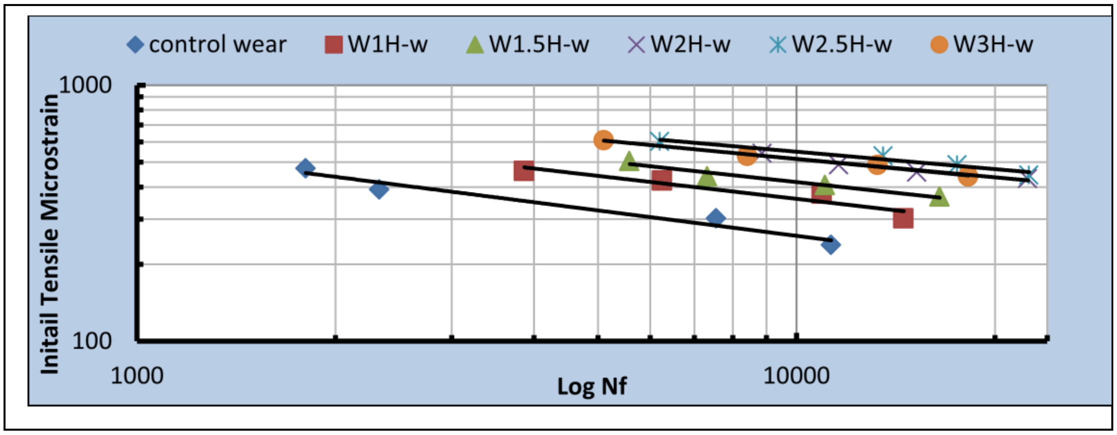

Figure 20. Effect of wet hydrated lime on fatigue cracking relationship **.**

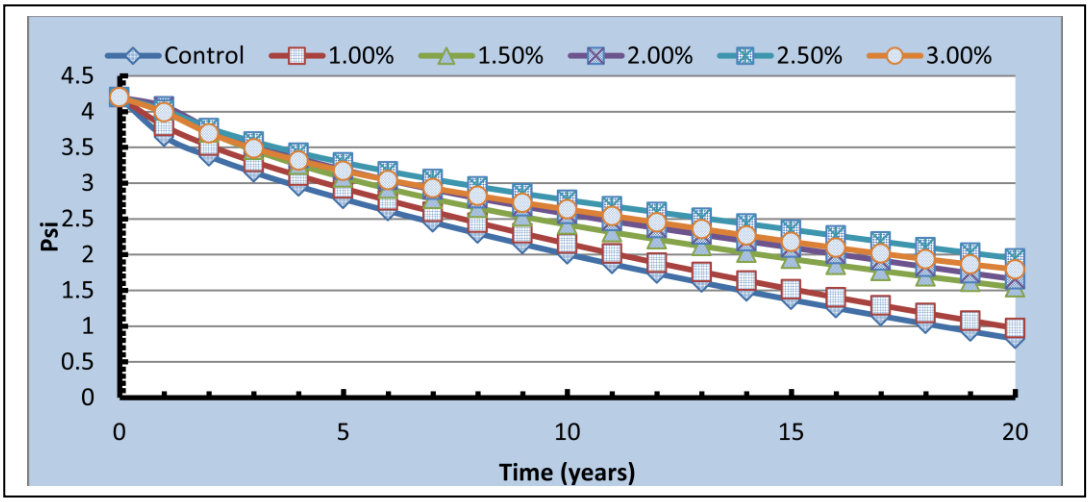

Figure 20. PSI- Time Relationship for control and mixes with dry hydrated lime**.**

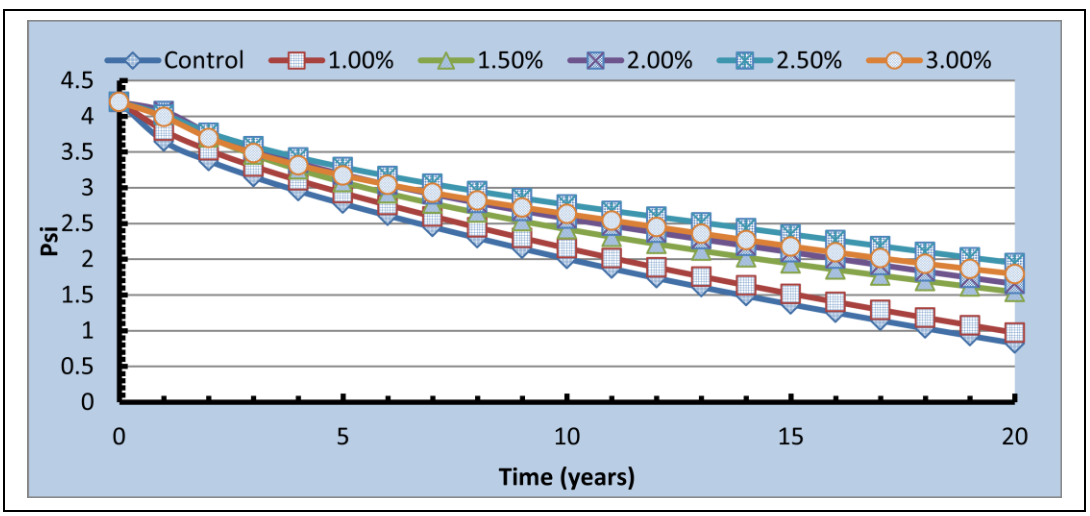

Figure 21 PSI- Time Relationship for control and mixes with wet hydrated lime.

Effect of Using Porcelanite as Partial Replacement of Fine Aggregate on Roller Compacted Concrete with Different Curing Methods

Dr. Abeer Abdulqader Salih
Assistant Professor
Mathematics and Science-Brookhaven College
email: asalih@dcccd.edu

Ziyad Majeed Abed
Assistant Lecturer
Engineering of Building and Construction - University of Technology
email: zma1978@gmail.com

ABSTRACT

Roller-Compacted Concrete is a no-slump concrete, with no reinforcing steel, no forms, no finishing and wet enough to support compaction by vibratory rollers. Due to the effect of curing on properties and durability of concrete, the main purpose of this research is to study the effect of various curing methods (air curing, 7 days water curing, and permanent water curing) and porcelanite (local material used as an Internal Curing agent) with different replacement percentages of fine aggregate (volumetric replacement) on some properties of Roller-Compacted Concrete and to explore the possibility of introducing practical Roller-Compacted Concrete for road pavement with minimum requirement of curing. Specimens were sawed from slabs of (380*380*100) mm for determination of Ultrasonic Pulse Velocity (UPV) and Voids volume. Results show that using (5) % porcelanite improved the results of UPV and Voids volume of Roller-Compacted Concrete (with air curing) as compared with reference Roller-Compacted Concrete (with permanent water curing) by percentages ranging from(3.6 to 28.9)% and (-8 to -15.5)% respectively.

Key words: Porcelanite, UPV, Voids volume, internal curing, roller compacted concrete, curing methods.

تأثير أستعمال مادة البورسيلنايت كأستبدال جزئي من الركام الناعم على الخرسانة المرصوصة بالحدل وبطرق انضاج مختلفة.

د.عبير عبد القادر صالح
أستاذ مساعد
الرياضيات والعلوم – كلية بروكهاڤين

زيـاد مجـيـد عـبـد
مدرس مساعــد
هندسة البناء والانشاءات – الجامعة التكنولوجية

الخلاصة

الخرسانة المرصوصة بالحدل هي الخرسانة عديمة الهطول والتي لا يتم فيها أستعمال حديد التسليح أو القوالب ولا تحتاج الى عملية الانهاء وكذلك يجب ان تكون ذات رطوبة كافية لتحمّل الحدل بواسطة الحادلات الهزازة.نتيجة لتأثير الانضاج على خصائص وديمومة الخرسانة لذا فإن الهدف الاساسي من البحث هو دراسة تأثير طرق مختلفة من الانضاج (الانضاج بالهواء ،الانضاج 7 ايام بالماء، الانضاج الدائمي بالماء) وبأستخدام البورسيلنايت (مادة محلية تستعمل كعامل أنضاج داخلي) وبنسب استبدال مختلفة من الركام الناعم (استبدال حجمي) على بعض خواص الخرسانة المرصوصة بالحدل وتحري مدى امكانية انتاج هذه الخرسانة لرصف الطرق لتكون اكثر عملية وبأستعمال الحد الادنى من متطلبات عملية الانضاج .يتم نشر الواح خرسانة بأبعاد (380*380*100) مم لعمل نماذج لفحوص الامواج فوق الصوتية والمسامية.تظهر النتائج ان استعمال (5%) بورسيلنايت يقوم بتحسين نتائج فحوص الامواج فوق الصوتية والمسامية للخرسانة المرصوصة بالحدل (بأستعمال الانضاج بالهواء) بالمقارنة مع الخرسانة المرصوصة بالحدل المرجعية (بأستعمال الانضاج الدائمي بالماء) بنسب تتراوح بين (3.6 to 28.9)% و- (-8 to -15.5) % على التوالي .

الكلمات الرئيسية: البورسيلنايت,فحص الامواج فوق الصوتية ,المسامية ,الانضاج الداخلي ,الخرسانة المرصوصة بالحدل,طرق أنضاج,أستبدال حجمي.

1. INTRODUCTION

The American Concrete Institute (ACI) committees 211.3R, 2009, and 116R, 2010, define Roller Compacted Concrete (RCC) as "concrete compacted by roller compaction; concrete that, in its unhardened state, will support a roller while being compacted". RCC is a zero-slump material that has to be compacted by roller to achieve the required density. RCC can be exposed directly to traffic, **European Ready Mixed Concrete Organization (ERMCO), 2012.**

Keifer, 1986 refers to that RCC having no reinforcements, no finishing, and is cast using vibratory and roller compaction. The application of RCC is mainly in the construction of dams, rapid placement of paving for highways and runways and for multi-layer placement of foundation.

At the 1930s, a form of RCC paving was reported in Sweden, **Anderson, 1986**. In North America, the first RCC pavement was identified by Seattle Office of **U.S. Army Corps of Engineers (USACE)** constructed about 1942, **ACI 325.10R, 2001.**

RCC compared with conventional slump concrete has less water to achieve a zero-slump concrete; consequently, less cement is required to produce an equivalent water to cement ratio. Reducing water in the mixture leads to less shrinkage and no bleed water, and less cement is one means of reducing thermal induced cracking. Roller Compacted Concrete Pavements mixes compared with conventional Portland Cement Concrete (PCC) contain larger volume of fine aggregate to ensure a uniform concrete mix with less surface voids, **Hansen, 1996.**

Three common ideas in roads construction were used in design of RCC; using rigid pavement concrete, using pavers and rollers (asphalt) and using proctor and density test (soil), as shown in **Fig. 1**.

2. MATERIALS CHARACTERISTICS

2.1 Cement

Sulphate Resisting Portland Cement (SRPC) (Type V) under commercial name of (Al-jeser) was used for RCC mixes throughout work. The physical properties, chemical analysis of the cement used and the compounds of cement calculated according to Bogue's equations, **ASTM C 150, 2005,** are given in **Tables 1** and **2.** The results conform to, **Iraqi specifications (IQS) (No.5:1984)**.

2.2 Coarse Aggregate

Aggregate predominately retained on the No.4 (4.75mm) sieve, in this work crushed coarse aggregate with a nominal size of (19 mm) was used and it was obtained from Al-Nibaai region. The gravel was sieved through sieve size of (25 mm) and washed with water, air dried, separated into different sizes, and stored in containers. Some properties of coarse aggregate are illustrated in **Table 3** according to (**IQS, No.45:1980**). The design overall gradation of aggregate is selected by using, **ACI 211.3R, 2009, ACI 325.10R, 2001,** and **State Commission of Roads and Bridges (SCRB) , 2003,** (type II binder course) dense gradation which is usually used for asphalt concrete pavement in Iraq and using the centerline of them. **Table 4** and **Fig. 2** illustrate the combined gradation used throughout the investigation.

2.3 Fine Aggregate

Al-ekhaider natural sand of 4.75 mm maximum size was used as fine aggregate in RCC mixes. The fine aggregate was sieved through sieve size (9.5 mm) to separate the aggregate particles of diameter greater than (9.5mm). The fine aggregate was then cleaned with water on sieve size 0.075mm (No.200 BS.) and after that it was air dried and separated into different sizes to be ready for use. Some properties of natural fine aggregate are illustrated in **Table 3** according to (**IQS, No.45:1980**).The grading of fine aggregates is shown in **Table 4**.

2.4 Porcelanite Aggregate

Porcelanite stone was used in this research in all mixes (except for reference mix). It was brought from Al-Rutba town in Al-Anbar Governorate and tested by **Iraqi Geological Survey Board (IGSB)**. It has a white color and is characterized by high permeability and low density. The large lumps were firstly crushed into smaller size manually with a hammer in order to use it as a partial replacement of fine aggregate with maximum size 4.75 mm, by screening on electrical sieve shaker. The replacement was (5, 8, 12, 16 and 20) % as a volumetric partial replacement percentages of the same sieve analysis and grading curve of fine aggregate. The required quantity of the porcelanite aggregate was washed with water in order to remove dust associated with crushing process of porcelanite stone. The porcelanite aggregate was soaked in water in the laboratory temperature for a suitable time period to bring the aggregate particles to saturation, which is recommended by, **ACI 211.2, 2004.Tables 5 and 6** show some physical and chemical analysis of fine porcelanite aggregate respectively.

2.5 Water

The water used in RCC mixes was potable water for both casting and curing of specimens.

3. PREPARATION OF RCC SLAB SAMPLES

3.1 Roller Compactor and Mould

The slab specimens used in this research were cast in steel mould having internal dimensions (380×380 mm) and depth of (100 mm). This mould consists of a steel plate base of (650×600×10 mm) surrounded by four steel angles with sections of (100×100×10 mm) and weight of (51 kg), as shown in **Fig. 3.**

The roller compactor apparatus, manufactured in a local workshop, is designed to simulate steel roller which is usually used in the field for compaction. It consists of steel skeleton as shown in **Fig. 4** and a solid cylinder (150 mm) in diameter, (330 mm) in length and (15 kg) in weight. The total weight of this apparatus is (36 kg). It is supplied with a container to carry the additional steel weights up to design load.

3.2 Mix design and proportions of RCC

RCC specimens are designed by modified proctor test according to, **ASTM D1557, 2002** (method C). This proportioning method involves establishing a relationship between the dry density and moisture content of the mix by compacting the mix in cylinder steel mould of (152.4mm) diameter and (116.4mm) height. A moisture-density test is used to determine the optimum moisture content which gives maximum dry density of RCC mixtures for each mix. The optimum moisture content is defined as the amount of water present in the mixture design that allows for maximum compaction.

In addition to reference RCC mixture, different percentages of saturated porcelanite content are used (5, 8, 12, 16, and 20) % by volumetric replacement of oven dried fine aggregate and different percentages of moisture content are used to determine the dry density-moisture content relationships and (14%) of cement content by weight of air dry aggregate, according to, **Shamil, 2011** results.

After determination the proportions of the mixes, the specimens are prepared. The total weight of aggregate which filled the above mould is approximately (3.5kg), for safety it is taken equal to be (4.5kg); this weight is separated by 7 sieves which are used in this work according to the retained percentage of these sieves multiplying the total weight of aggregate (4.5kg) by the retained percentage of each sieve.

The mixture is placed into the cylinder in five layers and each layer is compacted with (56) blows of a modified Proctor hammer of (4.5 kg) falling from (450 mm) height. When compaction is finished, the extension collar is removed and the surface of concrete is leveled with the mould, first weighting the mould with concrete, second the wet weighting of mixture is determined.

The above procedure is repeated with other percentages of moisture content. The specimen is withdrawn from mould by using loading jack and the wet specimen of mixture in the mould is weighed, the wet density can be calculated by using Eq. (1) as shown below:

$$\gamma_{wet} = Wm / Vol. \qquad (1)$$

The dry density can be found from Eq. (2):

$$\gamma_d = \gamma_{wet} / (1+ \omega) \qquad (2)$$

After that, the relationship between dry density and moisture content is plotted to find the optimum moisture content then the maximum dry density is calculated for every percentage of porcelanite as shown in **Fig. 5**. A total of 24 cylinder specimens were prepared for this research.

3.3 Casting of RCC slab specimens

3.3.1 Mixing

The same materials, gradation of aggregate and mix proportions which used in hammer compacted method; was used in casting RCC slabs. The retained percentage of aggregate on each sieve stayed the same, but the total aggregate content in this method was calculated to conform to the new volume of slab according to, **ACI 211.3R, 2009**. After mixing, the concrete was poured into the steel mould to construct slab specimen which was prepared for compaction.

3.3.2 Compaction

The mixture was placed in the slab mould and subjected to initial compaction on a vibrating table for 3 cycles of 30 seconds time interval. Such procedure is in agreement with that of, **Shamil, 2011**.The influence of this compaction is to create some initial compactive effort to the freshly laid surface, which is usually the case when using paving machine.

After initial compacting, the concrete mix is compacted using the roller apparatus. The mould was fixed in front of the roller compactor and subjected to three stages of rolling based on the work done by, **Sarsam, 2002,** to each stage15 passes were applied. This number of passes is suitable to achieve the good rolling with little effort, and the rolling action is taken in x-x direction, then the same sequence has been repeated in the y- y direction to insure the compaction of the slab sides as shown in **Fig. 6**. This process is used in three stages on slab specimen to obtain the designed dry density.

First stage: A total load of (1.1 kg/cm width) (using roller compactor weight) is implemented with 15 passes of the roller in each direction. The concrete is settled in a level position and completely fills the slab mould. This can represent the initial compaction in the field.

Second stage: The total load is increased to (3.2 kg/cm width) (using 69kg standard loads + roller compactor weight) with 15 passes in each direction. This may simulate the intermediate field compaction.

Third stage: The total load is increased to (5.3 kg/cm width) (by using 138kg standard loads + roller compactor weight) with 15 passes of the roller in each direction. At this stage, the slab surface is smooth and level. This represents the finishing compaction in the field.

3.3.3 Curing

After compaction, the slab specimens are leveled by hand trawling, and covered with polyethylene sheet and sealed with tape in the laboratory for about (24) hrs at laboratory temperature to prevent evaporation of moisture from the fresh concrete. After that, the specimens were cured with different curing methods according to, **Abed, 2014**, as followed:

- Water curing is for 1 day and then put in air until test.
- Water curing is for 7 days and then put in air until test.
- Permanent (continuous) water curing.

3.3.4 Obtaining Sawed Specimens

According to, **ASTM C42, 2004,** wet concrete diamond sawing process is used to cut the slabs to obtain cubes of (100 × 100 × 100 mm) and beams of (100×100×380 mm).

4. TESTS OF RCC SPECIMENS

4.1 Determination the Ultrasonic Pulse Velocity (UPV) test of RCC specimens

Ultrasonic Pulse transit times are measured by direct transmission method. This test is carried out according to, **ASTM C597, 2002,** on beam and cube specimens for the three different direction. Portable ultrasonic concrete tester known as (PUNDIT) with frequency 55 KHz and accuracy of 0.1 μ sec, is used for this purpose. Specimens were kept under curing method conditions until testing. The loading rate used in the test was 0.3 N/mm² per second. The test was conducted at ages of 7, 28, 56 and 90 days. The pulse transit path length is measured accurately and the time of its travelling was recorded. The pulse velocity is calculated by using Eq. (3).

$$V = L / T \tag{3}$$

4.2 Determination the Voids volume test of RCC specimens

Voids volumes are calculated according to, **ASTM C642, 2006**, in Eq. (4) as follows:-

1- The specimen is weighted and dried in an oven at a temperature of (100-110) °C for 24 hrs. . After removing the specimen from the oven, it is allowed to cool and is weighed and designated as (**A**).

2- The specimen is placed in suitable receptacles, covered with tap water and boiled for 5 hrs. . After that the specimen is allowed to cool for not less than 14 hrs. The specimen is surface dried by removing surface moisture with a towel, and weighed. This weight is to be the soaked, boiled, surface-dried mass (**C**).
3- The specimen is suspended by a wire and the apparent mass in water is determined. This weight is considered to be the apparent mass (**D**).

$$\text{Volume of permeable Voids, \%} = [(C-A)/(C-D)] \times 100 \quad (4)$$

5. DISCUSSIONS

Fig. 7 and **Fig. 8** show the relationship between the UPV and voids volume respectively with age of the RCC specimens for all mixtures of reference and internally cured RCC with (5, 8, 12, 16 and 20) % porcelanite as lightweight aggregate (LWA) replacement of fine aggregate and cured by different methods (air curing, 7 days water curing and permanent curing).

UPV (non-destructive) test is carried out in order to investigate the properties of concrete and also investigates the homogeneity of concrete due to internal curing (IC) agent (porcelanite aggregate) because of the sensitivity of the UPV as an indicator of changes in concrete properties. UPV results can be relied upon. The idea is testing the range of filling pores of the cement paste with cement hydration products thus causing them to get smaller and decreasing the interiors voids, and then increasing the density of cement paste, **Hoff, 2002.**

Generally, high results of UPV were recorded for internally cured RCC with 5% porcelanite replacement as compared with that of reference RCC and other percentages of porcelanite replacement. This increasing in UPV can be attributed to improving the density and homogeneity of RCC due to IC water which keeps on cement hydration. The micro cracks are inhibited and hence the UPV will be improved, **BS1881: part 203, 1986.** The 5% porcelanite using 7 days and permanent curing shows higher UPV than reference RCC due to the effect of IC.

Internal curing with porcelanite aggregate as partial fine aggregate replacement in percentages of (8, 12, 16 and 20) % decreases UPV of concrete compared to 5% porcelanite replacement. The decreasing in UPV can be attributed to; firstly, high moisture content due to high percentage of saturated porcelanite aggregate. Secondly, porcelanite as porous material make UPV decrease due to the high voids within RCC.

Leslie and Cheesman, 1949, and **IS: 13311-Part I, 2002,** listed UPV ranges to indicate the homogeneity and quality of concrete as shown in Tables (2-9) and (4.12). All calculated UPV results show that the internally cured and reference RCC specimens in all methods of curing and for all ages are higher than that of (4.575 and 4.5 Km/sec) respectively. This means homogenous RCC with high quality can be obtained by these proportions, compaction and curing methods.

Apparently, introduction of highly porous LWA into the dense cement matrix increases the voids volume and thus permeability and diffusivity of concrete. The results demonstrated that the voids volume of the RCC specimens that were cured in different curing methods decreases with the progress of the age; this may be due to the fact of the continuous hydration process and the ability of the paste to fill voids in the mixes.

Porcelanite may have a positive effect on RCC properties, as mentioned before, like improving elastic compatibility with cement paste that will lower micro cracking, improving

Interfacial Transition Zone (ITZ) between porcelanite and cement paste matrix which effect on permeability, eliminate or reduce cracks due to autogenous shrinkage.

For all that, the replacement with 5% porcelanite gave the lowest voids volume that can be achieved and which is better than that of reference RCC and other percentages of replacements. The percentage of decrease in voids volume at 5% porcelanite percentage for 28 and 90 day ages using air, and permanent curing methods compared to reference RCC is in the range of (9.7-34.4) % and (13.7-31.6) % respectively.

Voids volume of RCC specimens having other percentages of replacement of porcelanite in all methods of curing show higher percentages of variations than that of reference RCC, the range of variations is in the range of (-0.9-135.3) %. This behavior may be due to increase in the quantity of porcelanite aggregate with the increases in percentage of replacement which consequently increase the IC water which forms large pores inside concrete and reduces the integrity of the ITZ. This will increase the voids volume of RCC concrete. The other possible reason is the increase in Porcelanite replacement percentage leads to increasing the voids volume of fine aggregate which increases voids volume of the paste.

6. CONCLUSIONS

The following conclusions can be drawn from analysis of the results of experimental work which has been done to assess the effect of using porcelanite on RCC:

1. Porcelanite aggregate (light weight cheap and local material) could be used as an internal curing agent by a partial replacement material of fine aggregate.
2. Best percentage of porcelanite used is 5% as a percentage (volumetric) replacement of fine aggregate. This percentage gave an improvement in UPV and Voids volume of RCC.
3. Three methods of curing (air, permanent and 7 day water curing) were used in this study. Permanent water curing has great effect on UPV and Voids volume of RCC specimens than other curing methods for the same RCC mixture.
4. The results of Voids volume and UPV of 5% porcelanite replacement RCC and using air are less than that of the reference RCC using permanent water curing. This result could be very beneficial in practical work in road application fields.
5. UPV of RCC is improved by internal curing with 5% porcelanite replacement and has the highest value compared to the other mixes which ranges between (4.81-5.34 Km/s), (4.87-5.15 Km/s) for reference RCC and (4.6-5.13 Km/s) for others.
6. Voids volume of RCC samples with porcelanite percentage 5% cured with three methods of curing is lower than that with reference RCC cured with permanent curing at all ages. Reference RCC exhibits lower Voids volume than specimens cured with other curing methods and at (8, 12, 16 and 20) % porcelanite replacement.

REFERENCES

- Abed, Z.M., 2014, *Assessing the Effect of Using Porcelanite on Properties of Roller Compacted Concrete*, MSc. thesis, Department of Civil Engineering, University of Baghdad.

- ACI Committee 116R, 2010, *Cement and Concrete Terminology*, ACI Manual of Concrete Practice.

- ACI Committee 211-3R, 2009, *Guide for Selecting Proportions for No-Slump Concrete*, ACI Manual of Concrete Practice.

- ACI Committee 211-2, 2004, *Standard Practice for Selecting Proportions for Structural Lightweight Concrete*, ACI Manual of Concrete Practice.

- ACI Committee 325-10R, 2001, *State-of-the-Art Report on Roller-Compacted Concrete Pavements*, ACI Manual of Concrete Practice.

- Anderson, R., 1986, *Roller-Compacted Concrete Pavements Physical Properties*, CBI Report No. Ra 3:86, Swedish Cement and Concrete Research Institute, Stockholm, Sweden.

- ASTM C 42, 2004, *Standard Test Method for Obtaining and Testing Drilled Cores and Sawed Beams of Concrete*, Annual Book of ASTM Standards, Vol. 04.02,, PA., United States.

- ASTM C 150, 2005, *Standard Specification for Portland Cement*, Annual Book of ASTM Standards, Vol. 04.01, PA., United States.

- ASTM C597, 2002, *Standard Test Method for Pulse Velocity through Concrete*, Annual Book of ASTM Standards, Vol. 04.02, PA., United States.

- ASTM C 642, 2006, *Standard Test Method for Density, Absorption, and Voids in Hardened Concrete*, Annual Book of ASTM Standards, vol. 04.02, PA., United States.

- ASTM D1557, 2002, *Standard Test Methods for Laboratory Compaction Characteristics of Soil Using Modified Effort*, Annual Book of ASTM Standards, Vol. 04.08, PA., United States.

- British Standards, BS 1881 Part 203, 1986, *Recommendations for measurement of velocity of ultrasonic pulses in concrete*.

- European Ready Mixed Concrete Organization (ERMCO), 2012, *Guide to roller compacted concrete for pavements*, Draft 3.

- Hansen K.D., 1996, *Roller Compacted Concrete: A Civil Engineering Innovation*", Concrete International, March, pp. (49-53).

- Hoff, G.C., 2002, *"The Use of Lightweight Fines for the Internal Curing of Concrete"*, Northeast Solite Corporation.

- Iraqi Specifications, No.5, 1984, *The Portland Cement*.

- Iraqi Specifications, No.45, 1980, *Aggregates from Natural Sources for Concrete and Building Construction*.

- Indian Standards, 2002, *Method of Non-destructive testing of concrete*, Part 1: Ultrasonic pulse velocity, IS: 13311-Part I.

- Keifer, O.JR. , 1986, *Paving with Roller Compacted Concrete*, State of the Art, U.S., Army Corps of Engineers, North Pacific Division Portland, Oregon.

- Leslie, J. R. , and Cheesman, W.J., 1949, *An Ultrasonic Method Of Studying Deterioration and Cracking in Concrete Structures*, ACI Journal.

- Sarsam, S.I., 2002, *Evaluation of roller compacted concrete pavement properties*, Engineering and development scientific journal of Al-mustansiria University, Vol. 6, No.1.

- SCRB, 2003, *Standard specification for roads and bridges*, Ministry of Housing and construction, state commission of roads and bridges, Iraq.

- Shamil, A., 2011, *Laboratory investigation on Roller Compacted technique in Concrete construction*, M.Sc., Thesis, Department of Civil Engineering, University of Baghdad.

NOMENCLATURE

A= mass of oven-dried specimen in air, gm
C= mass of surface-dry specimen in air after immersion and boiling, gm
D= apparent mass of specimen in water after immersion and boiling, gm
V= pulse velocity (m/sec).
L= distance between transducers, (m), and
T= transit time (sec).
Vol. = the volume of the cylinder mould, cm³.
Wm = the wet weighting of mixture, gm.
γd = the dry density, gm/cm³.
γwet = the wet density, gm/cm³.
ω = the moisture content, %.

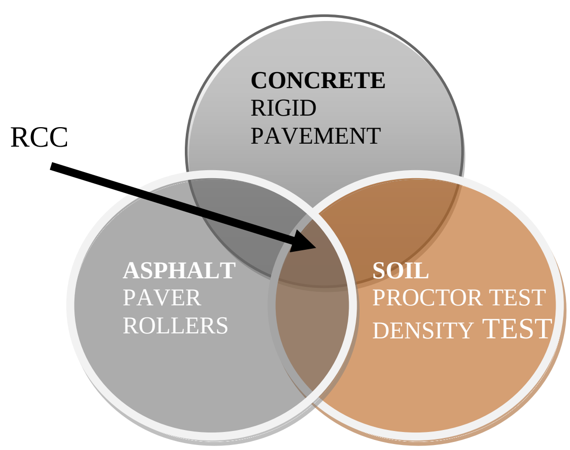

Figure 1. Multiple personalities, ***Adaska*** *and* ***Tull (PCA) (2011)***

Table 1. Physical properties of SRPC *****

Properties Physical	**Test Result**	***IQS (No.5:1984) limits***
Specific surface area, Blaine method, m^2/kg *	324	≥ 250
Setting time , Vicat's Method Initial setting , hr. : min Final setting , hr. : min	 1:30 3:40	 ≥ 45 minutes ≤ 10 hours
Compressive Strength MPa 3-days 7-days	 18.5 23.2	 ≥15 ≥23

* Performed by the *IGSB.*

Table 2. Chemical composition and main compounds of SRPC *

Oxide composition	**% by weight**	***IQS (No.5:1984) limits***
SiO2	21.58	----
CaO	62.2	----
MgO	2.75	≤ 5.0
Fe2O3	4.76	----
Al2O3	3.94	----
SO3	2.23	≤ 2.5
Loss on ignition	2.5	≤ 4.0
Insoluble residue	0.71	≤ 1.5
Lime saturation factor	0.88	0.66-1.02
Main compounds (Bogue's equations) **		
C3S	49.57	----
C2S	24.47	----
C3A	2.38	≤ 3.5
C4AF	14.48	----

* Performed by *IGSB.*

** According to, *ASTM C 150, 2005.*

Table 3. Properties of coarse and fine aggregate*

Type of aggregate	Bulk Specific Gravity	Absorption	SO_3 %
coarse aggregate	2.56	0.6	0.06
fine aggregate	2.76	1.2	0.3

* Performed in laboratory of Building Materials-University of Baghdad.

Table 4. Grain size distributed used for RCC

Sieve Size (mm)	Finer by weight %	Grading *SCRB 2003*	Grading *ACI 325.10R & ACI 211.3R*
25.4	100	100	100
19.2	94	90-100	82-100
12.5	80	70-90	72-93
9.5	71	56-80	66-85
4.75	56	35-65	51-69
2.36	40	23-49	38-56
0.3	12	5-19	11-27
0.075	3	3-9	2-8

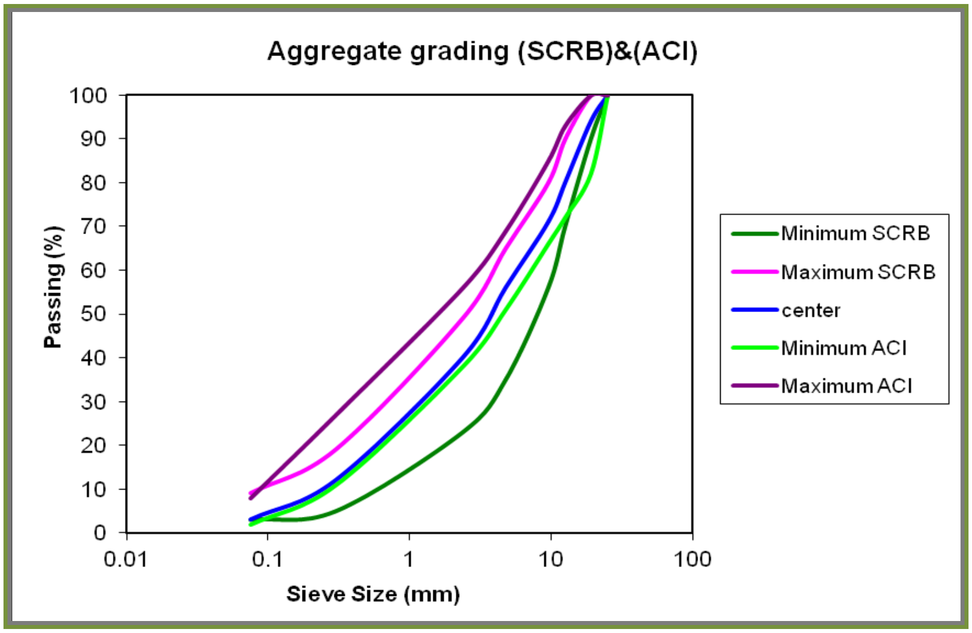

Figure 2. Grading of aggregate according to *SCRB (2003)*, *ACI 325.10R (2001)* and *ACI 211.3R (2009).*

Table 5. Some physical properties for porcelanite aggregate *

Property	Test result
Specific gravity	1.68
Absorption, %	42
Dry rodded unit weight ,kg/m³	860**

* Physical properties testing were performed by *IGSB.*
** Within the limits of *ASTM C330 (2005)* (1120 kg/m³ max.) for fine aggregate.

Table 6. Chemical properties for porcelanite aggregate *

Oxide composition	% by weight
SiO2	70
CaO	8.2
MgO	2.75
Fe2O3	0.98
Al2O3	3.33
SO3	0.1
Loss on ignition	9.5

* Chemical properties testing were performed by *IGSB*.

Table 7. Velocity criterion for concrete quality grading, IS: 13311- Part I (2002)

Pulse velocity by cross-probing,Km/sec.	Concrete quality grading
Above 4.5	Excellent
3.5 to 4.5	Good
3.0 to 3.5	Medium
Below 3.0	Doubtful

Table 8. Suggested UPV for concrete, Leslie and Chessman (1949).

General condition	Ultrasonic pulse velocity (Km/sec)
Excellent	> 4.575
Good	3.66 – 4.575
Questionable	3.05 – 3.66
Poor	2.135 – 3.05
Very poor	< 2.135

Figure 3. Mould of slab specimen

Figure 4. Roller compactor apparatus

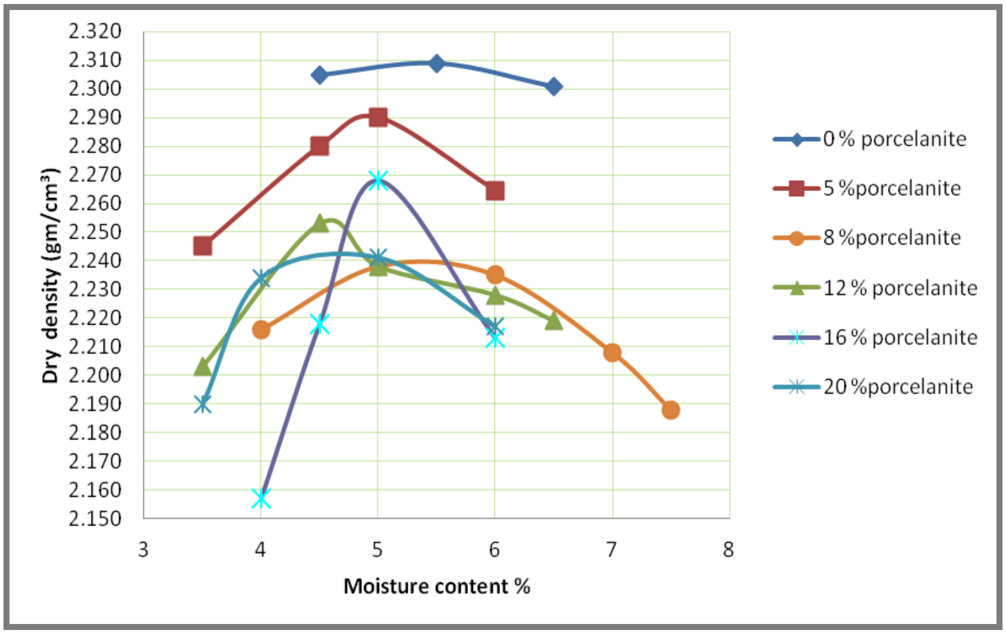

Figure 5. Dry density-moisture content relationships for different RCC mixtures

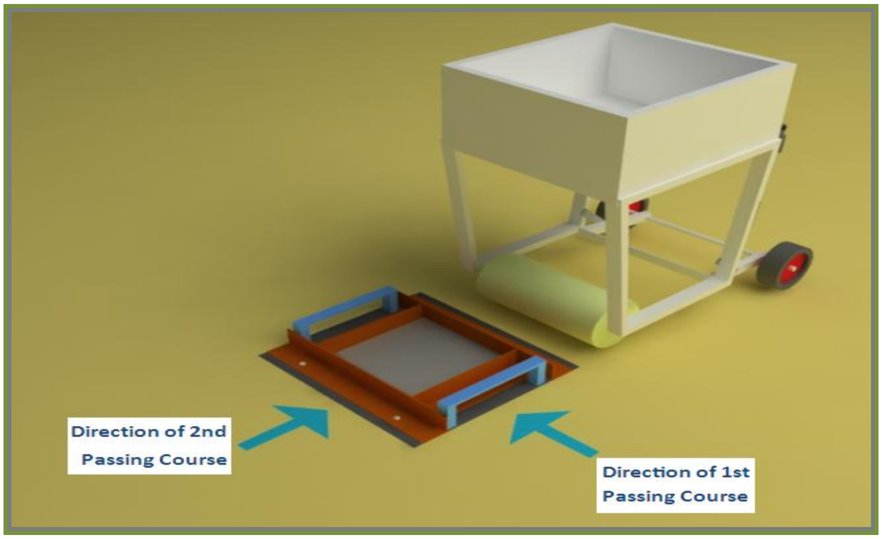

Figure 6. Direction of rolling compactor

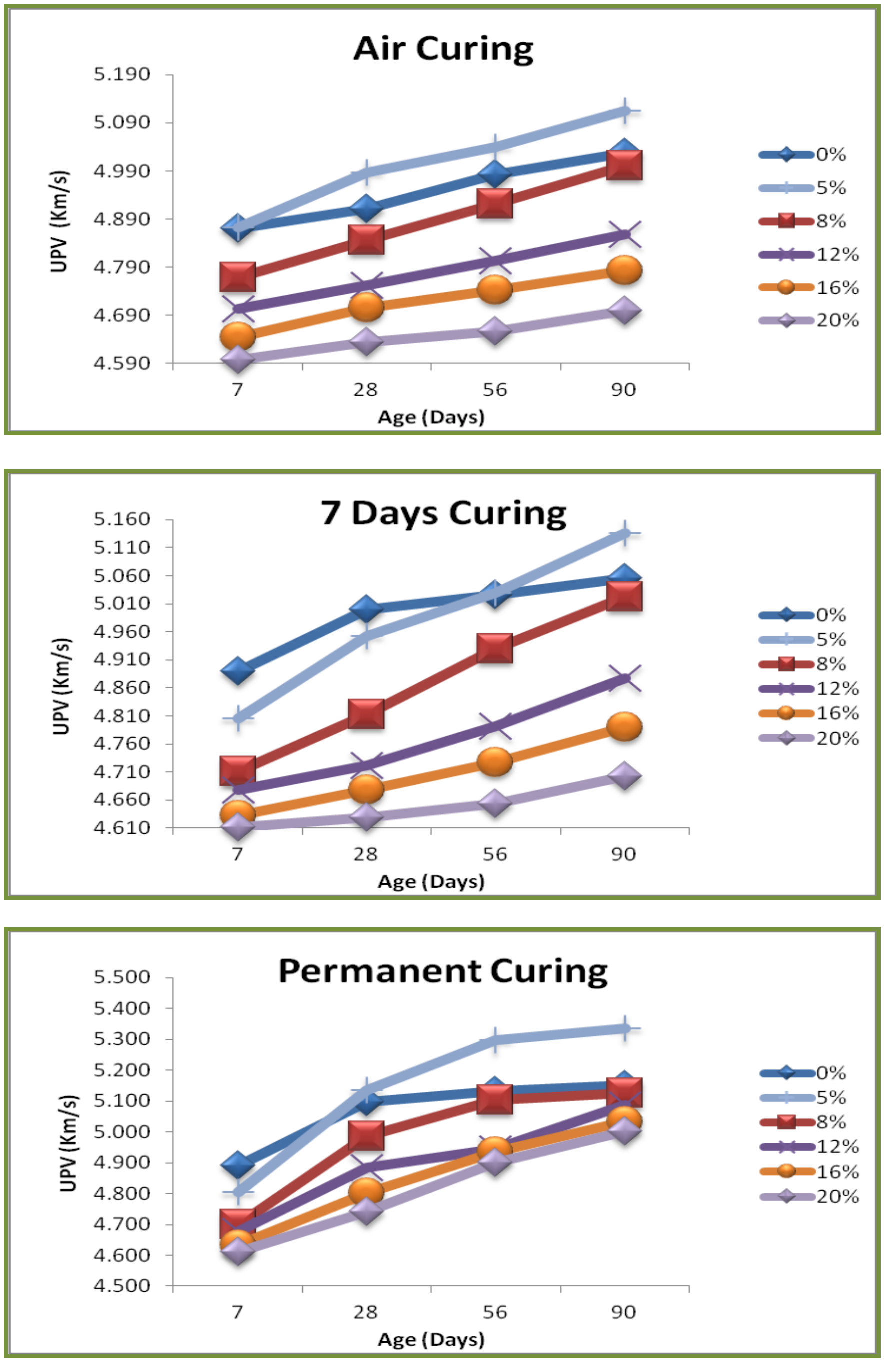

Figure 7. UPV development of RCC with porcelanite replacement percentages.

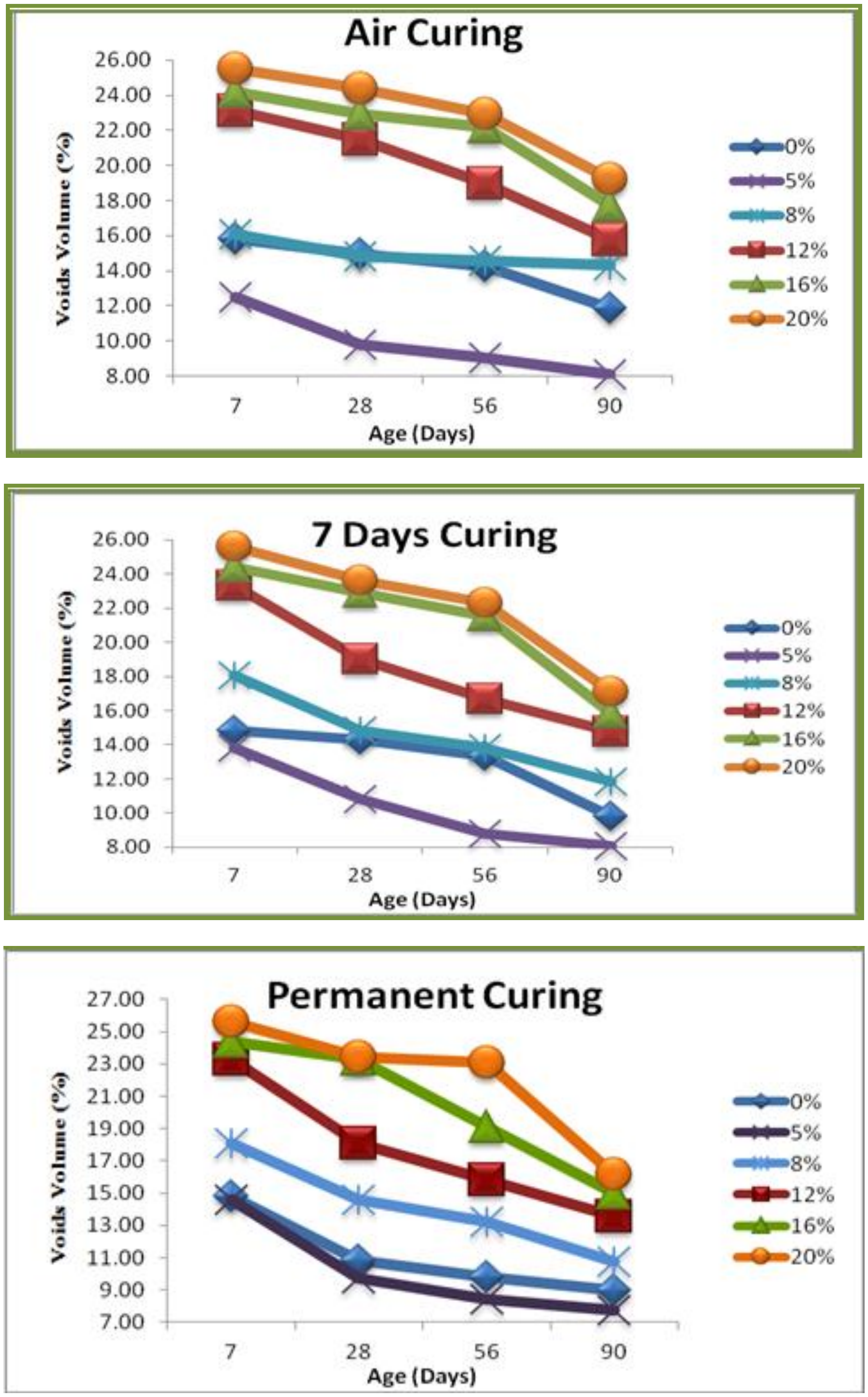

Figure 8. Voids volume development of RCC with porcelanite replacement percentages.

Response of Laced Reinforced Concrete One Way Slab to Repeated Loading

Abaas Abdulmajeed Allawi
Assistant Professor
College Engineering - University of Baghdad
E-mail:abbasallawi2004@yahoo.com

Hussain Askar Jabir
Assistant Lecturer
College Engineering - University of Wassit
E-mail:askar_hussain@yahoo.com

ABSTRACT

Test results of nine reinforced concrete one way slab with and without lacing reinforcement are reported. The tests were designed to study the effect of the lacing reinforcement on the flexural response of one way slabs. The test parameters were considered is the lacing steel ratios of (0, 0.0025, 0.0045, and 0.0065), flexural steel ratios of (0.0025, 0.0045, and 0.0065) and span to the effective depth ratios of (11, 13, and 16). Two specimens had no lacing reinforcement and the remaining seven specimens had the lacing reinforcement. Four point bending test were carried out, one of the specimens was tested under the static load applied gradually up to failure and the other specimens were tested under repeated load (5 cycles) loading-unloading to 80% of the ultimate load of the control specimen then loaded manually by the hydraulic jack up to failure. The specimens showed an improving in ultimate load capacity ranged between (54.54% - 100%) as a result of increasing the lacing steel ratio to (0.0065) and decreasing the span to effective depth ratio by 31.25% respectively with respect to the control specimen. Additionally the using of lacing steel reinforcement leads to reducing the residual deflection by about (57.24%) for the specimen with the largest lacing reinforcement compared with the control specimen (without lacing reinforcement).

Key words: laced one way slab**,** reinforced concrete, crack, residual deflection, repeated loading.

إستجابة البلاطات الخرسانية المسلحة الاحادية الاتجاه والحاوية على حديد متعرج للاحمال المتكررة

عباس عبد المجيد علاوي
أستاذ مساعد
كلية الهندسة-جامعة بغداد

حسين عسكر جابر
مدرس مساعد
كلية الهندسة-جامعة واسط

الخلاصة

تم في هذا البحث مناقشة النتائج العمليه لتسعة بلاطات خرسانيه احادية الاتجاه مسلحه وحاويةعلى تسليح متعرج. ان الغرض من هذا البحث هو دراسه تأثير استخدام التسليح المتعرج على سلوك واستجابة البلاطات الاحادية الاتجاه. وكانت المتغيرات هي نسبة حديد التسليح المتعرج وهي(0,0.0025,0 0.0045 , 0.0065), نسبة الحديد الرئيسي وهي (0.0025, 0.0045 , 0.0065) ونسبة الطول الصافي الى العمق الفعال للبلاطة وهي (13,16 , 11). اثنان من العينات لاتحتوي على حديد متعرج اما السبعة المتبقيه فكانت جميعها تحتوي على حديد التسليح المتعرج. تم فحص احدى العينات الغير حاوية على حديد متعرج ستاتيكيا الى الفشل بينما تم فحص العينات المتبقية تحت تاثير الاحمال المتكررة بخمسة دورات تحميلية الى حد 80% من قيمة الحمل الاقصى للعينة المفحوصة ستاتيكياً ثم تحميل العينة الى حد الفشل .بينت النتائج العملية بان التحمل الكلي للبلاطات تحسن بمقدار (54,54%) نتيجه لاستخدام الحديد المتعرج بنسبة (0.0065) و بمقدار (100%) كنتيجة لتقليل نسبة الطول الصافي الى العمق الفعال بمقدار (31,25%) للبلاطات الحاوية على حديد متعرج بنسب متساوية. من ناحيه اخرى فأن استخدام الحديد المتعرج قلل وبشكل ملحوظ مقدار الهطول الدائمي للبلاطات بنسبة (57,24%) للبلاطة ذات اعلى نسبة تسليح متعرج مقارنة مع البلاطة بدون حديد تسليح متعرج.

الكلمات الرئيسيه: البلاطة الاحادية الاتجاه ذات التسليح المتعرج , الخرسانة المسلحة, التشقق, الهطول الدائمي, التحميل المتكرر.

1. INTRODUCTION

Traditional reinforced concrete (RC) is known to have limited ductility and concrete confinement capabilities. The structural properties of RC can be improved by modifying the concrete matrix and by suitably detailing the reinforcements. A laced element is reinforced symmetrically, i.e., the compression reinforcement is the same as the tension reinforcement. The straight flexural reinforcing bars on each face of the element and the intervening concrete are tied together by the truss action of continuous bent diagonal bars as shown in **Fig. 1**. The dashed lacing bar indicates the configuration of the lacing bar associated with the next principal steel bar. In other words, the positions of the lacing bars alternated to encompass all temperature steel bars. Laced reinforced concrete (LRC) enhances the ductility and provides better concrete confinement, **UFC 3-340-02, 2008**.

The primary purpose of shear reinforcement is not to resist shear forces, but rather to improve performance in the large-deflection region by tying the two principal reinforcement mats together. In the design of conventional structures, the primary purpose of shear reinforcement is to prevent the formation and propagation of diagonal tension cracks, **Stanley Woodson, 1992**.

A repeated load is a force which is applied many times to a member, causing stress in the material that continually varies, usually through some defined range. If a stress is developed in a member and then released, the member is said to have been subjected to a cycle of stresses. Further, if a tensile stress has been developed, and released, and then a compressive stress is developed, and this stress then is released, the member is said to have been subjected to a reversed cycle of stresses or, briefly, to a reversal of stresses, the reversal of stresses is complete if the opposite stresses are of equal magnitudes.

Investigations were carried out by **Lakshmanan et al., 2008**, to study the behavior of laced reinforced concrete beams with and without steel fibers under shear loading. Reversed cyclic shear loading tests were also carried out on the LRC beams with and without steel fibers.

Behaviour of LRC and its application for blast resistant design has been discussed in details by **Lakshmanan, 2008**. Response of LRC beam under low shear, span to depth ratio is also presented. It was also observed that cyclic ductility is significantly lower than static ductility for these beams.

Behavior of the concrete one way slabs reinforced by the steel bars made of scrap metals and subjected to cyclic load with different cycles loads were conducted by **Adom-Asamoah and Kankam, 2009**, as a results of this study, the stiffness of slab, failure load, and the ultimate deflection were reduced when comparing the behavior of the specimen tested under monotonic load with that subjected to cyclic loading.

Sivagamasundari and Kumaran, 2011, investigated the behavior of the one-way slabs reinforced with Glass Fiber Reinforced Polymer GFRP bars and compared with those of traditionally reinforcement subjected to cyclic loading with variable and constant amplitude fatigue loads. A nonlinear finite element analysis is also performed by considering the material nonlinearity for the entire size of the specimens; a good agreement was evident on comparison the analytical model results with the experimental test results.

Anandavlli, 2012, applied reversed cyclic load on two Laced Steel Composite Concrete (LSCC) beams, one of them for 45° and another for 60° lacing angle. Reverse cyclic loading consists of loading and unloading the beam in both the directions alternatively.

2. RESEARCH SIGNIFICANCE

To know the effectiveness of the lacing reinforcement on the behavior of the one way slab. A better understanding of the contributions of the shear reinforcement will allow the designer to compare the benefits of using (or not using) shear reinforcement. The repeated response of laced reinforced concrete one way slab under four point bending test was studied experimentally. The tests focused on the influences of lacing steel ratio, flexural steel ratio and clear span to effective depth ratio of slab.

3. TEST SPECIMENS

The slabs were designed to reflect the interaction of the lacing reinforcement with the other primary parameters. All slabs were designed to be simply supported conditions, the dimensions, and steel reinforcement ratios were selected according to **ACI 318M-2014** code, and to satisfy and meeting with **UFC 3-340-02, 2008**, requirements for the laced reinforced concrete structures. Details of the test specimens, both with and without laced reinforced steel are discussed hereafter. The dimensions of the tested slabs are (2000mm × 700mm) and different thickness of (135mm, 160mm, and 185mm). Two of these slabs were without lacing reinforcement (reference specimens), and seven specimens were having the lacing reinforcement with 45º lacing angle, with various tension steel ratio (ρt=0.0025, 0.0045, and 0.0065) lacing steel ratio (ρs=0.0025, 0.0045, and 0.0065), and clear span to effective depth ratio (L/d=11, 13, 16), as shown in **Fig. 2**. A total of nine specimens (**SS45/0**, **RS45/0, RS45/25**, **RS45/45**, **RS45/65**, **RS25/45**, **RS65/45**, **RM45/25** and **RL45/25**) were tested. The specimen designation can be explained as follows. The first symbol indicates the type of load (S=static load and R=repeated load) the second symbol indicates the thickness of slab (S=small thickness=135mm, M=medium thickness=160mm, and L=large thickness=185mm), the third symbol before slash indicates the flexural steel ratio (25=0.0025, 45=0.0045, and 65=0.0065), and the last symbol denotes to the lacing steel ratio (0=no lacing reinforcement, 25=0.0025, 45=0.0045, and 65=0.0065). The entire characteristics and details of the tested specimens are listed in **Table 1**, and **Table 2** shows the details of each group.

The properties of the steel used in the reinforcing mats of the slabs are listed in **Table 3**. The specimens were constructed using a normal density concrete with a compressive strength of approximately 30 MPa. A mechanical mixer was used to produce the concrete using normal Portland cement, fine aggregate, and crushed coarse aggregate of 19 mm maximum nominal size. The mixing processes were performed according to the procedure of **ASTM C192-2002**. **Table 4** lists the final strengths based on the average values from the tests performed on at least three 150 x 300mm cylinders for each test specimen. The tensile strength of the concrete was determined by performing the split cylinder tests.

4. INSTRUMENTATION

The instrumentation of the slab specimens was designed to register the maximum quantity and most reliable data of local strains, deflections and crack widths, to achieve the behavior of the laced reinforced concrete one way slab. Uniaxial electrical resistance (foil) strain gauge was the adopted method to measure the strain in both concrete and steel. Two different sizes of pre-wired strain gages of (120Ω) resistance, made in Japan for TML, were used in the test, All the used types of strain gauges were normally installed by the recommended adhesive (CN-E and CN-Y) before which the contact surface was suitably prepared. In order to measure the vertical deflection of the tested slabs LVDT (Linear variable deferential transformer) was adopted tool to measure the deflection at mid span and at the two thirds part of the tested slab, were fixed to lower steel beams of the testing machine under the tension face of the specimens.

5. TEST PROCEDURE

All specimens were tested using the hydraulic testing frame. The specimens were a simply supported condition on the shorter opposite sides, where the specimen was placed inside the testing frame so that supports lines, points load, LVDT were fixed in their correct locations, as shown in **Fig. 3**. The specimens were loaded by two equal lines load at third parts of the tested slab (four point bending test). The static load was increased gradually by a step load of (3.63 kN) up to failure. Repeated load was applied by incremental loads gradually up to (80%) of the ultimate load level of the control specimen (**SS45/0**) and then release the load gradually to zero with (5 cycles) loading-unloading. Then the slabs were loaded manually up to failure by using a hydraulic jack of (500 kN) capacity.

At each loading stage, the test measurements included the magnitude of the applied load, deflection of the slab at three locations, cracks width, strain in steel reinforcement (tension and lacing steel bars), and strain in compressive face of slab were recorded. At the end of each test, the cracks propagated were marked and the crack pattern and mode of failure for each specimen were carefully examined.

6. TEST RESULTS AND DISCUSSION

6.1 General Behavior and Crack Patterns

For a simply supported one-way slab subjected to equal line loads at the third points, the middle third of the span is subjected to pure bending (such that it is under zero shear and maximum bending moment); whilst the remaining sections experience maximum shear force and varying bending moment. The middle third experiences the largest strains and therefore the concrete beneath undergoes cracking first. Then, the first crack growths slowly across the width of the slab (i.e. parallel to the supports). Development and formed of flexural cracks occurred parallel to that crack and slowly propagated throughout the thickness of the slab, on increasing the application of static load. **Fig. 4** shows the crack pattern of the static tested specimen at failure. It is clear from this figure that the generated flexural cracks are approximately parallel and did not show any cracking on either side of the specimen near the support regions. Also, the crack patterns of the specimens tested under repeated load **Fig. 5-a to 5-h** are approximately same that for the specimen under static load. Further development of cracks occurs and width of cracks, on increasing the number of loading cycles for the specimen under repeated load. Generally it is noticed that the cracks develops and growths throughout the slab thickness on increasing the applied load are parallel and vertically up to failure for the specimen without lacing reinforcement. While the cracks are curved and connected together through the slab thickness for the specimens with lacing reinforcement, and this overlap increase as the lacing steel ratio increased, as illustrated in **Fig. 6-a and 6-b** respectively. Finally, the modes of failure for specimens occurred by excessive yielding of tension steel reinforcement and followed by concrete crushing at the top surface of the slab at failure.

6.2 Cracking and Failure Loads

The experimental results for cracking and ultimate loads of all specimens are listed in **Table 5**. The first cracks (flexural) occurred at a load range of about (18.18% to 24.07%) of the ultimate load capacity of these specimens.

Also, from the experimental testing results, it is demonstrated that the ultimate load increased as the lacing steel ratio for the specimens **RS45/25**, **RS45/45** and **RS45/65** increased by about (22.73%, 45.45%, and 54.54%) respectively with respect to the specimen **RS45/0** (without lacing reinforcement). For the specimens of the different flexural steel reinforcement ratio and the same lacing steel ratio, it is observed that a slightly increase in the ultimate load capacity of the specimen **RS25/45** on that recorded for the specimens **RS45/45** and **RS65/45**. This is because of using the lacing reinforcement caused by decreasing the effect of the flexural reinforcement and this may be explained as the de-bonding between the concrete and the steel reinforcement for the specimen **RS25/45** occurs at the load level higher than that for the other two specimens. As expected, the ultimate load capacity increased by increasing the slab thickness, where the load increase by about (51.85% and 100%) for the specimens **RM45/25** and **RL45/25** respectively with respect to the specimen **RS45/25**.

6.3 Load-Deflection Response

The vertical deflection is measured at the middle of the slab and beneath the points load at each load step; the behavior of the specimens is compared with the behavior of control specimen for each group at the failure load stage. Generally, when a specimen is subjected to a gradually load increase, the deflection increases linearly with the load in an elastic range. After the cracks start developing, deflection of the slab increases at a faster rate. After cracks have developed in the slab, the load-deflection curve is approximately linear up to the yielding of flexural reinforcement after which the deflection continues to increase without an appreciable increment in load. Load-displacement response of the slab tested under static load is shown that the failure load is found to be (83.49 kN). Therefore, the amplitude of the repeated load is taken as 80% of this load as shown in **Fig. 7**.

It is demonstrated that as the lacing steel ratio increase, the deflection for the specimens **RS45/25**, **RS45/45**, and **RS45/65** decrease by about (27.83%, 47.94%, and 50.22%) respectively compare with that of the specimen **RS45/0** at the failure load, as illustrated in **Fig. 8**. For the specimens with the same ratio of the lacing steel reinforcement **RS25/45**, **RS45/45**, and **RS65/45** and the different flexural steel ratios, it is noticed that the load-deflection behavior is approximately identical, and there is a clear interaction between the curves as shown in **Fig. 9**. Then, the deflections were reduced by about (74.42% and 79.93%) for the specimens **RM45/25** and **RL45/25** respectively compared with the deflection at the failure load of the specimen **RS45/25**, this is due to the significant effect of increasing the slab thickness to increase the stiffness of the specimens, as shown in **Fig. 10**.

6.4 Residual Deflection Response

The experimental test results showed that there is an increase in deflection at the same point and the same increment of the load with an increase a number of cycles of loading for all the specimens. That causes slab not to return to the original position when the load decreased to zero level at the end of each cycle of loading. The lacing reinforced slab exhibited the lowest residual deflection and greatest stiffness. Among the five load cycles at a level of (80%) of the control specimen **SS45/0**, it is always the first cycle that is found to absorb more energy of the slab. Energy absorbed in the other cycles is found to be lower than that absorbed in the first cycle for the specimens.

It is noted that the increasing of the lacing steel ratio reduced the residual deflection for the specimens **RS45/25**, **RS45/45**, and **RS45/65** by about (9.6%, 45.55%, and 57.24%) respectively with respect to the specimen **RS45/0** as shown in **Fig. 11**. It's observed that the increasing of flexural steel reinforcement ratio for the specimens, **RS45/45** and **RS65/45** causes increasing in the residual deflection by about (52.94% and 73.53%) respectively with respect to the specimen **RS25/45**. This is due to increase the stiffness of the specimens, and the reinforcement in the slabs were not able to return to dissipate energy without permanent deformation, as illustrated in **Fig. 12**. Also, as the depth of the slab increases, the stiffness will be increased. As a result, the deflection at the peak load of the first cycle will be decreased, then the residual deflection for the specimens **RM45/25** and **RL45/25** are reduced by about (59.46 % and 77.22%) respectively with respect to the specimen **RS45/25** as shown in **Fig. 13**.

6.5 Load-Strain Relations

The load-strain relations of steel reinforcement and the compression concrete surface were measured to get a better understanding for the response and behavior of the laced one way reinforced concrete slab. Strain gauges of (60 mm) length were installed on the top concrete surface to measure the compressive strain of concrete. Generally, it is so clear that the effect of lacing reinforcement to restrain the flexural reinforcement through its plastic region for all specimens with lacing reinforcement compared with the specimen without lacing reinforcement **SS45/0**.

Figs. 14-a to 14-c illustrate that the flexural steel reinforcement is yielded with recorded the tensile strain by about (3121-4089) microstrains and the maximum compressive strain of the concrete was (2055) microstrain, while the lacing bars within the elastic range by the tensile strain of (806-994) microstrains at the service load stage of the specimens **RS45/0**, **RS45/25**, **RS45/45**, and **RS45/65B**. Then the compressive strain of the concrete reached to (3835-5340) microstrains and increasing the tensile microstrain of the lacing reinforcement to (2709-3157) at the ultimate load of specimens, while the flexural steel reinforcement were re-strained.

The effect of increasing the flexural steel ratio of the specimens **RS25/45**, **RS45/45** and **RS65/45** on the load-strain curves were illustrated in **Figs. 15-a to 15-c**. It can be seen that there is significant record in tensile strain of the flexural steel reinforcement by about (4014-5380) microstrains, the compressive strain of concrete was ranged by (1587-2173) microstrain and the lacing steel reinforcement was recorded (705-1126) microstrains at service load. Then compressive strain of the concrete reached to (4114-5621) microstrains, and the lacing steel reinforcement recorded the tensile strain by about (2113-3895) microstrains at the ultimate load of specimens, the similar re-strained behavior was previously explained for the flexural steel reinforcement is observed.

It is demonstrated that from **Figs. 16-a to 16-c** the flexural steel reinforcement is yielded with the tensile strain range of (3348-4514) microstrains, and recorded the compressive strain at the top surface of concrete by about (1318-1838) microstrains, while the lacing reinforcement recorded the tensile strain by about (504-1389) microstrains at the service load stage of the specimens **RS45/25**, **RM45/25**, and **RL45/25**. These values increase to (4208-4721) microstrains at the top of concrete and (2709-4856) microstrains for the lacing steel reinforcement at the ultimate load stage of specimens, while the flexural steel reinforcement is re-strained at the plastic region because the effective of using the lacing steel bars.

7. SUMMARY AND CONCLUSIONS

The main conclusions can be summarized as follows:-

1. The crack pattern and mode of failure for the specimen tested under repeated load were similar to that described in the similar specimen tested under static load.

2. The ultimate load for specimen tested under repeated load was smaller than that of similar specimen subjected to static load.
3. The first cracking load increased by about (40%) for the specimen with highest lacing steel ratio, and by about (116.67%) for the specimen with lowest L/d ratio with respect to the control specimen for each group.
4. The ultimate load showed increase with increasing the lacing steel ratio, where the ultimate load for the specimen with the highest lacing steel ratio was (54.54%) greater than the control specimen.
5. The ultimate load capacity enhanced by (100%) as a result of decreasing the (L/d) ratio to (31.25%) with respect of the control specimen.
6. The ultimate deflection for specimen subjected to repeated load was smaller than of similar specimen tested under static load.
7. It is observed that with the increase in the number of load cycles, the corresponding deflection and number of cracks increased.
8. Residual deflection reduced by about (57.24%) for the specimen with the largest lacing reinforcement compared with the control specimen (without lacing bars).
9. Repeated loading produces a residual deflection which increases with the increased the flexural steel ratio, and the (L/d) ratio.
10. The flexural steel reinforcement is not able to return to dissipate energy without permanent deformation.

REFERENCES

- ACI Committee 318, 2014, *Building Code Requirements for Structural Concrete ACI 318M-14 and commentary*, American Concrete Institute, Farmington Hills, 519 PP.

- Adom-Asamoah M. and Kankam C.K., 2009, *Flexural Behavior of One-Way Concrete Slabs Reinforced with Steel Bars Milled*, Materials and Design, Vol. 30, No. 5, PP.1737–1742.

- Anandavalli, N., 2012, *Experimental Investigation on LSCC Beams-Reversed Cyclic Loading*, Ph.D Thesis Faculty of Civil Engineering Anna University Chennai 600 025, March, 191 PP.

- ASTM C192/C192M-02, 2002, *Making and Curing Concrete Test Specimens in Laboratory,* Annual Book of ASTM Standards, American Society for Testing and Materials, Philadelphia, Pennsylvania, Vol. 4, 02, PP. 1-8.

- Lakshmanan, N., 2008, *Laced Reinforced Concrete Construction Technique for Blast Resistant Design of Structures*, Proc. Of the Sixth Structural Engineering Convention, SEC-2008, Chennai, India, PP. PII-1-14.

- Lakshmanan, N., Bharath Kumar, B.H., Uday Kumar, V., Balasubramanian, K., Krishnamoorthy, T.S., Chitra Rajagopal and Mishra, G.K., 2008, *Behaviour of RC Beams with Continuous Inclined Web Reinforcement under Reverse Cyclic Shear Loading with and without Steel Fibres*, BEFIB-2008 Symposium, Chennai, India, PP. 1119-1136.

- Sivagamasundari R. and Kumaran G., 2011, *Experimental Study on the Behaviour of Concrete One-Way Slabs Reinforced with GFRP Reinforcements under Constant and Variable Amplitude*, International Journal of Civil and Structural Engineering, Vol. 2, No. 2, November, PP. 547-569.

- Stanley C. Woodson, 1992, *Lacing Versus Stirrups an Experimental Study of Shear Reinforcement in Blast Resistant Structures*, U.S. Army Engineer Waterways Experiment Station, 3909 Halls Ferry Road, Vicksburg, March.

- UFC 3-340-02, 2008, *Structures to Resist the Effects of Accidental Explosions*, Unified Facilities Criteria, Department of Army, Navy and the Air Force, U.S.A., Washington, 05 December, 1867 PP.

Table 1. Characteristics of the tested slabs.

No.	Specimen designation	Slab thickness (mm)	$\frac{L}{d}$ ratio	Tension steel ratio (ρt)	Lacing steel ratio (ρs)	Lacing steel details	Flexural steel details
1	SS45/0	135	16	0.0045	0	Without lacing	$\emptyset 8\ mm\ at\ 100\ mm$
2	RS45/0	135	16	0.0045	0	Without lacing	$\emptyset 8\ mm\ at\ 100\ mm$
3	RS45/25	135	16	0.0045	0.002	$\emptyset 6\ mm\ at\ 100\ mm$	$\emptyset 8\ mm\ at\ 100\ mm$
4	RS45/45	135	16	0.0045	0.004	$\emptyset 6\ mm\ at\ 60\ mm$	$\emptyset 8\ mm\ at\ 100\ mm$
5	RS45/65	135	16	0.0045	0.006	$\emptyset 8\ mm\ at\ 70\ mm$	$\emptyset 8\ mm\ at\ 100\ mm$
6	RS25/45	135	16	0.0025	0.004	$\emptyset 6\ mm\ at\ 60\ mm$	$\emptyset 6\ mm\ at\ 100\ mm$
7	RS65/45	135	16	0.0065	0.004	$\emptyset 6\ mm\ at\ 60\ mm$	$\emptyset 8\ mm\ at\ 70\ mm$
8	RM45/25	160	13	0.0045	0.002	$\emptyset 6\ mm\ at\ 80\ mm$	$\emptyset 8\ mm\ at\ 80\ mm$
9	RL45/25	185	11	0.0045	0.002	$\emptyset 6\ mm\ at\ 70\ mm$	$\emptyset 8\ mm\ at\ 70\ mm$

Table 2. Details of slab groups.

Group	Description	Specimens
I	$\frac{L}{d} = 16$ $\rho t = 0.0045$ $\rho s\ Variable$ (Lacing)	*SS45/0 (ρs=0)* 1. *RS45/0 (ρs=0)* 2. *RS45/25 (ρs=0.0025)* 3. *RS45/45 (ρs=0.0045)* 4. *RS45/65 (ρs=0.0065)*
II	$\frac{L}{d} = 16$ $\rho s = 0.0045$ $\rho t\ Variable$	1. *RS25/45 (ρt=0.0025)* 2. *RS45/45 (ρt=0.0045)* 3. *RS65/45 (ρt=0.0065)*
III	$\rho t = 0.0045,$ $\rho s = 0.0025$ $\frac{L}{d} = Variable$	1. *RS45/25 (d=112.5mm, L/ d=16)* 2. *RM45/25 (d=137.5mm, L/ d=13)* 3. *RL45/25 (d=162.5mm, L/ d=11)*

Table 3. Properties of steel reinforcement.

Nominal diameter (mm)	Measured diameter (mm)	Yield stress fy (MPa)	Ultimate strength Fu (MPa)
6	5.83	724.4	777.4
8	7.87	626.24	775.34

Table 4. Mechanical properties of concrete.

Specimen ID	Compressive strength at time of specimen testing (MPa)		Modulus of rupture f_r at time of specimen testing (MPa)	Splitting tensile strength f_t at time of specimen testing (MPa)	Modulus of elasticity at time of specimen testing (GPa)
	f_{cu}	f'_c			
SS45/0	42.92	35.28	3.87	3.57	24.43
RS45/0	47.90	36.14	3.7	3.58	29.32
RS45/25	45.57	37.15	3.78	3.74	25.32
RS45/45	41.15	33.43	3.7	3.39	22.18
RS45/65	42.28	34.58	4.2	3.22	24.01
RS25/45	44.44	37.57	3.72	3.82	28.09
RS65/45	45.08	34.77	3.52	3.15	25.83
RM45/25	43.62	36.81	3.74	3.68	25.82
RL45/25	45.51	34.23	3.56	3.12	25.23

Table 5. Cracking and ultimate loads of test specimens.

Specimens		Crack load (Pcr) (kN)	Ultimate load (Pu) (kN)	% Pcr/Pu	%Increase in first cracking load with respect to control	%Increase in ultimate load with respect to control
	SS45/0	18.15	83.49	21.74	Ref.	Ref.
Group I	RS45/0	18.15	79.86	22.73	Control	Control
	RS45/25	21.78	98.01	22.22	20	22.73
	RS45/45	25.41	116.16	21.87	40	45.45
	RS45/65	25.41	123.42	20.64	40	54.54
Group II	RS25/45	21.78	119.79	18.18	Control	Control
	RS45/45	25.41	116.16	21.87	16.67	-3.03
	RS65/45	25.41	112.53	22.58	16.67	-6.06
Group III	RS45/25	21.78	98.01	22.22	Control	Control
	RM45/25	32.67	148.83	21.95	50	51.85
	RL45/25	47.19	196.02	24.07	116.67	100

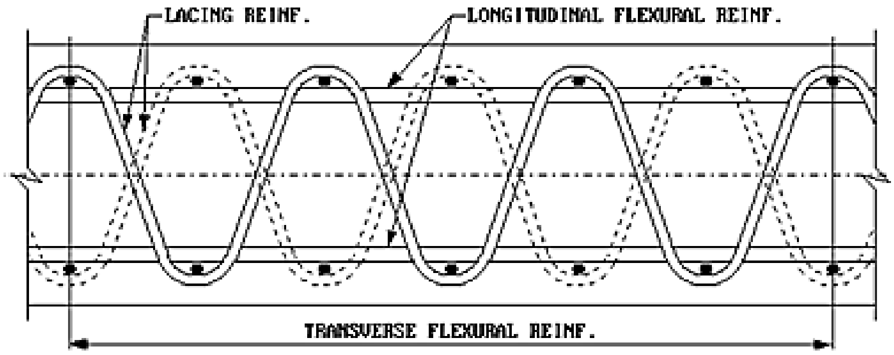

Figure 1. Typical laced reinforced concrete structural element.

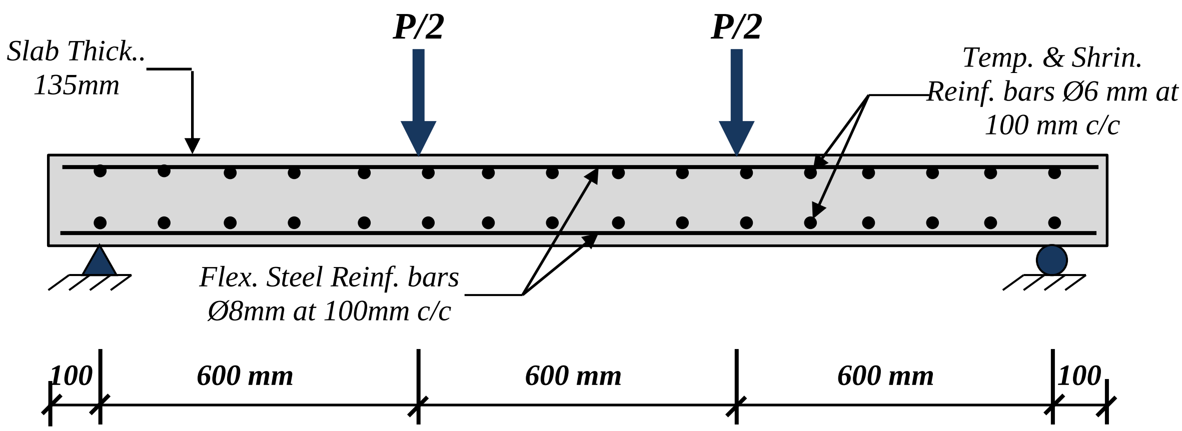

a. Longitudinal section in slab without lacing reinforcement.

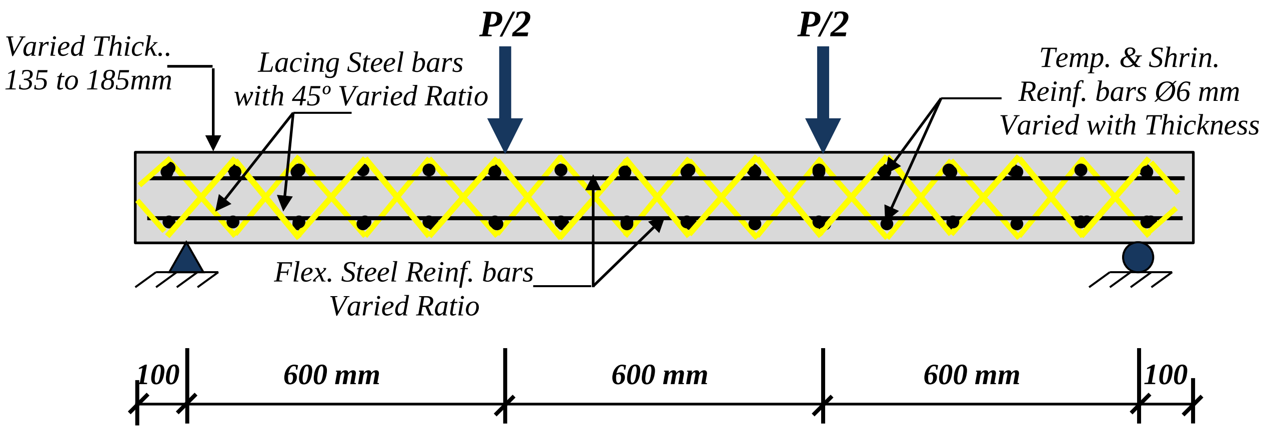

b. Longitudinal section in slab with lacing reinforcement.

Figure 2. Details and dimensions of the tested slab specimens.

a. Testing Machine.

b. Data Logger.

c. LVDTs Arrangement.

Figure 3. Photographs of specimen and instruments setup.

Figure 4. Cracks pattern at the tension face of the specimen SS45/0 after failure.

a. specimen RS45/0.

b. specimen RS45/25.

c. specimen RS45/45.

d. specimen RS45/65.

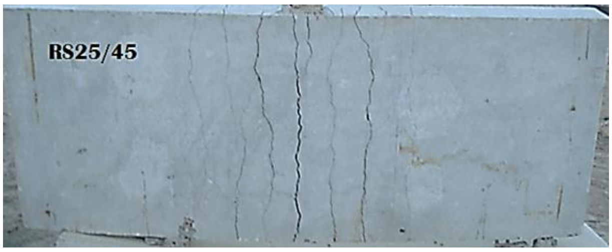

e. specimen RS25/45.

f. specimen RS65/45.

g. specimen RM45/25.

h. specimen RL45/25.

Figure 5. Cracks patterns at the tension face of the specimens tested under repeated load after failure.

a. specimen without lacing reinforcement.

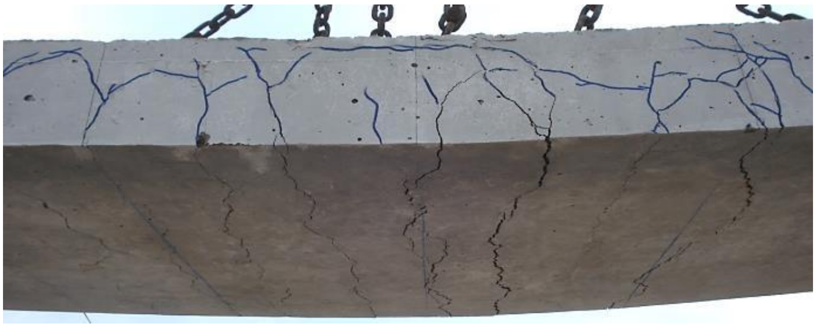

b. specimen with lacing reinforcement.

Figure 6. Typical cracks pattern at the side face of the specimens tested after failure.

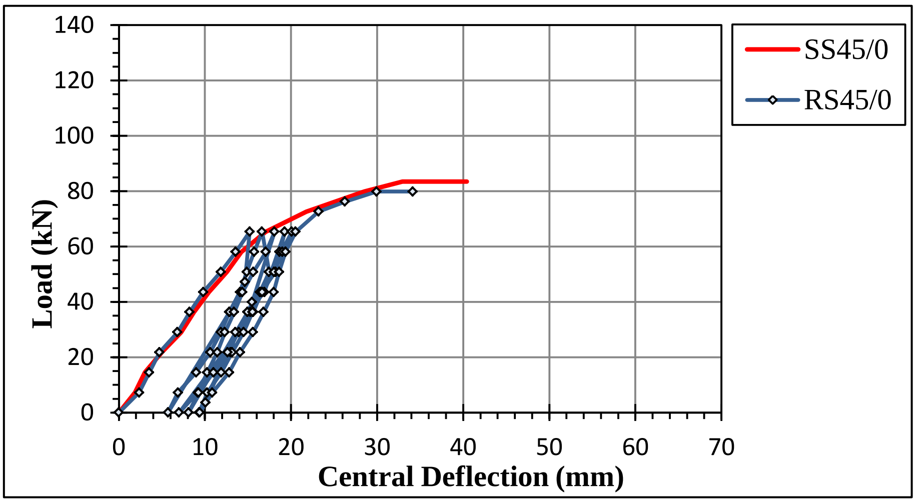

Figure 7. Load-central deflection behavior for the specimens without lacing reinforcement.

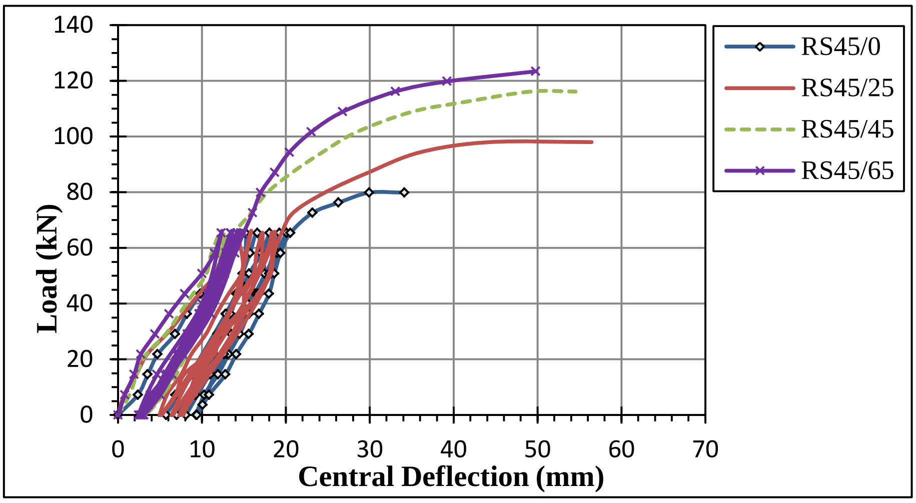

Figure 8. Influence of the lacing steel ratio on load-central deflection behavior for group (I).

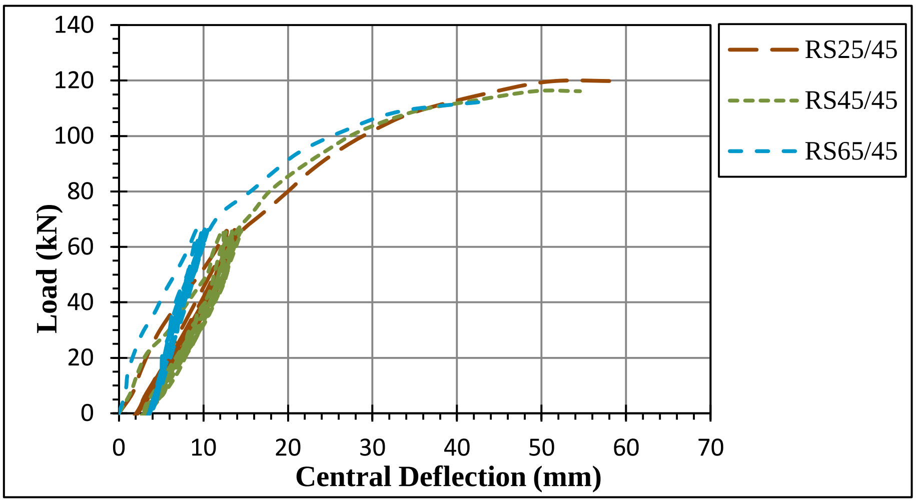

Figure 9. Influence of the flexural steel ratio on load-central deflection behavior for group (II).

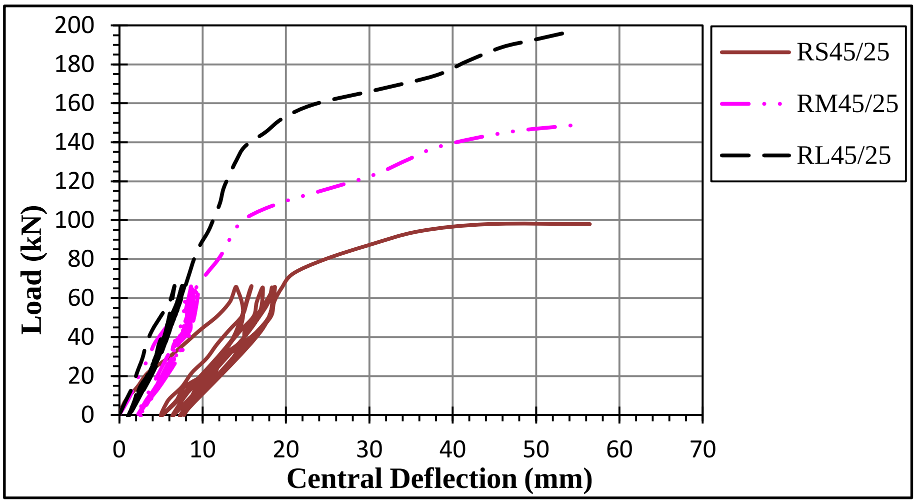

Figure 10. Influence of the L/d ratio on load-central deflection behavior for group (III).

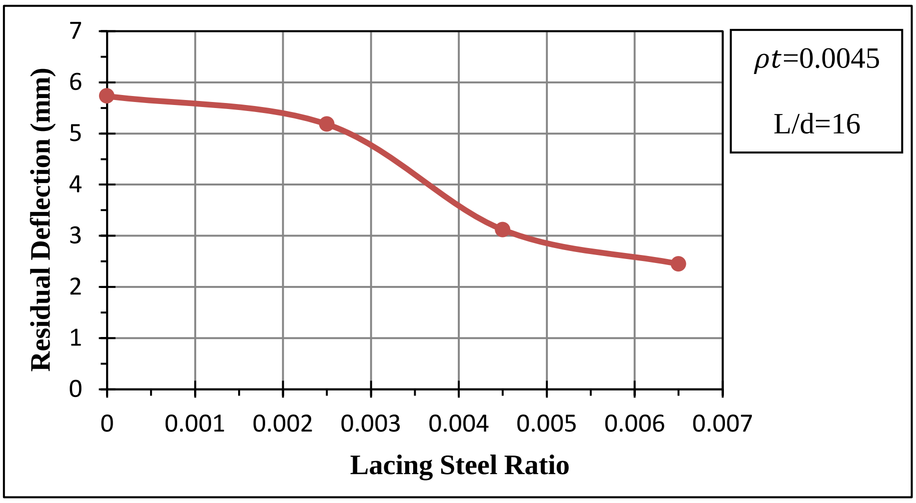

Figure 11. Influence of the lacing steel ratio on the central Residual deflection of group (I).

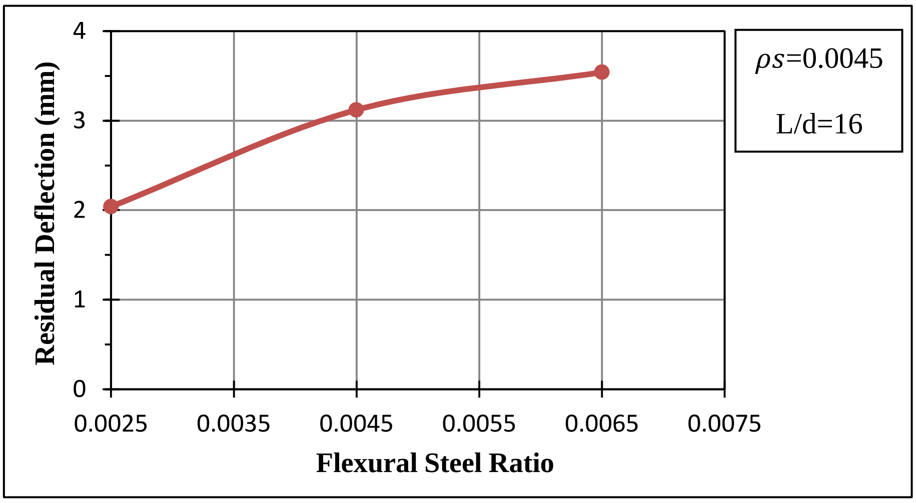

Figure 12. Influence of the Flexural steel ratio on the central Residual deflection of group (II).

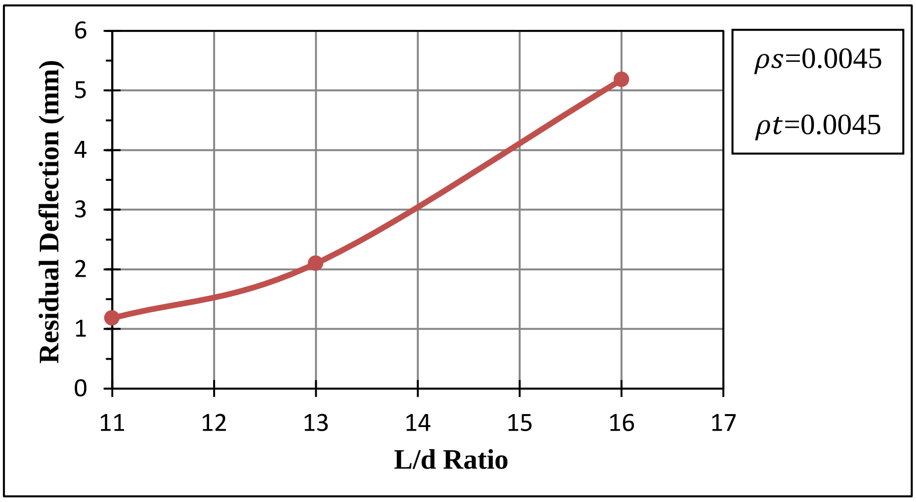

Figure 13. Influence of the L/d ratio on the central Residual deflection of group (III).

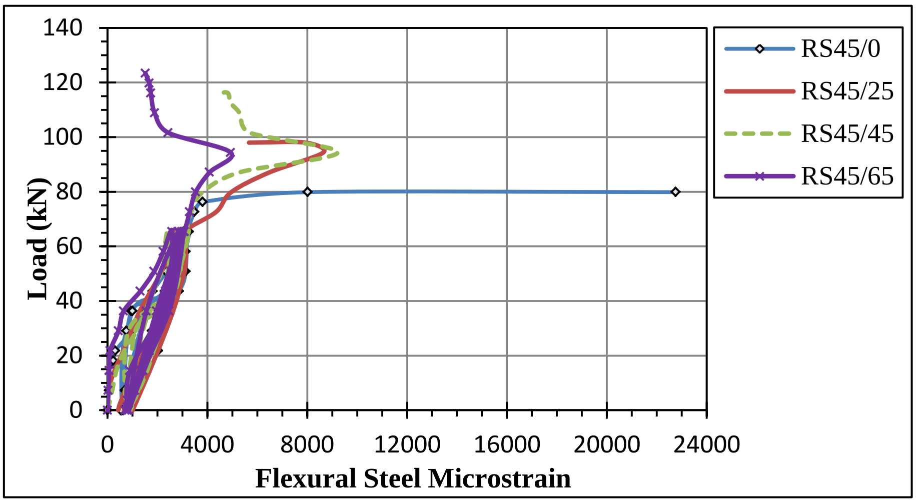

a. Load–strain curves at the flexural steel reinforcement.

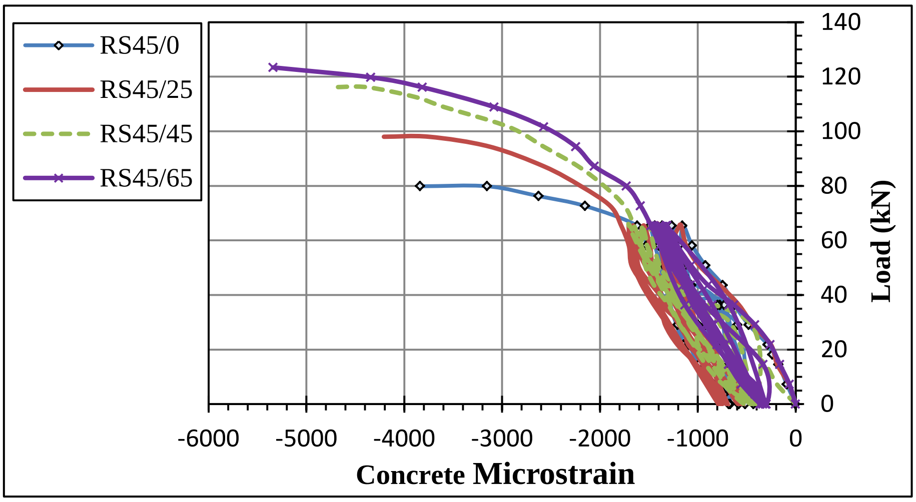

b. Load–strain curves at the top surface of concrete.

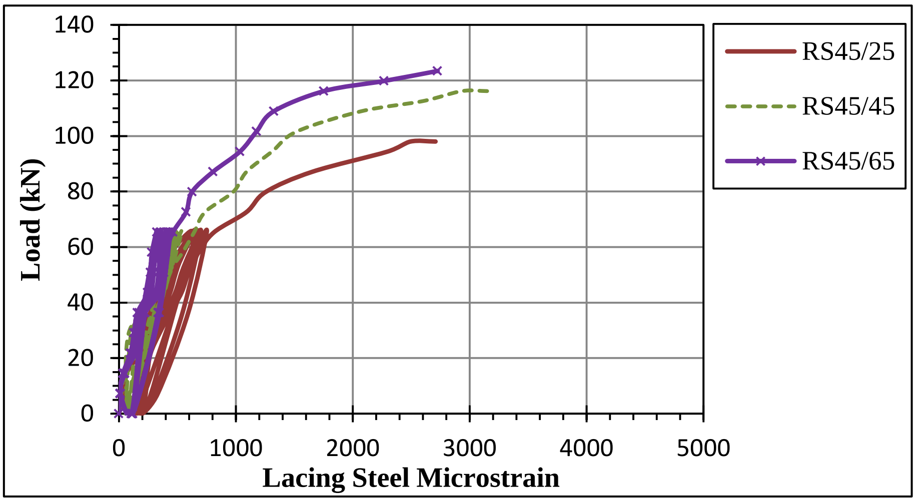

c. Load–strain curves at the lacing steel reinforcement.

Figure 14. Influence of the lacing steel ratio on load–strain curves at mid-span for group (I).

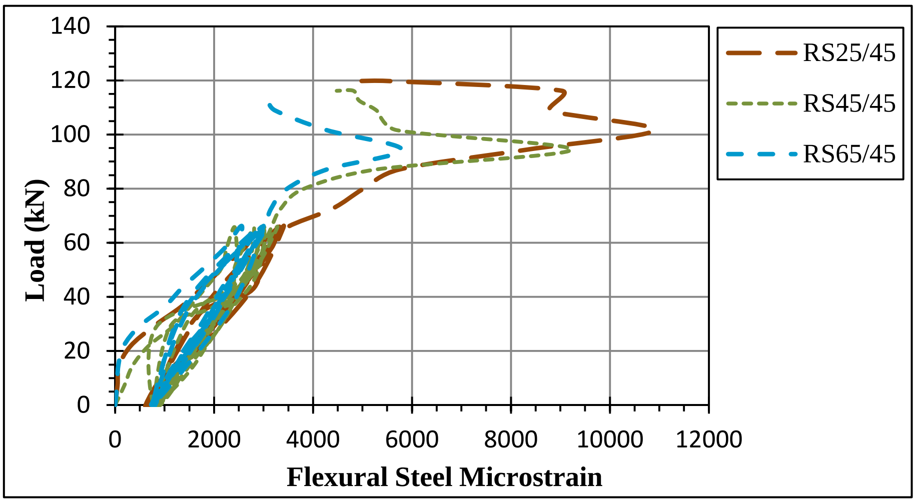

a. Load–strain curves at the flexural steel reinforcement.

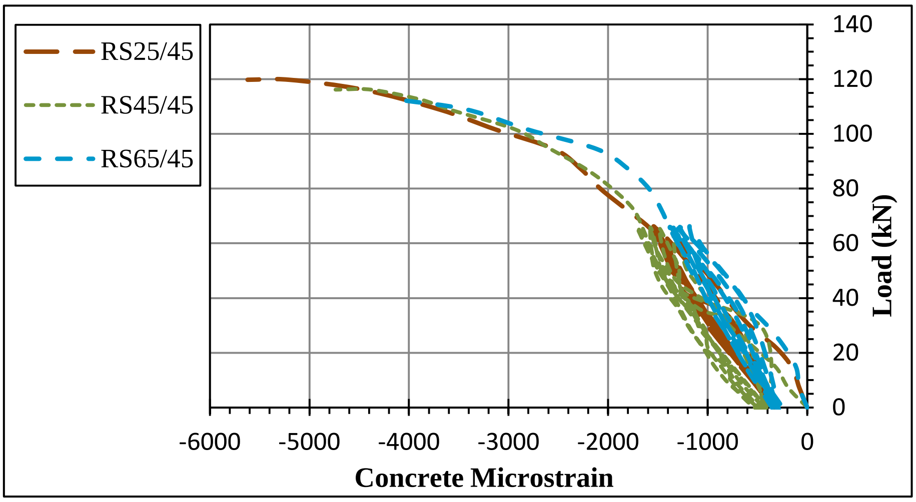

b. Load–strain curves at the top surface of concrete.

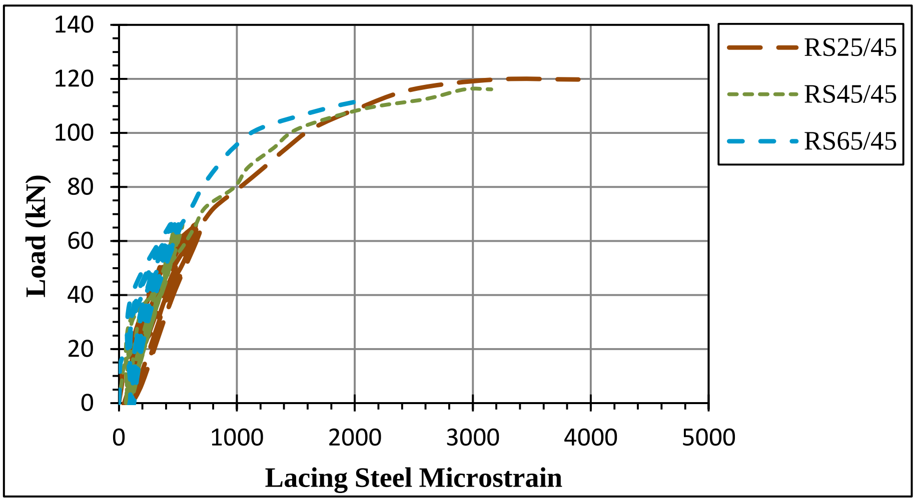

c. Load–strain curves at the lacing steel reinforcement.

Figure 15. Influence of the flexural steel ratio on load–strain curves at mid-span for group (II).

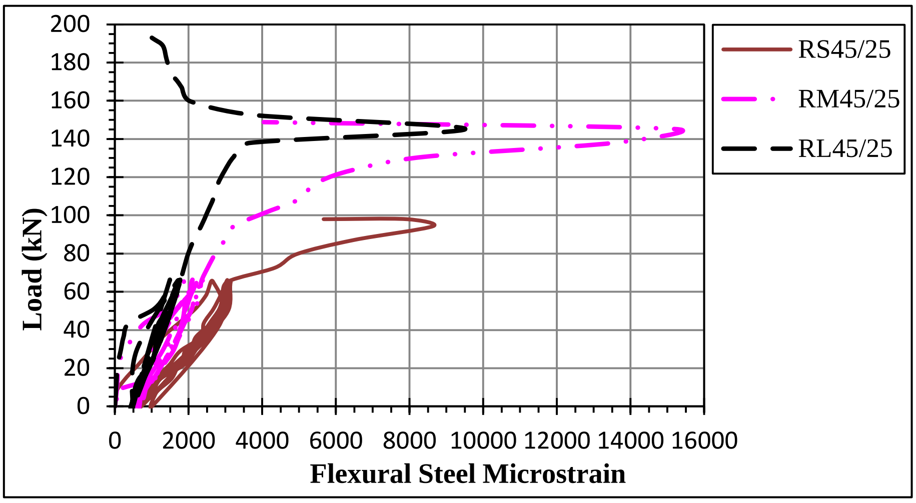

a. Load–strain curves at the flexural steel reinforcement.

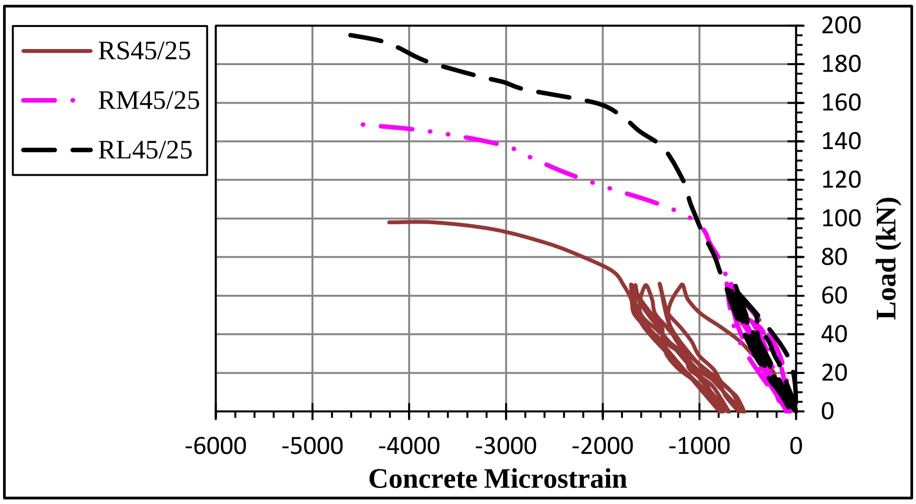

b. Load–strain curves at the top surface of concrete.

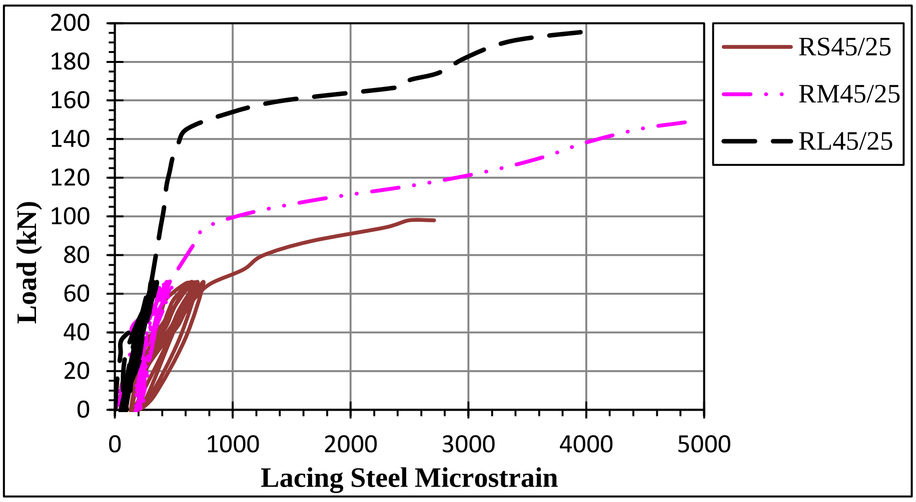

c. Load–strain curves at the lacing steel reinforcement.

Figure 16. Influence of the L/d ratio on load–strain curves at mid-span for group (III).

Evaluation of Maintenance Management in Iraqi Governmental Buildings

Qasim Mohammed Doos
Professor
College of Engineering – University of Baghdad
kasim_daws@yahoo.com

Kadhim Raheem Al-Saadwi
Assistant Professor
College of Engineering – University of Baghdad
kadhim1969@yahoo.com

Haider Khaleel Ibraheem
Researcher
College of Engineering – University of Baghdad
ebdaaco@yahoo.com

ABSTRACT

Impact of buildings in Iraq and other countries on the environment is obvious; this problem began to take scientific and humanitarian dimensions in order to reduce and eliminate this problem. This impact can be seen through the energy, water and raw materials consumed for the establishment, operation and maintenance of these buildings, as well as the emissions of hazardous gases and generations of solid wastes.

This work was conducted to assess the current maintenance managerial practice for the governmental buildings to stand on the main obstacle and extrapolation of measures by means of interviews with experts to determine the effective factors and closed questionnaire to state the features and the need for new building maintenance management system which may assist for modeling new building maintenance management system which may help to reduce the deterioration levels of governmental buildings and the emission of hazardous gases and solid waste with cost efficient approach.

Key words: Buildings, maintenance, sustainability, management.

تقييم اجراءات ادارة صيانة الابنية في العراق- نظرة مستدامة

قاسم محمد دوس
أستاذ
كلية الهندسة-جامعة بغداد

كاظم رحيم أرزيج
أستاذ مساعد
كلية الهندسة-جامعة بغداد

حيدر خليل ابراهيم
باحث
كلية الهندسة-جامعة بغداد

الخلاصة

ان تأثير المباني في العراق وغيرها من البلدان على البيئة يعتبر من الامور الجلية وان هذه المشكلة بدأت تأخذ ابعادها العلمية والانسانية بغية الحد من هذا التأثير، ويمكن ملاحظة ذلك من خلال استهلاك الطاقة والمياه والمواد الخام المستغلة لغرض انشاء وتشغيل وادامة هذه الابنية, فضلا عن انبعاث الغازات الخطرة وتوليد النفايات الصلبة.

تم اجراء هذه الدراسة لغرض تقييم الممارسات الإدارية الحالية للمباني الحكومية بواسطة اجراء مقابلات مع الخبراء من اجل تحديد العوامل الرئيسية التي تؤثر على الصيانة المستدامة للأبنية واستخدام اسلوب الاستبيان المغلق لتحديد الحاجة والملامح الرئيسية لنظام اداري جديد لصيانة المباني الحكومية والوقوف على العقبات الرئيسية واستقراء التدابير التي يمكن أن تساعد في استحداث نظام إدارة لصيانة المباني والذي قد يساعد على خفض مستويات تدهور المباني الحكومية والحد من الاثر البيئي الناتج بسبب انبعاث الغازات السامة والنفايات الصلبة ضمن نهج فعال من حيث التكلفة.

الكلمات الرئيسية: ابنية, صيانة, استدامة, ادارة

1. INTRODUCTION

Governmental buildings share the same fact that all of them need to be maintained to perform as they designed and constructed for, and to meet the new requirements of sustainability represented by its three aspects (Environment, Social, and Economy).

While more recent studies have considered the maintenance of buildings of the most important phases of the project management due to of the long time period represented by the ratio to the period of the project life, it has been found that the number of researches and studies written in this area in Iraqi literature is still humble.

Buildings in general are responsible for 48% of the emissions that affected the ozone layer, consumed 40% of natural resources, and about 60% of the total consumption of energy to be used for air conditioning and lightening**, Ahn, 2008. Fig.1** shows the CO_2 emission according to sectors. Instead of that and according to natural wear and tear, buildings systems and components deteriorate and need to be maintained by different methods of building maintenance practices. Governmental buildings in Iraq as the main concern of this research is very important and considered essential because of the huge amount of resources spent for constructing them; therefore the need for maintaining them as well as the current practices and procedures need to be assessed in order to find the main characteristics and features of the current system which may assist in improving the maintenance management procedures basing on best available scientific practices.

2. BUILDING MAINTENANCE CLASSIFICATION

Several types of building maintenance are used according to the availability of resources, experts and the criticality and emergent status of the deteriorated or broken part of the building. Maintenance can be identified through a number of specific types and can be classified in a number of different ways (In BS 3811: 1984 and, the European EN 13306, maintenance can be subdivided in the way described in **Figs. 2 , 3,** and **4**, **Chanter, and Swallow, 2007.**

2.1. Corrective Maintenance

This type is also known as breakdown, failure based, run to failure or unplanned maintenance, is the simplest type of classical maintenance policies where an item is used until it breaks/faults with the only activity centering on repair and servicing of the parts. Corrective maintenance can be subdivided according to whether it is executive or deferred to a later date, and perhaps included in a longer run maintenance plan **Cruzan, 2009**.

Corrective maintenance approach leads to more degradation of the building structure and systems, and therefore, the progress of future maintenance activities will be more difficult and more expensive.

In real condition, corrective maintenance might not be avoided in the building life cycle, as an example, the damage caused to buildings by natural calamities or accidents like wars. Often, building fabrics are maintained on a corrective basis.

Corrective maintenance is unrestrained and involuntary in nature therefore, if no alternative strategy put in place, the building structure will continue to deteriorate until exhaust of proper maintenance and this will lead to further decay, degradation, and failure.

The emphasis of this research is that corrective maintenance should be reduced to the minimum and it should be applied with less disturbance and disruption to works taking place inside and/or around the building.

2.2. Preventive Maintenance

Refers to situations where repairs and/or replacement take place without the incidence of any specific fault. The plan is to prevent failures. In many preventive maintenance models, the system is assumed to be as good as new after each maintenance whereas a more realistic situation is one in which the failure pattern of a preventively maintained system changes to somewhere between as good as new and as bad as old**, Lind, and Muyingo, 2012.** The preventive maintenance effects can be subdivided into a perfect, a non-effect and an imperfect effect where:

a- The perfect effect restores the system to good-as-new,
b- A non-effect to bad-as-old,
c- An imperfect effect to partly good.

Ryan Cruzan judged that it is from the technical point of view “Preventive maintenance is a scheduled program of regular inspections, adjustments, lubrication, or replacement of worn or failing parts in order to maintain an asset’s function and efficiency”**, Cruzan, 2009.**
Olanrewaju, and Abdul-Aziz, 2015 stated that preventive maintenance can make a reduction in the total maintenance costs by about 15 % if introduced properly**.** Preventive maintenance can be subdivided the following kinds:

2.2.1. Condition-based maintenance

Condition based maintenance (CBM) is kind of preventive maintenance where the object is inspected on a regular basis and the object serviced or replaced when a certain condition is observed. Sophisticated signal processing tools are used to monitor the condition of the buildings. As an example, vibration measurement, non-destructive testing, thermography, transducers, and spectroscopy make it possible to perform non-intrusive inspection in order to monitor the conditions of buildings. This kind of maintenance sometimes referred to as (predictive maintenance) **Saranga, 2002**.

2.2.2. Opportunistic maintenance

A new concept arises here that is Opportunistic maintenance: This concept covers the case where various things are done because there arises an “opportunity” to carry out a certain activity in a cost-effective way. Opportunistic maintenance figured as a sub form of condition-based maintenance (CBM) where maintenance and replacement decisions are based on the state of the rest of the system. Typically during the performance of a scheduled or unscheduled maintenance action, a situation might arise where it is cost effective to carry out corrective maintenance on another previously undetected failing item or to reschedule another maintenance activity so as to take the advantage of scale economies in the ongoing activity. Genetic algorithms or robust optimization can be used to decide on whether a particular item needs opportunistic maintenance and how cost effective this would be in comparison to a later grounding**, Lind, and Muyingo, 2012.**

2.2.3. Time-based maintenance

It is another kind of preventive maintenance, where tasks are performed at a frequency dictated by the passage of time, regardless of the actual condition of an item. This type of maintenance may at times create problems where not existed before**, Lind, and Muyingo, 2012.**

2.2.4. Proactive maintenance

Very similar to the condition based maintenance and is cheaper in the long run when compared with other strategies of maintenance **Olanrewaju, and Abdul-Aziz, 2015.**

It is focusing on the root cause instead of the symptoms of the damage. Cause and effect analysis, which is the determination of the mechanisms and causes of building faults, is crucial in proactive maintenance.
The basic assumption in proactive maintenance is the removal of the causes of defects from all sources. Then correction of the fundamental causes of building failures can be occurred, and the failure mechanisms can be gradually engineered out of each building system and this leads to improve the efficiency of the building. **Table1** describes the logic behind each maintenance type.

2.3. Maintenance vs. Improvement

It is essential to clarify the difference between maintenance and improvements; maintenance is the activities which return back the quality of service and the performance for each deteriorated system or sub system to the designed levels, while the improvement is meeting the new user and technical and regulations requirements **Fig. 5**, **Stanford, 2010**, sometimes maintenance concept has been referred to by the expression (adaptive concept) while improvement concept has been referred to by the expression (perfective concept).

2.3.1. Adaptive concept

This concept involves adjusting or adapting the service system for changing to a different service delivery. An example of this is changing the maintenance service of residential building to academic building or changing from lecturer's requirements to student's requirements

2.3.2 Perfective Concept

This concept involves developing or acquiring additional service system or improving the operation capability of the service system. This should not, however, be confused with refurbishment work, as it does not involve changing the physical outlook of the building but only the service provided.

3. METHODOLOGY

Building maintenance challenges need to be categorized and measured; therefore 18 key questions considered as the most important concerns on building maintenance management from the researcher point of view **Table2**, an open questionnaire built from these concerns in order to assess the current maintenance management practice in Iraq.
In order to prepare the assessment of the current maintenance management practice in Iraq the researcher conducted a survey for the governmental buildings maintenance management systems practice and procedures as:

3.1. Studying BMM System for Iraqi Governmental Buildings-Part One:

A form was designed with open questions stemmed from the main concerns **Table1** to determine the main characteristics and features of the current BMM system by means of personal interviews technique, the researcher spent around three months to make personal interviews with staff from the upper and middle grades in many governmental buildings management level personnel as shown in **Table3.**
The main inferences from this investigation were:
1- The BMM system is not clear, and on most cases the engineering affairs department is responsible for new constructions and major rehabilitations while maintenance department or units at most cases responsible for fixing the broken fixtures and broken systems; although there

is some kind of preventive maintenance processes in maintaining HVAC systems and electrical systems; there is no strict system for planning and execution for such practices. The maintenance of building parts are usually postponed until the availability of fund or to next rehabilitation.
2- Functional performance of building parts and components is more critical than conditional status on consideration of maintenance work.
3- Estimating of required funds basically based on the expenses of previous years, with a particular increment.
4- Replacement age and/or replacement models calculations are not conducted.
5- BMM software application was not detected.
6- Absence of electronic documentation for any of maintenance practices and information.
7- No user satisfaction evaluation was conducted.
8- No clear incentive system was connected with maintenance staff performance in order to encourage them.
9- Measuring maintenance works productivity is neglected.
10- Investigations of the causes of failure were not conducted in most cases.
11- The work of building maintenance is not subject to any quality standard.
12-The interviewees also asked to give their opinion about the main constraints that may affect the size and quality of the BMM system and the answers revealed that the main constraints are the building size, building type, number of stories, building age, type of use, type of occupiers and number of users. Another constraint is the budget deficits and the political, economic, environmental, cultural and social determinants of budget deficits.
13- The factors that most affecting maintenance management, from the interviewees' point of view depending on frequencies from the respondents answers. The researcher faced at this step one of the main difficulties which is the lack of understanding of sustainability and sustainable maintenance approach due to the recency of this concept which requires from the researcher strenuous efforts to clarify it to the interviewees. Initially, forty eight factors were identified then and by means of rigorous analysis, they were reduced to thirty two factors, the 32 factors were later reduced to 24 factors which agreed as the key factors or the criteria affecting the sustainable BMM, these factors are:

- Need for special experience.
- Building age.
- Initial cost.
- Maintenance cost.
- Community culture.
- Security aspects.
- Political issues.
- Need for special software.
- The ability to use recyclable materials.
- Time to response.
- Occupier health.
- Aesthetic appeal.
- Occupier safety.
- Occupier comfort.
- Wellbeing.
- Time to complete the work.
- Intense of use.
- Exposure to environmental effects.

- Pollution.
- Need for special tools and appliances.
- Ability to recycling.
- Amount of resources consumed each year.
- Amount of resources consumed for constructing the asset.
- Need for special standards.

3.1.1. Actual maintenance practice

For Iraqi governmental BMM procedure, it is concluded from the previous part of the work that the current building maintenance work; in general, follows the steps represented by **Fig.6**

3.2. Studying BMM System for Iraqi Governmental Buildings-Part Two:

This part of the assessment done by means of closed questionnaire consisted from two sections, the first section prepared to collect the general information about the experts who conduct the assessment while the second section is consisted from four questions to assess the current BMM.

3.2.1. Characteristics of respondents

Five questions set to collect the respondent personal information, the analyzed data showed that the majority of respondents (79.2%) are public sector employees and the rest are private sector employees **Table4**, 20% of the respondents from private sector and most of them are engineers (90%) **Table5**, and some of them having PhD degree (20%), all the rest have BSc degree, and 70% of the respondent from the private sector have experience more than 15 years and 20% more than 10 years only one respondent have experience less than 10 years **Table6**. Most of the respondent from the public sector were engineers and 95% of them having experience more than 10 years. Only 5% of them having diploma, 52% have BSc degree, 23% having master degree and 15% having PhD degree. 94% of all the respondents were engineers and 6% working on administrative specialist **Table7**.

3.2.2. Analysis of Questionnaire

On the first question it is suggested that the maintenance management for governmental buildings is very essential and it needs special care from all employees and especially from the top management, 64.5% from the respondents agree with this suggestion and more than 33% strongly agree while 2% were neutral with this suggestion **Fig. 7**, the mean of the responses was 4.31 according to the equation

$$\overline{x} = \frac{\sum_i x_i}{n} \qquad (1)$$

While the standard deviation of 512 according to the equation

$$s^2 = \frac{1}{N-1}\sum_{i=1}^{N}(x_i - \overline{x})^2. \qquad (2)$$

It can be concluded that the respondent agree with this suggestion.

On the second question, the respondent asked to give their opinion if there is real need to reconsider the current system of building maintenance management by improving the procedures using the scientific approaches and considering the sustainability principles in order to improve the social and community outreach and decrease the environmental impact beside the economic growth, more than 60% of the respondents agree and about 30% strongly agree with this opinion (half of them from the private sector, which means 70% of the respondents from the private sector strongly agree), little more than 10% of the respondent were neutral with this opinion all of them from the public sector, **Fig. 8** and **Table8** explain the statistics about the need for new sustainable system for BBM with more detail.
Third question is built upon the main conclusion reached from the survey conducted on the current maintenance management system on the part one of this study **Paragraph 3.1**,where it is found that there is no obvious existing sustainable maintenance management system and what is happening is correction action by maintenance units for what is broken while the engineering affairs offices generally prepare and manage contracts for rehabilitation between whiles, therefore the researcher seeks the expert opinions if they agree or not with this conclusion and define the degree of agreement. The results in **Fig. 9** were showing that more than 50% of the respondents agree, about 20% strongly agree and around 30% had a neutral opinion.
Due to the importance of this question as a main conclusion from the surveys conducted in the current maintenance management systems in Iraqi government, it has been decided to further analysis should be accomplished on the results of the answers of this question, therefore, ANOVA test was conducted to measure the differences among scientific degrees groups, as there are four basic assumptions used in ANOVA test:

1- The expected values of the errors are zero
2- The variances of all errors are equal to each other.
3- The errors are independent
4- They are normally distributed

The results are tabulated in**Table9**, it has been shown that the mean of all respondents is 3.85 which means almost all the respondents agree on the scale of this question as (agree = 4) with Std. dev. of .684 according to equation 2. Considering the scientific degree of the respondents, only one category which is the respondents who have diploma degree had standard error equal to 1, and Std. dev. equal to 1.414, that result can be considered reasonable since there were only two respondents in this category, for all other categories, the results are showing smaller error value and Std. dev., so the answer of this question can be considered as agreed with the researcher suggestion.
The fourth question of this part of questionnaire dealt with the method of delivering the complaints. Seven methods suggested which were (internal mail, email, web site, fax, mobile, phone, oral) another option is also applicable if the respondent have another method, the results were as in Figure 10 as we can see that around 44% encourage the use of mobile and around 29% suggested to use the email, and around 15% suggested to use the website, 8% of the respondents seems they encourage the traditional method of internal mail 75% of them had an experience more than 15 years **Table10.**

4. CONCLUSIONS

As a one of the most sensitive stages of the construction management process, it has been found that the maintenance stage is suffering from many deficiencies; planning and management practices for managing the maintenance of governmental buildings in Iraq also has been found not sufficient and it has been discovered that there is a consensus from the experts to the need of rethinking and reviewing these practices in order to find a scientific way for modifying and upgrading these practices to catch up with the rapidly developed international sustainable practices in this field of construction management.

REFERENCES

- Ahn G., 2008, *A Call to Action: Buildings Key to Corporate Sustainability*, Environmental Leaders, environmental and energy management news, official website, http://www.environmentalleader.com/2008/09/09/a-call-to-action-buildings-key-to-corporate-sustainability/#ixzz3xctiKsug.

- Chanter B., and Swallow P., 2007, *Building Maintenance Management*, Blackwell Publishing editorial ISBN: 978-1-4051-3506-1, 2nd edition.

- Cruzan R., 2009, *Manager's Guide to Preventive Building Maintenance*, Published by The Fairmont Press, Inc.700 Indian Trail Lilburn, GA 30047, ISBN-10: 088173-620-1.

- Lind H., and Muyingo H., 2012, *Building maintenance strategies: planning under uncertainty*, Property Management Vol. 30 No. 1, pp.14-28 Emerald Group Publishing Limited.

- Olanrewaju A. L., and Abdul-Aziz A.R., 2015, *Building Maintenance Processes and Practices-The Case of a Fast Developing Country*, Library of Congress Control Number: 2014952904, ISBN 978-981-287-262-3, Springer Singapore Heidelberg New York Dordrecht London.

- Saranga, H.,2002, *Relevant condition-parameter strategy for an effective condition-based maintenance*, Journal of Quality in Maintenance Engineering, Vol. 8 No. 1, pp. 92-105.

- Stanford H.W., 2010, *Building Maintenance Protection of Capital Assets*, The Fairmont Press, Inc., Indian Trail 700, Lilburn, GA 30047.

NOMENCLATURE

BMM= building maintenance management
BS= british standard
CBM= condition-based maintenance
CSR= corporate social responsibility
EN= european standard
HVAC= heating, ventilating, and air conditioning
Std. dev. = standard deviation
ANOVA= analysis of variance

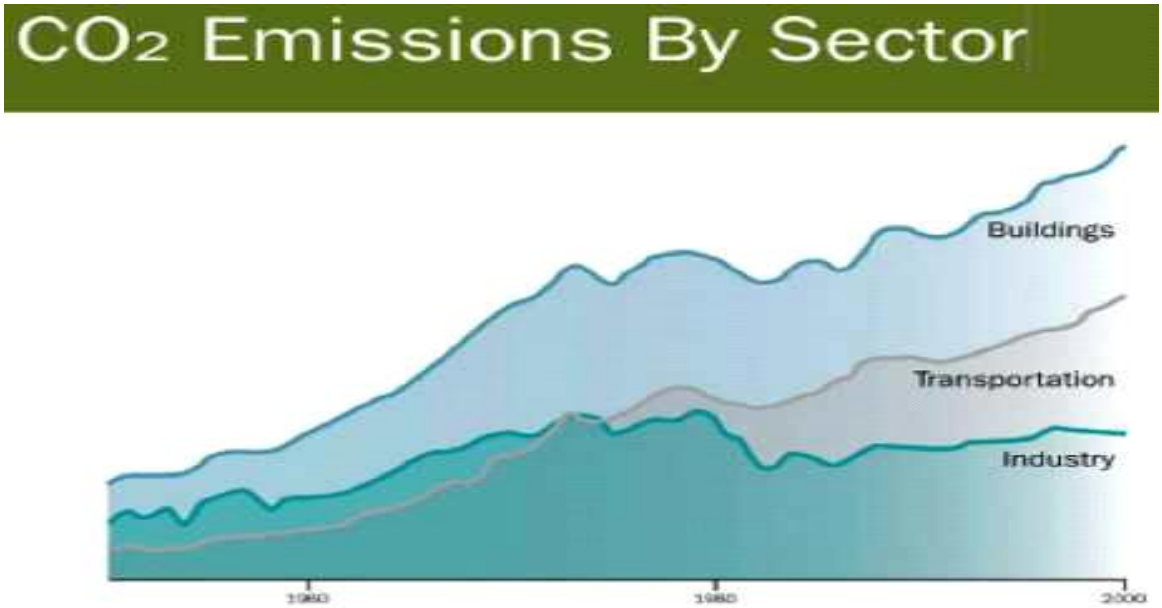

Figure1. The CO_2 emission according to sectors. **Ahn, 2008**

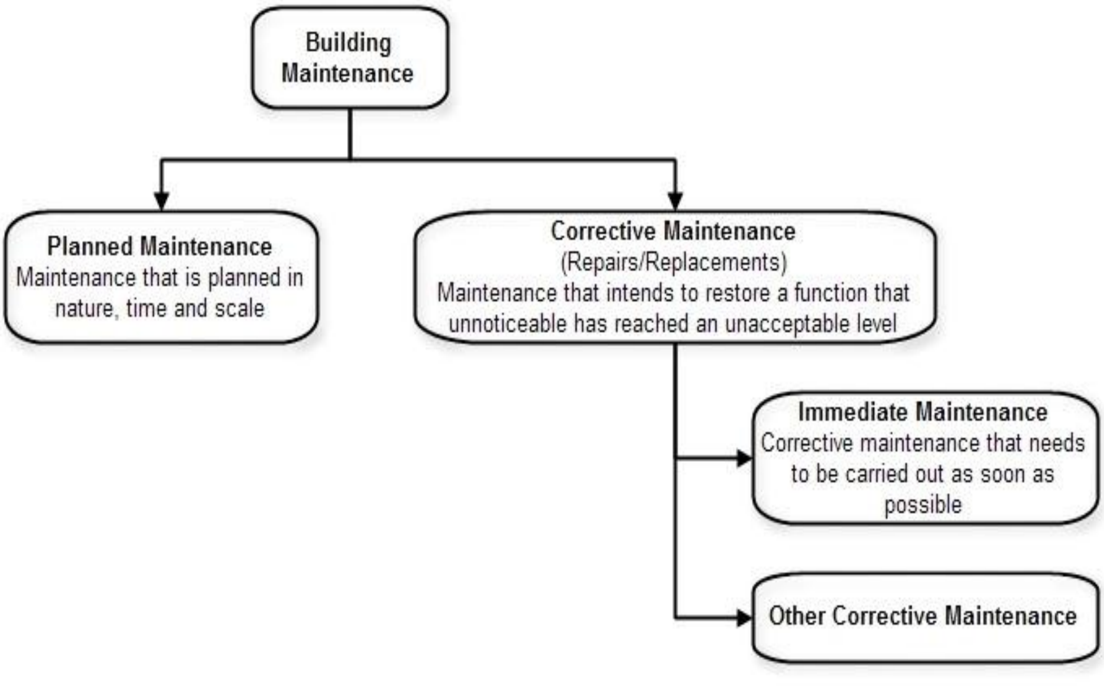

Figure2. Maintenance classifications according to planning requirements. **Chanter, and Swallow, 2007**

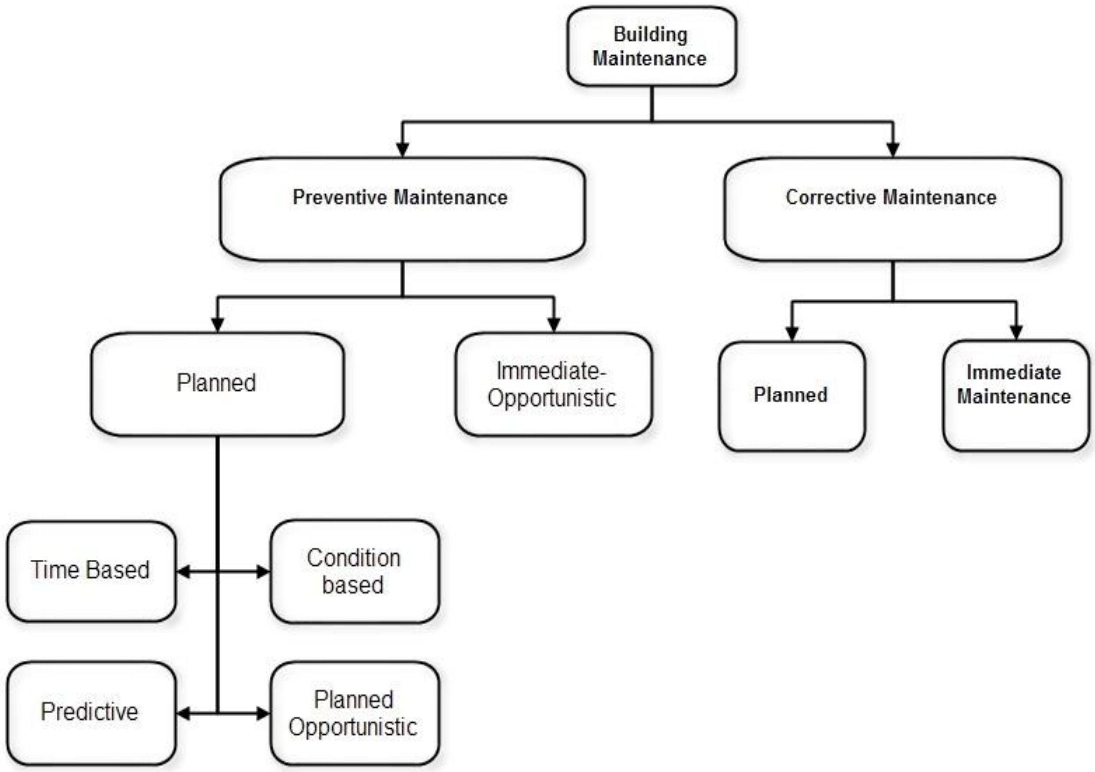

Figure3. Maintenance classifications according to maintenance type. **Chanter, and Swallow, 2007**

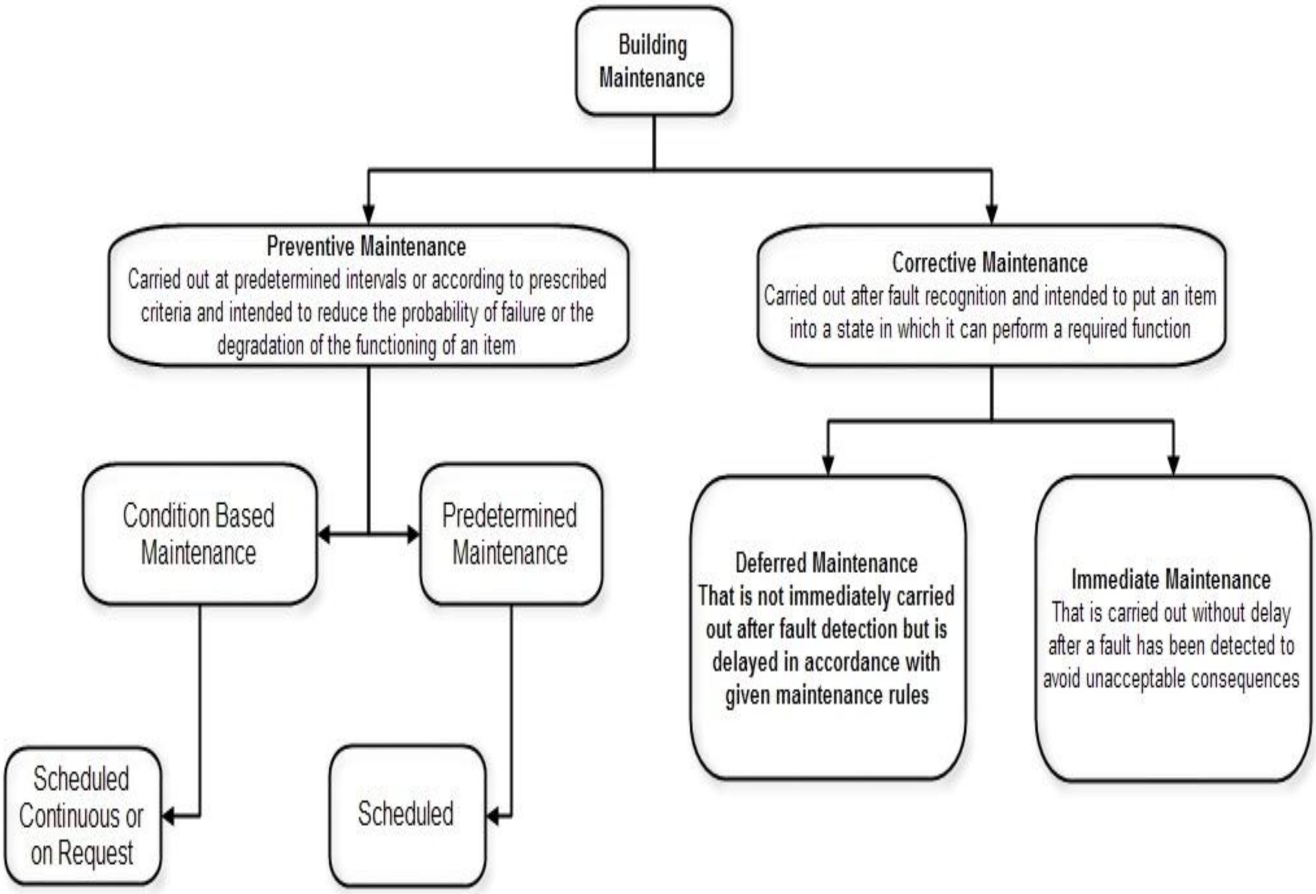

Figure4. Maintenance classifications according to maintenance type with details. **Chanter, and Swallow, 2007**

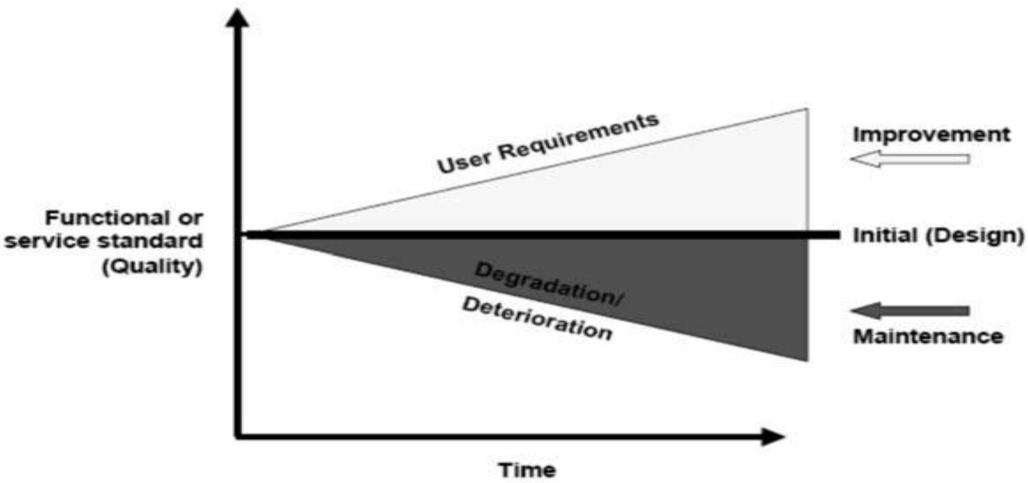

Figure5. Functionality/Quality vs. Time. , **Stanford, 2010**

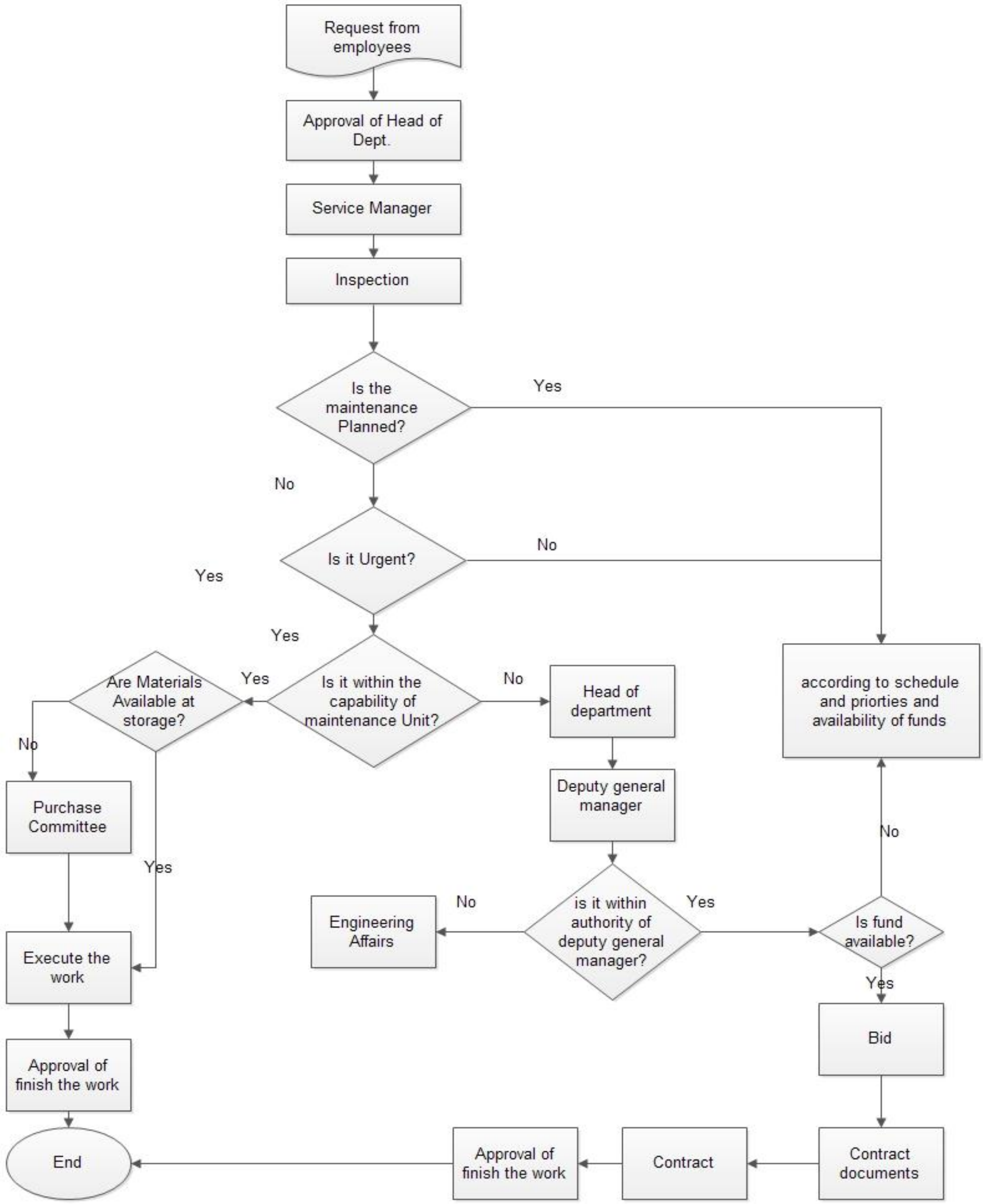

Figure6. Current building maintenance management procedure in Iraq.

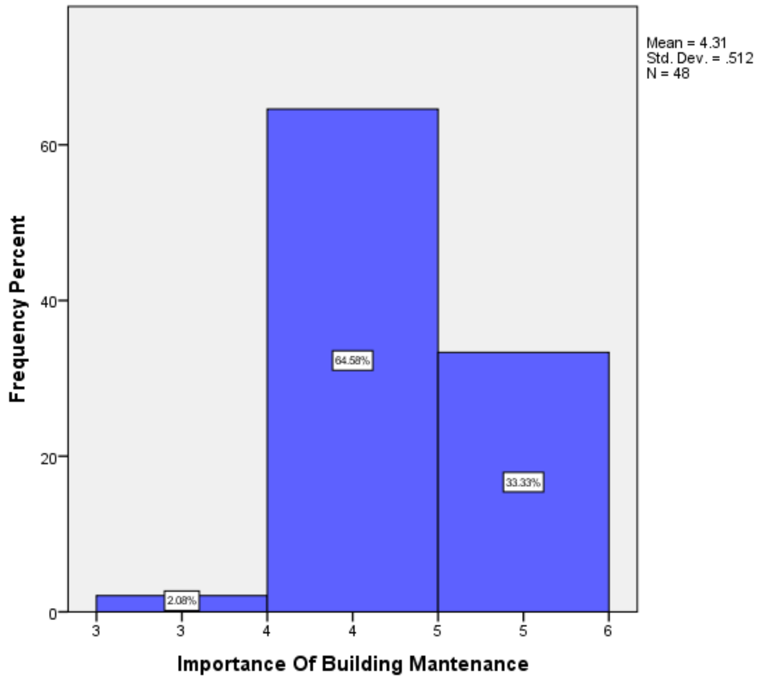

Figure7. Frequency of respondent's opinion on importance of building maintenance.

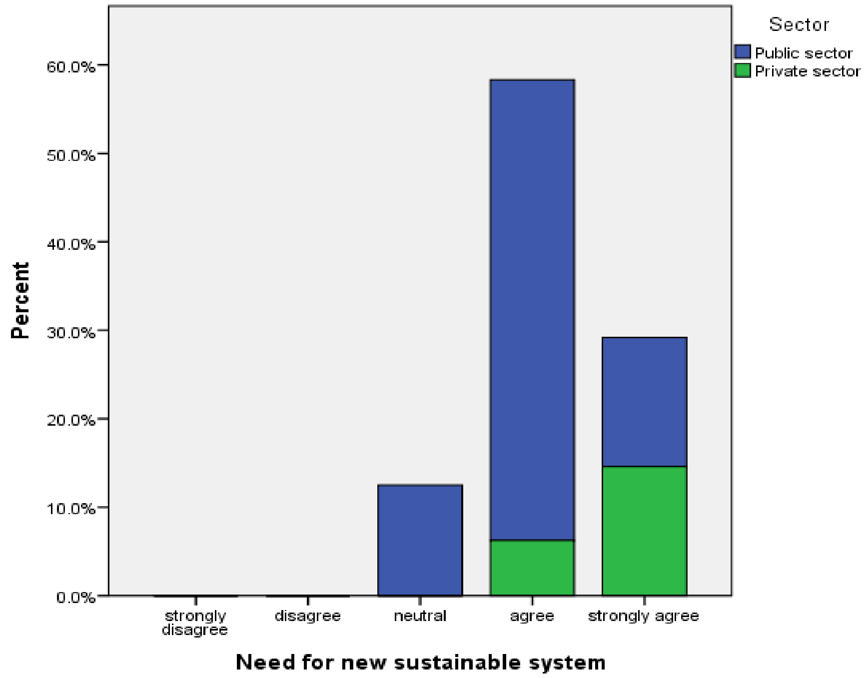

Figure8. Frequency of respondent's opinion on need for new sustainable system for maintenance management.

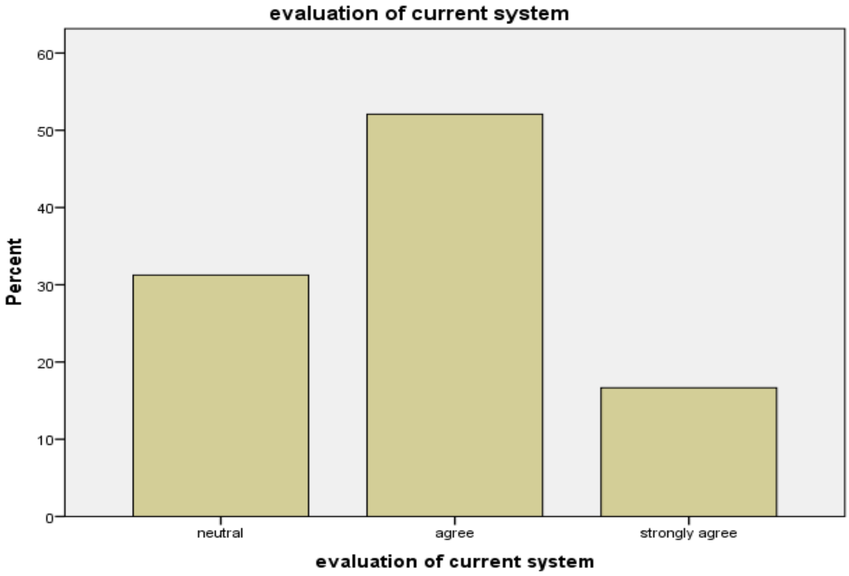

Figure9. Descriptive analysis for respondent's evaluation of current system.

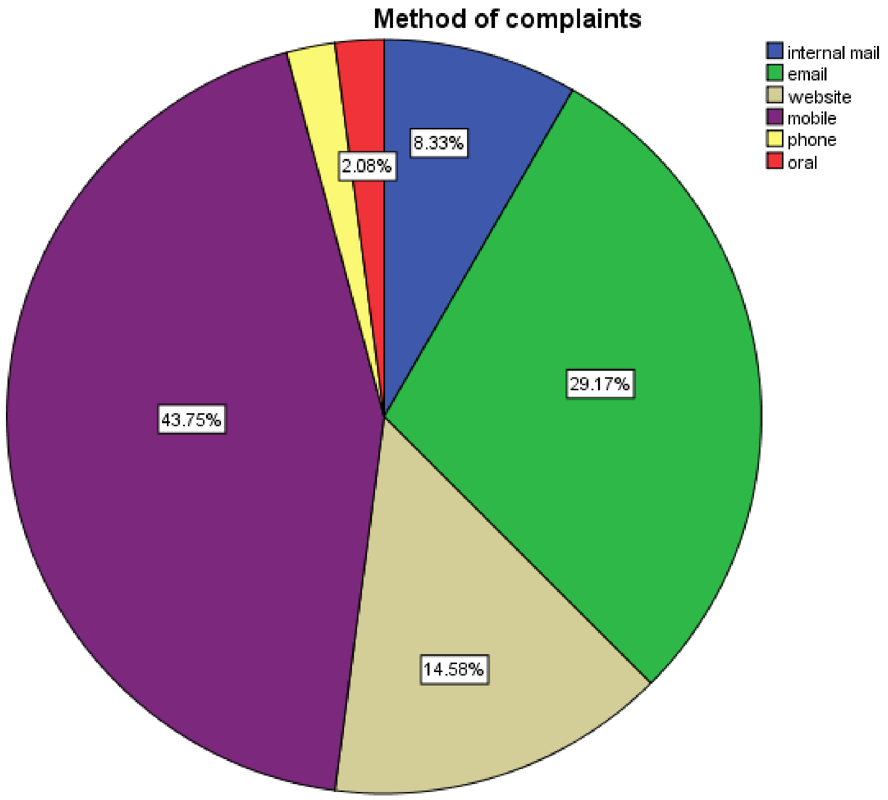

Figure10. Distribution of delivering maintenance complaint.

Table1. The logic behind maintenance types.

Maintenance Type	Logic
Corrective maintenance	Maintain when it failed
Preventive maintenance (Time-based)	Maintain it regularly
Preventive maintenance (condition-based)	Maintain it (just) before it failed
Opportunistic maintenance	Maintain it if it is cost effective
Proactive maintenance	Maintain the root causes the failure

Table2. Key questions for Sustainable building maintenance assessment.

Q1	Do you know everything about your buildings and your building maintenance management (BMM) systems and procedures? What condition they are in, where they are, their contribution to value, and what function they perform? Do you know the degree of accuracy of this information?
Q2	Do you know what is required from your BMM in the short, medium and long-term consideration?
Q3	Can your BMM deliver your buildings management objectives cost effectively?
Q4	Are you getting the best value for money from your BMM? (How could you get more value from them)?
Q5	Do you have perception about the capability in your BMM portfolio? Have some BMM systems become redundant, underused, too expensive or unprofitable?
Q6	Are you sure about the risks of your BMM and if they causing harm to people or to environment or if the risks are tolerable and at legally accepted levels?
Q7	Are your BMM-related expenditure (initial cost or capital investment and operating costs) excessive, optimal or insufficient, and if they correctly assigned across the BMM portfolio?
Q8	Do you have method to evaluate the benefits (performance, compliance, sustainability and risk reduction) of proposed work and, in the other hand, quantify the total impact in case of not performing such work, or delaying such actions?
Q9	Do you measure future problems for developing (such as risks, performance deterioration, or expenditure requirements) while obtaining short-term gains?
Q10	Do you consider to the other aspects of the organization that affect your BMM plan(s), such as knowledge, finance, people, and intangibles? In the other hand, do you consider the impact of your BMM plan(s) on these other aspects?
Q11	Are you reviewing the appropriateness of your BMM strategy in the consideration of changes in the financial, operating, and regulatory environment?
Q12	Do you continually improve your BMM system performance, and recognizing the benefits of the improvements? Are you knowing where and what improvements will be the most effective?
Q13	Are you having the necessary BMM policy, strategy and plan in order to ensure that you manage your BMM in a sustainable way?
Q14	Is your approach to sustainable management of the BMM taking appropriate account of the requirements and needs of your stakeholders and if so, do you open in the communication with those stakeholders?
Q15	Are the skills and wellbeing of your employees, working conditions, and contracted service providers given the required consideration?
Q16	Do you optimize your BMM processes and procedures in the consideration of the latest innovation and developments in technology
Q17	What are the main factors that affecting the sustainable maintenance from your point of view?
Q18	Do you have the ability to answer all of these questions confidently, and declare the answers to the interested parties?

Table3. Interviewee positions and date of interviews.

Interviewee Position	**Date of interview**
Assistant chief-University	Oct. 2014
Associate Dean for administrative affairs-University	Oct. 2014
Engineering Department Director-Establishment	Oct. 2014
Chief of maintenance department- Ministry	Oct. 2014
Associate manager-Secondary school	Oct. 2014
Manager - Secondary school	Nov. 2014
Director General of Engineering affairs- Ministry	Nov. 2014
Head - Medical center	Nov. 2014
Head -Police department	Nov. 2014
Director General- real estate registration office	Nov.2014
Maintenance managers (different organizations) (14 maintenance manager)	Oct 2014- Dec. 2014
Engineers working in maintenance department (different organizations) (22 engineers)	Oct 2014- Dec. 2014

Table4. Public sector/ Private sector percentage.

		Frequency	Percent	Valid Percent	Cumulative Percent
Valid	Public sector	38	79.2	79.2	79.2
	Private sector	10	20.8	20.8	100.0
	Total	48	100.0	100.0	

Table5. Cross tabulation between sector and specialist.

		Specialist		Total
		Engineering	Administrative	
Sector	Public sector	36	2	38
	Private sector	9	1	10
Total		45	3	48

Table6. Sector vs. experience crosses tabulation.

		Experience				Total
		between 5 and 10 years	between 10 and 15 years	between 15 and 20 years	more than 20 years	
Sector	Public sector	2	19	11	6	38
	Private sector	1	2	7	0	10
Total		3	21	18	6	48

Table7. Specialist percentage.

Specialist

		Frequency	Percent	Valid Percent	Cumulative Percent
Valid	Engineering	45	93.8	93.8	93.8
	Administrative	3	6.3	6.3	100.0
	Total	48	100.0	100.0	

Table8. Sector * Need for new sustainable system Cross tabulation.

Count

		Need for new sustainable system			Total
		neutral	agree	strongly agree	
Sector	Public sector	6	25	7	38
	Private sector	0	3	7	10
Total		6	28	14	48

Table9. Descriptive analysis for respondent's evaluation of current system depend on their scientific degrees.

evaluation of current system

	N	Mean	Std. Deviation	Std. Error	95% Confidence Interval for Mean		Minimum	Maximum
					Lower Bound	Upper Bound		
Diploma	2	4.00	1.414	1.000	-8.71-	16.71	3	5
B.Sc.	29	3.72	.649	.121	3.48	3.97	3	5
M.Sc.	9	4.22	.667	.222	3.71	4.73	3	5
PhD	8	3.88	.641	.227	3.34	4.41	3	5
Total	48	3.85	.684	.099	3.66	4.05	3	5

Table10. Experience * Method of complaints Cross tabulation.

		Method of complaints						Total
		internal mail	email	website	mobile	phone	oral	
Experience	between 5 and 10 years	0	1	1	0	0	1	3
	between 10 and 15 years	1	7	3	9	1	0	21
	between 15 and 20 years	2	5	2	9	0	0	18
	more than 20 years	1	1	1	3	0	0	6
Total		4	14	7	21	1	1	48

Application of Artificial Neural Network for Predicting Iron Concentration in the Location of Al-Wahda Water Treatment Plant in Baghdad City

Dr. Nawar Omran Ali Al-Musawi
Instructor
Engineering College-Baghdad University
E-mail:nawaromran@yahoo.com

ASTRACT

Iron is one of the abundant elements on earth that is an essential element for humans and may be a troublesome element in water supplies. In this research an AAN model was developed to predict iron concentrations in the location of Al- Wahda water treatment plant in Baghdad city by water quality assessment of iron concentrations at seven WTPs up stream Tigris River. SPSS software was used to build the ANN model. The input data were iron concentrations in the raw water for the period 2004-2011. The results indicated the best model predicted Iron concentrations at Al-Wahda WTP with a coefficient of determination 0.9142. The model used one hidden layer with two nodes and the testing error was 0.834. The ANN model could be used to predict future iron concentrations as the results from the verification of the ANN model for years 2012 and 2013 indicated good accuracy with a coefficient of determination R^2 = 0.8965.

Key Words: Iron, ANN model, Tigris River, Water treatment plant, Al-Wahda.

استخدام شبكة الخلايا العصبية لتوقع تركيز ايون الحديد في محطة الوحدة لمعالجة المياة في مدينة بغداد

د.نوار عمران علي الموسوي
مدرس
كلية الهندسة-جامعة بغداد

الخلاصه

يعتبر الحديد احد العناصر المهمة على الارض وذو اهمية اساسية للانسان وقد يسبب مشاكل كيمياوية في مياة الشرب, في هذا البحث تم بناء نموذج رياضي بالاعتماد على مبدا الخلايا العصبية في تقدير تركيز الحديد في موقع محطة الوحدة لمعالجة مياة الشرب وذلك عن طريق تقييم نوعية مياة نهر دجلة بالاعتماد على عنصر الحديد في مواقع المحطات السبعة لمعالجة مياة الشرب في مدينة بغداد وقد استخدم البرنامج الاحصائي SPSS في بناء النموذج الرياضي. تراكيز الحديد المستخدمة في النموذج كانت للفترة بين 2004-2011 وقد اظهرت النتائج من النموذج ان معامل التحديد هو 0.9142 وقد استخدم النموذج طبقة مخفية واحدة مع خليتين ونسبة خطا قيمتها 0.834.
اظهرت النتائج دقة النموذج الرياضي من حيث التقارب بين القيم الحقيقية والقيم المتوقعة في المستقبل وعند استخدام تراكيز الحديد للعامين 2012 و 2013 كانت النتائج ذات تقارب جيد وبمعامل تحديد0.8965.

الكلمات الرئيسة: الحديد, نموذج شبكة الخلايا العصبية, نهر دجلة, محطة معالجة المياة, الوحده.

1. INTRODUCTION

Water quality of different sources and quality changes is a subject of ongoing concern. Consequently there is a need for effective methods for modeling water quality parameters in surface water to control pollution and apply necessary managements. Different modeling approaches are applied to analyze water resources, Artificial Neural Network (ANN) is one of these approaches, and the advantages of ANNs are that they are able to represent both linear and nonlinear relationships of water resources data. Also ANN was found suitable for prediction purposes as they produce accurate results. **Chi.et al., 2006** applied ANNs for the classification and prediction of water quality of Yangtze River in China using DO, COD, NH_3 and pH values for the period from January 2003 to September 2005. The results showed sever pollution is reached in this river and many efforts should be taken for pollution control. **Musavi** and **Golabi, 2008.** selected an ANN model for water quality simulation of Karoo River in Iran. Several water quality parameters were chosen CO_3, HCO_3, SO_4, Cl, Na, Ca, Mg, K, Ec, TDS and SAR. The results showed that the ANN model was able to predict water quality in the river very successfully with more than 90% accuracy.
Mozejkod and **Gniot 2008** developed an ANN model for time series modeling of total phosphorous concentration in Odra River in Poland. The variables used in the model were temperature, pH, NO_3, DO, BOD, COD, SO_4, Cl_2, and SS. The models prediction matched reasonably with the observations. The correlation coefficient R was 0.865 and mean absolute error MAE was 0.024 mgP/dm^3. **Ali et al., (2009)** proposed ANN models for the prediction of TDS, EC and Turbidity in Johor River in Malaysia. The models predicted water quality parameters with high accuracy as the mean absolute error was 10% for the different models**.** In **2010, Vesna et al.,** developed an ANN model to predict DO in Gruza Reservoir in Serbia. The most effective inputs for the model were the pH and temperature, while Cl and total phosphate were found to be the least effective parameters. The correlation coefficient using the most effective inputs (pH, Temp., NO_3, NO_2, NH_3, conductivity, Fe, Mn) was 0.8478**. Hossein** and **Ehsan, (2011)** presented empirical multilayer ANN model to estimate water quality indices BOD and DO, in Marad Big River in Iran. The input data for the ANN model were EC, TDS, SS, Turbidity, Na, HCO_3, NO_3, NH_3 and PO_4. The models are capable to capture long-term trends observed for DO and BOD both in time and space. DO model had a correlation coefficient of 0.972 and for BOD 0.937**.**

In this research an AAN model is to be developed to predict iron concentrations in Tigris River in Baghdad city. The primary sources of iron in water are from natural geologic sources, also iron based materials, such as cast iron and galvanized steel pipes that have been widely used in water distribution systems .0.3 mg/L can cause water to turn a reddish brown color **Illinois Department of Public Health, 2010.**
The presence of iron and manganese in water cause threats to industrial and municipal water supplies, formation of scales, and blockage of water pipes thus leading to economic losses **Sodamade** and **Pearse, 2013**. Excessive ingested iron can cause excessive levels of iron in the blood that can damage the cells of the gastrointestinal tract, preventing them from regulating iron absorption. Humans experience iron toxicity above 20 milligrams of iron for every kilogram of mass, and 60 milligrams per kilogram is a lethal dose. Sullivan was the first to propose and continued to

reiterate that iron levels play a major role in producing atherosclerosis. **Sieliechi et al., 2010** stated that women, who have a reduced iron load, have strong protection against atherosclerosis, compared to men in the same age group. They suggested that iron can be involved in Alzheimer's disease. The important mechanism is the interaction of iron and cholesterol in promoting oxidative damage, causing both atherosclerosis and neuro degeneration. Excessive iron in water can stain clothing and can give a metallic taste to water or to food. Furthermore, iron deposits can build up in pressure tanks, water heaters, and pipelines, reducing the quantity and pressure of the water supply **OVIVO, 2010.**

In this research an Artificial Neural Network was developed to predict iron concentration in Tigris River at the location of Al-Wahda water treatment plant in Baghdad city through water quality assessment of iron parameter upstream (locations of seven water treatment plants upstream).

2. MATERIALS AND METHODS

2.1 Study Area Description

Tigris river water is considered the only source of potable water for the city of Baghdad, and the river divides the city into right (Karkh) and left (Risafa) sides with a flow direction from north to south. The study area within Baghdad City is located in the Mesopotamian alluvial plain between latitudes 33°14'-33°25' N and longitudes 44°31'-44°17' E, 30.5 to 34.85 m above mean sea level. The area is characterized by arid to semi-arid climate with dry hot summers and cold winters; the mean annual rainfall is about 151.8 mm **Al-Adili, 1998**. In Baghdad city, a tremendous increase in freshwater demand is required due to the rapid growth in population and accelerated industrialization. The quality of the flowing water is affected by the effluent discharges from various uncontrolled sources as domestic, industries, agriculture along the downstream stretch.

2.2 Data Collection and Analysis

The data used in this paper were provided from Mayoralty of Baghdad for the period from January 2004 to December 2013 which represented the monthly average values for iron concentration in the flowing water. These data were at the locations of the water treatment plant on the Tigris River. There are eight water treatment plants (WTPs) from the north to the south of Baghdad city, Al-Karkh, East Tigris, Al Wathba, Al Karama, Al Qadisia, Al Dora, Al Rasheed and Al Wahda WTPs as shown in **Fig.1**. All water treatment plants in Iraq are designed as conventional plants. This treatment process does not significantly affect the concentrations of the dissolved constituents. Therefore it's important to monitor iron concentrations of the influent to these treatment plants to provide treated water with permissible iron concentrations to the consumer.

2.3 ANN Model

A typical neural network consists of a large number of elements known as nodes. Each node is connected to other nodes by links with associated weights. These weights represent information used by the net to solve the case to be solved. The nodes are arranged in a number of layers. The first layer is the input layer where the inputs (dependent variables) are applied to the net. The last layer is the output layer where the outputs (independent) are extracted. The layers between the input and output are the hidden layers (one or more) with a number of nodes as proceeding elements. Many types of ANN are known, the popular is the multiple layer perceptron network. Important issues to design this network are the number of hidden layers and number of nodes they contain **Mozejko** and **Gniot, 2008**. A training process is carried out on a set of the input data as these data are divided into training and testing data. The learning process is based on the training data and testing data is used to verify the performance of the trained AAN. During the training process the weights of the input nodes are adjusted by several trails until the desired error function is obtained. The AAN is trained by minimizing this error in search space of weights **Chi et al., 2006.**

The SPSS software (Statistical Procedure for Social Science, version 20) was used to build the ANN model in this study. The model comprised seven nodes in the input layer which represent the influent iron concentration to the water treatment plants namely (Alkarkh, EastTigris, Wathba, Karama, Qadisia, Dora, and Rasheed), the output layer represents influent Iron concentration at Wahda water treatment plant. Many trials were performed, where in each run the software parameters were changed for selecting the best ANN model according to the highest correlation coefficient and the smallest testing error.

3. RESULTS AND DISSCUTION

3.1 Iron Concentration in Tigris River

The period under study was from 2004-2013, the data were collected are tabulated in **Table 1** in order to view the variation of iron concentration in raw water with respect to time and distance. **Fig. 2** and **3** indicated that the maximum iron concentration was 10.04 ppm at year 2011 in East Tigris WPT (upstream plant) and the minimum was 0.33 ppm in 2005 at Al Karama WTP (at the middle reach).

The main sources of iron in Tigris River are **Alsaqqar et al., 2015:**
1-The outlets of combined and storm sewers that discharge their wastewater directly in to the river.
2-The disposal of effluents from some industries: Al Taji gas factory, wool and textile factories upstream Al Karama WTP, vegetable oil factory, detergent factory and the cement factory near Al Wahda WTP.
3-Effluents from Al Dora refinery upstream Al Dora WTP and the effluent from Al Dora power plant which uses large amounts of water in the cooling towers.
4-There are several raw water pumping stations that provide irrigation water to the nearby lands. At the end of the working day, the flow is reversed in the pipes for cleaning the system from the sediments, this may lead to the corrosion of the pipes and cleaning water may contain iron concentrations.
5-Iron may precipitate in the coagulation and flocculation process in the WTPs, so high concentrations of iron are found in the settled sludge which is discharged into the river.

3.2 ANN Model for iron in Tigris River

The ANN model developed from the SPSS software is summarized in **Table. 2**. From the case processing summary the data (total of 70) were divided to 68.6% training, 15.7% testing and 15.7% holdout. The input data were from 2004 to 2011which represented the monthly average values for iron concentrations at the seven WTPs upstream to Wahda WTP.

The architecture of the ANN model is shown in the parameter estimates where two nodes are found in the hidden layer, H(1:1) and H(1:2) as shown in **Fig. 4**. In this section the weights of the input parameters from each hidden node is calculated.
The best ANN model representing iron concentrations at Al Wahda WTP had a coefficient of determination $R^2 = 0.9142$ as shown in **Fig. 5** and testing error 0.834 as shown in **Table 3**. While **Table 4 s**hows the parameters estimates. The importance of the independent variables is shown in **Table 5,** where Al Karama WTP had the highest importance of 30.52% and Al Rasheed WTP had 26.16% which affected the predicted values of Iron at Al Wahda WTP.

3.3 Verification of the Model

In order to verify the accuracy of the ANN model for predicting the iron concentrations at Al Wahda WPT the recorded data (observed) for years 2012 and 2013 were plotted against the predicted values (from the AAN model) as shown in **Fig. 6**. The model gave good accuracy with a coefficient of determination $R^2 = 0.8965$.

CONCLUSIONS

1- Iron concentrations in Tigris River are fluctuated.

2-The developed ANN model was suitable in predicting iron concentration in Tigris River with a coefficient of determination $R^2 = 0.914$. The model used one hidden layer with two nodes and the testing error was 0.834.

3- From the verification of the ANN model for years 2012 and 2013, the model gave good accuracy with a coefficient of determination $R^2 = 0.8965$ for predicting Iron concentrations in Tigris River.

REFERENCES

- Ali Najah, Ahmed E., Othman A. K. and Othman J., 2009, Prediction of Johor Water Qiality Parameters Using Artificial Neural Networks, European Journal of Scientific Research, Vol.28, No.3, pp 422-435.
- Alsaqqar, Awatif Soaded, A. Hashim, and A. Mahdi, 2015**,** Water Quality Index Assessment using GIS case study: Tigris river in Baghdad city, International Journal of Current Engineering and Technology, Vol.5, No.4, Aug 2015.
- S. Al-Adili, 1998, Geotechnical Evaluation of Baghdad Soil Subsidence and Their Treatment, Ph.D. Thesis, University of Baghdad, Iraq.
- Chi Zhou, Liang G., Haibing G. and Chuanyong P., 2006**, Pattern** Classification and Prediction of Water Quality by Neural Network with Particle Swarm Optimization, Proceedings of the 6th World Congress on Control and Automation June 21-23, Dalian, China.

- Hossein Banejad and Ehsan Olyaie, 2011, Application of an Artificial Neural Network Model to Rivers Quality Indexes Prediction Study, Journal of American Science, 7(1).
- Illinois Department of Public Health, 2010, Fact Sheet, Division of Environmental Health, Springfield. Updated Dec.
- Mayoralty of Baghdad, 2015, Baghdad Water Administration, Documented Data.
- Mozejko J. and Gniot R., 2008, Application of Neural Networks for the prediction of total Phosphorous Concentrations in Surface Waters, Polish J. of Environmental Study, Vol. 17, No. 3 pp 363-368.
- Musavi Jahromi S. H. and Golabi M., 2008, Application of Artificial Neural Networks in River Water Quality Modelling: Karoon River, Iran, Journal of Applied Sciences 8(12), pp 2324-2328.
- OVIVO, 2010, Municipal Drinking Water Removal, www.ovivowater.com, Tunisia.
- Sieliechi Joseph, Marie G., Joseph K. and Ion S, 2010, Effect of Water Treatment Residuals (Aluminum and Iron Ions) on Human Health and Drinking Water Distribution Systems, International Journal of Conservation Science, Vol. 1, Issue 3, July-September 2010, pp 175-182, www.ijcs.uaic.ro.

- Sodamade, G. A and Pearse, L. F., 2013, Removal of Iron and Manganese Using Rapid Sand Filtration, NSE Technical Transaction, Vol.47, No.3, July-September , Lagos – Nigeria.

- Vesna Rankovic, Jasna R., Ivana R., Aleksandar O. and Ljiljana C., 2010, Neural Network Modeling of Dissolved Oxygen in the Gruza Reservoir, Serbia, Ecological Modeling 221, pp 1239-1244.

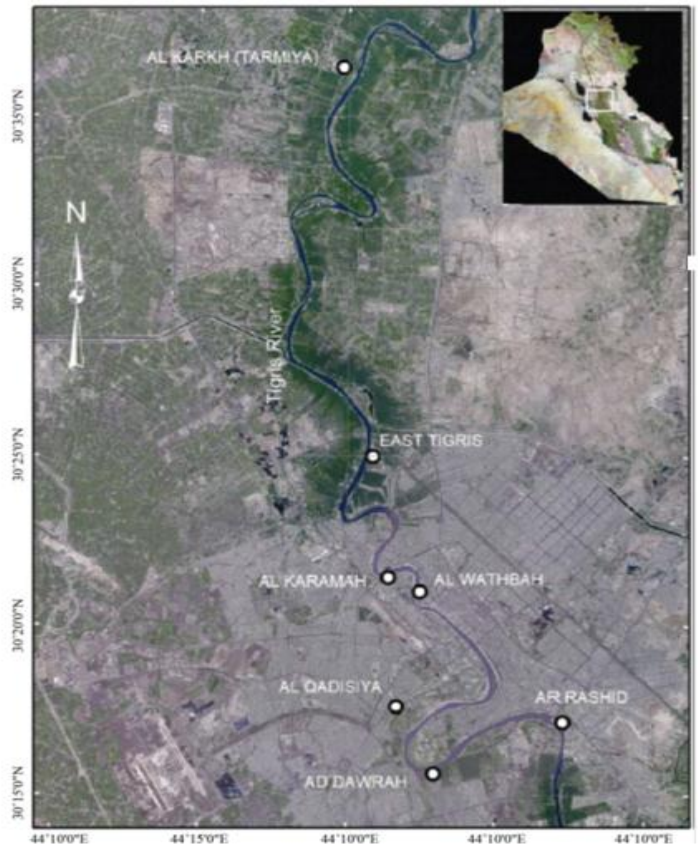

Figure 1 . Sampling locations across Tigris River, within Baghdad City. Location of the eight water treatment plants.

Table 1 . Variation of average annual iron concentration (ppm) in raw water with Respect to time and distance, Mayoralty of Baghdad, 2015

RAW	AL-KARKH	ESTTIGRIS	WATHBA	KARAMA	QADISIA	DORA	RASHEED	WAHDA	AVG
2004	1.00	1.13	1.13	1.54	1.58	1.42	2.14		1.42
2005	0.55	1.08	0.67	0.33	1.59	1.19	1.41		0.97
2006	1.70	1.92	2.88	0.84	2.79	2.93	2.56	2.11	2.22
2007	1.19	1.93	1.99	0.71	3.34	1.35	1.79	1.12	1.68
2008	0.50	1.25	0.89	0.32	1.37	0.66	0.70	0.66	0.79
2009	0.97	2.00	0.82	1.57	3.52	1.39	2.54	2.37	1.90
2010	0.84	1.81	0.63	2.61	2.46	2.69	1.21	1.23	1.68
2011	0.83	10.04	3.51	1.97	2.11	1.08	1.13	2.95	2.95
2012	0.63	2.72	1.97	1.51	1.58	0.50	0.89	0.80	1.33
2013	1.02	1.95	4.84	1.39	2.15	1.23	1.44	1.16	1.90
AVG	0.92	2.58	1.93	1.28	2.25	1.44	1.58	1.55	1.69

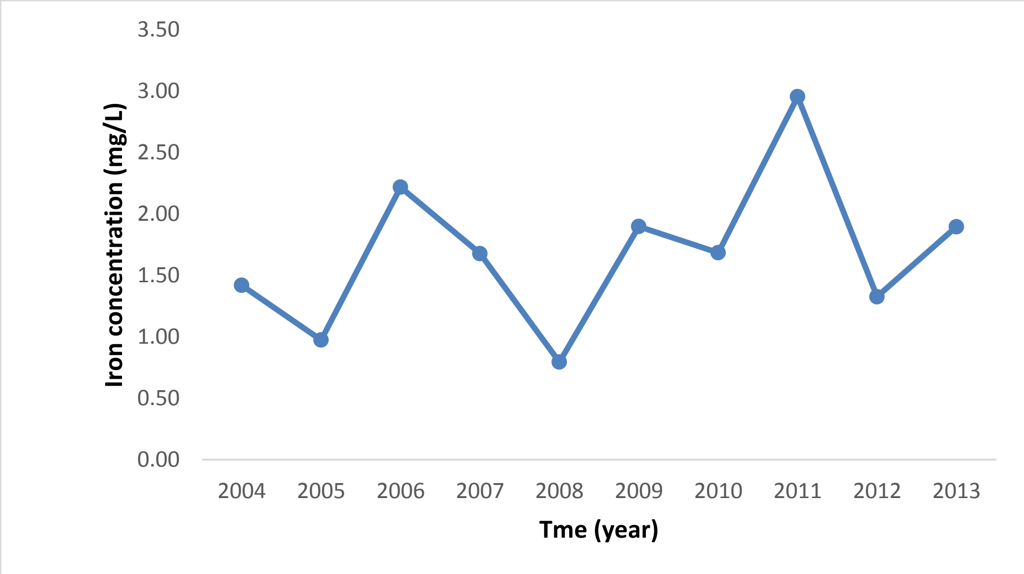

Figure 2. Variation of average annual iron concentrations (ppm) in raw water with respect to time

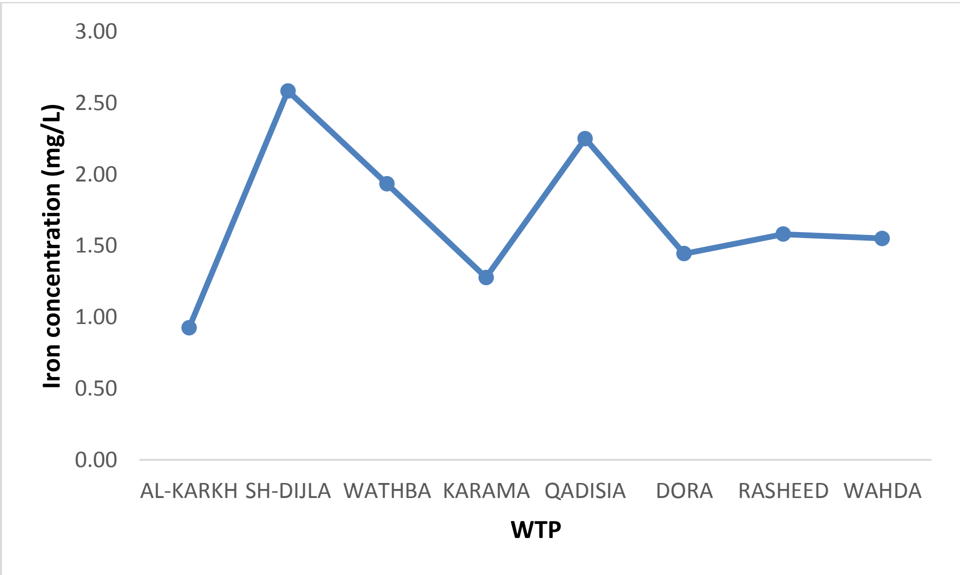

Figure 3. Variation of average annual iron concentrations (ppm) in raw water with respect to distance

Table 2. Case Processing Summary

		N	Percent
Sample	Training	48	68.6%
	Testing	11	15.7%
	Holdout	11	15.7%
Valid		70	100.0%
Excluded		0	
Total		70	

Table 3. Model Summary

Training	Sum of Squares Error	1.798
	Relative Error	.076
	Stopping Rule Used	1 consecutive step(s) with no decrease in error[a]
	Training Time	0:00:00.02
Testing	Sum of Squares Error	.697
	Relative Error	.834
Holdout	Relative Error	3.946

Dependent Variable: WAHDA

a. Error computations are based on the testing sample.

Table 4. Parameter Estimates

Predictor		Predicted		
		Hidden Layer 1		Output Layer
		H(1:1)	H(1:2)	WAHDA
Input Layer	(Bias)	-.325	.087	
	ALKARKH	.304	-.045	
	EASTTIGRIS	.226	.174	
	WATHBA	.082	.155	
	KARAMA	.777	.473	
	QADISIA	-.373	-.176	
	DORA	-.038	-.163	
	RASHEED	.968	-.249	
Hidden Layer 1	(Bias)			.417
	H(1:1)			1.207
	H(1:2)			-1.600

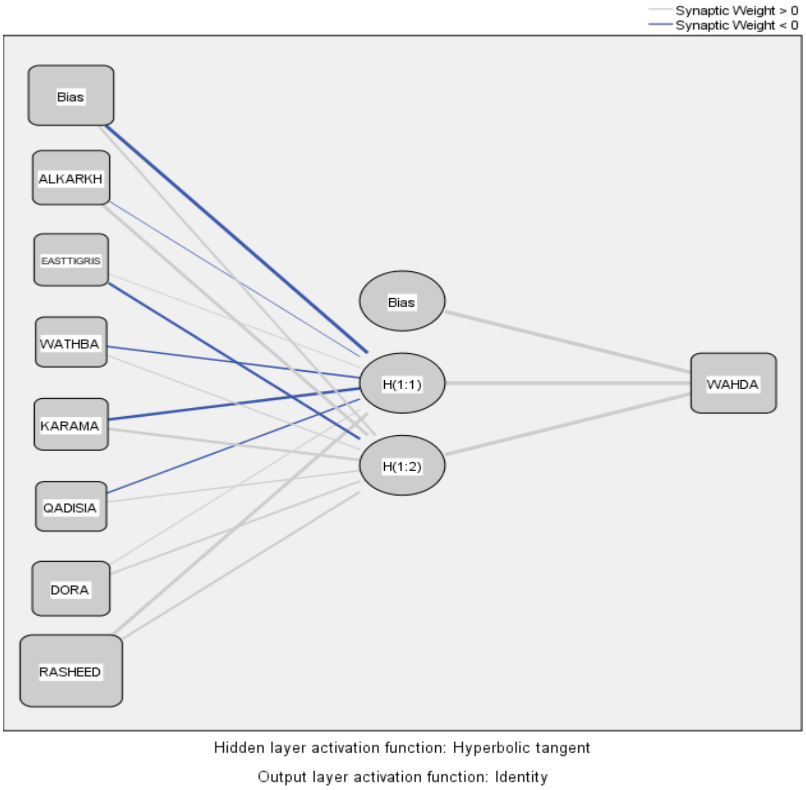

Figure 4. Architecture of the Artificial Neural Network Model

Table 5. Independent Variable Importance

WTP	Importance %
Alkarkh	7.06
Easttigris	10.15
Wathba	6.88
Karama	30.52
Qadisia	12.87
Dora	6.37
Rasheed	26.16

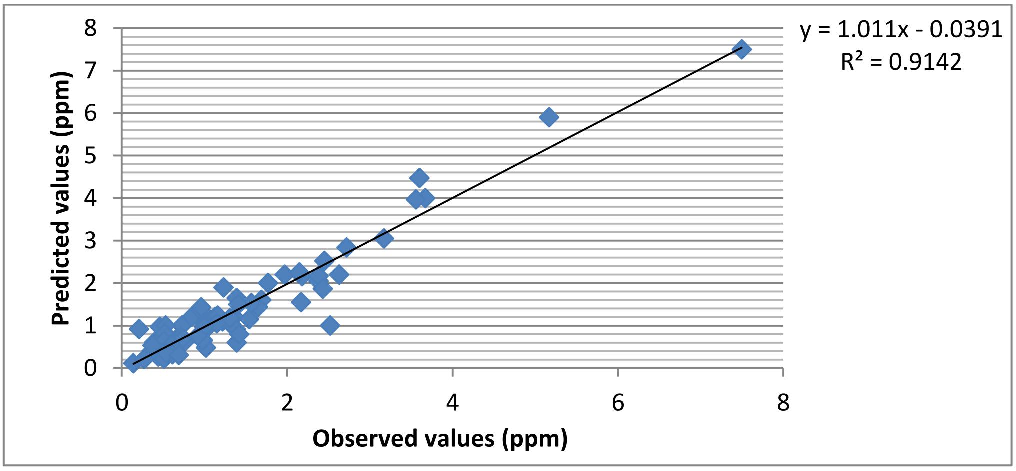

Figure 5. Coefficient of determination of the developed ANN model

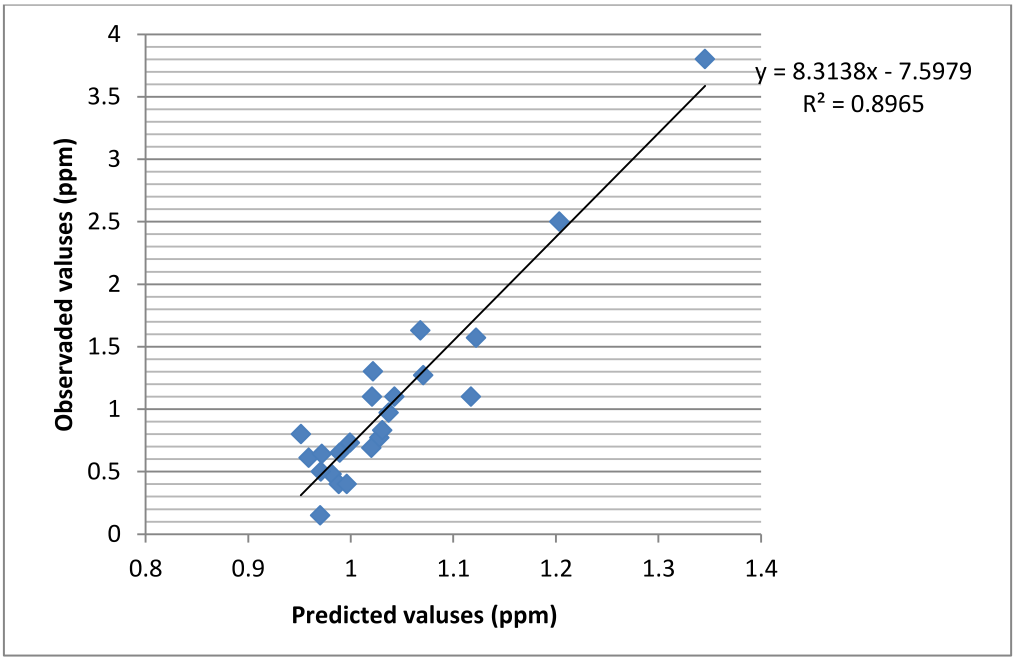

Figure 6. Verification of the ANN model for predicting Iron concentrations at Wahda WTP for years 2012-2013

Demulsification of Remaining Waste (Water In Oil Emulsions) After Removal Of Phenol In Emulsion Liquid Membrane Process

Najwa Saber Majeed
College of Engineering-University of Baghdad
Email: dr.najwa_saber@yahoo.com

Manal Adnan Mohammed
College of Engineering-University of Baghdad
Email: manaladnan24@yahoo.com

ABSTRACT

The aim of present work is to study the removal of phenol present in aqueous feed solution by the emulsion liquid membrane technique using kerosene as a diluent, sodium hydroxide as a stripping agent, and sorbitan monooleate (Span 80) as a surfactant. The parameters studied were: surfactant concentration, volume ratio of membrane phase to internal phase, and stirring speed. It was found that more than 98% of phenol can be removed at the conditions were surfactant concentration 2% (v/v), volume ratio of membrane phase to internal phase 5:1 and stirring speed 400 rpm. Maximum phenol extraction efficiency at 7 minutes of process time was observed. It was found that there was a good agreement between the standard kerosene and the upper layer that resulted after the demulsification of the remaining waste by applying centrifuge. Thus, it is possible to reuse this layer to prepare a new emulsion of the membrane phase.

Keywords: demulsification, phenol, emulsion liquid membrane, centrifuge, extraction time.

كسر الاستحلاب للمخلفات المتبقيه (مستحلبات الماء في النفط) بعد إزالة الفينول بعملية الغشاء السائل المستحلب

د. نجوى صابر مجيد
كلية الهندسة-جامعة بغداد

منال عدنان محمد
كلية الهندسة-جامعة بغداد

الخلاصة

الهدف من هذا العمل هو دراسة إزالة الفينول من المحاليل المائية باستخدام تقنية الغشاء السائل المستحلب بواسطة استخدام الكيروسين كمخفف، هيدروكسيد الصوديوم كعامل انتزاع و (Span 80) كمادة منشطة للسطوح. تم دراسة العوامل وهي: تركيز المادة المنشطة للسطوح, النسبة الحجمية لمرحلة الغشاء إلى المرحلة الداخلية، و سرعة التحريك. وقد وجد أن أكثر من 98٪ من الفينول يمكن ازالته عند الظروف وهي تركيز للمادة المنشطة للسطوح 2٪ (حجم / حجم)، النسبة الحجمية لمرحلة الغشاء إلى المرحلة الداخلية 5:1 , و سرعة التحريك 400 دورة في الدقيقة. و لوحظ ان أقصى كفاءة لاستخراج الفينول في 7 دقائق من وقت العملية. و وجد أن هناك توافق جيد بين الكيروسين القياسي والطبقة العليا الناتجه بعد عملية كسر الاستحلاب للمخلفات المتبقية من خلال تطبيق جهاز الطرد المركزي. وبالتالي, فإنه من الممكن إعادة استخدام هذه الطبقة لتحضير مستحلب جديد لمرحلة الغشاء.

الكلمات الرئيسية: كسر الاستحلاب, فينول، الغشاء السائل المستحلب، الطرد المركزي، وقت الاستخلاص.

1. INTRODUCTION

As the phenol is a significant basic material in various chemical, petrochemical and pharmaceutical processes, it and all derivatives have become very common organic water contaminants resulted from these industrial processes. Even at low concentration in water, phenol is considered a toxic material and has unfavorable impacts for ecosystems. Moreover, carcinogenic compounds are chlorophenols that are formatted from disinfection and oxidation processes due to the existence of phenol in natural waters **Hasanoğlu, 2013.** Less than 1 part per billion (ppb) of phenol in surface water has set as standard by the Environmental Protection Agency (EPA) because of the toxic nature of this compound. It is necessitated and very significant challenges as well as representing a dynamic field of research to remove phenol from industrial drainage by virtue of environmental laws and regulations governing safe discharge levels are being so strict **Meda et al., 2014**.

The available treatment methods used for removing phenol from aqueous solutions are divided into two major groups: traditional and advanced methods, according to the concentration of phenol, traditional methods involve adsorption, distillation, extraction, chemical oxidation, and biodegradation. The advanced methods are classified into membrane separation processes and photo oxidation processes **Mohammadi et al., 2015**. Membrane separation processes are one of the most widely researched and fastest growing separation processes of our century because of their advantages compared to traditional processes such as liquid-liquid extraction, distillation, absorption, etc. **Han and Row, 2010.** Liquid membrane separation offers an effective powerful process for different separation processes. Compared to traditional operations, emulsion liquid membrane processes have several attractive features such as high interfacial area, simple operation, relatively low cost, high efficiency, extraction and stripping in one stage, a non-dependence on equilibrium consideration and scope of continuous operation **Ravikumar et al., 2005**. Norman Li, **Li, 1974** was the first to introduce emulsion liquid membrane to increase the interfacial area to shorten the diffusion path, its invention for the separation has shown to be an easy method for the removal of chemicals from wastewater.

There are three types of emulsions: (1) oil in water emulsion (O/W) in this type, oil is the dispersed phase and water is the dispersion medium; (2) water in oil emulsion (W/O) in this type, water is the dispersed phase and oil is the dispersion medium; (3) multiple emulsions **Manikandan et al., 2014**. Multiple emulsions can be classified in two types; water/oil/water (W/O/W) or oil/water/oil (O/W/O) emulsions. In the first type the membrane is liquid oil and in the second type the membrane is water or an aqueous solution. The (W/O/W) type is the most familiar one. Multiple emulsions are widespread for industrial, pharmacy and medical applications by virtue of the existence of liquid membrane. The multiple emulsions are a result of forming small droplets in which smaller droplets inside them, the outer droplets are dispersed in an external phase. Liquid membrane is a layer which separates the small internal droplets from the external phase which is called the immiscible phase. Consequently, multiple emulsions are also called liquid emulsion membranes or liquid surfactant membranes **Ghosh, 2011**, **Cárdenas and Castro, 2003**. For instance, the system of caustic-in-oil emulsion that is shown in **Fig.1**, can be efficiently utilized to eject small amounts of phenol from a wastewater stream. Phenol is slightly soluble in oil, and then it will permeate easily from the outside water phase across the oil membrane into the internal aqueous caustic droplets. In this process the caustic will neutralize the phenol and tied it up as sodium phenate which is insoluble in oil and then it cannot diffuse back out again **Cahn and Li, 1974**. ELM process can be divided into four stages as shown in **Fig.2** and as follows : (1) emulsification of the internal phase and the membrane phase; (2) permeation (emulsion—external phase contacting); (3) settling (separation of external phase and the emulsion phase after extraction; and (4) demulsification to recover the membrane phase **Balasubramanian, 2014**, **Fassihi and Björkegren, 2012**.

After the extraction, the membrane should be broken. The demulsification or breaking of an emulsion is one of the most significant steps for the ELM process because it is defined as the overall effective cost of the process, as the membrane phase will be recycled **Balasubramanian and Venkatesan, 2014**.

There are three stages in the demulsification process divided as follow **Pabby, 2015**: (1) globules coalescence and growth, (2) globules settling, and (3) coalescence of the large water and oil globules with their respective external phases in the centrifugal coalesce**.**

Chemical or physical treatments methods are used for demulsification as follows **Pabby, 2015**: (1) Chemical treatment methods: these treatment methods include the addition of a demulsifier. There are effective demulsifying agents for particular applications such as acetone, n-butanol and 2-propanol. Even though, these methods are effective, they change the properties and prevent reuse because additional separation steps for recycling and recovery are required; (2) Physical treatment methods: these treatments involve centrifugation, heating, sedimentation, ultrasonics, high shear, solvent dissolution, microwave, and using high-voltage electrostatic fields. ELM can be demulsified effectively by centrifugation.

2. EXPERIMENTAL WORK

2.1 Materials

(1) Phenol crystals were supplied by Loba Chemie Pvt. Ltd. (Laboratory reagents & fine chemicals).
(2) Sodium hydroxide (NaOH) was supplied by Reagent World Inc.
(3) Sorbitan monooleate (Span 80) was supplied by Wuhan Kemi-Works Chemical Co., Ltd.
(4) Kerosene was supplied by midland Iraqi refineries company.

2.2 Experimental Procedure

For ELM system preparation, (W/O) emulsion was prepared by mixing the surfactant and diluent with NaOH solution as an internal stripping agent of 2 M, for the initial experiments, a surfactant (Span 80): diluent (kerosene) ratio of 2:98 was used. This mixture was emulsified using a high speed homogenizer, operating at a rotational speed of 10000 rpm for 1 minute of emulsification time to obtain a milky white color emulsion as shown in **Fig.3**. The emulsion was dispersed in the aqueous external phase containing 300 ppm phenol with volume ratio of membrane to external phase= 0.5 and stirred by an overhead stirrer with a desired speed for 4 min to form numerous small globules of emulsion so that good dispersion of the emulsion in the waste water was maintained for mass transfer of phenol, the emulsion must be freshly prepared each time before the extraction step.

Phenol permeated into the liquid membrane and reacted with NaOH, which was the internal stripping agent to form sodium phenolate and water. The reaction is shown in the following equation:

$$C_6H_5OH \quad + \quad NaOH \quad \longrightarrow \quad C_6H_5ONa \quad + \quad H_2O \qquad (1)$$

Sodium phenolate cannot diffuse back into the external phase through liquid membrane due to the selectivity of the membrane. Therefore, it was not detected in the external phase. Then, the mixture is separated by using separating funnel. As the external phase was heavier than the emulsion phase, it settled at the bottom. After the separation of the phases, the aqueous phase was carefully separated from the membrane phase, then the solution separated into two layers (the emulsion and the treated water), the steps were shown in **Fig.4** (steps 1 to 5). After 7 minutes of settling, samples were taken from the treated water (bottom layer) and analyzed by UV spectrophotometer to determine the percentage removal of phenol. After extraction, some big emulsion droplets at the upper layer of the mixture were collected. An experiment for demulsification was carried out on the top layer of solution (waste) by applying centrifuge, then emulsion was broken up and separated within 1 hour and 8000 rpm in order to separate the phases that compose the waste (the internal aqueous phase and the membrane phase) **Fig.5**. At the end of the process, a component of membrane phase (kerosene) can be recycled. The recovered-oil phase is reused for making emulsions for the liquid membrane process and should not contain any demulsifying chemicals.

2.3 Phenol Concentration Measurement

A 2mL of treated water sample was taken and analyzed by Spectrophotometer for measuring absorbance for phenol concentration. Detection of phenol can be observed at an absorbance value of 270 nm. The concentrations of phenol were estimated from the absorbance-phenol concentration calibration curve **Fig.6**. Then, the percentage removal of phenol was determined by the following equation:

$$\text{Removal of Phenol (\%)} = \frac{(c_0 - c_1)}{c_0} * 100 \qquad (2)$$

Where c_0 is the initial phenol concentration in the external phase and c_1 is the final phenol concentration in the sample after extraction.

3. RESULTS AND DISCUSSION

3.1 Effect of Process Variables on Removal of Phenol

In this work, three operating parameters, namely, surfactant concentration, volume ratio of internal phase to membrane phase (I/M) and stirring speed were studied. Volume ratio of membrane to external phase ratio= 1:2, internal agent concentration= 2 M, stirring time= 4 min, emulsification time =1 min. These conditions, as the optimal ones, were chosen based on preliminary experiments done and previous researches also the reports in other related literatures such as **Mortaheb et al., 2008**, **Ng et al., 2010**, and **Balasubramanian, 2014**

3.1.1 Effect of surfactant concentration

Surfactant concentration was shown to play a dominate role in the phenol removal and as an emulsifier for the liquid membrane also act as a protective barrier between the external phase and the internal phase, preventing the leakage of emulsion. It is very important to check the effect of surfactant concentration on the behavior of removal efficiency of phenol by ELM, The surfactant concentration has been studied in the range 1 to 5% (v/v).

Figs.7 to 9 and **Figs.10 to 12** show the effect of surfactant concentration on the behavior of phenol removal at different conditions [stirring speed (100-600) rpm and membrane to internal phase ratio (1:1–6:1) (v/v)] respectively. All these figures indicate that: Too little concentration of surfactant 1% (v/v) makes the emulsion breaks easily so that the extraction efficiency was poor because the coverage of the membrane interface was incomplete at low surfactant concentration. The addition of more surfactant (1 to 2) % (v/v), increased the removal of phenol due to the decreasing of the surface tension and results in smaller globules size of the W/O stable emulsion, which leading to a higher mass transfer area with a maximum extraction rate. Excessive amount of surfactant (3 to 5)% (v/v), increases the viscosity of the membrane phase which decreases the removal of phenol through the highly viscous membrane, this can be attributed to the fact that the increase in emulsion viscosity resulting from the increasing surfactant concentration leads to the augmentation of mass transfer resistance due to presence of excessive surfactant at the external–membrane phase interface, resulting in less transfer of phenol molecules to the internal phase. These observations are in good agreement with most investigators **Manikandan et al., 2014**, **Othman et al., 2006** and similar observations were made by **Ng et al., 2010** and **Dâas and Hamdaoui, 2010**. Therefore, Span 80 of concentration 2% (v/v) was found to be the optimum that producing maximum extraction efficiency greater than 98%, this value was fixed for all other experiments. Also it was investigated from these figures that the optimum values of stirring speed was 400 rpm and volume ratio of membrane phase to internal phase was 5:1.

3.1.2 Effect of stirring speed

Stirring speed was an important factor in the mass transfer rate of phenol through the liquid membrane. The stirring speed at which external phase and emulsion were mixed was found to have a profound effect on the extraction of phenol from the feed.

Figs.13 to 15 and **Fig.16 to 18** represent the relationship between stirring speed and the percentage removal of phenol at different conditions [surfactant concentration (1-4) (v/v)% and volume ratio of membrane to internal phase (1:1–5:1)], the stirring speed has been studied in the range 100 to 500 rpm. For lower stirring speed (100 rpm), the extraction efficiency was low because the formations of larger emulsion globules involving a decrease of the area for mass transfer. Also it was observed that higher stirring speed (over than 100 rpm) lead to the formation of smaller sized globules, which increases the interfacial area between the external phase and the membrane phase, leading to enhanced surface area for mass transfer so that the extraction efficiency increases. Further increase in the level of stirring would increase the interfacial area and the mass transfer coefficient. The area for mass transfer increases but the membrane ruptures, spilling the internal stripping phase into the outer external phase. However, this is true up to certain level of stirring beyond which an increase in the level is likely to break the emulsion droplets thereby reducing the degree of extraction. Increasing the stirring speed above (400rpm) not only decreases the extraction efficiency, but also affects the stability of emulsion. This notice is in good agreement with some researchers **Chiha et al., 2006** and **Kaghazchi et al., 2006**.

In addition, the shear induced breakage of fragile emulsion droplets near the tip of the impeller or impact on the wall of a contactor imposes upper limit on the speed of stirring. At the same time swelling is also increased due to water transport from external to internal phase. Therefore, the extraction performance would be a tradeoff between the two effects of agitation speed and swelling phenomena. These observations were in good agreement with most investigators **Othman et al., 2006** and **Dâas and Hamdaoui, 2010**. Therefore, the best value of stirring speed was found to be 400 rpm. Also, it was investigated from the above figures that the optimum values of surfactant concentration was 2%v/v and volume ratio of membrane phase to internal phase was 5:1.

3.1.3 Effect of volume ratio of membrane phase to internal phase

The volume ratio of membrane phase to internal phase has a significant effect on removal of phenol using ELM. This parameter can affect the surfactant concentration at the interface of the membrane / external phases. The results are shown in **Fig.19 to 21** and **Fig.22 to 24**. In order to form a stable and effective W/O emulsion, the volume ratio must exceed 1:1 **Luo et al., 2014**.

The effect of the volume ratio of membrane to internal phase on the percentage removal of phenol was studied by changing the volume of membrane phase while keeping the volume of the internal phase constant. Variation of this phase ratio produced emulsions with different properties, including size, stability, and extraction capacity. Optimal phase ratio produces proper size of emulsion. The first observation was the increasing in the volume ratio of membrane phase to internal phase makes both the extraction and swelling rates strongly improved, this is due to the absolute amount of each component in the membrane phase was raised. At low volume ratio of (1:1), the volume of membrane solution is not enough to enclose the overall stripping solution (internal phase) thus producing large emulsion globule leading to low extraction efficiency. The produced emulsion tends to have thin wall therefore increasing leakage possibility.

When volume ratio of membrane phase to internal phase is increased from 2 to 4, the transport rate and extraction efficiency of phenol increase, this can be due to the fact that an increase in the membrane phase volume ratio increases the thickness of the membrane phase and the viscosity of the emulsion phase, resulting in enhanced mass transfer and more stable emulsion droplets can be formed by an increment of the membrane phase to encapsulate the internal agent. An increase in membrane to internal phase volume ratio from 4 to 5 resulted in a sharp rise in the average effect. This can be explained by the more stable emulsion due to the higher concentration of the surfactant at the interface of the membrane/external phases. In addition, it was also found that increasing the volume ratio of membrane to internal phase beyond 5:1 did not enhance phenol removal because a high volume ratio of membrane phase to internal phase means that less stripping agent (NaOH) is available for phenol stripping, also because too much membrane phase produces thick emulsion wall which is not favorable for the extraction process. This phenomenon could be due to the built-up resistance around the membrane at the high membrane to internal phase ratio. The increase in thickness of the membrane offered resistance that slowed down the phenol permeation rate.

However, higher ratio requires higher stirring speed due to the increase in viscosity of the mixture. If the speed is constant at 400 rpm then it will reduce phenol extraction due to unsuitable mixing of phases because of higher proportion of the more viscous phase. Thus, a volume ratio of membrane phase to internal phase of 5:1 was selected as the optimal volume ratio. This observation is in good agreement with most investigators **Luo et al., 2014**, **Ahmad et al., 2013**, and **Mortaheb et al., 2008**. Also, it was investigated from these figures that the optimal values of stirring speed and Span 80 concentration were 400 rpm and was 2(v/v)% respectively.

3.2 Studying the Optimal Time for Extraction

The extraction time is one of the most important parameters in emulsion liquid membrane systems, it is defined as the dispersion time of emulsion to the external phase. The effect of various extraction times (1–25 min) on the performance of phenol extraction efficiency were studied to select the optimum time for extraction of phenol and the results were shown in **Fig. 25**. Short extraction time leads to the emulsion breakage due to the large size of droplet which leads for their coalescence, so that phenol removal efficiency was low, because the time was not enough for the separation of emulsion from treated water. Also it was observed that the extraction performance of phenol increased when the extraction time increased for the first 5 min, and reached maximum extraction at 7 minutes of process time.

An increase in extraction time from 5 to 7 resulted in a sharp rise in the average effect. This can be due to the separation process was completed between emulsion and treated water. After 7 min, it was observed a slight increase in the extraction efficiency of phenol, so that 7 minutes of extraction time was taken as the optimum time, because there is no significant increases in removal of phenol so that no need to wait for longer time (longer extraction time only enhance the emulsion swelling). With further increase of the extraction time up to 15 min, the extraction efficiency of phenol decreases because some membrane droplets begin to break and therefore, the phenol remaining in the external phase. The mass transfer in ELM system occurs very fast thus, 7 minutes of extraction time was the optimum condition for this system which gave the maximum extraction of phenol. These observations are in good agreement with most investigators **Othman et al., 2006**, **Gasser et al., 2008**, and **He et al., 2015**.

3.3 Demulsification

After applying centrifuge, the upper layer was tested by using (GC) by IBN SINA FACTORY. Comparison between the standard kerosene and the upper layer was shown in **Fig.26**, indicates that there is a good agreement between them so that this layer can be reused for membrane phase.

CONCLUSIONS

1. It was demonstrated that the ELM technique was very promising in the treatment of aqueous solutions containing phenol.
2. The maximum predicted value for the percentage removal of phenol using ELM is 98.95% at the optimum parameters.
3. The increase of surfactant concentration increases the removal efficiency to a certain extent of 2% (v/v), an excess of surfactant concentration lead to decrease percentage of phenol removal. The suitable Span 80 concentration used in liquid membrane component was 2% (v/v) that provides good emulsion stability during the ELM process.
4. The higher stirring speed the higher percentage of phenol removal until 400 rpm and excessive speed enhance the decrease percentage of phenol removal when other conditions of the process
5. The removal efficiency of phenol increases with increasing volume ratio of membrane phase to internal phase up to 5:1 and decreases thereafter when other conditions of the process remained constant remained constant.
6. The extraction performance of phenol increased when the extraction time increased for the first 5 min, and reached maximum extraction at 7 minutes of process time. With long extraction time, the extraction efficiency of phenol decreases.
7. There was a good agreement between the standard kerosene and the upper layer obtained after centrifugation of the waste, so that this layer can be reused for membrane phase to prepare a new emulsion.

REFERENCES

- Ahmad, A.L., Kusumastuti, A., Buddin, M.S., Derek, D.C.J. and Ooi, B.S., 2013, *Emulsion Liquid Membrane For Cadmium Removal: Experimental Results And Model Prediction*. Jurnal Teknologi, 65(4).
- Balasubramanian, A. and Venkatesan, S., 2014, *Optimization Of Removal Of Phenol From Aqueous Solution By Ionic Liquid-Based Emulsion Liquid Membrane Using Response Surface Methodology*. CLEAN–Soil, Air, Water,42(1), pp.64-70.
- Balasubramanian, A., 2014, *Removal Of Phenolic Compounds From Aqueous Solution Using Emulsion Liquid Membrane Containing Ionic Liquid.*
- Cahn, R.P. and Li, N.N., 1974, *Separation Of Phenol From Waste Water By The Liquid Membrane Technique.* Separation Science, 9(6), pp.505-519.
- Cárdenas, A. and Castro, E., 2003, *Breaking Of Multiple Emulsions under Osmotic Pressure and the Effect of W1/O Relation.* INTERCIENCIA-CARACAS-, 28(9), pp.534-538.
- Chiha, M., Samar, M.H. and Hamdaoui, O., 2006, *Extraction of Chromium (VI) From Sulphuric Acid Aqueous Solutions by A Liquid Surfactant Membrane (LSM).* Desalination, 194(1), pp.69-80.
- Dâas, A. and Hamdaoui, O., 2010, *Extraction Of Bisphenol A From Aqueous Solutions By Emulsion Liquid Membrane*. Journal of Membrane Science, 348(1), pp.360-368.
- Fan, H., 1999, *Chemical Reactions and Mass Transport In Eemulsion Liquid Membrane*.

- Fassihi, R. and Björkegren, S., 2012, *A Study Of The Heavy Metal Extraction Process Using Emulsion Liquid Membranes*.
- Gasser, M.S., El-Hefny, N.E. and Daoud, J.A., 2008, *Extraction Of Co(II) From Aqueous Solution Using Emulsion Liquid Membrane*. Journal of hazardous materials, 151(2), pp.610-615.
- Ghosh, S., 2011, *Formulation and Charecterisation of Multiple Emulsions with Various Additives*. Int J Res Pharm Bio Sci, 2(2).332.
- Han, D., and Row, K. H., 2010, *Recent Applications Of Ionic Liquids Iin Separation Technology*. Molecules, 15(4), pp. 2405-2426.
- Hasanoğlu, A., 2013, *Removal Of Phenol From Wastewaters Using Membrane Contactors: Comparative Experimental Analysis Of Emulsion Pertraction*. Desalination, 309, pp. 171-180.
- He, J., Li, Y., Xue, X., Ru, H., Huang, X. and Yang, H., 2015, *Extraction of Ce (iv) From Sulphuric Acid Solution By Emulsion Liquid Membrane Using D2EHPA As Carrier*. RSC Advances, 5(91), pp.74961-74972.
- Kaghazchi, T., Kargari, A., Yegani, R. and Zare, A., 2006, *Emulsion liquid Membrane Pertraction of L-Lysine from Dilute Aqueous Solutions by D2EHPA Mobile Carrier*. Desalination, 190(1), pp.161-171.
- Li, N.N., 1974, *Separating Hydrocarbons With Liquid Membranes*. U.S. Patent RE27, 888.
- Luo, J., Li, J. and Wang, B.M., 2014, *Study On Mg2+ Removal From Ammonium Dihydrogen Phosphate Solution By An Emulsion Liquid Membrane*. Hemijska industrija, 68(3), pp.341-346.
- Manikandan, G.N., Bogeshwaran, K., Jamuna, P. and Sandhya, S., 2014, *A Review On Emulsion liquid Membranes On Heavy Metal Separation,* International Journal of ChemTech Research, Vol.6, No.9, pp 4328-4.
- Meda, V., Lope, T., Tyler, R., Baik, O. D., and Soltan, J., 2014, *Treatment Of Phenol In Water Using Microwave-Assisted Advanced.*
- Mohammadi, S., Kargari, A., Sanaeepur, H., Abbassian, K., Najafi, A., and Mofarrah, E., 2015, *Phenol Removal from Industrial Wastewaters: A Short Review.* Desalination and Water Treatment, 53(8), pp. 2215-2234.
- Mortaheb, H.R., Amini, M.H., Sadeghian, F., Mokhtarani, B. and Daneshyar, H., 2008, *Study On a new surfactant for Removal Of phenol from wastewater by emulsion liquid membrane*. Journal of hazardous materials, 160(2), pp.582-588.
- Ng, Y.S., Jayakumar, N.S. and Hashim, M.A., 2010, *Performance Evaluation Of Organic Emulsion Liquid Membrane On Phenol Removal*. Journal of hazardous materials, 184(1), pp.255-260.
- Othman, N., Mat, H. and Goto, M., 2006, *Separation of Silver from Photographic Wastes by Emulsion Liquid Membrane System*. Journal of membrane science, 282(1), pp.171-177.
- Pabby, A.K., Rizvi, S.S. and Requena, A.M.S. eds., 2015, *Handbook Of Membrane Separations: Chemical, Pharmaceutical, Food, And Biotechnological Applications*. CRC press.
- Ravikumar, K., Pakshirajan, K., Swaminathan, T. and Balu, K., 2005, *Optimization Of Batch Process Parameters Using Response Surface Methodology For Dye Removal By A Novel Adsorbent*. Chemical Engineering Journal, 105(3), pp.131-138.

- Rousseau, E.R.W., 2009, *Handbook Of Separation Process Technology*. John Wiley & Sons.

Abbreviations

ELM	emulsion liquid membrane
GC	gas chromatography
M/I	membrane phase / internal phase
O/W	oil in water emulsion
O/W/O	oil in water in oil
rpm	rotation per minute
W/O	water in oil Emulsion
W/O/W	water in oil in water

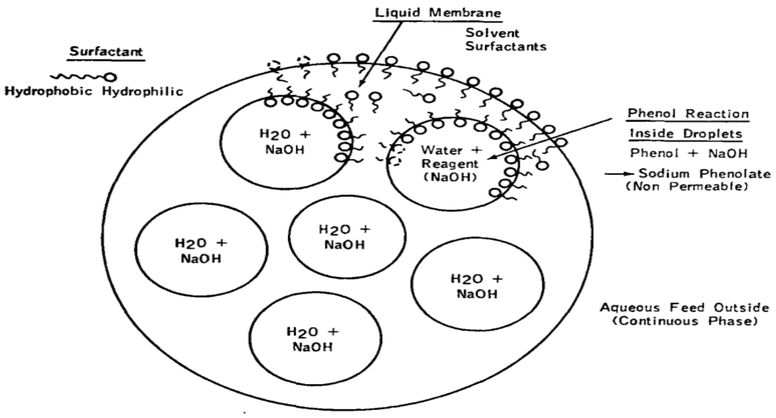

Figure 1. Schematic diagram of liquid membrane system for phenol removal **Rousseau, 2009**.

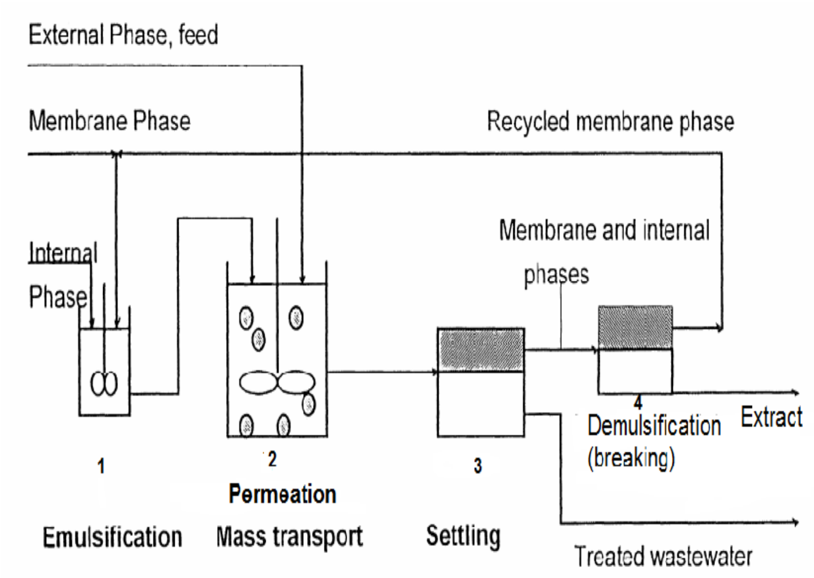

Figure 2. The operational steps in the ELM process **Fan, 1999**.

Figure 3. Milky white color liquid membrane.

Step 1: adding membrane phase to internal phase

Step 2: mixing for 1 min to get milky white emulsion

Step 3: adding emulsion to phenol solution

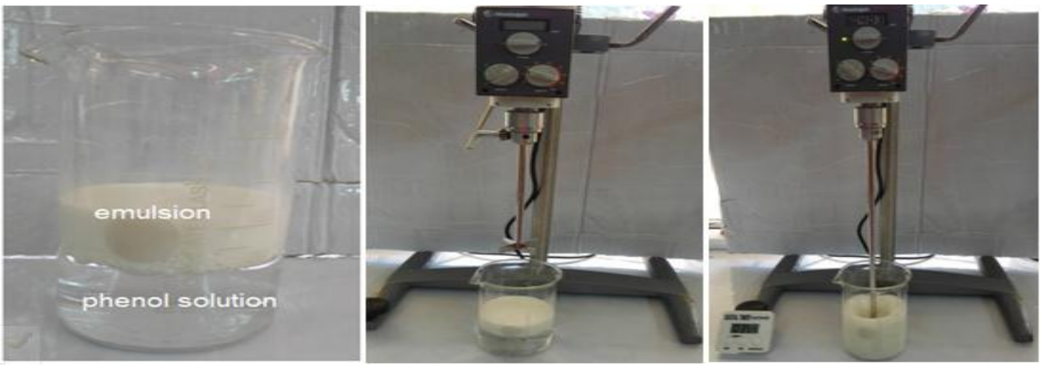

Step 4: emulsion and phenol solution are separated into two layers mix do not without stirring

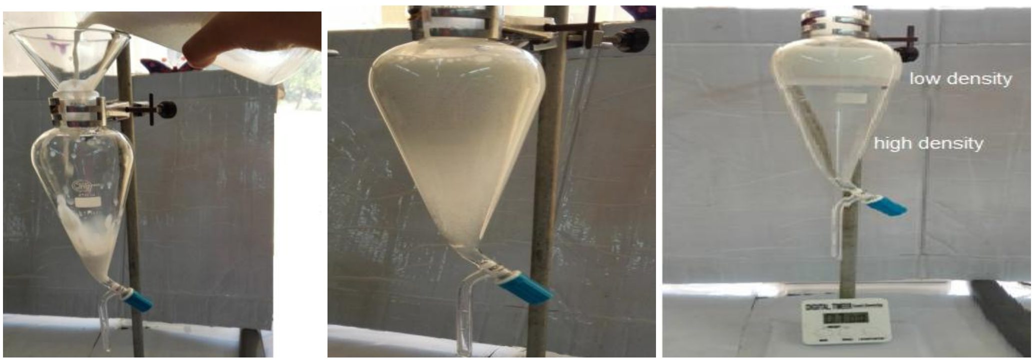

Step 5: adding the mixture to a separating funnel and waiting for 7 min to take the sample.

Figure 4. Experiment procedure steps (1 to 5).

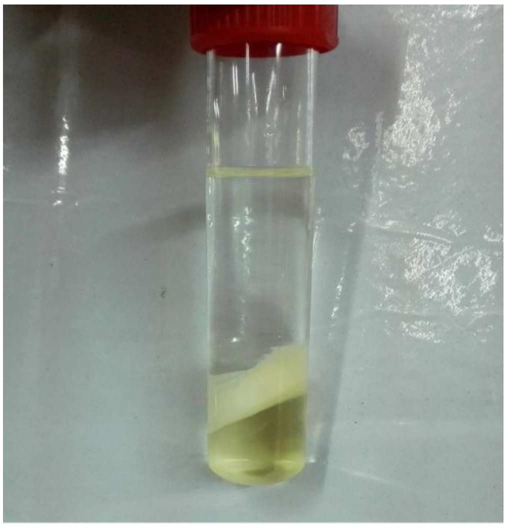

Figure 5. The separated phases after demulsification

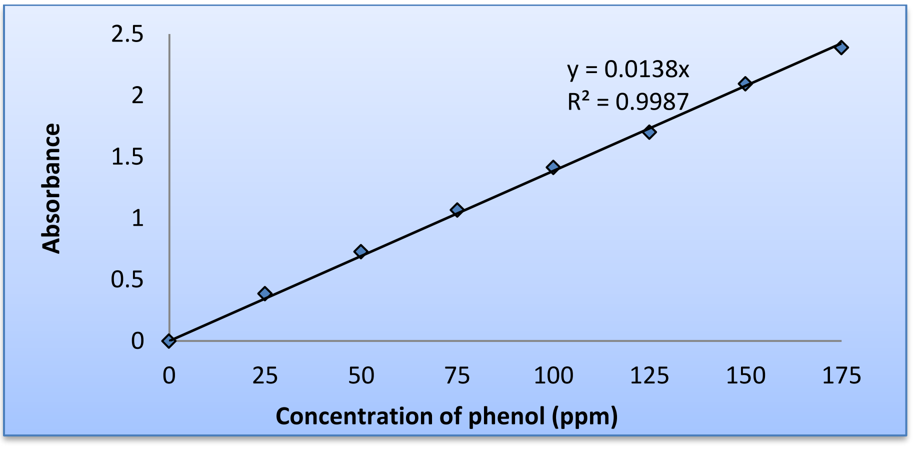

Figure 6. Calibration curve of phenol adsorption.

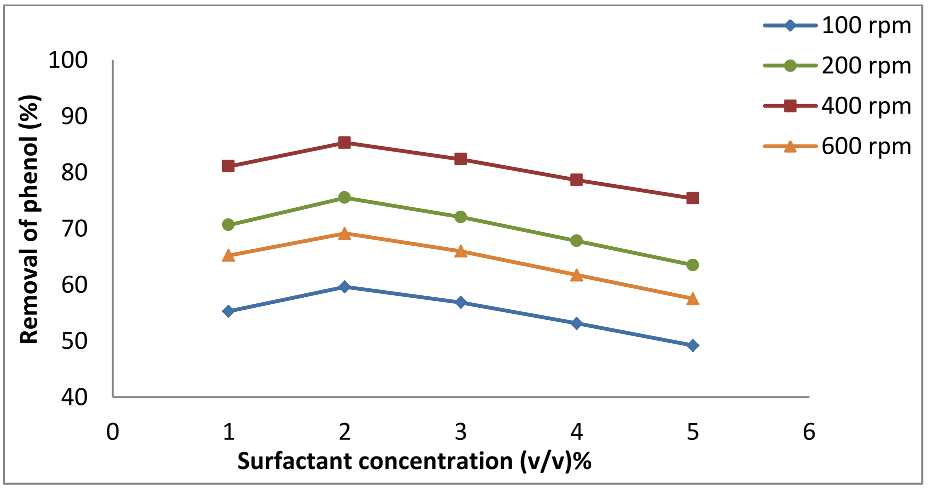

Figure 7. Effect of surfactant concentration on removal of phenol at different stirring speed, volume ratio of membrane phase to internal phase= 1:1.

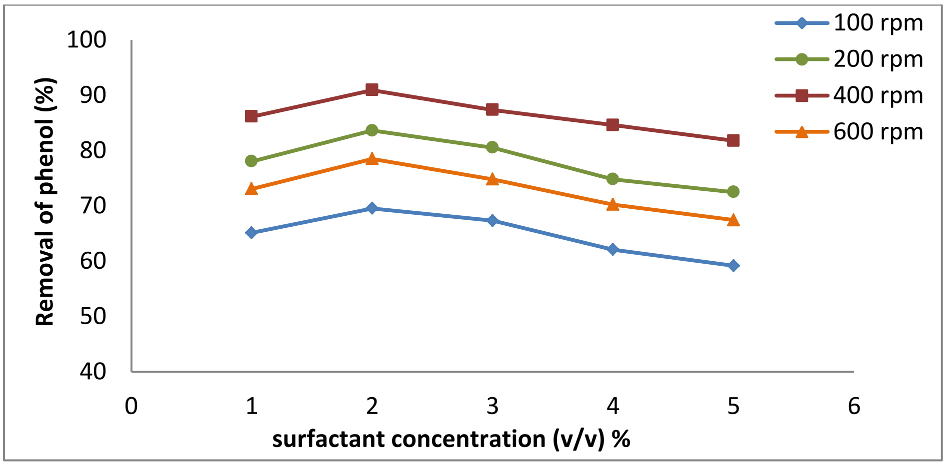

Figure 8. Effect of surfactant concentration on removal of phenol at different stirring speed, volume ratio of membrane phase to internal phase= 3:1.

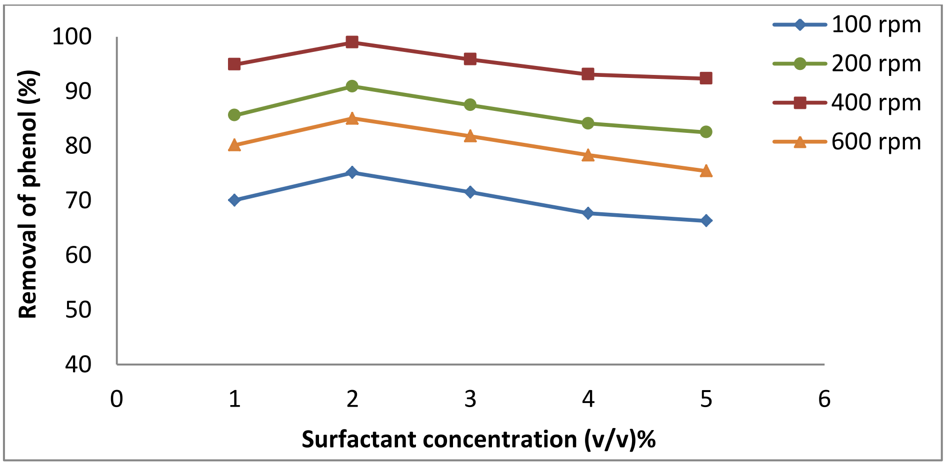

Figure 9. Effect of surfactant concentration on removal of phenol at different stirring speed, volume ratio of membrane phase to internal phase= 5:1.

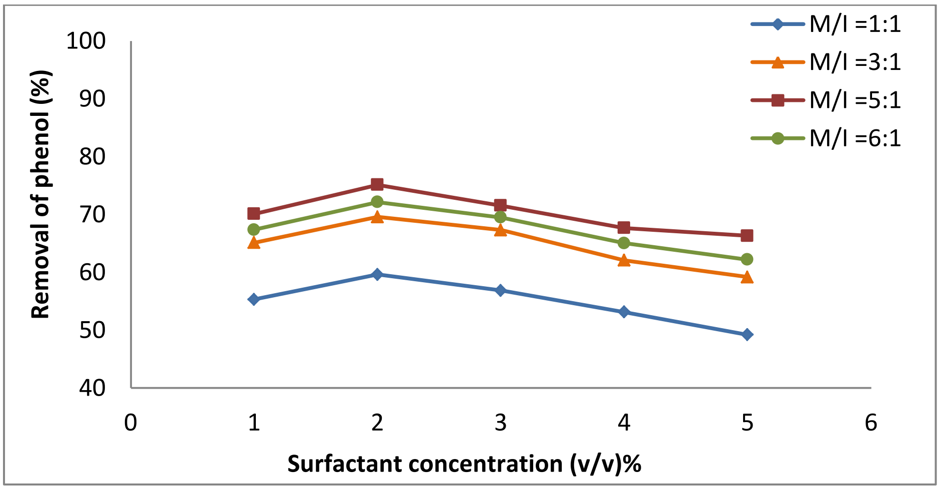

Figure 10. Effect of surfactant concentration on removal of phenol at different volume ratio of membrane phase to internal phase, stirring speed= 100 rpm.

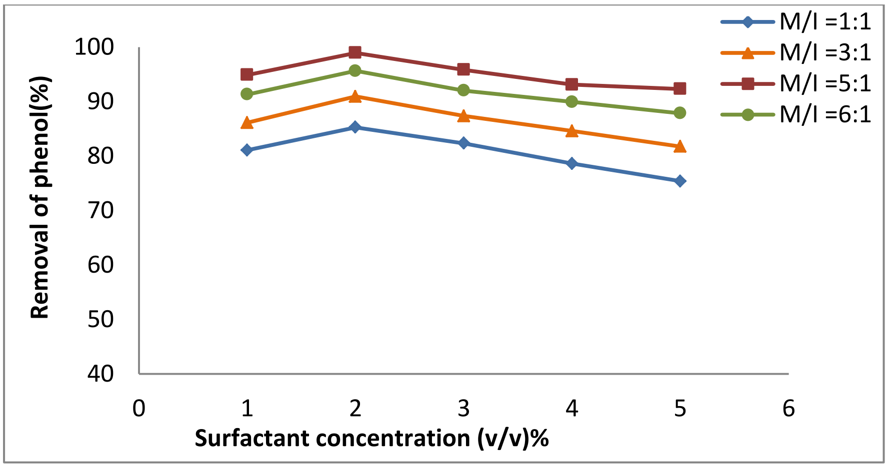

Figure 11. Effect of surfactant concentration on removal of phenol at different volume ratio of membrane phase to internal phase, stirring speed = 400 rpm.

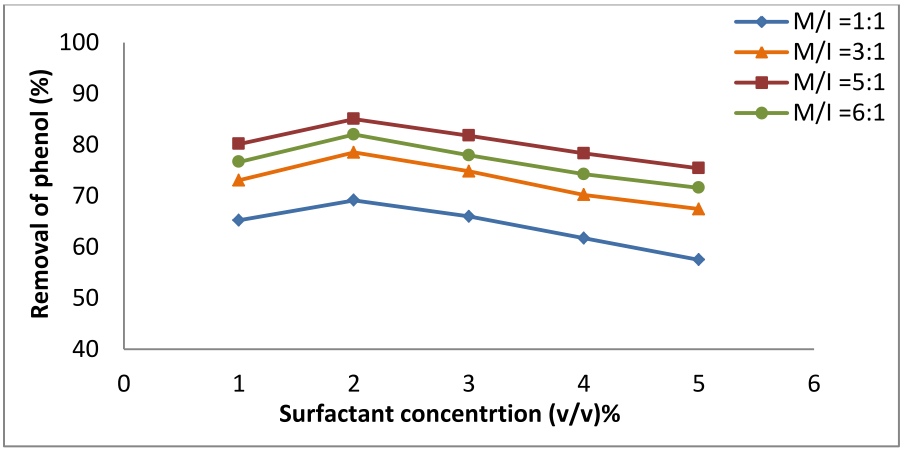

Figure 12. Effect of surfactant concentration on removal of phenol at different volume ratio of membrane phase to internal phase, stirring speed= 600 rpm.

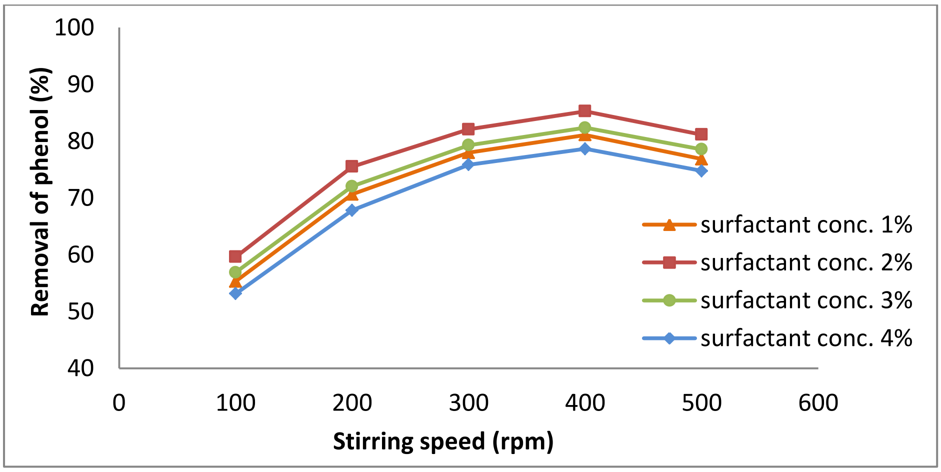

Figure 13. Effect of stirring speed on removal of phenol at different surfactant concentration, volume ratio of membrane phase to internal phase= 1:1.

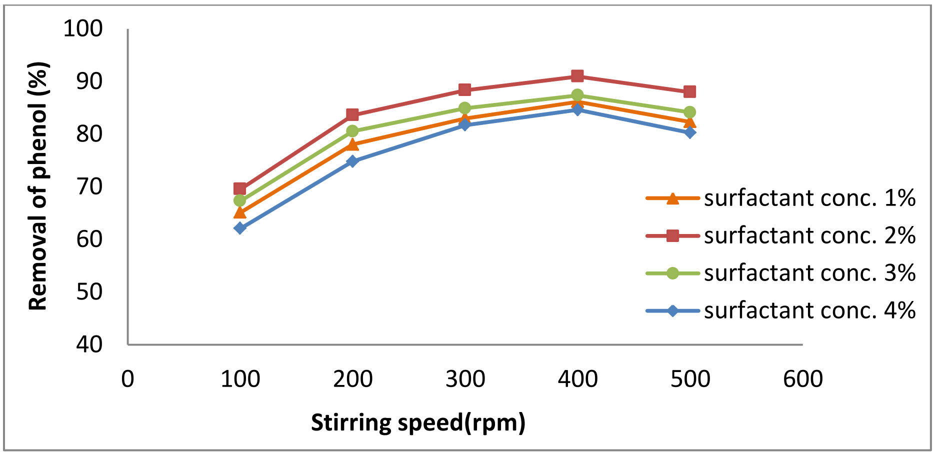

Figure 14. Effect of stirring speed on removal of phenol at different surfactant concentration, volume ratio of membrane phase to internal phase= 3:1.

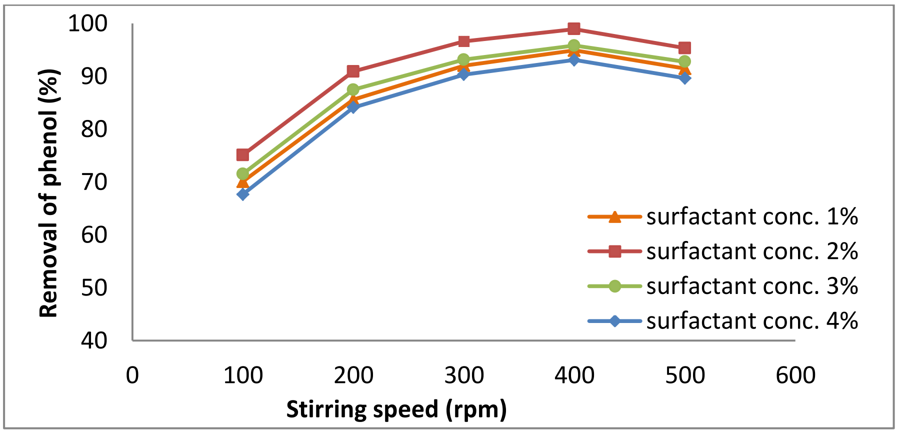

Figure 15. Effect of stirring speed on removal of phenol at different surfactant concentration, volume ratio of membrane phase to internal phase= 5:1.

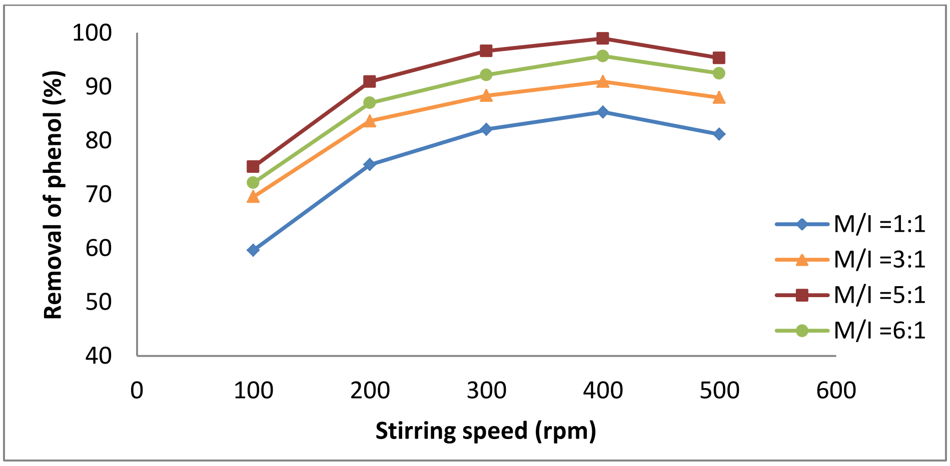

Figure 16. Effect of stirring speed on removal of phenol at different volume ratio of membrane phase to internal phase (M/I), surfactant concentration= 2%v/v.

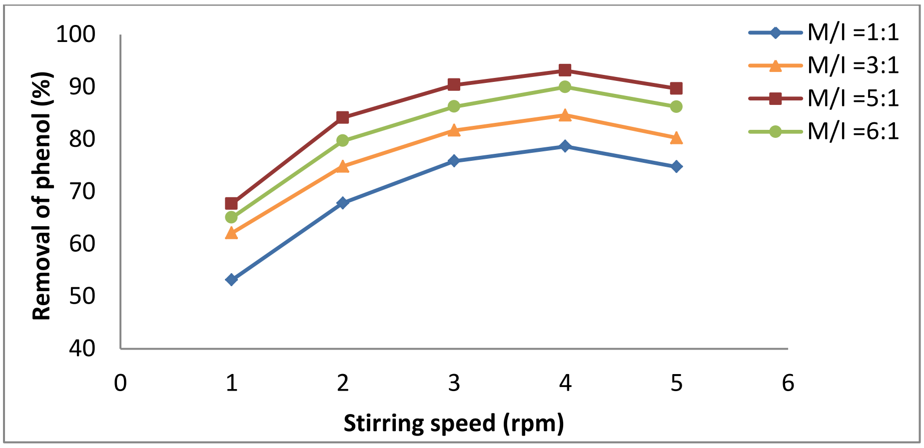

Figure 17. Effect of stirring speed on removal of phenol at different volume ratio of membrane phase to internal phase (M/I), surfactant concentration= 4%v/v.

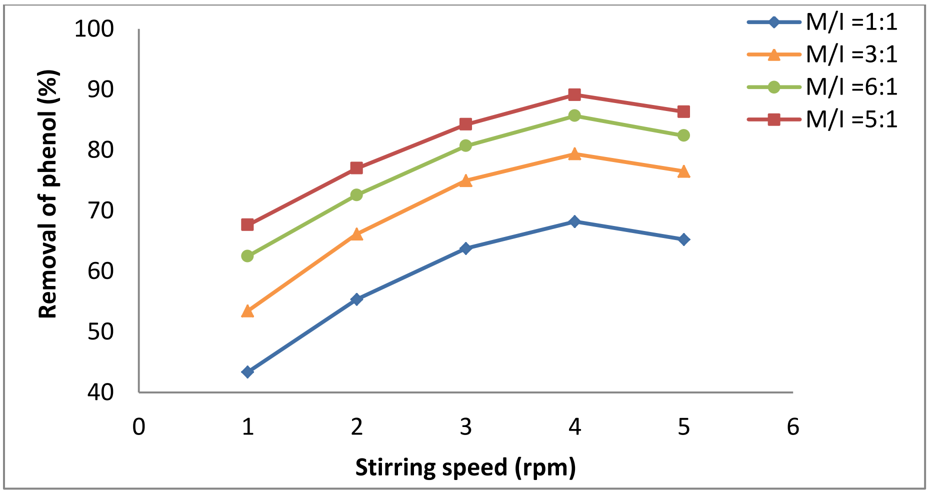

Figure 18. Effect of stirring speed on removal of phenol at different volume ratio of membrane phase to internal phase (M/I), surfactant concentration= 6%v/v.

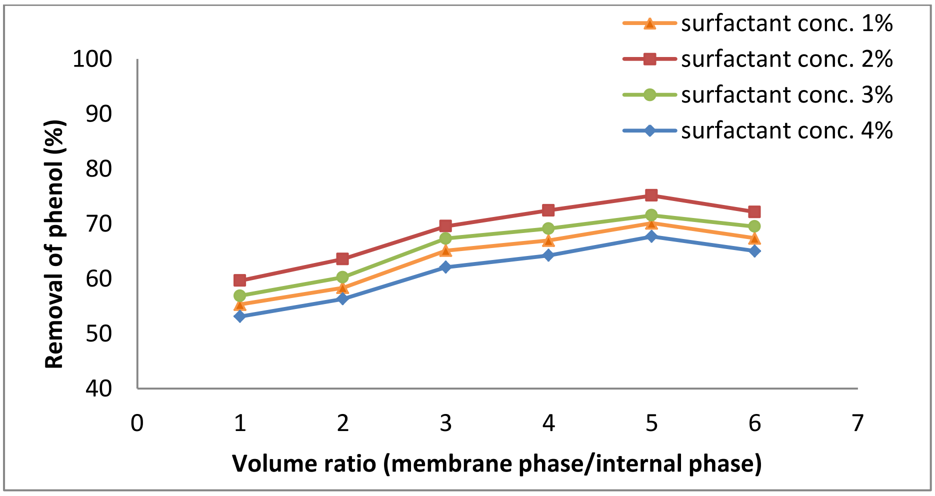

Figure 19. Effect of volume ratio of the membrane phase to internal phase on removal of phenol at different surfactant concentration, stirring speed= 100 rpm.

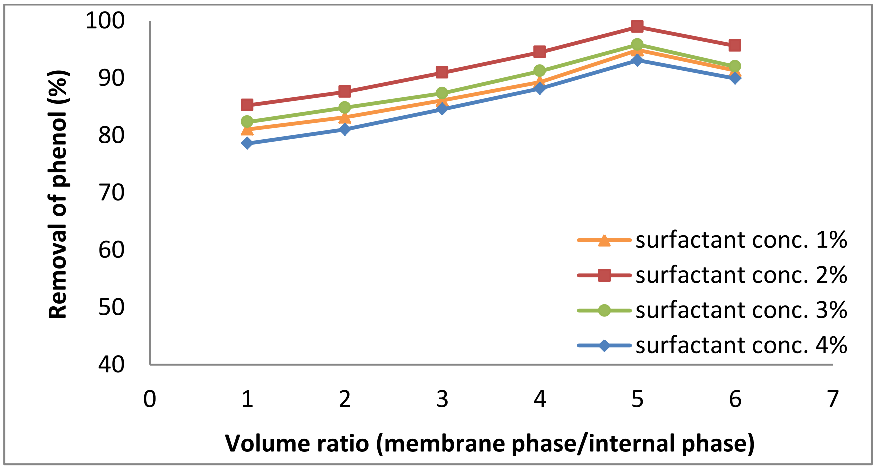

Figure 20. Effect of volume ratio of membrane phase to internal phase on removal of phenol at different surfactant concentration, stirring speed= 400 rpm.

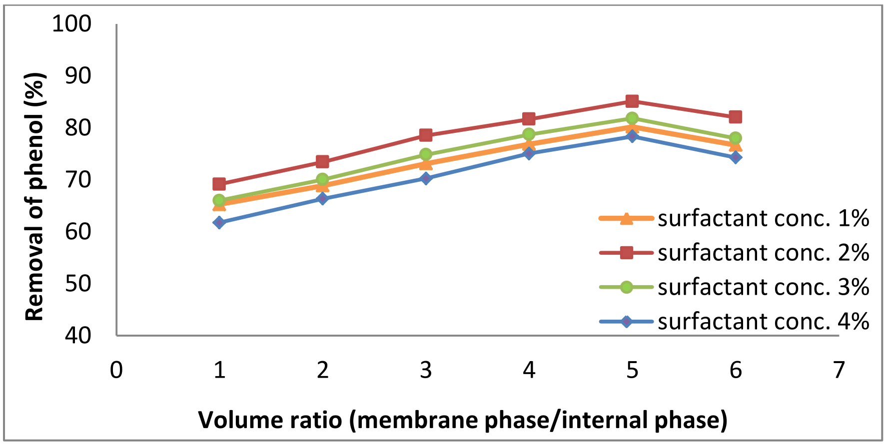

Figure 21. Effect of volume ratio of membrane phase to internal phase on removal of phenol at different surfactant concentration, stirring speed= 600 rpm.

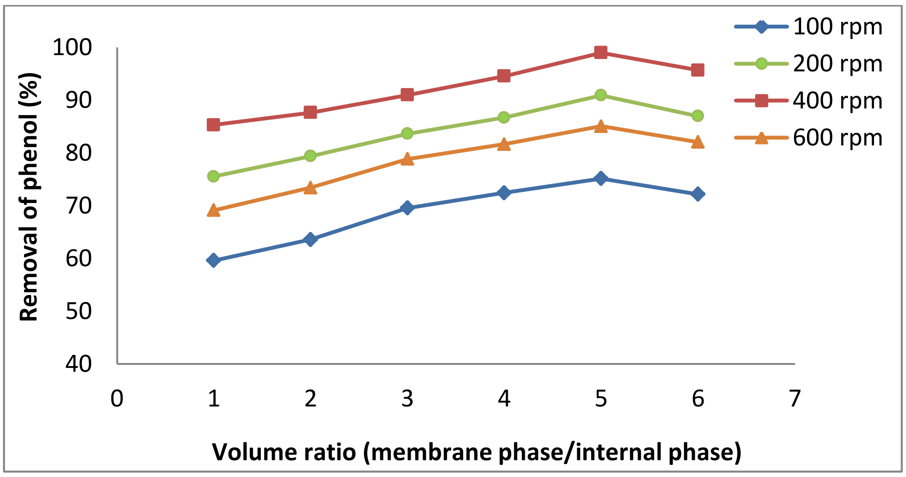

Figure 22. Effect of volume ratio of membrane phase to internal phase on removal of phenol at different stirring speed, surfactant concentration= 2%v/v.

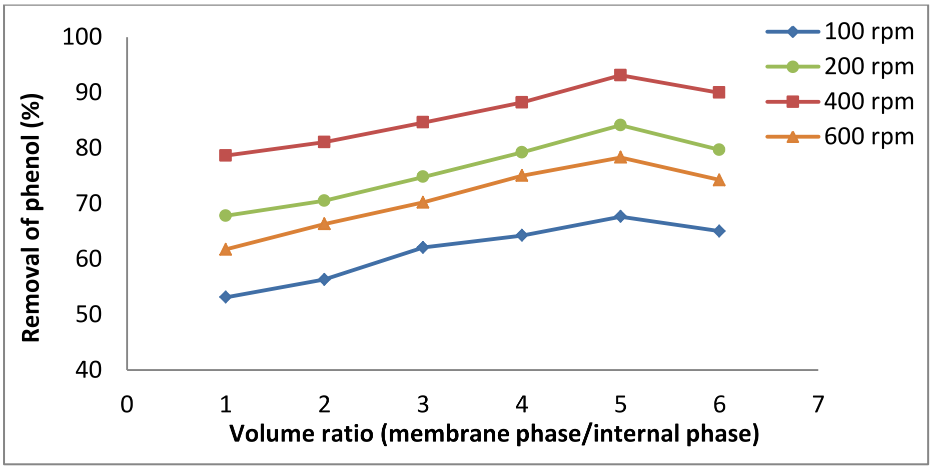

Figure 23. Effect of volume ratio of membrane phase to internal phase on removal of phenol at different stirring speed, surfactant concentration= 4%v/v.

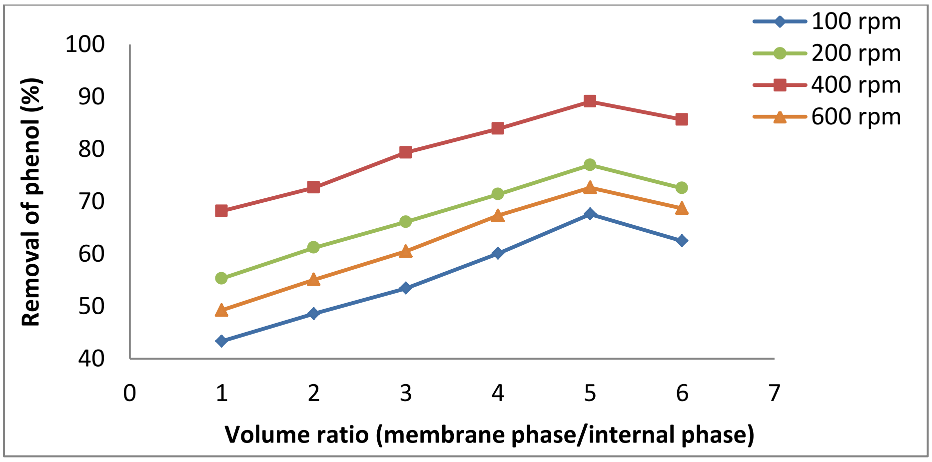

Figure 24. Effect of volume ratio of membrane phase to internal phase on removal of phenol at different stirring speed, surfactant concentration =6% v/v.

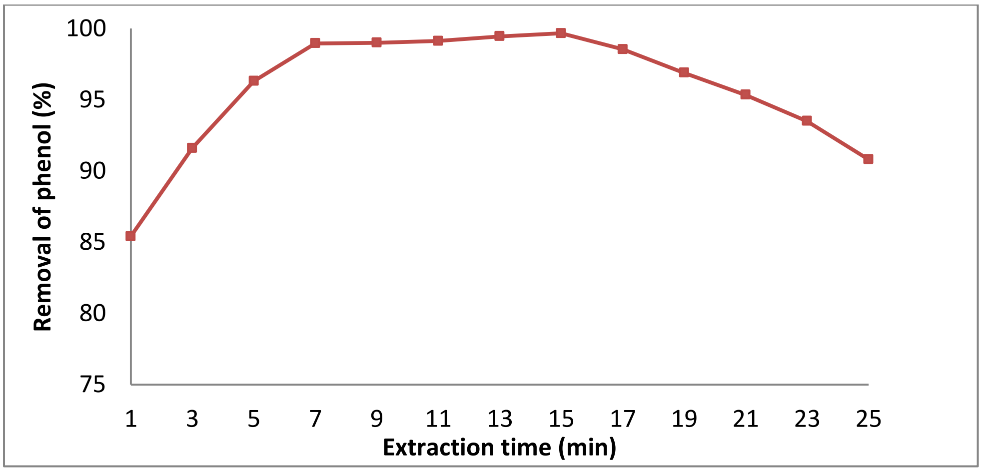

Figure 25. Effect of extraction time on the removal of phenol, experimental conditions were: ratio of membrane to external phase ratio= 1:2v/v, concentration of Span 80= 2(v/v) %, ratio of membrane to internal phase= 5:1v/v, NaOH concentration=2 M, stirring speed= 400 rpm, stirring time= 4 min and emulsification time= 1 min.

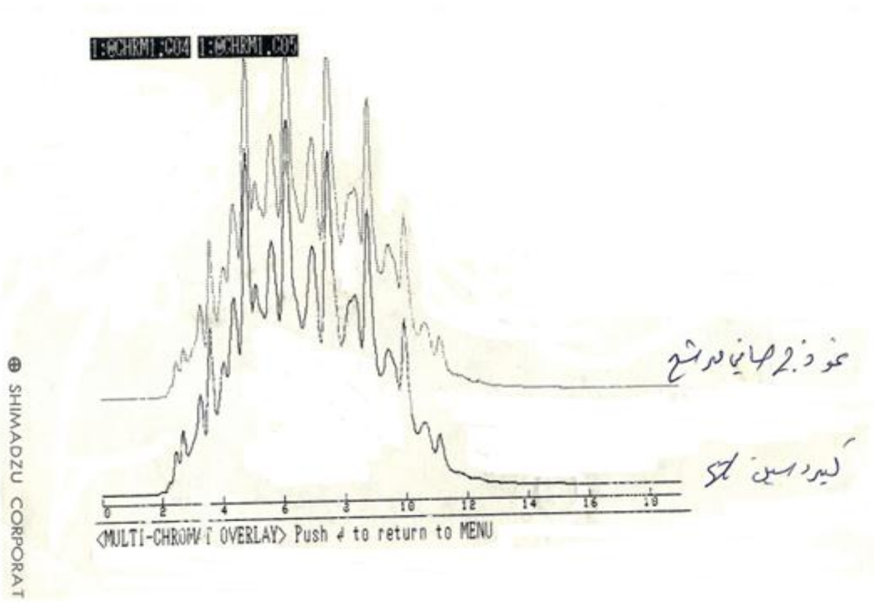

Figure 26. Comparison between the standard kerosene and the upper layer after demulsification

Movement of Irrigation Water in Soil from a Surface Emitter

Ibrahim Abbas Dawood
Graduate Student
College of Engineering-University of Baghdad
Email:abrahimabbas@yahoo.com

Safa Noori Hamad
Professor
College of Engineering-University of Baghdad
Email:safaanori12@yahoo.com

ABSTRACT

Trickle irrigation is one of the most conservative irrigation techniques since it implies supplying water directly on the soil through emitters. Emitters dissipate energy of water at the end of the trickle irrigation system and provide water at emission points. The area wetted by an emitter depends upon the discharge of emitter, soil texture, initial soil water content, and soil permeability. The objectives of this research were to predict water distribution profiles through different soils for different conditions and quantify the distribution profiles in terms of main characteristics of soil and emitter. The wetting patterns were simulated at the end of each hour for a total time of application of 12 hrs, emitter discharges of 0.5, 0.75, 1, 2, 3, 4, and 5 lph, and five initial volumetric soil water contents. Simulation of water flow from a single surface emitter was carried out by using the numerically-based software Hydrus-2D/3D, Version 2.04. Two approaches were used in developing formulas to predict the domains of the wetted pattern. In order to verify the results obtained by implementing the software Hydrus-2D/3D a field experiment was conducted to measure the wetted diameter and compare measured values with simulated ones. The results of the research showed that the developed formulas to express the wetted diameter and depth in terms of emitter discharge, time of application, and initial soil water content are very general and can be used with very good accuracy.

Key words: wetting patterns, trickle irrigation, wetted diameter, wetted depth.

حركة مياه الري في التربه من منقط سطحي

إبراهيم عباس داود
طالب ماجستير
كلية الهندسة- جامعة بغداد

صفاء نوري حمد
أستاذ
كلية الهندسة- جامعة بغداد

الخلاصة

الري بالتنقيط هو أحد تقنيات الري الممكننة التي تعتمد على توفير المياه للتربة من خلال المنقطات. إن الغرض الرئيسي لإستخدام المنقطات هو تُشتيت طاقة المياه في نهاية منظومة الري وتجهيز المياه على هيئة تصاريف قليله. وتعتمد المنطقة المبتلة بتصاريف المنقطات على تصريف المنقطة ونسجة التربة والمحتوى الرطوبي الإبتدائي للتربة بالإضافة الى نفاذية التربة. تتلخص أهداف هذا البحث بنمذجة التوزيع الرطوبي في مقد التربة لمختلف أنواع الترب بالإضافة الى إستنباط علاقات للتعبير عن توزيع الرطوبة في مقد التربة بدلالة أهم خواص التربة والمنقطات. تمت نمذجة أنماط الترطيب في نهاية كل ساعة من وقت التشغيل الكلي ولمدة إثنتى عشرة ساعة وتم تحديد تصاريف المنقطات ب 0,5 و0,75 و 1 و 2 و 3 و 4 و5 لتر/ ساعة بالإضافة الى خمسة محتويات رطوبية إبتدائية مختلفة. وقد إستخدم برنامج Hydrus إصدار2,04 لمحاكاة أنماط الترطيب من منقطة على سطح التربة. كما تم إستخدام أسلوبين لإستنباط علاقات للتعبير عن أنماط الترطيب. ولغرض التحقق من نتائج العلاقات المستنبطة تم إجراء تجارب حقلية لقياس القطر المبتل ومقارنته مع القيم المحسوبة. أظهرت نتائج البحث أن المعادلات المستنبطة للتعبير عن قطر وعمق الإبتلال بدلالة تصريف المنقط ووقت الأرواء والمحتوى الرطوبي الإبتدائي شاملة ويمكن إستخدامها مع دقة جيدة.

الكلمات الرئيسة: أنماط الترطيب, الري بالتنقيط, القطر المبتل, العمق المبتل.

1. INTRODUCTION

Trickle irrigation is one of the most conservative irrigation techniques since it implies supplying water directly on soil through emitters. A typical trickle irrigation system includes a pump, filters, main and sub main lines, manifolds, laterals, fittings, and emitters. Emitters dissipate the energy of water at the end of the trickle irrigation system and provide water directly on the soil. The area wetted by an emitter depends upon the discharge, soil texture, soil moisture content, and soil permeability. So far many researches developed mathematical, empirical, and numerical means to represent the wetted surface area and the inverted bulb-shaped cross-section of the soil profile **Schwartzman, and Zur, 1986,** and **Amin, and Ekhmaj, 2006**. Others developed computerized software to simulate the shape of wetting profile through the soil. Hydrus 2D/3D is one of the software that can be used to simulate water distribution profile through soil under a point source for a variety of conditions, including scheduling of irrigation, discharge of emitters, volumes of water, and initial moisture content of the soil. A brief review of previous related researches is illuminated below.

Schwartzman, and Zur, 1986 developed empirical formulas to estimate the dimensions of the soil wetted from a surface point-source. Their formula was based upon results of their experiments that were conducted on two types of soils namely Gilat loam and Sinai sand and for emitter discharges 1.19 $*10^{-6}$ and 5.6$*$ 10^{-6} m^3/s. Their empirical formulas are:

$$W = 27.28\, V^{0.22} \left(\frac{K_s}{Q}\right)^{-0.17} \tag{1}$$

and

$$Z = 9.24\, V^{0.63} \left(\frac{K_s}{Q}\right)^{0.45} \tag{2}$$

where:

W = wetted diameter, cm,
V = volume of applied water, l,
Q = discharge of the point source, lph,
K_s = saturated hydraulic conductivity of the soil, cm/hr, and
Z = wetted depth, cm.

Lafolie, et al., 1989 presented an improved numerical model to simulate saturated-unsaturated water flow in general and from a trickle source in particular. **Elmaloglou, and Grigorakis, 1997** analyzed infiltration through homogeneous unsaturated soil from a surface drip line. They used two flow rates for each soil and solved the flow equation numerically and the linearized form analytically. **Hammami, et al., 2002** analyzed axi-symmetrical water distribution from a surface point source by solving Richards' equation using an alternating direction implicit finite difference method. They presented an expression to predict the wetted soil depth below an emitter; the expression requires measuring the radius of the wetted soil surface and utilizing known values of the hydraulic conductivity of the soil, initial water content, and water content through the wetting front.

Amin and Ekhmaj, 2006 developed an empirical formula to estimate surface wetted radius and vertically wetted distance from a surface emitter. Their formula was based upon average change of water content within the wetted zone, total volume of applied water, application rate, and saturated hydraulic conductivity. They verified and modified the formula of **Schwartzman**

and Zur, 1986 by including the average change in water content as a parameter. Their formulas are as follows:

$$W = 12.54\, \Delta\theta^{-0.5626} V^{0.2686} Q^{-0.0028} {K_s}^{-0.344} \quad (3)$$

$$Z = 6.19\, \Delta\theta^{-0.383} V^{0.365} Q^{-0.101} {K_s}^{0.195} \quad (4)$$

where:
$\Delta\theta$ = average change of volumetric water content in the wetted zone, cm^3/cm^3.

From their experiments they found that soil texture, volume of applied water, and discharge of emitter are the most important factors that affect the vertical and horizontal domains of wetted zone.

Kandelous, et al., 2011 used Hydrus-2D/3D to analyze the wetting patterns from three different configurations of emitters, including an axi-symmetrical two-dimensional wetting from a point source; a two-dimensional wetting from a line source; and a three-dimensional wetting from a point source. Their results indicated that wetting patterns from subsurface drip irrigation prior to the overlapping of the wetting patterns can be accurately described by using an axi-symmetrical two-dimensional domain.

Boštjan, et al., 2014 used Hydrus-2D/3D to study the effect of discharge of a surface emitter and initial moisture content of the soil on the extent of the wetted bulb. They modified the parameters of the model of Schwartzman and Zur by using their results of simulation.

The objectives of this research were to predict water distribution profiles through different soils and different conditions and quantify the distribution profiles in terms of main characteristics of soil and emitter. The wetting patterns from a surface point-source were simulated by using two systems of textural classifications namely the United States Department of Agriculture, USDA, and United Kingdom, UK. Simulation of water flow from a single surface emitter was carried out by using the numerically-based software Hydrus-2D/3D, Version 2.04. Two approaches were then used to develop formulas to predict the domains of the wetted patterns. In order to verify the results obtained by implementing the software Hydrus-2D/3D a field experiment was conducted to measure the wetted radius and compare measured values with simulated ones. The results of the research showed that the developed formulas to express the wetted diameter and depth in terms of emitter discharge, application time, and initial soil water content are very general and can be used with very good accuracy. Trickle irrigation was improved by a lot of researches and studies. One of the improvements of trickle system design concern the methods of estimating wetting patterns. Analytical, empirical, and numerical models were used to predict wetting patterns from a point source.

2. MATERIALS AND METHODS

In this research, modeling of water flow under single surface emitter was carried out by using the numerically-based software Hydrus-2D/3D, Version 2.04. This software is based upon Microsoft-Windows and was developed by **Šimůnek, et al., 2006**. The software is composed of the computational computerized program and an interactive user interface .

The hydraulic properties of an unsaturated soil, θ(h) and K(h), in Richard’s equation depends upon the pressure head. Hydrus-2D/3D includes the following analytical tools to estimate the hydraulic properties of the soil [**Brooks, and Corey, 1964.**; **van Genuchten, 1980.**; **Vogel, and Císlerová, 1988.**; **Durner, 1994.**; and **Kosugi, 1996.**] as follows:

$$\theta(h) = \begin{cases} \theta_r + \dfrac{\theta_s - \theta_r}{(1 + |\alpha h|^n)^m} & h < 0 \\ \theta_s & h \geq 0 \end{cases} \tag{5}$$

$$K(h) = K_s S_e^l \left[1 - \left(1 - S_e^{1/m}\right)^m\right]^2 \tag{6}$$

where:

$$S_e = \frac{\theta - \theta_r}{\theta_s - \theta_r}\,, \qquad m = 1 - \frac{1}{n} \tag{7}$$

and
S_e = effective saturation, dimensionless,
θ_s = saturated volumetric water content of the soil, cm^3/cm^3,
θ_r = residual water content, cm^3/cm^3,
n = pore-size distribution index, dimensionless,
α = inverse of the air-entry value (or bubbling pressure), cm^{-1}, and
l = pore-connectivity parameter, dimensionless.

Hydrus-2D/3D utilizes Galerkin's finite-element method to solve Eq. (5) through (7). The hydraulic parameters $\theta_s, \theta_r, K_s, n, \alpha$, l, and the initial distribution of soil-water content are required to run the model. Since water flow from a surface-point source is three dimensional axi-symmetric, half of the domain needs to be simulated in Hydrus-2D/3D [**Gardenas, et al., 2005;** and **Kandelous, and Šimůnek, 2010b.**]. Therefore, the simulated horizontal dimension of the wetting pattern represents half of the wetted diameter. In this research, simulations were carried out on a rectangular domain 100 cm wide and 150 cm deep; a single surface emitter is placed at the top left-hand corner of the domain.

Along the upper boundary the flux was considered to be zero except along the boundary of the emitter where a constant flux was assumed to represent the emitter. Along the bottom boundary free drainage was assumed while on all remaining boundaries a zero flux was assumed [**Fig.1**].

On a fixed surface area, that represents the area of infiltration, a constant flux boundary was applied; this area is achieved when a steady state condition is attained and it represents the area that would be obtained when the flux has been redistributed with the pressure head at the surface being equal to zero. The radius of the constant-flux boundary condition is calculated by assuming that the flow rate per unit area is equal to the saturated hydraulic conductivity of the soil, since the pressure head is zero, i.e.:

$$q_f = \frac{Q_e}{A} = K_s \tag{8}$$

where:
Q_e = flow rate, cm^3/hr,
A = surface area = πr^2, cm^2,
q_f = flux per unit area, cm/hr, and
r = radius of the infiltration surface area, cm.

Wetting patterns from a surface point source were simulated by using two systems of textural classifications namely the United States Department of Agriculture, USDA, and United Kingdom, UK. The soil characteristics of the two systems are shown in **Table 1** and **Table 2**, respectively.

The wetting patterns for both systems of classification were predicted at the end of each hour for a total time of irrigation of 12 hrs. Emitter discharges of 0.5, 0.75, 1, 2, 3, 4, and 5 lph were used to simulate the wetting patterns. Five initial volumetric soil water contents were used in the simulation process. Accordingly the total number of simulations conducted to carry out the basic analysis was 9660 runs.

3. FIELD WORK

In order to verify the results obtained by implementing the software Hydrus-2D/3D a field experiment was conducted to measure the wetted radius and compare measured values with simulated ones. The experiments were conducted at Al-Raied Research Station of the National Center for Water Resources Management, Ministry of Water Resources, in Abu-Graib, 25 km west of Baghdad. The research site is located at 33˚20′ north latitude and 44˚12′ east longitude.

The soil texture of the research station is classified as silty clay loam. The apparent specific gravity is 1.14 which indicates a high organic content of the soil and emitter discharges used were 2.5, 3.75, 5, and 6 lph. **Table 3** shows other physical properties of the soil that were obtained from a laboratory analysis of soil samples.

4. DOMAIN OF THE WETTING PATTERN, FIRST APPROACH

In this approach a multiple-regression analysis was used to develop empirical formulas to predict wetted diameter and depth. For each soil texture the data obtained by applying Hydrus-2D/3D software for different discharges, initial soil water contents, and application time were used to conduct a multiple-regression analysis. The software entitled Statistica Version 10 was used to conduct the analysis. The software is based upon an optimization procedure to find the best fit formula for a given set of conditions. By doing so an empirical formula was obtained to predict wetted diameter and depth for each soil texture as identified by the saturated hydraulic conductivity .

Statistical parameters were used to test the discrepancy between the results obtained from the developed formulas and those obtained from Hydrus-2D/3D software. These parameters include root mean square error, RMSE, and modeling efficiency, EF. These parameters are expressed as follows:

$$RMSE = \sqrt{\frac{\sum_{i=1}^{n}(M_i - S_i)^2}{n}} \tag{9}$$

$$EF = 1 - \frac{\sum_{i=1}^{n}(M_i - S_i)^2}{\sum_{i=1}^{n}(M_i - \bar{M})^2} \tag{10}$$

where:

n = number of values,
M = values predicted by using Hydrus-2D/3D software,
S = values obtained from the developed formulas, and
$\bar{M}$ = mean of values obtained from Hydrus-2D/3D software.

Table 4 shows the developed formulas which express the wetted diameter and wetted depth in terms of emitter discharge, initial soil water content, and application time for the USDA soil classification system. The table also shows the values of the statistical parameters including modeling efficiency and root-mean square error. From the results depicted in the table it is clear that the RMSE between the values predicted by using Hydrus-2D/3D software and those obtained from the developed formulas ranged from 0.08 cm to 2.24 cm, while the EF was greater than 97%. Similar formulas to predict the wetted diameter and depth for the UK soil classification system are shown in **Table 5**. From the results depicted in the table it can be seen that the RMSE ranged from 0.42 cm to 2.40 cm, while the EF was greater than 96%.

5. DOMAIN OF THE WETTING PATTERN, SECOND APPROACH

An attempt was made to reduce the number of formulas needed to predict the wetted diameter and depth. To accomplish the results of simulation obtained by using Hydrus-2D/3D software for both systems of soil classification, USDA and UK, were sorted according to pre specified six ranges of saturated hydraulic conductivity. Then for each range an empirical formula was obtained by using regression analysis through Statistica software. Thus, as should be expected the developed formulas depend upon the saturated hydraulic conductivity. **Table 6 and Table 7** show the formula developed to predict wetted diameter and depth together with the statistical parameters for both systems of soil classification. As can be noted that although the formulas are simpler in form but the values of the RMSE was slightly increased and the EF values were slightly reduced.

6. VERIFICATION OF THE RESULTS

Verification of the developed formulas was done by comparing the values of the wetted diameter obtained from the formulas with values obtained from experimental work, results from Hydrus-2D/3D software, and results obtained from the formulas developed by **Schwartzman and Zur, 1986** and **Amin and Ekhmaj, 2006. Table 8** shows the results of such comparison and considered statistical criteria.

It is clear from **Table 8** that the developed formulas and results obtained from Hydrus-2D/3D software are closest to the measured values. However, the results obtained from the other two models differ appreciably from measured values. This discrepancy was mainly because those models were empirically derived for a given range of saturated hydraulic conductivity and do not include the initial water content.

7. SUMMARY AND CONCLUSIONS

Wetting patterns from a surface point source were simulated by using two systems of soil textural classifications namely the United States Department of Agriculture, USDA, and United Kingdom, UK. Simulations were carried out by using the numerically-based software Hydrus-2D/3D, Version 2.04, which solves Richard’s equation of nonlinear movement of water in unsaturated soils. The soils were classified as functions of the saturated hydraulic conductivity. In order to verify the results obtained by implementing the software Hydrus-2D/3D a field experiment was conducted to measure the wetted radius and compare measured values with simulated ones .

Two approaches were used in developing formulas to predict the domains of the wetted pattern. A nonlinear regression analysis provided by Statistica Version 10 was used to develop empirical formulas to predict wetted diameter and depth. A comparison was carried out between the results from the formulas with values obtained from experimental work, results from Hydrus-2D/3D software, and results obtained from the formulas developed by **Schwartzman and Zur,**

1986 and **Amin and Ekhmaj, 2006.** The developed formulas and results obtained from Hydrus-2D/3D software were closest to the measured values.

REFERENCES

- Amin, M. S. M., and Ekhmaj, A. I. M., 2006, *DIPAC-Drip Irrigation Water Distribution Pattern Calculator,* In: 7th International Miro Irrigation Congress, PWTC, Kuala Lumpur, Malaysis.
- Angelakis, A. N., Rolston, D. E., Kadir, T. N., and Scott, V. H., 1993a, *Soil-Water Distribution under Trickle Source,* J. Irrig. Drain. Eng., ASCE, vol. 119, no. 3, pp. 484-500.
- Boštjan, N., Cedric, K., Frederic, C., and Marina, P., 2014, *Numerical Investigation of the Influence of Texture, Surface Drip Emitter Discharge Rate and Initial Soil Moisture Condition on Wetting Pattern Size,* Irrig. Sci., vol. 32, no. 6, pp. 421-436.
- Carsel, R.F., and Parrish, R. S., 1988, *Developing Joint Probability Distributions of Soil Water Retention Characteristics,* Water Resour. Res., vol. 24, pp. 755-769.
- Elmaloglou, S., and Grigorakis, G., 1997, *Linear and Nonlinear Models of Infiltration from Surface Line Source of Trickle Irrigation,* ICID Journal, vol. 46, no. 2, pp. 81-92.
- Gardenas, A., Hopmans, J. W., Hanson, B. R., Šimůnek, J., 2005, *Two Dimensional Modeling of Nitrate Leaching for Various Fertigation Scenarios under Micro-Irrigation,* Agricultural Water Management, vol. 74, pp. 219-242.
- Hammami, M., Daghari, H., Balta, J., and Maalej, M., 2002, *Approach for Predicting the Wetting Front Depth Beneath a Surface Point Source: Theory and Numerical Aspect,* Irrig. and Drain, vol. 51, pp. 347-360.
- Kandelous, M. M. and Šimůnek, J., 2010b, *Numerical Simulation of Water Movement in a Subsurface Drip Irrigation System under Field and Laboratory Conditions Using HYDRUS-2D,* Agricultural Water Management, vol. 97, pp. 1070-1076.
- Kandelous, M. M., Šimůnek, J., van Genuchten, M. Th., and Malek, K., 2011, "*Soil Water Content Distributions Between Two Emitters of a Subsurface Drip Irrigation System,* Soil Sci. Soc. Amer. J., vol. 75, no. 2, pp. 488-497.
- Lafolie, F., Guennelon, R., and Van Genuchten, M. Th., 1989, *Analysis of Water Flow under Trickle Irrigation: I. Theory and Numerical Solution,* Soil Sci. Soc. Amer. J., vol. 53, pp. 1310-1318.
- Li, J., Zhang, J., and Ren, L., 2003, *Water and Nitrogen Distribution As Affected By Fertigation of Ammonium Nitrate from a Point Source,* Irrig. Sci., vol. 22, no. 1, pp. 12-30.
- Schaap, M. G., Leij, F. J., and van Genuchten, M. Th., 2001, *ROSETTA: A Computer Program for Estimating Soil Hydraulic Properties with Hierarchical Pedotransfer Functions,* Journal of Hydrology, vol. 251, pp. 163–176.
- Schwartzman, M., and Zur, B., 1986, *Emitter Spacing And Geometry of Wetted Soil Volume,* J. Irrig. Drain. Eng., ASCE, vol. 112, no. 3, pp. 242–253.
- Šimůnek, J., van Genuchten, M. T., and Šejna, M., 2006,*The Hydrus Software Package for Simulating Two- And Three-Dimensional Movement of Water, Heat, And Multiple Solutes in Variably-Saturated Media,* Technical Manual, ver. 1.0, PC Progress, Prague, Czech Republic.

NOMENCLATURE

K_s = saturated hydraulic conductivity of the soil, cm/hr,
l = pore-connectivity parameter, dimensionless.
n = pore-size distribution index, dimensionless,
Q = discharge of the point source, lph,
t =time, hrs,
V = volume of applied water, liters,
W = wetted diameter, cm,
Z = wetted depth, cm,
α = shape parameter (coefficient in the soil water retention function), 1/cm,
θ_i = initial soil water content, cm^3/cm^3,
θ_r = residual water content, cm^3/cm^3,
θ_s = saturation volumetric soil-water content, cm^3/cm^3.

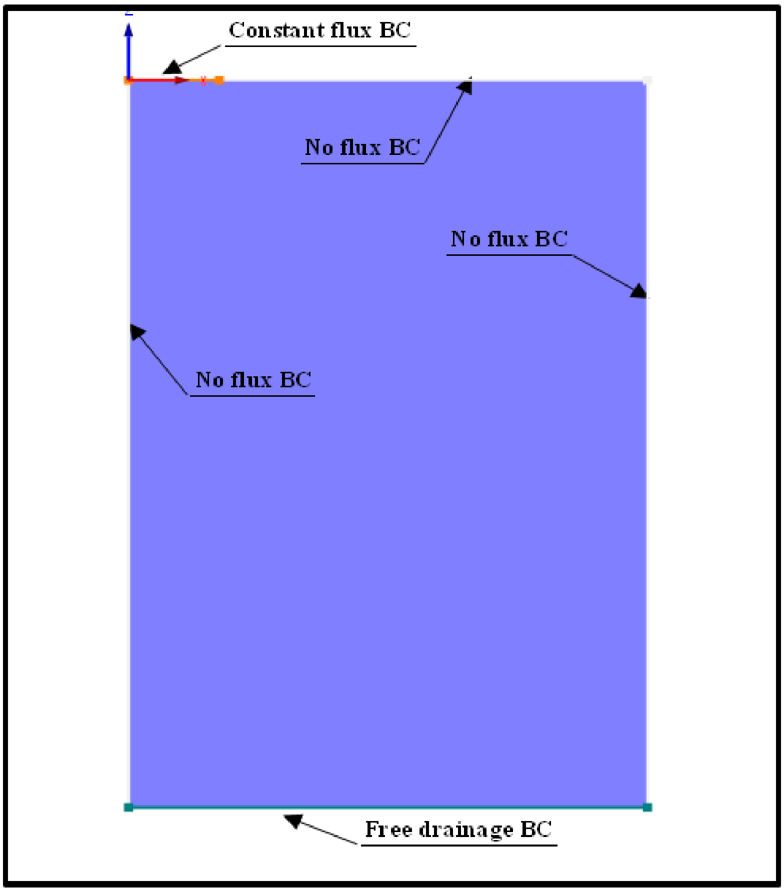

Figure 1. Schematic representing the boundary conditions used in numerical simulations.

Table 1. Hydraulic parameters of the soil for twelve texture class of the USDA soil-texture triangle [according to **Carsel and Parish, 1988.**].

No	K_s -cm/hr-	θ_r -cm³/cm³-	θ_s -cm³/cm³-	α -cm⁻¹-	n	**Textural class**
1	29.70	0.045	0.430	0.145	2.68	Sand
2	14.60	0.057	0.410	0.124	2.28	Loamy Sand
3	4.42	0.065	0.410	0.075	1.89	Sandy Loam
4	1.31	0.100	0.390	0.059	1.48	Sandy Clay Loam
5	1.04	0.078	0.430	0.036	1.56	Loam
6	0.40	0.067	0.450	0.020	1.41	Silty Loam
7	0.26	0.095	0.410	0.019	1.31	Clay Loam
8	0.25	0.034	0.460	0.016	1.37	Silt
9	0.20	0.068	0.380	0.008	1.09	Clay
10	0.12	0.100	0.380	0.027	1.23	Sandy Clay
11	0.07	0.089	0.430	0.010	1.23	Silty Clay Loam
12	0.02	0.070	0.360	0.005	1.09	Silty Clay

Table 2. Hydraulic parameters of soil for eleven textural classes of the UK soil texture triangle as obtained from the program of Rosetta Lite [Schaap, et al., (2001)].

No	K_s -cm/hr-	θ_r -cm^3/cm^3-	θ_s -cm^3/cm^3-	α -cm^{-1}-	n	Textural class
1	24.50	0.050	0.380	0.070	3.08	Sand
2	5.10	0.040	0.380	0.040	1.82	Loamy Sand
3	1.70	0.050	0.410	0.010	1.65	Sandy Silt Loam
4	1.67	0.040	0.390	0.030	1.40	Sandy Loam
5	1.28	0.060	0.470	0.010	1.67	Silt Loam
6	0.74	0.100	0.490	0.020	1.21	Clay
7	0.62	0.080	0.390	0.030	1.23	Sandy Clay
8	0.59	0.070	0.380	0.030	1.31	Sandy Clay Loam
9	0.56	0.100	0.500	0.010	1.41	Silty Clay
10	0.49	0.080	0.460	0.010	1.57	Silty Clay Loam
11	0.45	0.080	0.430	0.010	1.48	Clay Loam

Table 3. Physical properties of the soil at the research station.

Texture *			Average apparent specific gravity	Soil Water content at 33 kPa, % by vol.	Soil Water content at 1500 kPa, % by vol.	Soil Water content initial, by vol.	Hydraulic Conductivity, K_s, cm/hr
Silty Clay Loam							
Sand (%)	Silt (%)	Clay (%)					
17.2	48.8	34	1.14	34.85	18.9	19.9	4.7

Table 4. Empirical formulas to predict wetted diameter and wetted depth by using regression analysis for USDA soil classification system.

K_s, cm/hr	Wetted Diameter W, cm	EF	RMSE, cm	Wetted Depth, Z, cm	EF	RMSE, cm
29.7	$20.5\, Q^{0.183}\, t^{0.161}\, {\theta_i}^{-0.098}$	0.97	1.34	$36.6\, Q^{0.369}\, t^{0.547}\, {\theta_i}^{0.273}$	0.99	1.20
14.59	$30.9\, Q^{0.203}\, t^{0.205}\, {\theta_i}^{0.030}$	0.98	1.20	$36.8\, Q^{0.350}\, t^{0.531}\, {\theta_i}^{0.365}$	0.99	1.16
4.42	$42.1\, Q^{0.261}\, t^{0.240}\, {\theta_i}^{0.141}$	0.99	1.20	$19.4\, Q^{0.340}\, t^{0.533}\, {\theta_i}^{0.250}$	0.99	1.08
1.31	$51.6\, Q^{0.343}\, t^{0.154}\, {\theta_i}^{0.133}$	0.98	1.98	$14.0\, Q^{0.257}\, t^{0.711}\, {\theta_i}^{0.427}$	0.98	1.57
1.04	$56.4\, Q^{0.360}\, t^{0.151}\, {\theta_i}^{0.150}$	0.98	2.24	$12.7\, Q^{0.183}\, t^{0.717}\, {\theta_i}^{0.481}$	0.98	1.10
0.40	$64.3\, Q^{0.433}\, t^{0.070}\, {\theta_i}^{0.057}$	0.99	1.94	$5.7\, Q^{0.037}\, t^{0.821}\, {\theta_i}^{0.446}$	0.99	0.36
0.26	$78.4\, Q^{0.461}\, t^{0.038}\, {\theta_i}^{0.035}$	0.99	1.50	$4.7\, Q^{0.005}\, t^{0.843}\, {\theta_i}^{0.551}$	0.99	0.20
0.25	$78.9\, Q^{0.464}\, t^{0.035}\, {\theta_i}^{0.030}$	0.99	1.41	$3.9\, Q^{0.001}\, t^{0.803}\, {\theta_i}^{0.470}$	0.99	0.16
0.20	$86.8\, Q^{0.468}\, t^{0.032}\, {\theta_i}^{0.024}$	0.99	1.46	$4.0\, Q^{0.002}\, t^{0.836}\, {\theta_i}^{0.477}$	0.99	0.27
0.12	$107.5\, Q^{0.484}\, t^{0.014}\, {\theta_i}^{0.011}$	0.99	0.87	$2.7\, Q^{0.005}\, t^{0.790}\, {\theta_i}^{0.517}$	0.99	0.14
0.07	$137.7\, Q^{0.492}\, t^{0.007}\, {\theta_i}^{0.005}$	0.99	0.57	$1.8\, Q^{0.001}\, t^{0.713}\, {\theta_i}^{0.474}$	0.99	0.08
0.02	$253.8\, Q^{0.497}\, t^{0.002}\, {\theta_i}^{0.001}$	0.99	0.35	$0.9\, Q^{0.006}\, t^{0.636}\, {\theta_i}^{0.335}$	0.98	0.09

Table 5. Empirical formulas to predict wetted diameter and wetted depth by using regression analysis for UK soil classification system

K_s, cm/hr	Wetted Diameter W, cm	EF	RMSE, cm	Wetted Depth, Z, cm	EF	RMSE, cm
24.5	$25.0\ Q^{0.195}\ t^{0.182}\ \theta_i^{-0.100}$	0.96	1.90	$60.9\ Q^{0.319}\ t^{0.528}\ \theta_i^{0.450}$	0.99	2.40
5.10	$49.9\ Q^{0.254}\ t^{0.292}\ \theta_i^{0.184}$	0.99	0.91	$25.7\ Q^{0.284}\ t^{0.474}\ \theta_i^{0.300}$	0.99	0.70
1.70	$68.4\ Q^{0.296}\ t^{0.263}\ \theta_i^{0.277}$	0.99	2.00	$28.5\ Q^{0.200}\ t^{0.530}\ \theta_i^{0.521}$	0.99	1.14
1.67	$46.7\ Q^{0.328}\ t^{0.199}\ \theta_i^{0.109}$	0.99	1.87	$11.9\ Q^{0.261}\ t^{0.620}\ \theta_i^{0.245}$	0.98	1.17
1.28	$58.9\ Q^{0.327}\ t^{0.211}\ \theta_i^{0.189}$	0.98	2.44	$17.2\ Q^{0.166}\ t^{0.598}\ \theta_i^{0.432}$	0.98	1.23
0.74	$50.2\ Q^{0.413}\ t^{0.090}\ \theta_i^{0.041}$	0.99	1.72	$4.9\ Q^{0.103}\ t^{0.850}\ \theta_i^{0.300}$	0.99	0.71
0.62	$57.7\ Q^{0.413}\ t^{0.085}\ \theta_i^{0.065}$	0.99	1.83	$7.9\ Q^{0.087}\ t^{0.874}\ \theta_i^{0.490}$	0.98	1.03
0.59	$61.6\ Q^{0.408}\ t^{0.094}\ \theta_i^{0.088}$	0.99	2.14	$9.8\ Q^{0.108}\ t^{0.843}\ \theta_i^{0.569}$	0.99	0.97
0.56	$59.2\ Q^{0.419}\ t^{0.087}\ \theta_i^{0.064}$	0.99	2.11	$6.0\ Q^{0.056}\ t^{0.783}\ \theta_i^{0.379}$	0.99	0.43
0.49	$67.9\ Q^{0.413}\ t^{0.092}\ \theta_i^{0.099}$	0.99	2.37	$9.3\ Q^{0.047}\ t^{0.760}\ \theta_i^{0.543}$	0.99	0.42
0.45	$70.1\ Q^{0.417}\ t^{0.087}\ \theta_i^{0.098}$	0.99	2.40	$9.4\ Q^{0.045}\ t^{0.771}\ \theta_i^{0.565}$	0.99	0.44

.

Table 6. Empirical formulas to predict wetted diameter by using regression analysis and statistical analysis for groups soils.

No	K_s, cm/hr	Wetted Diameter W, cm	EF	RMSE, cm
1	29.7-24.5	$162.1\ Q^{0.19}t^{0.18}K_s^{-0.66}\theta_i^{-0.17}$	0.96	1.87
2	14.59-4.42	$50.7\ Q^{0.24}t^{0.22}K_s^{-0.15}\theta_i^{-0.10}$	0.97	5.35
3	1.7-1.04	$1.4\ Q^{0.31}t^{0.24}K_s^{7.10}\theta_i^{0.19}$	0.96	4.36
4	0.74-0.40	$45.0\ Q^{0.41}t^{0.09}K_s^{-0.47}\theta_i^{0.05}$	0.99	2.05
5	0.26-0.2	$32.3\ Q^{0.46}t^{0.04}K_s^{-0.64}\theta_i^{0.03}$	0.99	1.50
6	0.12-0.02	$39.1\ Q^{0.49}t^{0.01}K_s^{-0.47}\theta_i^{0.008}$	0.99	1.40

Table 7. Empirical formulas to predict wetted depth by using regression analysis and statistical analysis for groups soils.

No	K_s, cm/hr	Wetted Depth, Z, cm	EF	RMSE, cm
1	29.7-24.5	$29.3\ Q^{0.34} t^{0.54} K_s^{0.13} \theta_i^{0.35}$	0.99	2.56
2	14.59-4.42	$13.2\ Q^{0.34} t^{0.53} K_s^{0.35} \theta_i^{0.32}$	0.99	1.60
3	1.7-1.04	$2.3\ Q^{0.22} t^{0.56} K_s^{4.13} \theta_i^{0.38}$	0.97	1.82
4	0.74-0.40	$4.45\ Q^{0.09} t^{0.86} K_s^{-0.96} \theta_i^{0.41}$	0.95	1.75
5	0.26-0.2	$64.9\ Q^{0.003} t^{0.83} K_s^{2.02} \theta_i^{0.50}$	0.98	0.50
6	0.12-0.02	$20.2\ Q^{0.004} t^{0.77} K_s^{0.94} \theta_i^{0.51}$	0.97	0.30

Table 8. Comparison of measured wetted diameters with those simulated by various techniques.

Emitter discharge, lph	Time, hrs	Wetted diameter[6] W, cm				
		Measured[1]	Hydrus[2]	Simulated[3]	Amin[4]	Zur[5]
2.5	1	44	42.0	44.4	24.6	30.0
	2	49	50.7	53.2	29.6	34.9
	3	54	57.3	59.1	33.0	38.2
3.75	1	50	48.3	49.2	27.4	35.1
	2	58	57.7	60.0	33.0	40.9
	3	65	64.8	65.7	36.8	44.7
5.0	1	51	53.5	53.0	29.5	39.3
	2	61.5	63.3	63.5	35.6	45.8
	3	68	70.8	70.7	39.7	50.0
6.0	1	55	57.1	55.5	31.0	42.2
	2	64	67.1	66.6	37.3	49.1
	3	70	75.0	74.1	41.6	53.7
RMSE (cm)			2.5	2.7	24.4	15.6
EF			0.91	0.9	-8.5	-2.9

[1] measured wetted diameter from field work.
[2] simulated wetted diameter by using Hydrus software.
[3] simulated wetted diameter by using the formulas in **Table 4** and **Table 5**.
[4] simulated wetted diameter by using **Amin, and Ekhmaj, 2006.**
[5] simulated values of wetted diameter by using **Schwartzman, and Zur, 1986.**
[6] saturated hydraulic conductivity equals 4.7 cm/hr and initial soil water content equals 19.9%.

The Effect of Vehicle Body Shapes on the Near Wake Region and Drag Coefficient: A Numerical Study

Hayder Kareem Sakran
Assistant Lecturer
College of Engineering- University of AL Muthanna
E-mail:hsakran@my.bridgeport.edu

ABSTRACT

The purpose of this paper is to gain a good understanding about wake region behind the car body due to the aerodynamic effect when the air flows over the road vehicle during its movement. The main goal of this study is to discuss the effect of the geometry on the wake region and the aerodynamic drag coefficient. Results will be achieved by using two different shapes, which are the fastback and the notchback. The study will be implemented by the Computational Fluid Dynamic (CFD) by using STAR-CCM+® software for the simulation. This study investigates the steady turbulent flow using k-epsilon turbulence model. The results obtained from the simulation show that the region of the air separation behind the vehicle varies with the variation of the body design. The minimum drag coefficient can be achieved with notch-back since the separation of the air is less as compared with fastback end. These results are demonstrated by pressure distribution and velocity distribution which offer a good understanding of the flow behavior around the vehicle bodies.

Keywords: computational fluid dynamic, k-ε turbulence model, numerical simulation, wake region.

تأثير اشكال المركبات على منطقة الضغط المنخفض و معامل الكبح: دراسة عددية

حيدر كريم سكران
مدرس مساعد
كلية الهندسة/ جامعة المثنى

الخلاصة

ان الغرض من هذه الدراسة هو الحصول على مفهوم افضل حول منطقة الضغط المنخفض او ما تسمى بمنطقة الضعف المتولدة في الاجزاء الخلفية للمركبات بسبب تاثير ديناميكية الهواء عند جريانه حول المركبات اثناء حركتها. ان الهدف الرئيسي لهذه الدراسة هو مناقشة تاثير الشكل الخارجي للمركبات على منطقة الضغط المنخفض و كذلك على معامل الكبح . تُستخلص النتائج باختبار شكلين مختلفين من المركبات و حسب تصميمهما الخارجي وهما الاشكال ذات النهايات السريعة (Fastback) و الاشكال ذات النهايات المثلومة (Notchback). ستُوظف هذه الدراسة بواسطة ديناميكيا الموائع الحسابية (CFD) باستعمال برنامج المحاكاة (STAR-CCM+® software). تعتمد هذه الدراسة الجريان الاضطرابي المستقر (steady turbulent flow) باستعمال معادلات الجريان الاضطرابي (k-epsilon turbulence models). وقد اظهرت النتائج المستحصلة من المحاكاة ان اختلاف منطقة فصل الهواء خلف المركبة يعزى الى اختلاف تصميم هيكل المركبة. و يمكن الحصول على اقل معامل للكبح في الاشكال ذات النهايات المثلومة (Notchback) لان منطقة فصل الهواء تكون اقل في هذه الاشكال مقارنة مع الاشكال ذات النهايات السريعة (Fastback). و برهنت منحنيات توزيع الضغط و السرعة التي تم الحصول عليها من خلال المحاكاة صحة النتائج وبدورها تساعد على فهم سلوك جريان الهواء حول هياكل المركبات.

الكلمات الرئيسية : ديناميكيا الموائع الحسابية, معادلات الجريان الاضطرابي, دراسة عددية و منطقة الضعف.

1. INTRODUCTION

Automobiles companies produce too many differences of body designs, and every design has specific features. However, people do not know the benefits of these designs because they look for the beautiful shape with appropriate cost when they decide to buy a car.

When vehicles move, air flows over the outer circumference of the vehicle. The air is distributed with different magnitude of velocities behind the body of the vehicle as shown in **Fig.1.**

The separation will happen when the fluid flow does not follow the shape of the surface so it detaches or separates, causing the wake region to be generated in the rear end of the vehicle, **Hucho, 2013,** and **Katz, 2006**. This region will be developed behind the vehicle body because of the separation of the air at the back of the vehicle. A separation causes two regions depending on their location from the rear of the car. The first region, which is developed when the separation happened close behind the vehicle, is known as the near wake region, and the second one, which is developed when the separation happened further behind the vehicle, is known as the far wake region as shown in **Fig.2.**

The structure of the vortex depends on the geometry of the vehicle and the history of its upstream flow, the geometry also affects the relative size of the wake region as shown in **Fig.3**. A lot of investigations have been employed to study the effect of the geometry of the moving bodies on the aerodynamic performance especially for the automobiles since it has a very significant relation with the fuel consumption. The aerodynamic drags of a road vehicle are responsible for a huge part of the vehicle fuel consumption and cause up to 50% of the total vehicle fuel consumption at highway speeds**, Sudin, et al. 2014**. The rear end shape has a worthy relation with the drag and it can help to design an acceptable shape with minimum rear lifts without increasing the drag coefficient, **Fukuda, et al. 1995.** The investigation of the stability characteristic of Notchback- type vehicle under the influence of transient aerodynamics by Large-Eddy Simulation (LES) turbulence model shows a strong impact on unsteady flow structure around the rear end of the vehicle **Cheng, et al., 2011**.The mean pressure results show a significant increment in the base pressure with the drag reduction which strongly influences the unsteady base pressure and velocity spectral at a Strouhal number- which is a useful dimensionless value for analyzing oscillating unsteady fluid flow in dynamics problems - of 0.07,**Khalighi, et al., 2001.**

The time average analysis expresses a strong interaction among boundary layers, drag coefficient and pressure at the rear end of the vehicle, **Vanraemdonck,** and **Vantooren, 2008.** It is obvious that the topological features of the time-average flow are independent of the averaging time T and grid-size, **Franck, et al., 2009**. The time-averaged structure of the wake of a fastback type road vehicle has a pair of vortices placed one above another. The trailing edges of these vortices are parallel to the longitudinal axis of the vehicle, **Ahmed, 1983.**

A lot of turbulence models have been investigated to analyze the air attitude at the rear end of the vehicles. The numerical simulation using shear stress transport turbulence model can predict recirculation which is more intensive and it can give results which are very close to the experimental investigations in their accuracy, **Guilmineau, 2003**. The examination of the aerodynamic damping mechanism- which is the reduction of vibrations by the inherent stability of a body or of its control surface- in sedan-type vehicle shows that the unsteady aerodynamics is apparent as having undesirable effect on vehicles stability. Investigating LES turbulence model shows an important influence of transient flow structure above the near section of the sedan- type vehicle, **Cheng, et al., 2011**. Wall boundary cases with separation and reattachment using the Durbin's k-ε-v^2 turbulence model give very good accurate results. The turbulence model and the near wall grid are not the only parameters that can affect the results of the drag coefficient. It is possible to make the CFD more accurate with a suitable selection of a different scheme, **Liu,** and **Alfred, 2003.**

This work tackles the effect of different vehicle geometry on the airflow attitude in the wake region and calculates the aerodynamic drag coefficient. It takes the three most common body geometries of the small car which are fastback, square back, and notchback as shown in **Fig.4.** All these designs have the same shape of the front region, which is so close to Ahmed body, but with different design of the back section. Every design has a specific effect on the aerodynamic features when the air flows over these bodies.

It focuses on the near wake region of two different geometries, which are the fastback and the notchback because the square back and the fastback have a common parameter (slant angle) which is considered to be 25 degrees close to the fastback shape as shown in **Fig.5.** The simulation has been achieved by using a computational fluid dynamics code, STAR-CCM+, to simulate the flow around bodies. Pressure distribution, velocity vector, and the drag coefficient that developed behind the body of the vehicle are collected after the simulation done to have a good understanding about the effect of the vehicle geometry on the drag coefficient and other results.

2. PROBLEM DEFINITION

The three–dimensional domain has been generated with structural hexahedral mesh. The boundary layers have been resolved using trimmer mesh, 0.4 m base size, and 7 prism layers to study the boundary conditions carefully. The computational domain is generated with 8m long, 0.4m wide and 3m high. Furthermore, the fastback geometry is 1.044m long, 0.288 m high and 0.4 m wide. The notchback geometry size is 1.184m long, 0.288 m high and 0.4 m wide as shown in **Figs.6**, **7**, and **8.** Because the three-dimensional domain is very complicated, the simulation will take more time to be achieved. Thus, the computational domain is converted to two-dimensional one which is more suitable in this study since the body is symmetry with the z-direction as shown in **Fig.9**. The structural mesh consists of 13389 cells, 377490 faces, and 19022 vertices as shown in **Figs.10**, and **11.** The boundary conditions and the turbulence model (k-ε) have been used to solve the problem. The problem is carried out as a bluff body that is much close to Ahmed body. A fully submerged with the surrounding air has been assumed. The numerical analysis is employed to emphasize the near wake region and to study its effect on the airflow behavior and the drag coefficient magnitude.

The two-dimensional geometry has been created by using STAR-CCM+® to simulate a steady state conditions and incompressible fluid flow problem. The problem specification and the boundary conditions are explained in **tables 1**, and **2** for the two cases.

3. TURBULENCE MODELS

STAR-CCM+® software is one of the CFD commercial tools that are used to simulate problems and to solve the governing equation for the flow around the vehicle body and other computational fluid dynamics problems relying on the boundary conditions. The Navier-Stoke equation is a complex equation that has a lot of unknown terms and its calculation needs to apply turbulence model to be solved. Air flow over the vehicle is governed by Reynolds Average Navier-Stokes equations (RANS) in order to study the flow around the vehicle as explained below:

$$\frac{\partial p}{\partial t}+div(\rho U)=0 \tag{1}$$

$$\rho\frac{\partial U_i}{\partial t_i}+\rho\frac{\partial}{\partial x_j}(U_iU_j+\overline{u'_ju'_i})=-\frac{\partial P}{\partial x_i}+\frac{\partial}{\partial x_j}(2\mu S_{ij}) \tag{2}$$

The term ($\overline{u'_ju'_i}$) is known as the Reynolds stress tensor which is also considered as stress term due to fluctuating velocities.

Boussinesq assumption has been applied to compute Reynolds stress tensor.

$$-\rho\overline{u'_ju'_i}=\mu_t\left[\frac{\partial U_i}{\partial x_i}+\frac{\partial U_j}{\partial x_j}\right]-\frac{2}{3}\rho k\delta_{ij}=2\mu_t\delta_{ij}-\frac{2}{3}\rho k\delta_{ij} \tag{3}$$

The software has been set up with k-ε turbulence model to solve the governing equation directly. The k-ε turbulence model has two model equations which are the turbulence kinetic energy k and its dissipation rate ε. It is widely used to have a better result and to enhance the stability with convergence.
The k and ε have been employed to describe velocity scale ϑ and length scale ℓ as follows:

$$\vartheta=k^{1/2} \tag{4}$$

$$\ell=\frac{k^{2/3}}{\varepsilon} \tag{5}$$

The eddy viscosity can be specified by applying the dimensional analysis as follows:

$$\mu_t=C\rho\vartheta\ell=\rho C_\mu\frac{k^2}{\varepsilon} \tag{6}$$

C_μ is a dimensionless constant, it equals to 0.09.

The transport equations for k and ε can also be specified as follows:

$$\frac{\partial(\rho k)}{\partial t}+div(\rho kU)=div\left[\frac{\mu_t}{\sigma_k}grad\cdot k\right]+2\mu_tS_{ij}\cdot S_{ij}-\rho\varepsilon \tag{7}$$

$$\frac{\partial(\rho\varepsilon)}{\partial t}+div(\rho\varepsilon U)=div\left[\frac{\mu_t}{\sigma_\varepsilon}grad\cdot\varepsilon\right]+C_{1\varepsilon}\frac{\varepsilon}{k}2\mu_tS_{ij}\cdot S_{ij}-C_{2\varepsilon}\rho\varepsilon\frac{\varepsilon^2}{k} \tag{8}$$

$\sigma_k = 1.00$, $\sigma_\varepsilon = 1.30$, $C_{1\varepsilon} = 1.44$, $C_{2\varepsilon} = 1.92$ all of these terms are adjustable constants.

4. RESULTS AND DISCUSSION

After completing mesh generation, the solution has been obtained when the convergence is done. The solution has two different groups of results depending on the conditions of the problem. The drag coefficient C_D is computed as follows:

$$C_D = \frac{F_D}{\frac{1}{2}\rho U^2 A_x} \tag{9}$$

F_D is the drag force, ρ is the fluid (air) density, U is the upstream velocity, and A_x is the projected area of the body in x direction. C_k, C_B, C_s, and C_D represent the drag coefficient at the nose, back, the rear slope and the total, respectively.

The simulation reached to convergence in approximately 57000 times of iterations for the notchback and 58000 times of iterations for the fastback, this happened because each problem has its boundary conditions specially the shape of the geometry. The simulation has done with convergence the results as shown in **Figs.12** and **13** that show the residual for the problem simulation.

Figs.14 and **15** shows the drag coefficient for different places of the vehicle body since the body has been divided into three places which are nose, slope, and back as shown in **Fig.16** and each one has individual magnitude of the drag.

This study focuses on the drag value and compares the computed results for two models. The drag value can be computed from Eq. (9); however, in this study the results of the drag coefficients are obtained from **Figs.14** and **15** since they are clear to be mentioned. **Tables 3** and **4** show the results of the drag coefficient for the specific problem. The total drag coefficient for the fastback is 0.698 and for the notchback is 0.654.

Figs.17 and **18** explain the pressure contour for the vehicle body that moves through the air and they display the behavior of the pressure distribution for the entire body. The differentiation of the pressure distribution is considered at the wake region since the difference between the two cases is restricted at the rear region.

Figs.19 and **20** show the velocity contour of the airflow over the entire body and it is easy to mention that the velocity at the wake region for the notchback is less than the velocity for the fastback.

In addition, **Figs .21, 22, 23,** and **24** that show velocity magnitude and velocity vector can confirm the results. The pressure at wake region for the notchback is more than the pressure at the wake region for the fastback. *"Pressure is low at locations where the flow velocity is high, and pressure is high at locations where the flow velocity is low".* **Cengel**, and **Cimbala**, **2006**.

Fig.25 shows a comparison of the two trailing vortexes in the near wake for both models which is clearly defined in these plots. It can be observed that the recirculation region for the fastback is bigger than the recirculation region for the notchback and it is obvious to understand that the drag coefficient for the fastback is bigger.

The shape of the rear edge of the bodies controls the velocity and pressure distribution in this region then affects the drag value for the total body.

5. CONCLUSIONS

In the present paper, the performance of airflow over different geometries of vehicle bodies which are the notchback and the fastback at the same boundary conditions, has been investigated numerically by Computational Fluid Dynamics (CFD) using k-ε turbulent models and the simulation was made by STAR-CCM+® software. The simulation shows strong results of the effect of the geometries on the drag coefficient and the air attitude in the back region of vehicles.

Figures and analysis in this study reveal the effects of the back end configuration on the flow field, drag coefficient, and air separation for body of vehicles, it is probable to conclude that:

1. The notchback end has a less drag coefficient and less area of separation than that for fast back end. This is because of the difference in shape especially in the rear back.
2. The results achieved were very in agreement with the theoretical understanding of the air flow over bodies.
3. Air and any other fluid attitudes depend on the shape of the body that the fluid would flow over it.

REFERENCES

- Ahmed, S. R., 1983, *Influence of Base Slant on the Wake Structure and Drag of Road Vehicle*, Transaction of ASME, Journal of Fluid Engineering, vol.105, PP. 429-434.

- Cengel,Y., and Cimbala, J., 2006, *Fluid mechanics: Fundamentals and applications*, McGraw-Hill, New York.

- Cheng, S. Y., Tsubokura, M., Nakashima, T., Nouzawa, T. and Okada, Y., 2011, *A Numerical Analysis of Transient Flow Past Road Vehicles Subjected to Pitching Oscillation*, Journal of Wind Engineering and Industrial Aerodynamics, vol. 99, No.5, PP. 511-522.

- Cheng, S. Y., Tsubokura, M., Nakashima, T., Okada, Y., and Nouzawa, T., 2011, *Large Eddy Simulation of Flow Past Road Vehicles Subjected to Pitching Oscillation*, 20th AIAA Computational Fluid Dynamics Conference.

- Fukuda, H., Yanagimoto, K., China, H., and Nakagawa, K., 1995, *Improvement of Vehicle Aerodynamics by Wake Control*, JSAE review, vol. 6, No.2, PP.151-155.

- Franck, G., Nigro, N., Storti, M., and D'elia, J.,2009, *Numerical Simulation of the Flow Around the Ahmed Vehicle Model*, Latin American applied research, vol.3, No.4, PP. 295-306.

- Guilmineau, E., 2003, *Numerical Simulation of Flow around a Simplified Car Body*, ASME/JSME 4th Joint Fluids Summer Engineering Conference, American Society of Mechanical Engineers.

- Hucho, W., 2013, *Aerodynamics of Road vehicles: from Fluid Mechanics to Vehicle Engineering*, Elsevier.

- Katz, J., 2006, *Race Car Aerodynamics: Designing for Speed*, Bentley Publisher.

- Khalighi, B., Zhang, S., Koromilas, C. , Balkanyi, S. R. , Luis P. B., Iaccarino, G. and Moin, P.,2001, *Experimental and Computational Study of Unsteady Wake Flow behind a Bluff Body with a Drag Reduction Device*, SAE Technical Paper.

- Liu, Y., and Alfred. M., 2003, *Numerical Modeling of Airflow over the Ahmed Body*, Proceedings of the 11th Annual Conference of the CFD Society of Canada.

- Richards, K. A., 2000, *Computational Modeling of Pollution Dispersion in the Near Wake of a Vehicle,* Proceedings of the MIRA international conference on aerodynamics.

- Sudin, M. N., Abdullah, M. A., Shamsuddin, S.A., Ramli, F. R. and Tahir, M. M.,2014, *Review of Research on Vehicles Aerodynamic Drag Reduction Methods,* International Journal of Mechanical & Mechatronics Engineering, Vol. 14, No. 2,PP. 35-47.

- Vanraemdonck, G. M. R., and Vantooren, M. J. L., 2008, *Time-averaged Phenomenological Investigation of a Wake behind a Bluff Body*, BBAA VI International Colloquium on: Bluff Bodies Aerodynamics & Applications. Vol. 51.

NOMENCLATURE

A_x = projected area of the body in x direction, m^2.
C_D = the total drag coefficient.
C_k = the nose drag coefficient.
C_B = the back drag coefficient.
C_s = the slope drag coefficient.
C_μ, σ_ε, $C_{1\varepsilon}$, $C_{2\varepsilon}$, σ_k = model constants.
F_D = the drag force, N.
L = characteristic length, m.
S_{ij} = the strain rate tensor, 1/s.
U = the upstream velocity, m/s.
u = velocity, m/s.

Greek symbols.

ε = turbulent dissipation rate, m^2/s^3.
k = turbulent kinetic energy, m^2/s^2.
ℓ = turbulent length scale, m.
μ_t = turbulent viscosity, Ns/m^2.
ρ = density of the air, kg/m^3.
υ = kinematic viscosity, m^2/s.
ϑ = velocity scale, m/s^1.

Subscripts

i; j = referring x- and y-directions respectively.

Table1. Fluid properties.

Fluid properties	
Fluid/Material	Air
Density	Constant, $\rho = 1.225\ kg/m^3$
Velocity	40 m/s
Time domain	steady
Turbulence model	k-ε turbulence model

Table 2. The simulation settings.

Simulation Settings	
Domain	Two Dimensional
Density	Constant, $\rho = 1.225\ kg/m^3$
Velocity	40 m/s
Time domain	Steady
Turbulence model	k-ε turbulence model
Solver	Segregated
Fluid/Material	Air
Mesh properties	Trimmer mesh, 7 prism layers; Base size 0. 4m

Table 3. The results of the drag coefficient for fastback.

Drag Coefficient for Fastback	
C_D	0.698
C_B	0.248
C_K	0.125
C_S	0.325

Table 4. The results of the drag coefficient for notchback.

Drag Coefficient for Notchback	
C_D	0.654
C_B	0.236
C_K	0.175
C_S	0.243

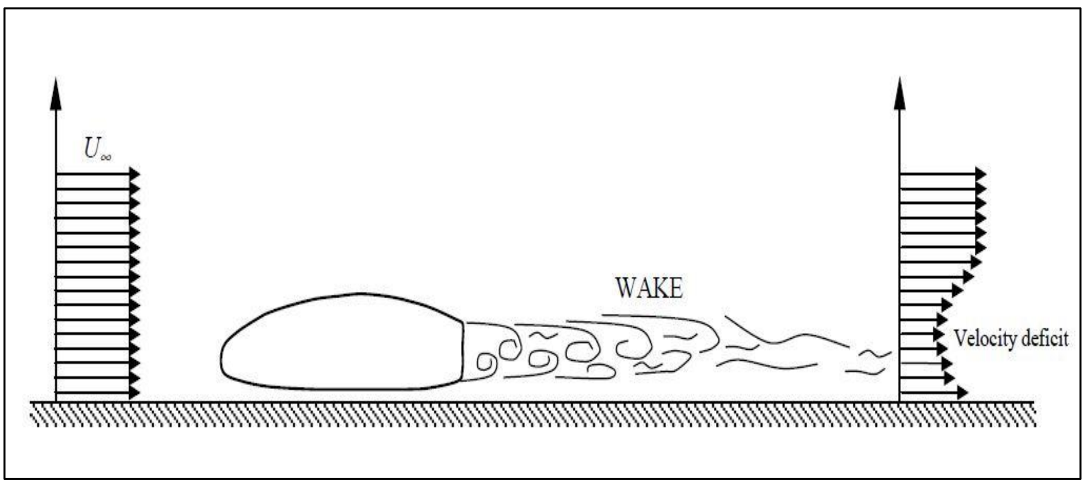

Figure 1. A wake region behind the vehicle, **Katz, 2006.**

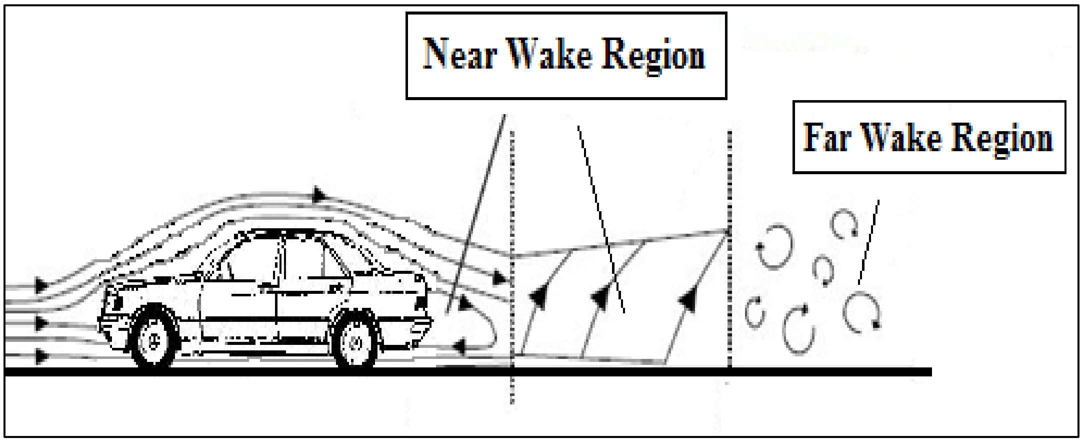

Figure 2. The near and the far wake regions, **Richards, 2000.**

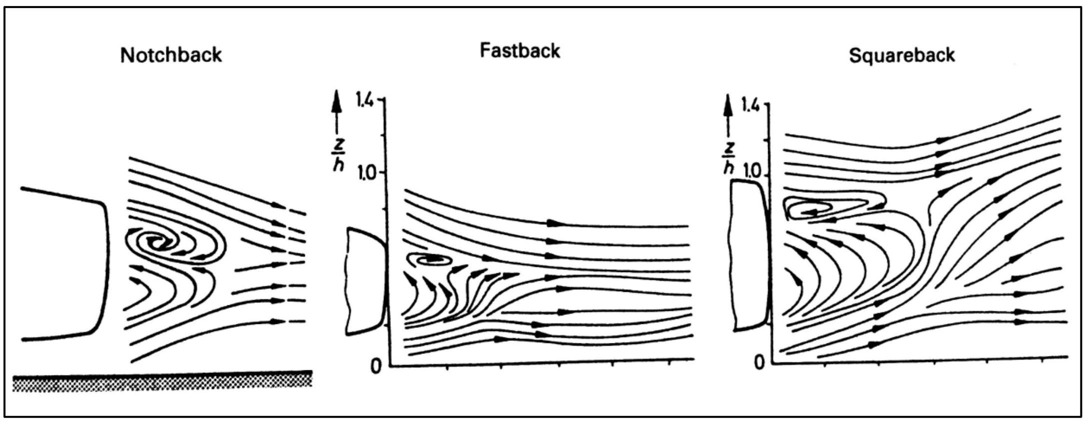

Figure 3. Vortices behind the vehicles, **Hucho, 2013.**

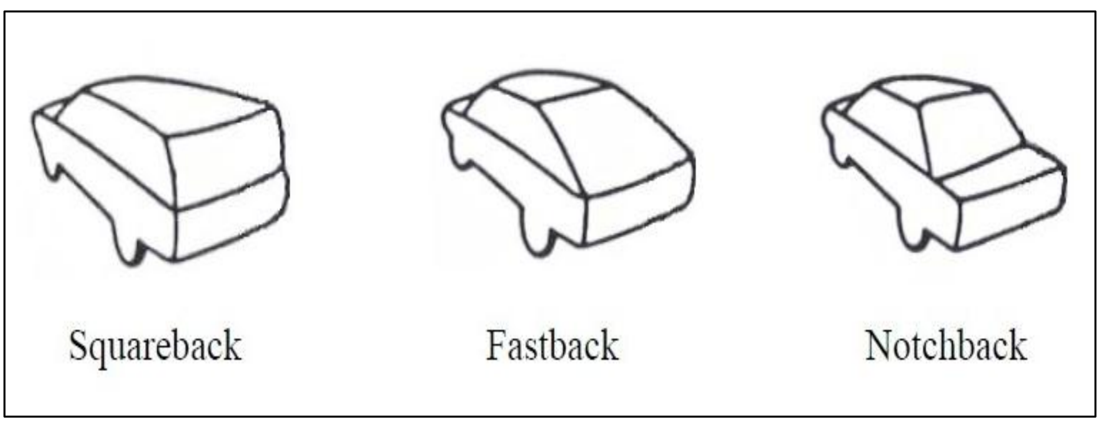

Figure 4. The common body geometries for the small car, **Richards, 2000.**

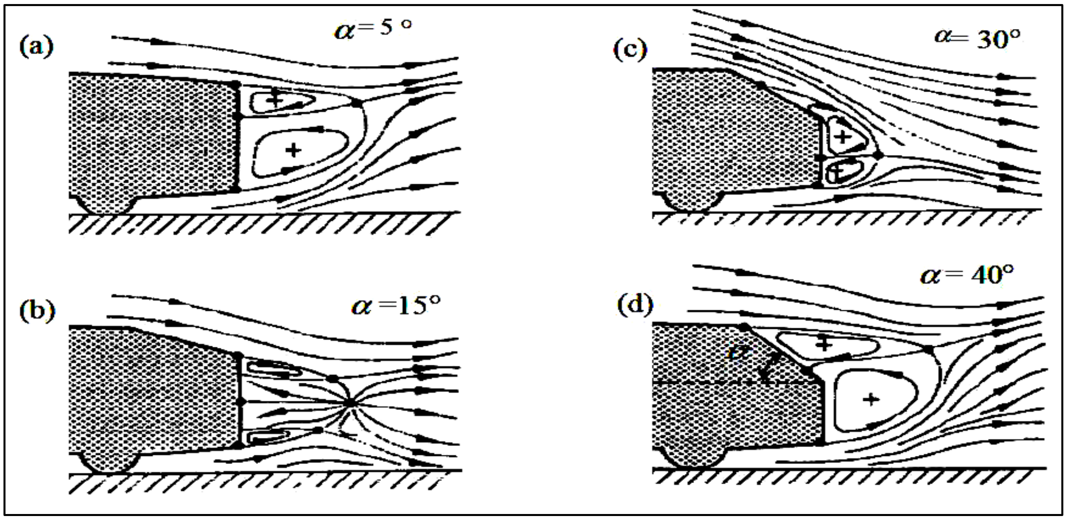

Figure 5. Different base degree of Slant angle, **Ahmed, 1983.**

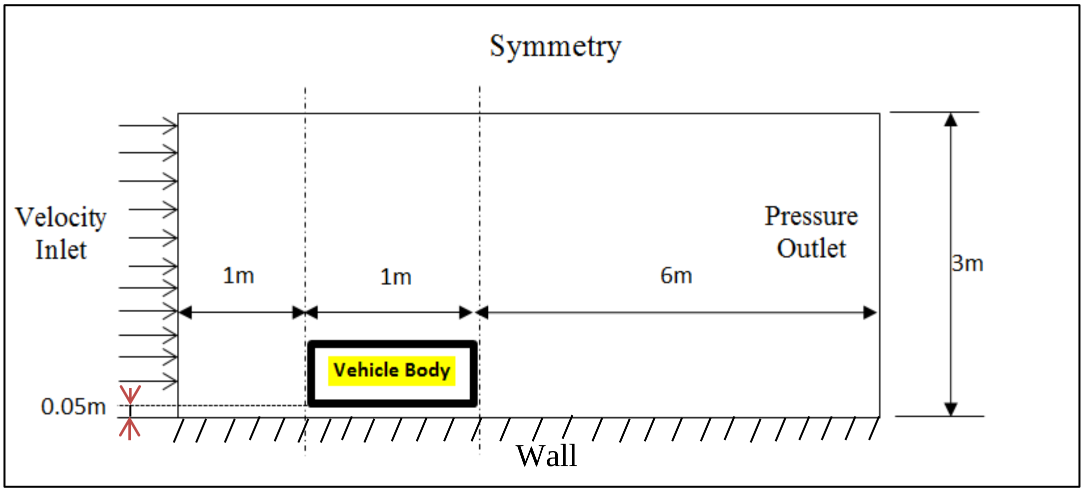

Figure 6. 2D Computational domain.

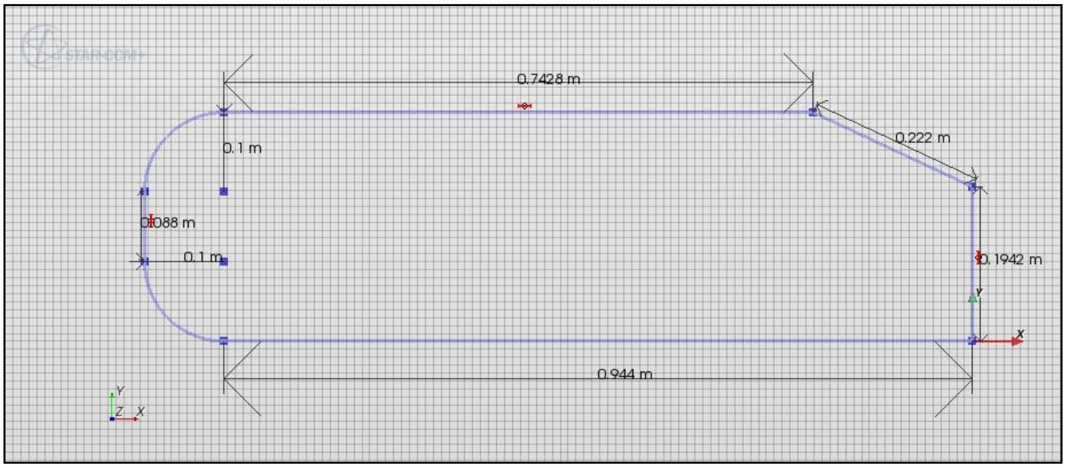

Figure 7. The cross-section of fastback geometry with 25 slant angle degree.

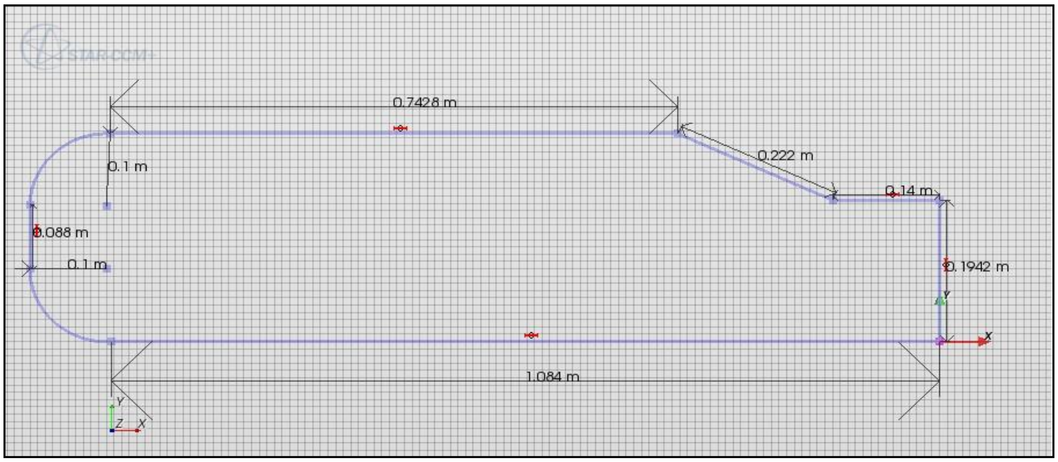

Figure 8. The cross-section of notchback geometry with 25 slant angle degree.

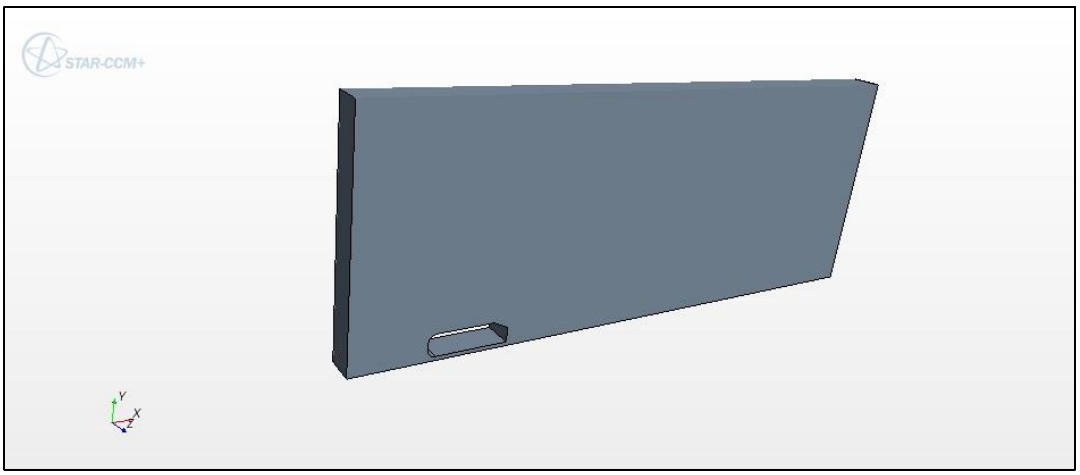

Figure9. The 3D computational domain.

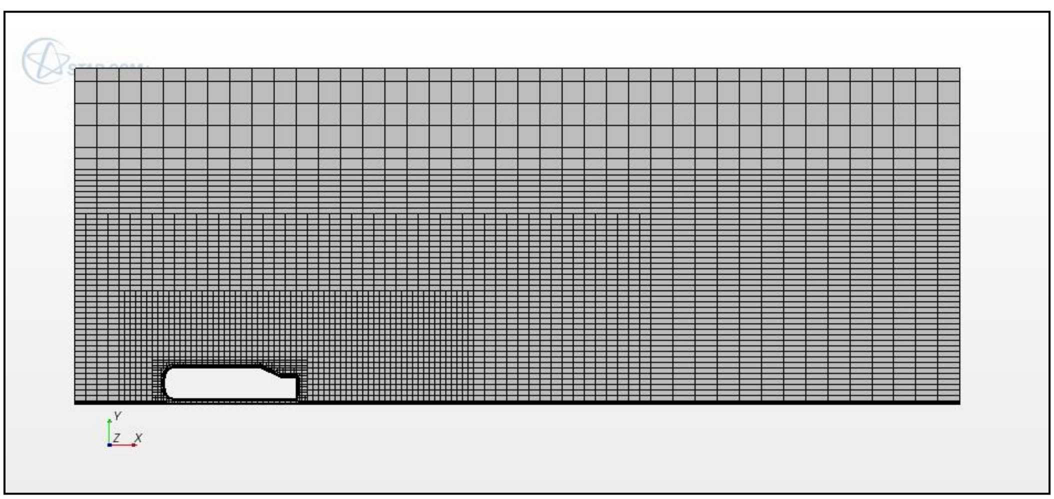

Figure 10. The cross-section of notchback geometry with 0.4 mesh base size.

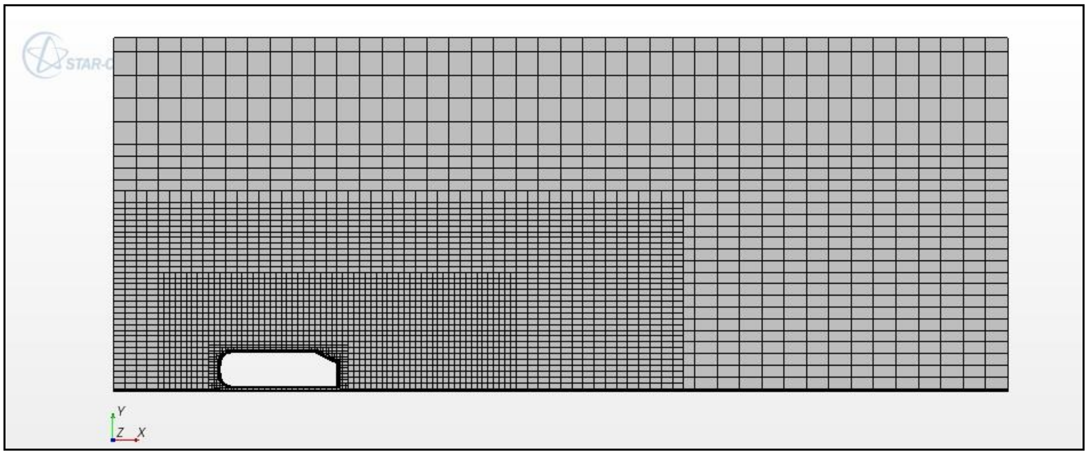

Figure 11. The cross-section of fastback geometry with 0.4 mesh base size.

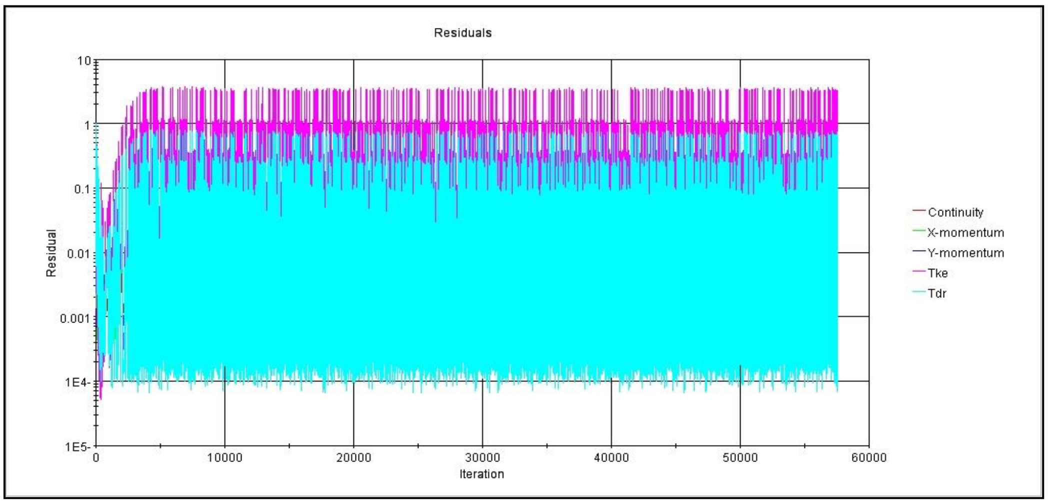

Figure 12. Residual history for fastback.

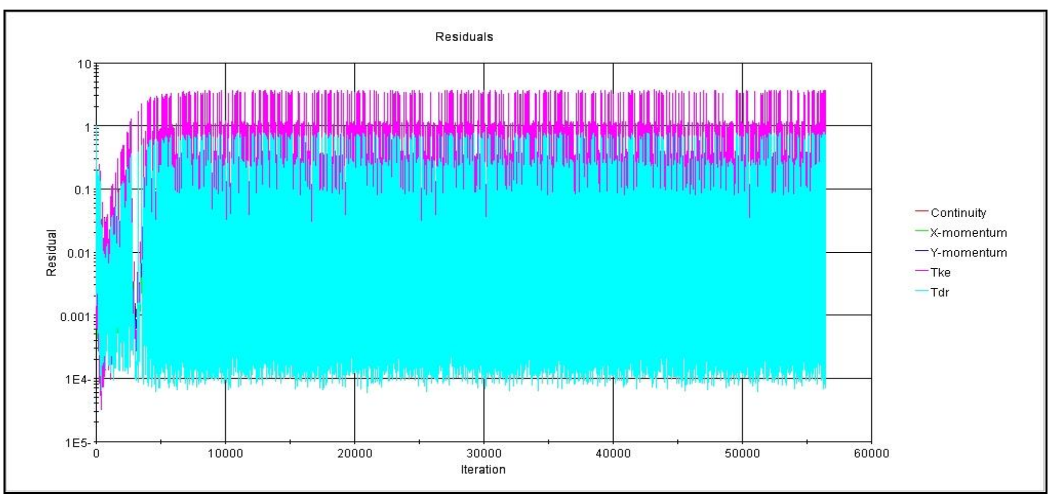

Figure 13. Residual history for notchback.

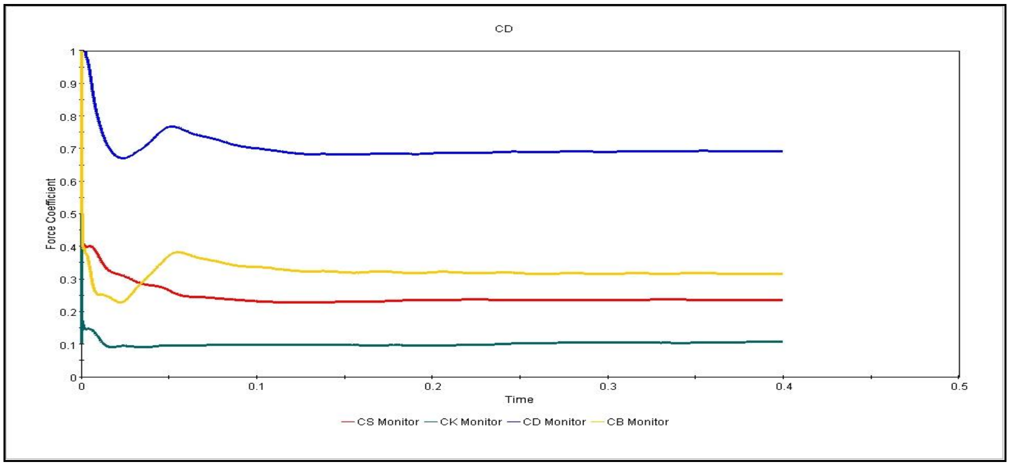

Figure 14. Drag coefficient for fastback.

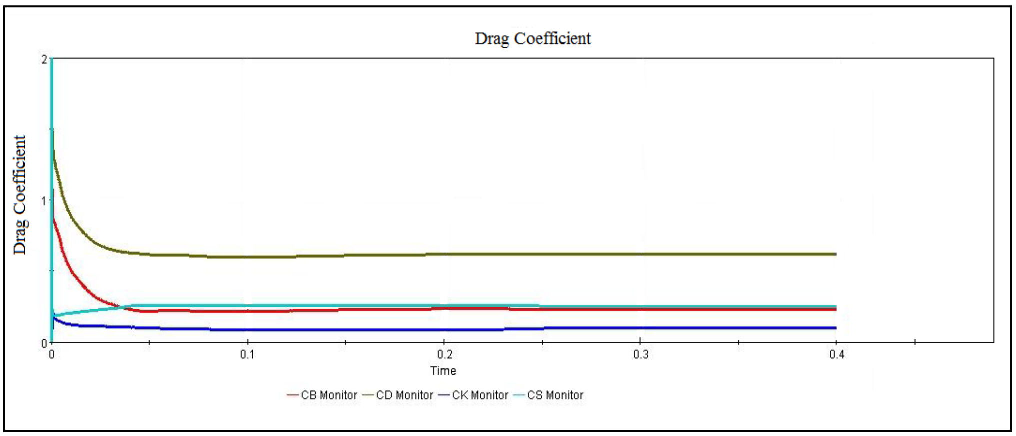

Figure 15. Drag coefficient for notchback.

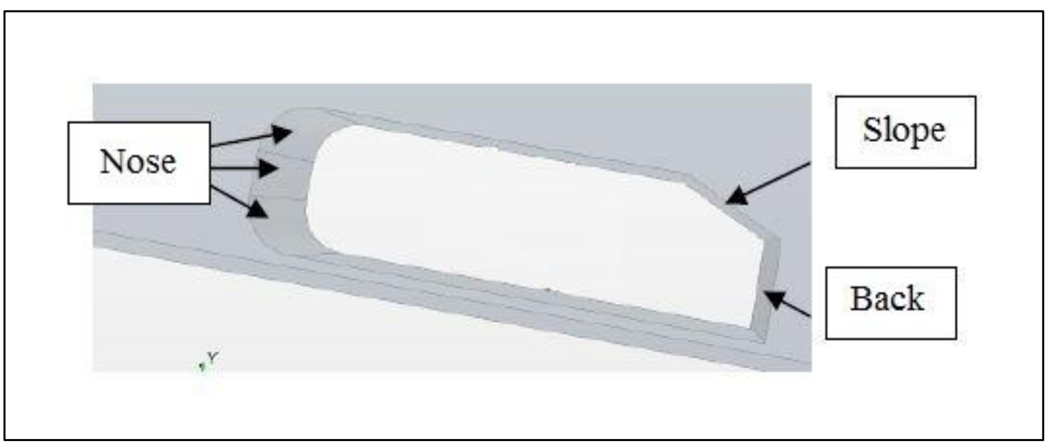

Figure 16. Divisions of the experimental area of the body.

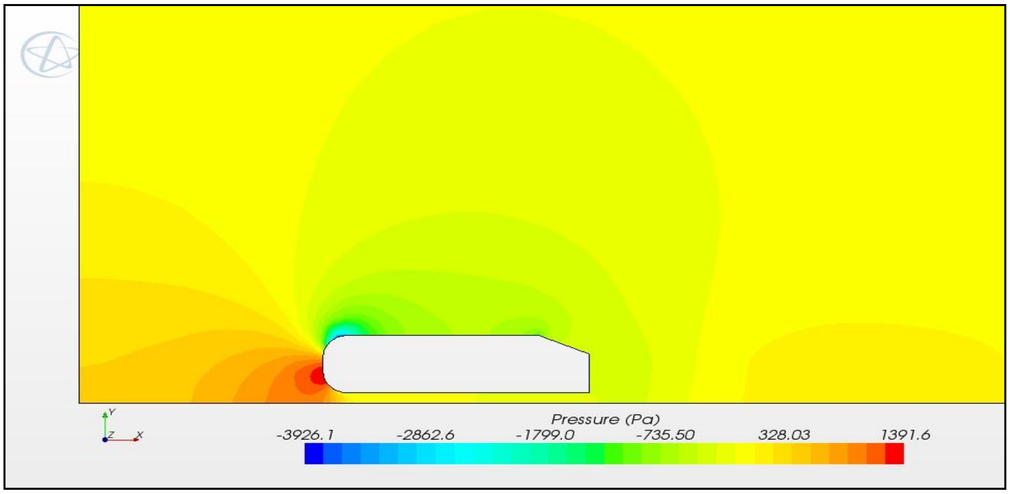

Figure 17. Pressure Contour for fastback.

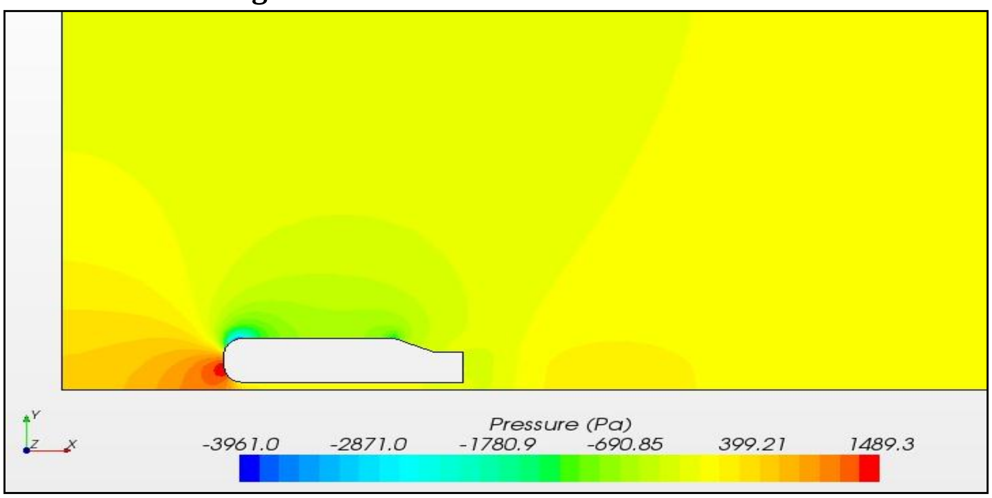

Figure 18. Pressure contour for notchback.

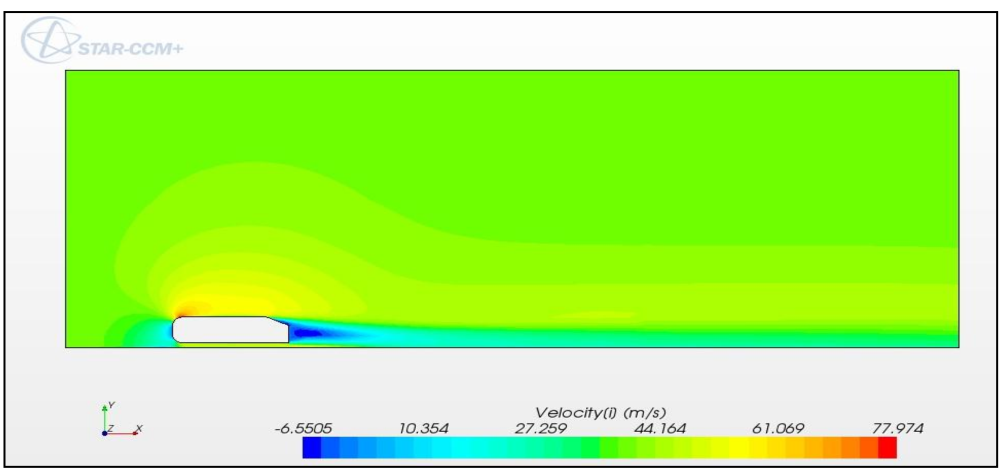

Figure 19. Velocity contour for fastback.

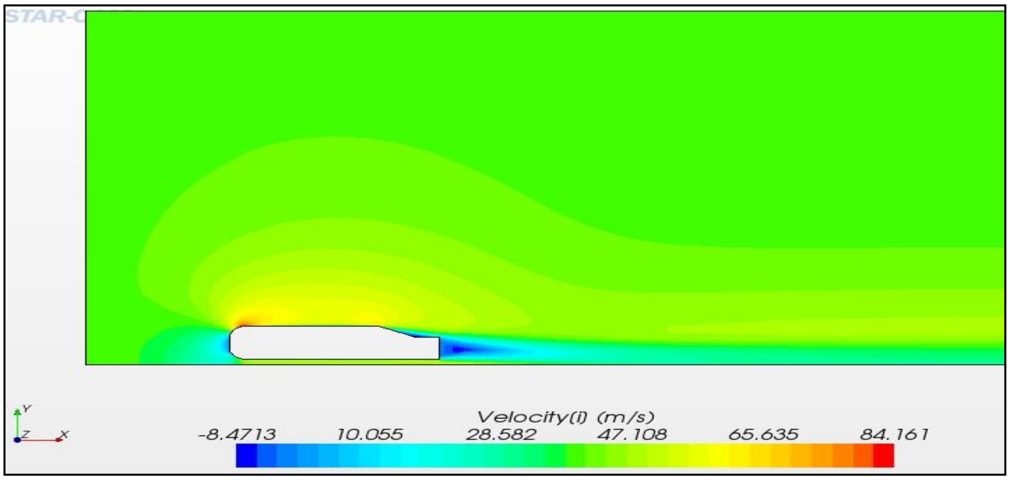

Figure 20. Velocity contour for notchback.

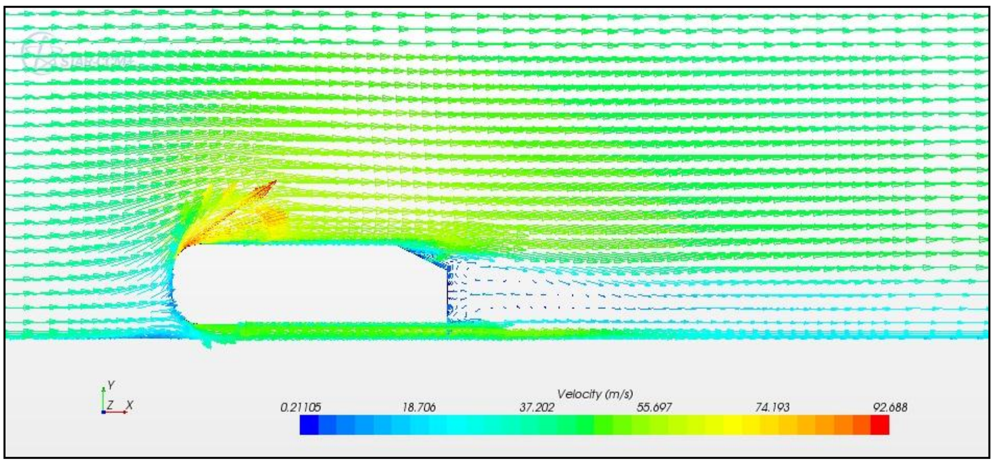

Figure 21. Velocity vectors for fastback.

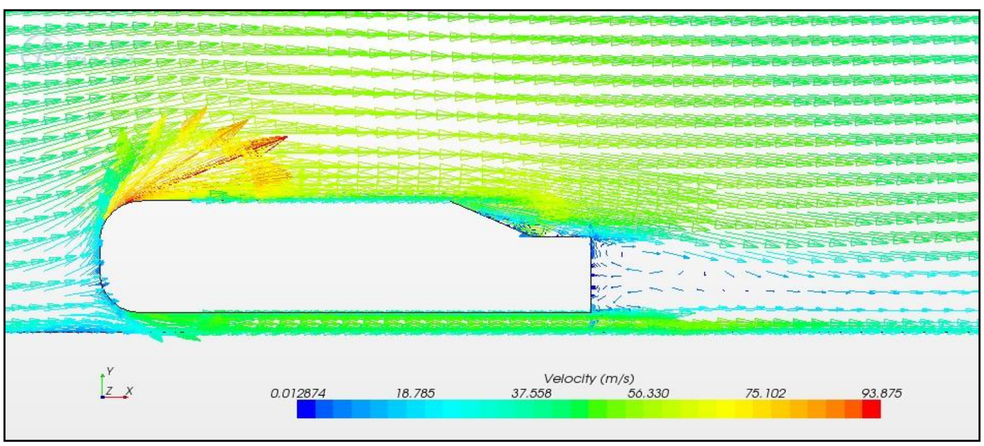

Figure 22. Velocity vector for notchback.

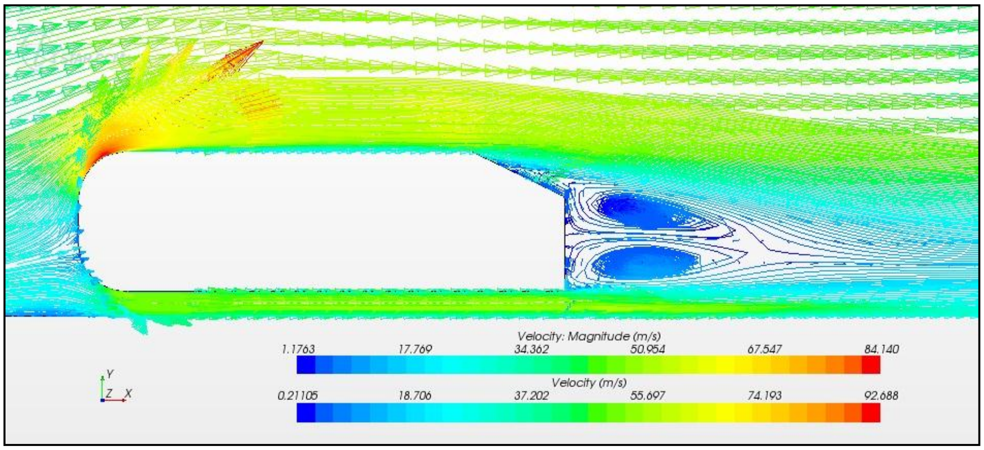

Figure 23. Velocity magnitude for fastback.

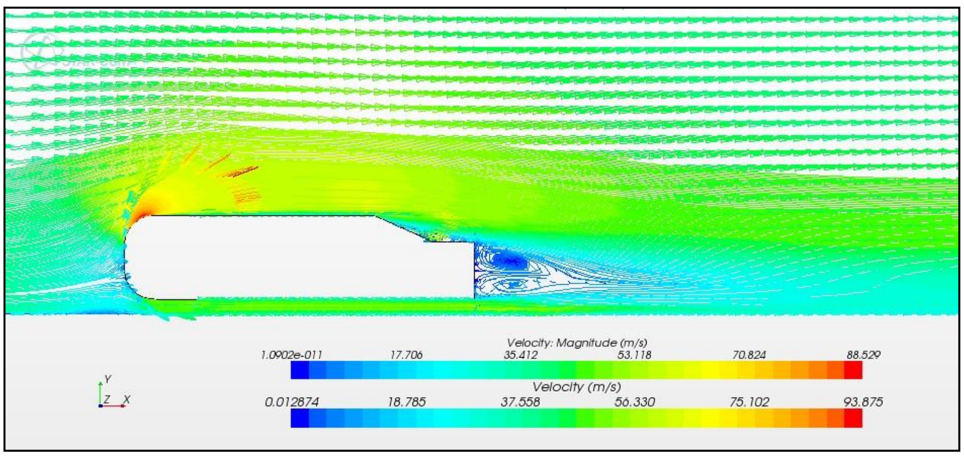

Figure 24. Velocity magnitude for notchback.

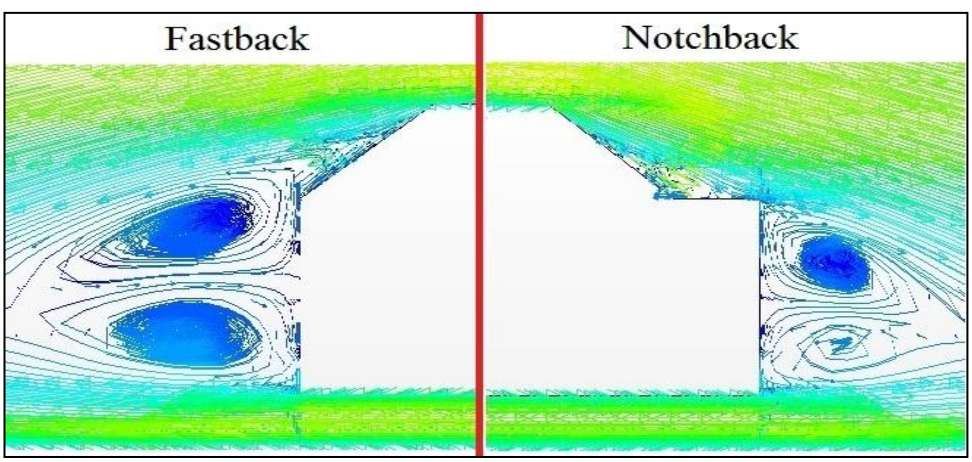

Figure 25. Comparing the wake region between the fastback and the notchback.

Sliding Mode Vibration Suppression Control Design for a Smart Beam

Mohsin N. Hamzah
Assistant Professor
University of Technology
Mechanical Engineering Dept.
dr.mohsin@uotechnology.edu.iq

Shibly Ahmed Al-Samarraie
Assistant Professor
University of Technology
Control & Systems Engineering Dept.
60132@uotechnology.edu.iq

Imad Abdulhussein Abdulsahib
Assistant lecturer
University of Technology
Mechanical Engineering Dept.
emad099@yahoo.com

ABSTRACT

Active vibration control is the main problem in different structure. Smart material like piezoelectric make a structure smart, adaptive and self-controlling so, they are effective in active vibration control. In this paper piezoelectric elements are used as sensors and actuators in flexible structures for sensing and actuating purposes, and to control the vibration of a cantilever beam by using sliding mode control. The sliding mode controller (SMC) is designed to attenuate the vibration induced by initial tip displacement which is equal to 15 mm. It is designed based on the balance realization reduction method where three states are selected for the reduced model from the 24^{th} states that describe the cantilever beam according to the FEM. These states are most controllable and observable. The stability and control performance for the proposed SMC are proved using candidate Lyapunov function and the equivalent control concept. The control spillover, which is the sources of instability, is completely avoided as ensured within the control performance proof.

Numerical simulations are preformed to test the vibration attenuation ability of the proposed SMC. For 15 mm initial tip displacement, the piezoelectric actuator was found able to reduce the tip displacement to about (0.2) mm within (2.5 s), while it is equal to (3.5) mm with the open loop case. Moreover, the induced chattering in system response, due to the discontinuous control action, is removed by approximating the signum function by a continuous arctan function. As a result a smoother response are obtained with the same control performance as can be shown in the sliding variable, the control input voltage and the tip displacement plots.

Keywords: Active vibration control, Finite Element, sliding mode control, sliding mode observer, spillover.

تصميم مسيطر منزلق الشكل لتخميد الاهتزازات للعتبة الذكية

محسن نوري حمزة
أستاذ مساعد
الجامعة التكنولوجية
قسم الهندسة الميكانيكية

شبلي احمد السامرائي
أستاذ مساعد
الجامعة التكنولوجية
قسم هندسة السيطرة والنظم

عماد عبد الحسين عبد الصاحب
مدرس مساعد
الجامعة التكنولوجية
قسم الهندسة الميكانيكية

الخلاصة

ان السيطرة على الاهتزازات تعتبر من المشاكل الرئيسية في مختلف الهياكل. تستخدم المواد الذكية مثل المواد الكهروضغطية لجعل الهياكل ذكية، ذاتية السيطرة، وهي فعالة في السيطرة على الاهتزازات. في هذه البحث تم استخدام المواد الكهروضغطية كمتحسسات ومؤثرات في الهيكل المرن ولغرض السيطرة على الاهتزاز للعتبة باستخدام المسيطر المنزلق الشكل. تم تصميم مسيطر المنزلق الشكل والذي من شأنه تخفيف الاهتزاز الناجم عن ازاحة طرف العتبة بمقدار 15 ملم، تم استخدام طريقة (Balance realization) لاختيار نموذج مخفض حيث يكون هذا النموذج أكثر قابلية على السيطرة والتخمين. تم اختيار ثلاثة متغيرات حالة للنموذج المخفض عن النظام الأصلي والذي كان بعدد 24 متغير. هذه المتغيرات الثلاثة التي تم اختيارها هي الأكثر قابلية على السيطرة والتخمين. الاستقرار وفعالية السيطرة للمسيطر (SMC) المقترح تم اثباته باستخدام (Lyapunov function) ومفهوم السيطرة المكافئ. ان تداعيات المسيطر والتي هي من مصادر عدم الاستقرار تم تجنبها بشكل كامل من خلال أداء المسيطر. باستخدام المحاكاة العددية تم اختبار قدرة نظام السيطرة المقترح لتقليل وتخميد الاهتزاز. تم ازاحة طرف العتبة 15 مم، حيث وجد بان المؤثرات (actuator) للمادة الكهرضغطية (piz) قادرة على تقليل الازاحة إلى حوالي 0.2 ملم بعد 2.5 ثانية، في حين أنه يساوي 3.5 ملم في الحالة الحرة. أيضا تم التغلب على ظاهرة التذبذب (chattering) باستخدام دالة التقريب لدالة الإشارة عن طريق دالة ظل الزاوية القوسي ونتيجة لذلك تم الحصول على استجابة أكثر سلاسة وبنفس الأداء للمسيطر كما تم مشاهدته بالنسبة لمخططات السطح المنزلق، فولتية المسيطر وكذلك إزاحة راس العتبة.

الكلمات الرئيسية: السيطرة الفعالة على الاهتزازات، العناصر المحددة، المسيطر المنزلق الشكل، المخمن المنزلق الشكل، التداعيات

1. INTRODUCTION

The increasing demand of high structural performance requirements has led to the developments of smart materials and structures. A smart structure has the capability to respond to change external environment (such as loads, temperature and shape) as well as to change internal environment (such as damage or failure).This technology has numerous applications, such as active vibration and buckling control, shape control, damage assessment and active noise control. The development of these smart or structures offer great potential or use in advanced aerospace, hydrospace, nuclear, and automotive structural applications, **Bandyopadhyay, 2005**.

The system is called a smart structure because it has the ability to perform self-controlling. One way of making the structure as smart is done by the use of piezoelectric materials. The technology of smart materials and structures especially piezoelectric smart structures has become mature over the last decade. The application of piezoelectric smart structures is the control and suppression of unwanted structural vibrations, **Balamurugan, 2000**.

The main advantages of piezoelectric actuators are fast response, high power density and large force output. Piezoelectric materials can be effectively used for active vibration control with fast response and easy implementation. The electricity for the piezoelectric is produced by pressure (Direct Effect) Conversely, a piezoelectric material deforms when it is subjected to an electric field (Converse Effect). The piezoelectric sensor senses the external disturbances and generates voltage due to direct piezoelectric effect while piezoelectric actuator produces force due to converse piezoelectric effect which can be used as controlling force**, Kumar, et al., 2014.**

To simulate the behavior of mechanical structures under inertia and external loads, very few analytical solutions for specific situations are available. For this reason, the discretization of these structures is the basic step for a static and dynamic further analysis. One possibility for this step is provided by the finite element method. In mathematical terms, finite elements are a numerical method for solving systems, and generally used to eliminate all spatial derivatives by increasing, at the same time, the number of the resulting new equations in the system, **Sachs, 2004.**

The structure is modeled to retain large number of degrees of freedoms. In active vibration control, the use of smaller order model has computational advantages. Therefore, it is necessary to apply a model reduction techniques in order to get a reduced model size for which the control law can be designed. One of these techniques is based on balance realization method, **Inman,**

2006. For closed-loop system, it is not always possible to get a control law that causes eigenvalues to have the required and desired values. This problem raises the concept of controllability. The system is completely controllable if every state variable can be affected in such a way as to cause it to reach a particular value within a finite amount of time by some unbounded control. Then more useful measure is provided for asymptotically stable systems of the form given by equations by defining the controllability gramian. Gramian matrices can be used for checking if a system is controllable and observable, **Zhou, et al., 1999**.

To control vibration of a piezoelectric smart structure, a controller usually designed based on a reduced order model (ROM) of the system form; whereas, finite element models inevitably have a large number of degrees of freedom. When such a ROM based controller is applied to the full order system, actuator forces for reducing the vibration of the lower modes will also influence the residual modes of the structure and produce undesirable vibration due to the un-modeled dynamics. This phenomenon is known as control spillover**, Meirovitch, 1990**. Spillover phenomenon occurs because the unmodeled dynamics, which are not included in reduce order model, will be excited. Different control techniques have been suggested and investigated in the control of smart structure. Some of these studies are linear quadratic regulator (LQR) approach, **Dorf, 2003**, sliding mode control, **Utkin, et al., 2009**, H_2 control, H_∞ control, **Oveisi and Nestorović, 2014.**

The sliding mode control method, first proposed in the early fifties, is one of the control design methods to dominate the uncertainties and disturbances acting on the systems. It is been obtained as significant research attention since early sixties in the former USSR and has been widely applied in a variety of applications, **Bartolini, 2003, Biswas, 2009, Qaiser, 2009.** Sliding mode control (SMC) is a particular type of the so-called Variable Structure Control (VSC) that changes the control direction to drive the system to a specified manifold in the state space and then keep the system within a neighborhood of this manifold. Sliding mode control is designed a controller such that the motion of the system tends to slide mode surface. Therefore designing a SMC consists of two stages; finding a sliding surface (defined as a desired linear combination of system states such as displacement, velocity, and acceleration) to stabilize the controlled system, and find a control force to drive the response trajectory into the sliding surface with an exponential speed in time, **Itik and Salamci, 2005**.

The main feature of sliding mode control is its insensitivity to some class of uncertainties, which makes it attractive in the control applications for uncertain systems. The sliding mode control method has some advantages such as robustness to parameter uncertainty, insensitivity to bounded disturbances, fast dynamic response, and easy implementation of the controller, **Magnani, 2007, Ferrara and Vecchio, 2009,** and **Capisani, 2009**. The method enables the decoupling of overall system motion into independent partial components of low dimension and as a result reduces the complexity of feedback design Sliding mode theory has been recognized as a robust control approach in treating disturbances and modeling uncertainties through the concepts of sliding surface design and equivalent control, **Utkin, et al., 2009**.

The aim of the present paper is to design sliding mode control to attenuate the vibration of a smart cantilever beam using piezoelectric element. The model utilized for control design purpose is the reduced order model that is obtained according to the balance realization method. Based on the equivalent control the performance of the proposed SMC is ensured via satisfying the control performance condition. Consequently the control spillover is eliminated by satisfying this condition.

2. SMART CANTILEVER SYSTEM MODEL

The model of cantilever flexible beam studied here is given in **Fig.1.** The cantilever beam bonded with the same place pair of piezoelectric sensor / actuator near the fixed end. By using the Euler-Bernoulli beam equation, the infinite dimensional mathematical expression of the beam can be written as follows, **Bandyopadhyay, 2007**.

$$c^2 \frac{\partial^4 w(x,t)}{\partial x^4} + \frac{\partial^2 w(x,t)}{\partial t^2} = 0, \tag{1}$$

where $c^2 = EI/\rho \mathrm{A}$, $w(x,t)$ is the deflection along the x-axis, E is the Young's modulus, I is the moment of inertia, A is the cross sectional area, and ρ is the density of the beam. The partial differential equation (PDE) given by Eq. (1) can be solved by using the supposed mode approach, which yields finite dimensional ordinary differential equation set.

The dynamic equation of the smart structure is obtained by using both regular beam element and piezoelectric beam elements. The mass and stiffness matrices of the smart structure include sensor/actuator mass and stiffness, **Chhabra, et al., 2012**. The entire structure is modelled in state space form using the Finite Element Method (FEM) by dividing the structure into six equal finite elements. The sensor and actuator were integrated on the top and bottom surfaces at the second element from the fixed end of the beam. A beam element is considered with two nodes at its end. Each node having two degree of freedom (DOF) (translation and rotation) is considered. The mass and stiffness matrix is derived using shape functions for the beam element. When a system vibrates, it undergoes back and forth motion, it has transverse displacements, so all positions vary with time, and therefore, the system has velocities and accelerations. The equation of motion, involves a fourth order derivative w.r.t.(x) and a second order derivative w.r.t. time (acceleration) The solution of the Eq. (1) is assumed as a cubic polynomial function of (x) given by:

$$w(x) = a_1 + a_2 x + a_3 x^2 + a_4 x^3 \tag{2}$$

where $w(x)$ is displacement function which satisfies the fourth order partial differential equation (1). The constants a_1 to a_4 are obtained by using the boundary conditions given below at both the nodal points (fixed end and free end). Consider the derivative of $w(x)$ as:

$$\frac{\partial w}{\partial x} = a_2 + 2a_3 x + 3a_4 x^2 \tag{3}$$

then at $x = 0$, $w(x) = a_1 = w_1$ and $\frac{\partial w}{\partial x} = a_2 = \theta_1$. Also at $x = l$,
$w(x) = w_2 = a_1 + a_2 l + a_3 l^2 + a_4 l^3$, and $\frac{\partial w}{\partial x} = \theta_2 = a_2 + 2a_3 l + 3a_4 l^2$

where $w_1, \theta_1, w_2, \theta_2$ are Degree of Freedom at node 1 and 2, respectively and l is the length of the regular beam. The relation between $w_1, \theta_1, w_2, \theta_2$ and the constants a_1 to a_4 is represented in a matrix form as,

$$\begin{bmatrix} w_1 \\ \theta_1 \\ w_2 \\ \theta_2 \end{bmatrix} = \begin{bmatrix} 1 & 0 & 0 & 0 \\ 0 & 1 & 0 & 0 \\ 1 & l & l^2 & l^3 \\ 0 & 1 & 2l & 3l^2 \end{bmatrix} \begin{bmatrix} a_1 \\ a_2 \\ a_3 \\ a_4 \end{bmatrix} \tag{4}$$

Solving for a_1 to a_4 yields;

$$\begin{bmatrix} a_1 \\ a_2 \\ a_3 \\ a_4 \end{bmatrix} = \begin{bmatrix} 1 & 0 & 0 & 0 \\ 0 & 1 & 0 & 0 \\ -\frac{3}{l^2} & -\frac{2}{l} & \frac{3}{l^2} & -\frac{1}{l} \\ \frac{2}{l^3} & \frac{1}{l^2} & -\frac{2}{l^3} & \frac{1}{l^2} \end{bmatrix} \begin{bmatrix} w_1 \\ \theta_1 \\ w_2 \\ \theta_2 \end{bmatrix} = \frac{1}{l^3} \begin{bmatrix} l^3 & 0 & 0 & 0 \\ 0 & l^3 & 0 & 0 \\ -3l & -2l^2 & 3l & -l^2 \\ 2 & l & -2 & l \end{bmatrix} \begin{bmatrix} w_1 \\ \theta_1 \\ w_2 \\ \theta_2 \end{bmatrix} \tag{5}$$

Substituting the constants obtained from (5) into (2) and by rearranging the terms, the final form for $w(x)$ is obtained as:

$$w\,(x) = \frac{1}{l^3}\ [\,(\,l^3 - 3lx^2 + 2x^3)\ \ (\,l^3x - 2l^2x^2 + \ x^3l)\ \ (\,3lx^2 - 2x^3\,)\ \ (\,-l^2x^2 + lx^3\,)] \begin{bmatrix} w_1 \\ \theta_1 \\ w_2 \\ \theta_2 \end{bmatrix} \tag{6}$$

or $\quad w\,(x) = \ N^T\, q \qquad (7)$

where N is the shape function and q is the displacements at the nodes, which are given by

$$N = \frac{1}{l^3}\ [\,(\,l^3 - 3lx^2 + 2x^3)\ \ (\,l^3x - 2l^2x^2 + \ x^3l)\,(\,3lx^2 - 2x^3\,)\,(\,-l^2x^2 + lx^3\,)]^T \tag{8}$$

$$q = \ [w_1\ \theta_1\, w_2\ \theta_2\,]^T \tag{9}$$

The strain energy U and the kinetic energy T for the beam element with uniform cross section in bending is obtained as:

$$U = \frac{E_b\, I_b}{2} \int_{l_b} \left[\frac{\partial^2 w}{\partial x^2}\right]^2 dx \quad = \frac{E_b I_b}{2} \int_{l_b} [w''\,(x\,,t\,)]^{\,T}\ \ [w''(x\,,t\,)]\, dx \tag{10}$$

$$T = \frac{\rho_b A_b}{2} \int_{l_b} \left[\frac{\partial\, w}{\partial t}\right]^2 dx \quad = \frac{\rho_b A_b}{2} \int_{l_b} [\dot{w}\,(x\,,t\,)]^{\,T}\ [\dot{w}(x\,,t\,)]\, dx \tag{11}$$

where ρ_b is the mass density of the beam material, A_b is the cross sectional area of the beam, I_b is the moment of inertia of the beam, and E_b is the modulus of elasticity of the beam material. The equation of motion of the regular beam element is obtained by using the Lagrangian equation:

$$\frac{d}{dt}\left[\frac{\partial\, T}{\partial \dot{q}_i}\right] + \left[\frac{\partial\, U}{\partial q_i}\right] = [F_i] \tag{12}$$

For free vibration, $F_i = 0$. The strain energy U and the kinetic energy T in terms of the shape function N and q are

$$T = \frac{\rho_b A_b}{2} \int_{l_b} [N^T \dot{q}]^T [N^T \dot{q}]\, dx = \frac{\rho_b A_b}{2} \int_{l_b} \dot{q}^T N N^T \dot{q}\, dx$$
$$= \dot{q}^T \left(\frac{\rho_b A_b}{2} \int_{l_b} N N^T dx \right) \dot{q} = \frac{1}{2} \dot{q}^T M_b \dot{q} \qquad (13)$$

Accordingly

$$\frac{\partial T}{\partial \dot{q}_i} = M_b \dot{q} \qquad (14)$$

$$\frac{d}{dt} \left[\frac{\partial T}{\partial \dot{q}_i} \right] = M_b\, \ddot{q} \qquad (15)$$

where M_b is the mass matrix of regular beam

$$M_b = \rho_b A_b \int_{l_b} N N^T dx = \frac{\rho_b A_b l_b}{420} \begin{bmatrix} 156 & 22l_b & 54 & -13l_b \\ 22l_b & 4l_b^2 & 13l_b & -3l_b^2 \\ 54 & 13l_b & 156 & -22l_b \\ -13l_b & -3l_b^2 & -22l_b & 4l_b^2 \end{bmatrix} \qquad (16)$$

Also for the strain energy,

$$U = \frac{E_b I_b}{2} \int_{l_b} [N_2^T\, q]^T [N_2^T\, q]\, dx = \frac{E_b I_b}{2} \int_{l_b} q^T N_2 .\, N_2^T q\, dx$$
$$= q^T \left(\frac{E_b I_b}{2} \int_{l_b} N_2 N_2^T\, dx \right) q = \frac{1}{2}\, q^T K_b\, q \qquad (17)$$

one can obtain

$$\left[\frac{\partial U}{\partial q_i} \right] = K_b\, q \qquad (18)$$

$$K_b = E_b I_b \int_{l_b} N_2 N_2^T\, dx \qquad (19)$$

where K_b is the stiffeness matrix of regular beam

$$K_b = E_b I_b \int_{l_b} N_2 N_2^T\, dx = \frac{E_b I_b}{l^3} \begin{bmatrix} 12 & 6l & -12 & 6l \\ 6l & 4l^2 & -6l & 2l^2 \\ -12 & -6l & 12 & -6l \\ 6l & 2l^2 & -6l & 4l^2 \end{bmatrix} \qquad (20)$$

Eventually the equation of motion according to the Lagrangian equation is:

$$M_b\, \ddot{q} + K_b q = f_b \qquad (21)$$

or

$$\frac{\rho_b A_b}{420}\begin{bmatrix}156 & 22l_b & 54 & -13l_b\\ 22l_b & 4l_b^2 & 13l_b & -3l_b^2\\ 54 & 13l_b & 156 & -22l_b\\ -13l_b & -3l_b^2 & -22l_b & 4l_b^2\end{bmatrix}\begin{bmatrix}\ddot{w}_1\\ \ddot{\theta}_1\\ \ddot{w}_2\\ \ddot{\theta}_2\end{bmatrix} + \frac{E_b\, I_b}{l^3}\begin{bmatrix}12 & 6l_b & -12 & 6l_b\\ 6l_b & 4l_b^2 & -6l_b & 2l_b^2\\ -12 & -6l_b & 12 & -6l_b\\ 6l_b & 2l_b^2 & -6l_b & 4l_b^2\end{bmatrix}\begin{bmatrix}w_1\\ \theta_1\\ w_2\\ \theta_2\end{bmatrix} = \begin{bmatrix}F_1\\ M_1\\ F_2\\ M_2\end{bmatrix} \quad (22)$$

where F_1 , F_2, M_1, M_2 are the forces and the bending moments acting on nodes 1 and 2 respectively **Fig.1**. When PZT patches are assumed as Euler-Bernoulli beam elements the elemental mass and stiffness matrices of PZT beam element can be computed in similar fashion as**, Bandyopadhyay, 2007**.

$$M_b = \frac{\rho_p A_p l_p}{420}\begin{bmatrix}156 & 22l_p & 54 & -13l_p\\ 22l_p & 4l_p^2 & 13l_p & -3l_p^2\\ 54 & 13l_p & 156 & -22l_p\\ -13l_p & -3l_p^2 & -22l_p & 4l_p^2\end{bmatrix} \quad (23)$$

$$K_b = \frac{E_p\, I_p}{l^3}\begin{bmatrix}12 & 6l_p & -12 & 6l_p\\ 6l_p & 4l_p^2 & -6l_p & 2l_p^2\\ -12 & -6l_p & 12 & -6l_p\\ 6l_p & 2l_p^2 & -6l_p & 4l_p^2\end{bmatrix} \quad (24)$$

The smart beam element is obtained by sandwiching the regular beam element in between the two PZT patches **Fig. 1**.
In which $EI = E_b\, I_b + 2E_p\, I_p$ is the flexural rigidity and $\rho\mathrm{A} = b(\rho_b t_b + 2\rho_p t_p)$ is the mass per unit length of smart beam element, t_p is the thickness of PZT patches thickness of Actuator and Sensor, and $I_p = \frac{b\, t_a^3}{12} + bt_a\left(\frac{t_a+t_b}{2}\right)^2$. So the elemental mass and stiffness matrices of smart beam element are:

$$M_e = \frac{\rho\,\mathrm{A}\, l_b}{420}\begin{bmatrix}156 & 22l_b & 54 & -13l_b\\ 22l_b & 4l_b^2 & 13l_b & -3l_b^2\\ 54 & 13l_b & 156 & -22l_b\\ -13l_b & -3l_b^2 & -22l_b & 4l_b^2\end{bmatrix} \quad (25)$$

$$K_e = \frac{E\,I}{{l_p}^3}\begin{bmatrix}12 & 6l_b & -12 & 6l_b\\ 6l_b & 4l_b^2 & -6l_p & 2l_b^2\\ -12 & -6l_b & 12 & -6l_b\\ 6l_b & 2l_b^2 & -6l_b & 4l_b^2\end{bmatrix} \quad (26)$$

2.1 Sensor and Actuator Equations

The sensor equation is derived from the direct piezoelectric equation, which is used to calculate the total charge created by the strain in the structure. Piezoelectric materials can be used as strain rate sensors. When used so, the output charge can be transformed into the sensor current $i(t)$, **Bandyopadhyay, 2007**.

$$i\,(t) = z\, e_{31}\, b \int_{x_i}^{x_i+l_b} N_2{}^T \dot{q}\, dx \tag{27}$$

where, z = $\frac{t_b}{2} + t_a$ and N_2 is the second spatial derivative of the shape function, e_{31} is the piezoelectric stress constant.

The output current of the piezoelectric sensor measures the moment rate of the flexible beam. This current is converted into the open circuit sensor voltage $V_s(t)$ using a signal-conditioning device with the gain G_c**, Bandyopadhyay, 2007**.

$$V_s(t) = [\,0 \quad -G_c z\, e_{31}\, b \quad 0 \quad G_c\, z\, e_{31}\, b\,] \begin{bmatrix} \dot{w}_1 \\ \dot{\theta}_1 \\ \dot{w}_2 \\ \dot{\theta}_2 \end{bmatrix} = Sc\,[\,0 \quad -1 \quad 0 \quad 1] \begin{bmatrix} \dot{w}_1 \\ \dot{\theta}_1 \\ \dot{w}_2 \\ \dot{\theta}_2 \end{bmatrix} = p^T \dot{q} \tag{28}$$

where $S_c = G_c\, z\, e_{31}\, b$ and p is a constant vector depends on the type of sensor, its characteristics and its location on the beam. The actuator equation is derived from the converse piezoelectric equation. The strain developed ϵ_x by the electric field E_f on the actuator layer is given by, **Jalili, 2010.**

$$\epsilon = dE_f \tag{29}$$

where, $E_f = \frac{V_a(t)}{t_a}$ is the electric field, and $V_a(t)$ is the input voltage applied to the piezoelectric actuator in the thickness direction t_a. Then the stress σ_a that developed by the actuator is given by**, Bandyopadhyay, 2007**.

$$\sigma_a = E_p\, d_{31} \left(\frac{V_a\,(t)}{t_a}\right) \tag{30}$$

where E_p is the Young's modulus of the piezoelectric and d_{31} is piezoelectric strain constant.
The bending moment in a small cross section of the piezoelectric element is given by:

$$dM_a = E_p\, I_p\, \frac{d^2 w}{dx^2} \tag{31}$$

The resultant moment M_a acting on the beam element due to the applied voltage V_a is determined by integrating the stress in Eq. (30) throughout the structure thickness as:

$$M_a = E_p\, d_{31} z\, V_a(t) \tag{32}$$

The control force f_{ctrl} produced by the actuator that is applied on the beam element is obtained as**, Bandyopadhyay, 2007**.

$$f_{ctrl} = E_p d_{31} b\, z\, [\, -1\ 0\ 1\ 0\,]^T\, V_a(t) \tag{33}$$

Alternatively, f_{ctrl} can be expressed as:

$$f_{ctrl} = h\, V_a\, (t) \tag{34}$$

where,

$$h = E_p\, d_{31}\, b\, z\, [\, -1\ 0\ 1\ 0\,]^{\mathrm{T}} \tag{35}$$

3. DYNAMIC EQUATION OF SMART STRUCTURE

The dynamic equation of the smart structure is obtained by using both the regular and piezoelectric beam elements (local matrices) given by Eq. (25) and Eq. (26). The mass and stiffness of the bonding or the adhesive between the master structure and the sensor / actuator pair is neglected. The mass and stiffness of the entire beam, which is divided into six finite elements with the piezo-patches placed at only one discrete location is assembled using the FEM technique and the assembled matrices (global matrices) M and K are obtained. The equation of motion of the smart structure is given by**, Bandyopadhyay, 2007**.

$$M\ddot{q} + Kq = f_{ext} + f_{ctrl} = f \tag{36}$$

where M, K, f_{ext}, f_{ctrl} and f are the global mass matrix, global stiffness matrix of the smart beam, the external force applied to the beam, the controlling force from the actuator and the total force coefficient vector respectively.
The generalized structural modal damping matrix D is introduced into Eq. (36) by using**, Balamurugan and Narayanan, 2000, Clough, 2007.**

$$D = \alpha M + \beta K \tag{37}$$

where α and β are the frictional damping constant and the structural damping constant respectively. When applying the cantilever beam boundary condition, the system equation of motion for the 6-element cantilever beam is:

$$M\,\ddot{q} + D\dot{q} + Kq = f \tag{38}$$

For free vibration condition f_{ext} equal to zero, so the remaining applied force on the system is the controlling force f_{ctrl} exerted by the controller.

3.1 State Space Model of the Smart Structure

Many design tools and model reduction in modern control theory need a state space form for the mathematical model of a plant. Consequently, the smart flexible cantilever beam mathematical model can be written in state space form as follows;

Let $q = \begin{bmatrix} q_1 \\ q_2 \end{bmatrix} = \begin{bmatrix} x_1 \\ x_2 \end{bmatrix} = x$, $\dot{q} = \begin{bmatrix} \dot{q}_1 \\ \dot{q}_2 \end{bmatrix} = \begin{bmatrix} \dot{x}_1 \\ \dot{x}_2 \end{bmatrix} = \begin{bmatrix} x_3 \\ x_4 \end{bmatrix}$, and $\ddot{q} = \begin{bmatrix} \dot{x}_3 \\ \dot{x}_4 \end{bmatrix}$ then the 6-element smart cvantilever beam sate space model is;

$$M \begin{bmatrix} \dot{x}_3 \\ \dot{x}_4 \end{bmatrix} + D \begin{bmatrix} x_3 \\ x_4 \end{bmatrix} + K \begin{bmatrix} x_1 \\ x_2 \end{bmatrix} = f_{ctrl} \tag{39}$$

which yields

$$\begin{bmatrix} \dot{x}_3 \\ \dot{x}_4 \end{bmatrix} = -M^{-1} D \begin{bmatrix} x_3 \\ x_4 \end{bmatrix} - M^{-1} K \begin{bmatrix} x_1 \\ x_2 \end{bmatrix} + M^{-1} h\, V_a(t) \tag{40}$$

or

$$\begin{bmatrix} \dot{x}_1 \\ \dot{x}_2 \\ \dot{x}_3 \\ \dot{x}_4 \end{bmatrix} = \begin{bmatrix} 0 & I \\ -M^{-1} K & -M^{-1} D \end{bmatrix} \begin{bmatrix} x_1 \\ x_2 \\ x_3 \\ x_4 \end{bmatrix} + \begin{bmatrix} 0 \\ M^{-1} h \end{bmatrix} V_a(t) \tag{41}$$

And in a matrix form

$$\dot{x} = Ax(t) + Bu(t) \tag{42}$$

where $x = \begin{bmatrix} x_1 \\ x_2 \\ x_3 \\ x_4 \end{bmatrix}$, $A = \begin{bmatrix} 0 & I \\ -M^{-1} K & -M^{-1} D \end{bmatrix}$, $B = \begin{bmatrix} 0 \\ M^{-1} h \end{bmatrix}$ and $u(t) = V_a(t)$.

with approperate zero and identity matrices dimensions. The sensor voltage is taken as the output of the system and the output equation is obtained as:

$$y(t) = V_s(t) = p^T \dot{q} = p^T \begin{bmatrix} x_3 \\ x_4 \end{bmatrix} \tag{43}$$

Thus, the sensor output equation in state space form is given by:

$$y(t) = [0 \quad p^T] \begin{bmatrix} x_1 \\ x_2 \\ x_3 \\ x_4 \end{bmatrix} \tag{44}$$

or,

$$y(t) = Cx(t) \tag{45}$$

where $C = [0 \quad p^T]$. The single input single output state space model (state equation and the output equation) of the smart structure developed for the system is given by Eqs. (42) and (45):

$$\left.\begin{aligned} \dot{x} &= Ax(t) + Bu(t) \\ y &= Cx(t) \end{aligned}\right\} \tag{46}$$

With

$$\left.\begin{aligned} A &= \begin{bmatrix} 0 & I \\ -M^{-1}\,K & -M^{-1}\,D \end{bmatrix}_{24*24} \\ B &= \begin{bmatrix} 0 \\ M^{-1}h \end{bmatrix}_{24*1} \\ C &= \begin{bmatrix} 0 & p^{T} \end{bmatrix}_{1*24} \end{aligned}\right\} \tag{47}$$

In the following section, the state space model is reduced via balance realization to a form and dimension more appropriate for controller and observer design.

3.2 Model Reduction

In the finite element modeling, the structure is modeled to retain large number of degrees of freedoms. In active vibration control, the use of smaller order model has computational advantages. Therefore, it is necessary to apply a model reduction technique to the state space representation. The reduced order system model extraction techniques solve the problem of the complexity by keeping the essential properties of the full model only**, Inman, 2006**. For the present work the 24th order system model obtained from the finite element model is reduced to the three order using a model reduction technique based on balance realization. The approach taken for reduction the order of a given model based on deleting the coordinates, or modes, that are the least controllable and observable. To implement this idea, a measure of the degree of controllability and observability is needed. However, an alternative, more useful measure is provided for asymptotically stable systems of the form given by equations by defining the controllability grammian, denoted by W_C, as

$$W_C^2 = \int_0^{\infty} e^{At}\, BB^T e^{A^T t} dt \tag{48}$$

And the observability grammian, denoted by W_O, as **, Inman, 2006**.

$$W_O^2 = \int_0^{\infty} e^{A^T t}\, C^T C e^{At} dt \tag{49}$$

The matrices A, B, and C defined as in Eq. (47). The properties of these matrices provide useful information about the controllability and observability of the closed-loop system. If the system is controllable (or observable), the matrix W_C (or W_O) is nonsingular**, Williams and Lawrence, 2007.** These grammians characterize the degree of controllability and observability by quantifying just how far away from being singular the matrices W_C and W_O are**, Janardhanan, 2013.**

Applying the idea of singular values as a measure of rank deficiency to the controllability and observability grammians yields a systematic model reduction method. The matrices W_C and W_O are symmetric and hence are similar to a diagonal matrix. There is equivalent system for which these two grammians are both equal and diagonal. Such a system is called balanced system, also W_C and W_O must satisfy the two Liapunov-type equations:

$$\left.\begin{array}{l} A\,W_C^2 + W_C^2\,A^T = -BB^T \\ A^T\,W_O^2 + W_O^2\,A = -C^T C \end{array}\right\} \tag{50}$$

Now to transform the system to a balance realization form, this requires the determination of a transformation matrix P that will transform the system in Eq. (46) to:

$$\left.\begin{array}{l} \dot{x}' = A'x' + B'u \\ y = C'x' + Du \end{array}\right\} \tag{51}$$

where $A' = P^{-1}AP$, $B' = P^{-1}B$ and $C' = CP$. The controllability and observability grammians matrices are diagonal and equal to

$$\widehat{W}_C = \widehat{W}_O = \Sigma = diag(\sigma_1, \sigma_2, \dots \dots, \sigma_n)$$

where $\widehat{W}_C$ and $\widehat{W}_O$ are the controllability and observability grammians for system after applying the transformation P and the numbers σ_i are the singular values of the grammians and are ordered such that, $\sigma_i > \sigma_{i+1}$, $i = 1,2, \dots\dots, n$
Therefore the pair (A', B') could be uncontrollable pair since some of σ_j could be equal to zero. Indeed there exists a subsystem (i.e., a reduced order model) which is still controllable and observable.

Now the choice

$$P = G^{-1}U\Sigma^{\frac{1}{2}} \tag{52}$$

will transform the grammians W_c^2 and W_O^2 to become equal and transform the system in Eq. (46) to a balanced realization form. Namely,

$$\widehat{W}_C = \widehat{W}_o = \Sigma \tag{53}$$

where Σ can be written in terms of two set of the singular values $\sigma_{(1)}$ and $\sigma_{(2)}$ as

$$\Sigma = \begin{bmatrix} \sigma_{(1)} & 0 \\ 0 & \sigma_{(2)} \end{bmatrix} \tag{54}$$

In this representation $\sigma_{(1)}$ describes the "strong" sub-systems to be retained and $\sigma_{(2)}$ the "weak" sub-systems to be deleted. Conformally partitioning the matrices as

$$\left.\begin{array}{l} A' = \begin{bmatrix} A_{11} & A_{12} \\ A_{21} & A_{22} \end{bmatrix} \\ B' = \begin{bmatrix} B_1 \\ B_2 \end{bmatrix} \\ C' = \begin{bmatrix} C_1 & C_2 \end{bmatrix} \end{array}\right\} \tag{55}$$

and truncating the model, retaining $A_{1r} = A_{11}$, $B_r = B_1$ and $C_r = C_1$ as the reduced system, and deleting the "weak" internal subsystems**, Inman, 2006.**

4. SLIDING MODE CONTROL DESIGN

This section is devoted to design a sliding mode controller to the smart cantilever beam using its reduced order model. The sliding mode control approach is recognized as one of the efficient tools to design robust controllers for complex high-order nonlinear dynamical systems which are operating under parameter's uncertainty or in presence of disturbance inputs**, Al-khazraji and Hamzaoui, 2006**. Sliding mode theory has been recognized as a robust control approach in treating disturbances and modeling uncertainties through the concepts of sliding surface design and equivalent control. The equivalent control method means replacement of discontinuous control on the intersection of switching surfaces by a continuous one such that the state velocity vector lies in the tangential manifold**, Utkin, et al., 2009.**

The major advantage of the sliding mode control design approach is the low sensitivity to the system model parametric variations and disturbances which eliminates the necessity of exact modeling**, Bandyopadhyay, 2005.** The sliding mode design method consists of two steps. The first step, a sliding surface is designed so that the state trajectory of the plant forced to the required surface, and the second step is to design a control law such that the system remains on the sliding surface. Therefore, the design of SMC includes the determination of sliding surface and controller design**, Balamurugan and S. Narayanan, 2000.**

To design a sliding mode control to the reduced order model of the smart beam the Reduced Model (RM) and the Residual Model (RSM)**, Dorf, 2003.** are presented here as follows; according to the balance realization the linear state model for the cantilever beam, as given in Eq. (51) are rewritten as follow;

$$\left.\begin{aligned}\dot{x}_r &= A_{1r}x_r + A_{1R}x_R + B_1u\\ \dot{x}_R &= A_{2r}x_r + A_{2R}x_R + B_2u\\ y &= C_rx_r + C_Rx_R\end{aligned}\right\} \tag{56}$$

where $x_r \in \mathcal{R}^r$, is the *reduced model states*, $x_R \in \mathcal{R}^{n-r}$ is the *residual model states*, and

$$A = \begin{bmatrix} A_{1r}^{r\times r} & A_{1R}^{r\times(n-r)} \\ A_{2r}^{(n-r)\times r} & A_{2R}^{(n-r)\times(n-r)} \end{bmatrix},$$
$$B = \begin{bmatrix} B_1^{r\times 1} \\ B_2^{(n-r)\times 1} \end{bmatrix},$$
$$C = \begin{bmatrix} C_r^{1\times r} & C_R^{1\times(n-r)} \end{bmatrix}$$

where the pair (A_{1r}, B_1) is a controllable pair with highest controllability and observability grammian. The RM of Eq. (51) from Eq. (56) is

$$\dot{x}_r = A_{1r}x_r + A_{1R}x_R + B_1u \tag{57}$$

In order to design a SMC for the reduced model, and as a first step, it is required to transform Eq. (57) to the so-called Regular Form (RF). The sliding mode control had two-stage design procedure which is the selection a switching manifold and then finding control enforcing sliding mode in this manifold, these two stage becomes simpler for systems in RF. The regular form consists of two blocks; the first block does not depend on control, whereas the dimension of the second block coincides with that of the control**, Utkin, et al., 2009.** The RM is decomposed first to the form;

$$\left.\begin{aligned}\dot{x}_{r1} &= A_{1r11}x_{r1} + A_{1r12}x_{r2} + A_{1R1}x_R + B_{11}u\\ \dot{x}_{r2} &= A_{1r21}x_{r1} + A_{1r22}x_{r2} + A_{1R2}x_R + B_{12}u\end{aligned}\right\} \quad (58)$$

where:

$$x_r = \begin{bmatrix} x_{r1} \\ x_{r2} \end{bmatrix}, x_{r1} \in \mathcal{R}^{r-\alpha}, x_{r2} \in \mathcal{R}^{\alpha}$$

$$A_{1r} = \begin{bmatrix} A_{1r11}^{(r-\alpha)\times(r-\alpha)} & A_{1r12}^{(r-\alpha)\times\alpha} \\ A_{1r21}^{\alpha\times(r-\alpha)} & A_{1r22}^{\alpha\times\alpha} \end{bmatrix}, \quad A_{1R} = \begin{bmatrix} A_{1R1} \\ A_{1R2} \end{bmatrix} \quad \text{and } , B_1 = \begin{bmatrix} B_{11}^{(r-\alpha)\times\alpha} \\ B_{12}^{\alpha\times\alpha} \end{bmatrix}$$

The required transformation matrix to the RF is presented in the following proposition.
Proposition (1) The RM as given in Eq. (58) is transformed to the RF via the following transformation;

$$z = \begin{bmatrix} z_1 \\ z_2 \end{bmatrix} = T_r x_r = \begin{bmatrix} I_{(r-\alpha)} & -B_{11}B_{12}^{-1} \\ O_{\alpha\times(r-\alpha)} & I_\alpha \end{bmatrix} \begin{bmatrix} x_{r1} \\ x_{r2} \end{bmatrix} \quad (59)$$

where I and O are the identity and zero matrices respectively with the matrix size given as the subscript.
Proof: The validity of the transformation T_r can be proved as follows; first it is needed to show that T_r is a nonsingular matrix and then to show that the RM is transformed to the regular form via T_r. The transformation matrix T_r is nonsingular since**, Bernstein,2009.**

$$\begin{aligned}\det(T_r) &= \det \begin{bmatrix} I_{(r-\alpha)} & -B_{11}B_{12}^{-1} \\ O_{\alpha\times(r-\alpha)} & I_\alpha \end{bmatrix} \\ &= \det I_{(r-\alpha)} \det I_\alpha = 1\end{aligned}$$

Secondly, the RM in terms of the new state z is;

$$\dot{z} = T_r A_{1r} T_r^{-1} z + T_r A_{1R} x_R + T_r B_1 u \quad (60)$$

All what it is necessary to prove it is that the control term $T_r B_1 u$ doesn't appear in $\dot{z}_1$. Namely;

$$T_r B_1 = \begin{bmatrix} I_{(r-\alpha)} & -B_{11}B_{12}^{-1} \\ O_{\alpha\times(r-\alpha)} & I_\alpha \end{bmatrix} \begin{bmatrix} B_{11} \\ B_{12} \end{bmatrix} = \begin{bmatrix} O_{(r-\alpha)\times\alpha} \\ \hat{B}_{12} \end{bmatrix}$$

Accordingly the RM dynamics becomes (The RF model);

$$\left.\begin{aligned}\dot{z}_1 &= \hat{A}_{r11}z_1 + \hat{A}_{r12}z_2 + \hat{A}_{R1}x_R \\ \dot{z}_2 &= \hat{A}_{r21}z_1 + \hat{A}_{r22}z_2 + \hat{A}_{R2}x_R + \hat{B}_{12}u\end{aligned}\right\} \quad (61)$$

Where

$\hat{A}_{1r} = T_r A_{1r} T_r^{-1} = \begin{bmatrix} \hat{A}_{r11} & \hat{A}_{r12} \\ \hat{A}_{r21} & \hat{A}_{r22} \end{bmatrix}$, and

$\hat{A}_{1R} = T_r A_{1R} = \begin{bmatrix} \hat{A}_{R1} \\ \hat{A}_{R2} \end{bmatrix}$

Remark 1: By considering the transformation matrix T_r, which it is devoted to the RM state only, one can easily find the overall **non-singular** transformation matrix to system model state x (Eq. (51)) in the form

$$\hat{x} = \begin{bmatrix} z_1 \\ z_2 \\ x_R \end{bmatrix} = T_{rT} x = \begin{bmatrix} T_r^{r\times r} & O_{r\times(n-r)} \\ O_{(n-r)\times r} & I_{(n-r)\times(n-r)} \end{bmatrix} x \tag{62}$$

And accordingly Eq. (51) is transformed to

$\dot{\hat{x}} = T_{rT} A T_{rT}^{-1} \hat{x} + T_{rT} B u$

Or

$$\left.\begin{aligned} \dot{z}_1 &= \hat{A}_{r11} z_1 + \hat{A}_{r12} z_2 + \hat{A}_{R1} x_R \\ \dot{z}_2 &= \hat{A}_{r21} z_1 + \hat{A}_{r22} z_2 + \hat{A}_{R2} x_R + B_{12} u \\ \dot{x}_R &= \hat{A}_{r31} z_1 + \hat{A}_{r32} z_2 + \hat{A}_{R3} x_R + B_2 u \end{aligned}\right\} \tag{63}$$

Equation (63) can be named as the Total Regular Form (TRF) model where the RF model (Eq. (61)) is the upper part of it.

Note (1) that $\det(T_{rT}) = \det(T_r) = 1$ and the total transformation from x to $\hat{x}$ is

$$\hat{x} = T_{rT} T_o x = T x \tag{64}$$

where

$$T = T_{rT} T_o \tag{65}$$

$T_o = P^{-1}$

Remark 2: In the RF model in Eq. (61) the terms $\hat{A}_{1R2} x_R$ and $\hat{A}_{1R1} x_R$ are the **matched** and **unmatched** disturbances**, Castaños and Fridman,2006.**

Proposition (2): For the RF model in Eq. (61) with $\alpha = 1$, the sliding mode controller that will regulate the system state x to the origin is given by

$$u = u_0 + u_s \tag{66}$$

where

$$s = z_2 + G z_1, G \in \mathcal{R}^{1\times(r-1)} \tag{67}$$

$$u_0 = -B_{12}^{-1}\left(\hat{A}_{r21} z_1 + \hat{A}_{r22} z_2 + G\hat{A}_{r11} z_1 + G\hat{A}_{r12} z_2\right) \tag{68}$$

$$u_s = k * sgn(s) \tag{69}$$

$$k = |B_{12}|^{-1}\left|\hat{A}_{R2} + G\hat{A}_{R1}\right| * \sup_{t\geq 0}|x_R| + k_o \ , \ k_o > 0$$
(70)

With the selection of the matrix G such that;

i. the matrix $\left(\hat{A}_{r11} - \hat{A}_{r12} G\right)$ is Hurwitz
ii. the matrix $(A + BH)$ must has $(n-1)$ negative roots plus one equal to zero value where

$$H = -B_{12}^{-1}\left[\left(\hat{A}_{r21} + G\hat{A}_{r11}\right) \quad \left(\hat{A}_{r22} + G\hat{A}_{r12}\right) \quad \left(\hat{A}_{R2} + G\hat{A}_{R1}\right)\right] T \tag{71}$$

iii. the following *control performance condition* is satisfied;

$$R^C = \min_{i=1\to n}|R_i^C| > \min_{i=1\to n}|R_i^O| = R^O \quad (72)$$

Where R_i^C represents the real term of the i^{th} eigenvalue of $(A + BH)$ except zero and R_i^O represents the real term of the i^{th} eigenvalue of A. The zero eigenvalue of $(A + BH)$ is due to constrain the system state to the sliding manifold $s = 0$.

Proof: the objective of the SMC is to direct the sliding variable s to the origin using a discontinuous control action. Accordingly, a SMC is designed such that it makes the derivative of the candidate Lyapunov function $V(s) = \frac{1}{2}s^2$ negative definite. The time derivative of V is

$\dot{V}(s) = s * \dot{s}$

and the time derivative of s is

$\dot{s} = \dot{z}_2 + G\dot{z}_1 = \hat{A}_{r21}z_1 + \hat{A}_{r22}z_2 + \hat{A}_{R2}x_R + B_{12}u + G\hat{A}_{r11}z_1 + G\hat{A}_{r12}z_2 + G\hat{A}_{R1}x_R$

Select the control law as

$u = u_0 + u_s$

Where u_0 and u_s are the nominal (continuous) and the discontinuous control terms, the $\dot{s}$ then becomes;

$$\begin{aligned}\dot{s} &= \hat{A}_{r21}z_1 + \hat{A}_{r22}z_2 + G\hat{A}_{r11}z_1 + G\hat{A}_{r12}z_2 + B_{12}u_0 + B_{12}u_s + \hat{A}_{R2}x_R + G\hat{A}_{R1}x_R \\ &= B_{12}u_s + (\hat{A}_{R2} + G\hat{A}_{R1})x_R\end{aligned}$$

Where the control term u_0 is selected to eliminate the known terms in $\dot{s}$ as;

$u_0 = -B_{12}^{-1}(\hat{A}_{r21}z_1 + \hat{A}_{r22}z_2 + G\hat{A}_{r11}z_1 + G\hat{A}_{r12}z_2)$

The term $(\hat{A}_{R2} + G\hat{A}_{R1})x_R$ is the unknown term due to the unmeasurable (or estimated) states x_R and for which u_s is devoted as follows;

$u_s = k * sgn(s)$

To this end $\dot{s}$ becomes;

$$\begin{aligned}\dot{s} &= B_{12} * k * sgn(s) + (\hat{A}_{R2} + G\hat{A}_{R1})x_R \\ &= -|B_{12}| * k * sgn(s) + (\hat{A}_{R2} + G\hat{A}_{R1})x_R\end{aligned}$$

where $B_{12} < 0$. The discontinuous gain k is determined such that $\dot{V}(s) < 0$. So let k be given by

$k = |B_{12}|^{-1}|\hat{A}_{R2} + G\hat{A}_{R1}| * \sup_{t\geq 0}|x_R| + k_o$, $k_o > 0$

Then $\dot{V}(s)$ becomes

$$\begin{aligned}\dot{V}(s) = s\dot{s} &= s\{-|B_{12}| * k * sgn(s) + (\hat{A}_{R2} + G\hat{A}_{R1})x_R\} \\ &= -|\mathrm{s}||B_{12}| * k + s(\hat{A}_{R2} + G\hat{A}_{R1})x_R \\ &< -|\mathrm{s}||B_{12}| * k + |s||(\hat{A}_{R2} + G\hat{A}_{R1})x_R| = -|\mathrm{s}|(|B_{12}| * k - |\hat{A}_{R2} + G\hat{A}_{R1}||x_R|) \\ &= -|\mathrm{s}|\{|B_{12}| * (|B_{12}|^{-1}|\hat{A}_{R2} + G\hat{A}_{R1}| * \sup_{t\geq 0}|x_R| + k_o) - |\hat{A}_{R2} + G\hat{A}_{R1}||x_R|\} \\ &= -|\mathrm{s}|\{k_o + |\hat{A}_{R2} + G\hat{A}_{R1}|(\sup_{t\geq 0}|x_R| - |x_R|)\}\end{aligned}$$

Since $(\sup_{t\geq 0}|x_R| - |x_R|) > 0 \ \forall t$, then $\dot{V}(s) < 0$. This will lead to $s = \dot{s} = 0$ after a finite interval of time. To this end, the attractiveness of the sliding variable s is proved but then it is required to show that the RM is asymptotically stable during sliding mode and also to derive the matrix H that will ensure the asymptotic stability of the control system. To show that the RM, as given in Eq. (61), Eq. (67) is solved to z_2 when $= 0$, to get $z_2 = -Gz_1$. Then sub z_2 in the first equation in Eq. (61) to obtain the dynamics of z_1 during sliding motion

$$\dot{z}_1 = \hat{A}_{r11}z_1 + \hat{A}_{r12}(-Gz_1) + \hat{A}_{R1}x_R = \left(\hat{A}_{r11} - \hat{A}_{r12}G\right)z_1 + \hat{A}_{R1}x_R$$

For a controllable pair $\left(\hat{A}_{r11}, \hat{A}_{r12}\right)$ the matrix G can be selected such that the matrix $\left(\hat{A}_{r11} - \hat{A}_{r12}G\right)$ is Hurwitz, which also determine the sliding motion dynamics. Now the objective is to derive the matrix H during sliding mode based on the equivalent control as follow;

$$[\dot{s}]_{eq} = 0 = \hat{A}_{r21}z_1 + \hat{A}_{r22}z_2 + \hat{A}_{R2}x_R + B_{12}u_{eq} + G\hat{A}_{r11}z_1 + G\hat{A}_{r12}z_2 + G\hat{A}_{R1}x_R$$

Solving for u_{eq}

$$u_{eq} = -B_{12}^{-1}\left\{\hat{A}_{r21}z_1 + \hat{A}_{r22}z_2 + \hat{A}_{R2}x_R + G\hat{A}_{r11}z_1 + G\hat{A}_{r12}z_2 + G\hat{A}_{R1}x_R\right\}$$

$$= -B_{12}^{-1}\left\{\left(\hat{A}_{r21} + G\hat{A}_{r11}\right)z_1 + \left(\hat{A}_{r22} + G\hat{A}_{r12}\right)z_2 + \left(\hat{A}_{R2} + G\hat{A}_{R1}\right)x_R\right\}$$

$$= -B_{12}^{-1}\left[\left(\hat{A}_{r21} + G\hat{A}_{r11}\right) \quad \left(\hat{A}_{r22} + G\hat{A}_{r12}\right) \quad \left(\hat{A}_{R2} + G\hat{A}_{R1}\right)\right]\begin{bmatrix} z_1 \\ z_2 \\ x_R \end{bmatrix}$$

$$= -B_{12}^{-1}\left[\left(\hat{A}_{r21} + G\hat{A}_{r11}\right) \quad \left(\hat{A}_{r22} + G\hat{A}_{r12}\right) \quad \left(\hat{A}_{R2} + G\hat{A}_{R1}\right)\right]\hat{x}$$

$$= -B_{12}^{-1}\left[\left(\hat{A}_{r21} + G\hat{A}_{r11}\right) \quad \left(\hat{A}_{r22} + G\hat{A}_{r12}\right) \quad \left(\hat{A}_{R2} + G\hat{A}_{R1}\right)\right]Tx_o$$

$\rightarrow u_{eq} = Hx$ where

$$H = -B_{12}^{-1}\left[\left(\hat{A}_{r21} + G\hat{A}_{r11}\right) \quad \left(\hat{A}_{r22} + G\hat{A}_{r12}\right) \quad \left(\hat{A}_{R2} + G\hat{A}_{R1}\right)\right]T$$

Now sub u_{eq} in Eq. (46) to get

$$\dot{x} = A\,x + BHx = (A + BH)x$$

For the control system to be asymptotically stable the matrix $(A + BH)$ must be Hurwitz. But since the state is constrained to the sliding manifold $s = 0$ during sliding motion ($s = 0$ is a hyperplane of dimension $n - 1$ in the state space) so one of the eigenvalue of $(A + BH)$ is equal to zero. Accordingly, the remaining $n - 1$ eigenvalues must be of negative real part. Finally, the performance of the proposed SMC to suppress the smart material vibration is determined by the eigenvalues of the control system during sliding motion. If the minimum (but differ from zero) absolute real term of the i^{th} eigenvalue of $(A + BH)$ is greater than that for the original system$A$, then the control system will attenuate and suppress the smart cantilever vibration effectively. This idea is coined in condition (72).

The sliding mode controller, as in Eq. (66), that grantted asymptotic stabilty of the reduce model, may also cause the unstability for the system dynamic which named the control spillover**.** In the following section the avoideness of spillover problem is proved to happen if the SMC staisfies the performance condition as given in proposition (2).

4.1 Control Spillover Problem and control performance condition

To control vibration of a smart structure, a controller is usually designed based on a reduced order model of the system. When such a reduce order model based controller is applied to the full order system model, the actuating force that reduce the vibration of the lower modes will also influence the residual system model of the structure. Consequently it may produce undesirable vibration due to the unmodeled dynamics. This phenomenon is known as control spillover, **Meirovitch, 1990 .**

In the proposed SMC presented in proposition 2, the control spillover is avoided via the second condition imposed on the selection of the matrix G. Morover the smart cantilver beam dynamics with the SMC will be given by;

$$\dot{x} = A\,x + BHx = (A + BH)x \tag{73}$$

which represent the whole model matrix after applying the sliding mode control.

Remark (3): the smart cantilver beam dynamics as given in Eq. (73) is derived based on the equivalent control concept in SMC theory.

Remark (4): The second condition ii. can be used in measuring the performance of the proposed controller; where a higher vibration suppression can be achieved for large difference between R^{C} and R^{O}.

5. SIMULATION RESULTS AND DISCUSSION

In this section the simulation results for a smart cantilever beam, which is subjected to an initial tip deflection, are presented. MATLAB software is used as a simulator to the cantilever beam system. The physical and geometrical specifications for the beam are given in **Table 1** below. To show that the derived model represents the system dynamics at least with respect to the dominant natural frequencies, the natural frequencies of the beam (Eq. 47) are calculated and compared with the natural frequencies obtained from the ANSYS program. The results are shown in **Table 2** with a good agreement.

The balance realization and order reduction process for the system model had been performed to reduce its states form (24) states to (3) states, without significant affect to its dominant mode. This is demonstrated in **Fig.2** in the Bode plot. The number of states is equal to the selected singular values in **Table 3** for the diagonal elements of matrix Σ (the diagonal elements are the singular values of the grammians σ_i, $i = 1,2,\ldots\ldots,n$). Acoordingly the reduced order model matrices are determined according to section three with approperate dimension and only three states. By using the reduce order model states $x_r \in \mathcal{R}^3$, the designed sliding mode controller is applied to the cantilever beam and the system is simulated for 15 mm initial tip displacement. To investigate the stability of the smart cantilever, (the total system model with the SMC), the eigenvalues are determined based on the equivalent control, i.e., during sliding motion. The new system eigenvalues are presented in the second column of **Table 4**. In this table, in the second column, one of the eigenvalues (before the last one) is nearly equal to zero, while the minimum (but differ from zero) absolute real term is greater than that for the original system A (the first column). This agrees with what has been pointed in section four.

For the first set of numerical simulation, a (0.00001) second is used as a period of integration to the sliding mode control system. In **Fig.3**, the controlled tip displacement is compared with the open loop case. The ability of the SMC in stabilizing the tip displacement is clarified in this figure where it required about 2.5 second only. In addition, the control input voltage to the piezoelectric element, shown in **Fig.4**, is switched between 200 and -200 volt. This is a consequence of the discontinuous nature of the proposed SMC. Additionally the sliding variable is plotted in **Fig.5** where it reaches zero value after a very small period of time. The oscillation of the sliding variable is because that the sliding variable dynamics is affected also by the remaining states which ignored during getting the reduced order model.

In the real application of the suggested controller, it may be difficult to use 0.00001 second as sampling time for the control input where it is required to change the control voltage after each 0.00001 second. In order to access the real situation, the time period for the control input is taken equal to 0.0025 second. Consequently, the second set of numerical simulation use these time numerical values. The control performance is similar to the first set of simulation as clarified in **Figs.6**, **7 and 8** for the sliding variable, the tip displacement and the control input voltage respectively where, as can be seen, the vibration suppression ability is nearly the same as in the first set of simulation. This enhances the applicability of the suggested controller.

From **Figs.4 and 8** it can be seen that the control input voltage to the piezoelectric still actuated in full value in spite of the sliding variable equals zero approximately. This makes system chatter because the control voltage switches between the full input voltage due to the oscillation of the sliding variable s around the zero with a very small amplitude. To remove or attenuate the chattering effect, the *signum* function Eq. (69) is replaced by a continuous approximate function (the arc tan function), **Edwards, et al., 1998**. It is given by;
$sgn(s) \approx \frac{2}{\pi} * \tan^{-1}(10 * s)$. Replacing $sgn(s)$ by the approximation given above will prevent chattering and smoothing the values of the input voltage as shown in Fig (9). Eventually the sliding variable and the tip displacement are shown in **Figs.10 and 11** respectively, which proves that the control performance is as in the case of using signum function but with control voltage tends to zero after the beam vibration is die out.

6. CONCLUSIONS

In this paper, the sliding mode was designed to suppress the vibration induced in a cantilever smart beam subjected to an initial tip displacement. The state space model is obtained using the finite element approach and modal analysis resulting after appropriate modal reduction. During the theoretical calculations, the 24^{th} order system model obtained from the finite element model is reduced to the three order using a model reduction technique based on balance realization without affecting its dominant modes. For the proposed SMC, the control system stability and the control performance condition are derived in Eq. (71) and inequality (71) respectively. When the $(A + BH)$ matrix has $(n-1)$ negative roots plus one equal to zero the control system is asymptotically stable and the control spillover is avoided. These results were proved by making the derivative of the candidate Lyapunov function negative definite and using the equivalent control concept and also clarified in **Table 4** where 23 negative real eigenvalues plus one value very close to zero (1.056e-09). In addition, the control performance was maintained at the desired level via satisfying inequality (72) as can be detected in **Table 4** where the largest eigenvalue (has negative sign) for the closed loop system is smaller than that for the open loop case. The numerical simulations prove the effectiveness and performance of the proposed SMC where the cantilever beam vibration is suppressed in effective way when compared to the open loop case. Finally, and in order to overcome the chattering problem the signum function was replaced with the approximation given by the arctan function with appropriate parameters. The chattering is attenuated; the sliding variable and the control voltage input are accordingly smoothed as shown in **Figs.9 to 11** with the same control performance.

REFERENCES

- Al-khazraji, A. and Hamzaoui, A., 2011, *Robust Tracking Control Of Uncertain Dynamic Nonlinear Systems Via Type-2 Fuzzy Sliding Mode Approach*, *International Federation of Automatic Control (IFAC)*, vol. 18, pp. 4181-4185.

- Balamurugan, V. and Narayanan, S., 2000 *Active Vibration Control of Piezolaminated Smart Beams*, PP. 103-114.

- Bandyopadhyay, B., 2005, Vibration Control of Smart Structure Using Second Order Sliding Mode Control, IEEE Conference on Control Applications, PP. 1691-1696.

- Bandyopadhyay, B., 2007, *Modeling, Control and Implementation of Smart Structures*, germany Verlag Berlin Heidelberg.

- Bartolini, G., and Pisano, A., 2003, *A Survey of Applications of Second-Order Sliding Mode*, International Journal of Control, vol. 76, no. 9, pp. 875-892.

- Bernstein, D. S., 2009, *Matrix Mathematics*, New Jersey: Princeton University Press.

- Biswas, et al., 2009, *Sliding mode control of quadruple tank process*, Mechatronics, vol. 19, pp. 548-561.

- Capisani, L. M.,2009, *Design and Experimental Validation of A Second-Order Sliding-Mode Motion Controller for Robot Manipulators*, International Journal of Control, vol. 82, no. 2, pp. 365-377.

- Castaños, F. and Fridman, L., 2006, *Analysis and Design of Integral Sliding Manifolds for Systems With Unmatched Perturbations*, IEEE Transactions On Automatic Control, vol.51, No. 5, pp. 853-858.

- Chhabra, D., Narwal, K., and singh, P., 2012, *Design and Analysis of Piezoelectric Smart Beam for Active Vibration Control*, International Journal of Advancements in Research & Technology, vol.1, No.1.

- Clough, R. W., 2003, *Dynamics Of Structures*, USA: Computers & Structures, Inc.

- Dorf, R. C., 2003, *Optimal Control System*, New York: CRC Press LLC.

- Edwards, C., Spurgeon, S. K., and Patton, J. R., 1998, *Sliding Mode Control, Theory and Applications*. Taylor & Francis.

- Ferrara, A., and Vecchio, C., 2009, *Second order sliding mode control of vehicles with distributed collision avoidance capabilities*, Mechatronics, vol. 19, pp. 471-477.

- Inman, D. J., 2006, *Vibration with Control*, USA: John Wiley & Sons Ltd.

- Itik, M. and Salamci, U., 2005, *Active Vibration Suppression of a Flexible Beam via Sliding Mode and H∞. Control*, IEEE Conference on Decision and Control, and the European Control Conference , vol. 44, pp. 1240-1245.

- Jalili, N.,2010, *Piezoelectric-Based Vibration Control*, USA: Springer Science Business Media, LLC.

- Janardhanan, D., 2001, *Model Order Reduction and Controller Design Techniques*.

- Kumar, S., Srivastava, R. and Srivastava, R.K., 2014, *Active Vibration Control Of Smart Piezo Cantilever Beam Using Pid Controller*, International Journal of Research in Engineering and Technology, vol. 3, No. 1, PP.392-399.

- Magnani, A. F., 2007, *Motion Control of Rigid Robot Manipulators via First and Second Order Sliding Modes*, J Intell Robot Syst, vol. 48, pp. 23-36.

- Meirovitch, L., 1990, *Dynamics and Control of Structures*, USA: John Wiley & Sons.

- Oveisi, A., and T. Nestorović, 2014, *Robust Mixed H_2/H_∞Active Vibration Controller In Attenuation Of Smart Beam*, Mechanical Engineering , vol. 12, No. 3, pp. 235-249.

- Qaiser, S. H., 2009, *Estimation of Precursor Concentration In A Research Reactor by Using Second Order*, Nuclear Engineering and Design, vol. 239, pp. 2134-2140.

- Sachs, G., 2004, *Intrinsic Dynamic Analysis And Control Design Of Integrally Actuated Helicopter Blades*, Usa: Cand.-Ing. Johannes Traugott.

- Utkin V. I., Guldner J., and Shi J., 2009, *Sliding Mode Control in Electro-mechanical Systems*, CRC Press. Taylor & Francis Group.

- Williams, R. L. and Lawrence, D. A., 2007, *Linear State-Space Control Systems*, USA: John Wiley & Sons, Inc.
- Zhou, K., Salomon, G., and Wu, E., 1999, *Balanced Realization And Model Reduction For Unstable Systems*, International Journal Of Robust And Nonlinear Control, vol. 9, pp. 183-198.

NOMENCLATURE

$a1$ to $a4$	constants used in solution of the displacement function, dimensionless.
A_b	cross-section area of the beam element, mm^2.
A_p	cross-section area of the piezoelectic element, mm^2.
A	state matrix.

b	width of the beam, mm.
B	input matrix.
c	constant which equal to $\sqrt{EI/\rho A}$
C	output matrix.
d_{31}	piezoelectric constant, m/V.
e_{31}	piezoelectric stress/charge constant, VmN^{-1}
E_b	young modulus of the beam, GPa.
E_p	young modulus of the piezoelectric, GPa.
f_{ext}	external force, N.
f_{ctrl}	control force, N.
$F_{1,} F_2$	force acting at the node, N
G_c	signal condition device, dimensionless.
h	constant vector.
$i(t)$	sensor current, Amps.
k_b	stiffness matrix of the beam element.
k_p	stiffness matrix of the piezoelectric element.
l_b	length of the beam element, mm.
L	length of beam, mm.
M_b	mass matrix of the beam element.
M_p	mass matrix of the piezoelectric element.
N	shape function.
q	vector displacement.
$\dot{q}$	velocity vector.
$\ddot{q}$	acceleration vector.
t_a	thickness of the actuator, mm.
t_b	thickness of the beam, mm.
T	kinetic energy.
u	control input, Volt.
U	Strain enegy.
V_a	actuaor voltage, Volt.
V_s	sensor voltage, Volt.
$w(x,t)$	displacement function.
w	dgree of freedom.
α , β	damping coefficient, dimensionless.
ε	strain.
ρ_b	density of the beam, kg/m^3
ρ_p	Density of the piezoelectric patch kg/m^3

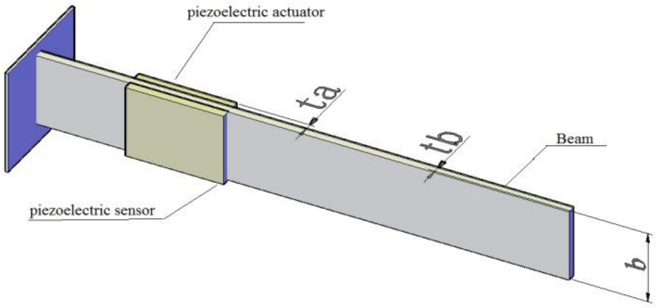

Figure 1. Clamped-free flexible smart beam model

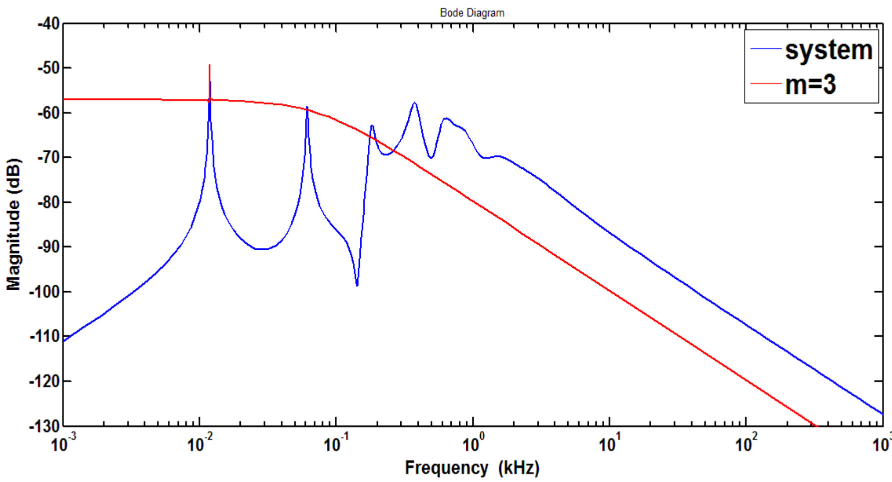

Figure 2. Bode plot

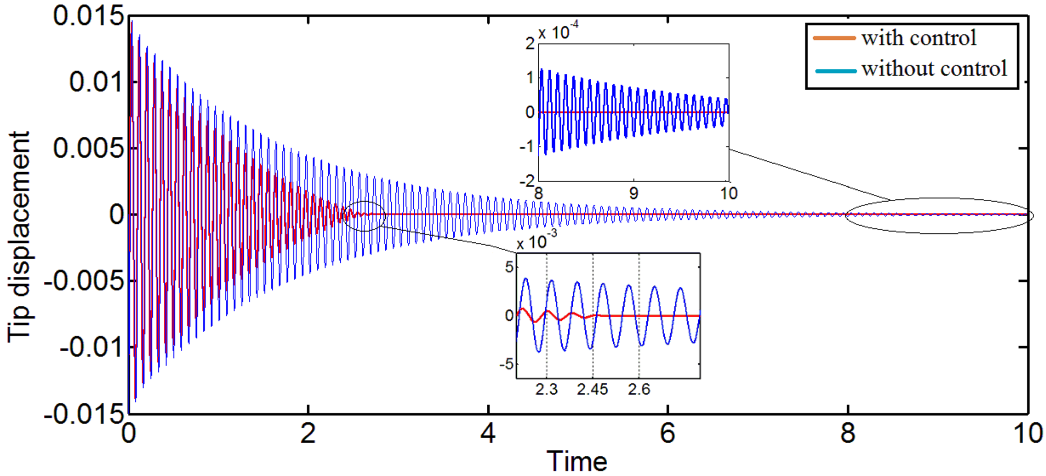

Figure 3. Tip Displacement for open loop and closed loop control system

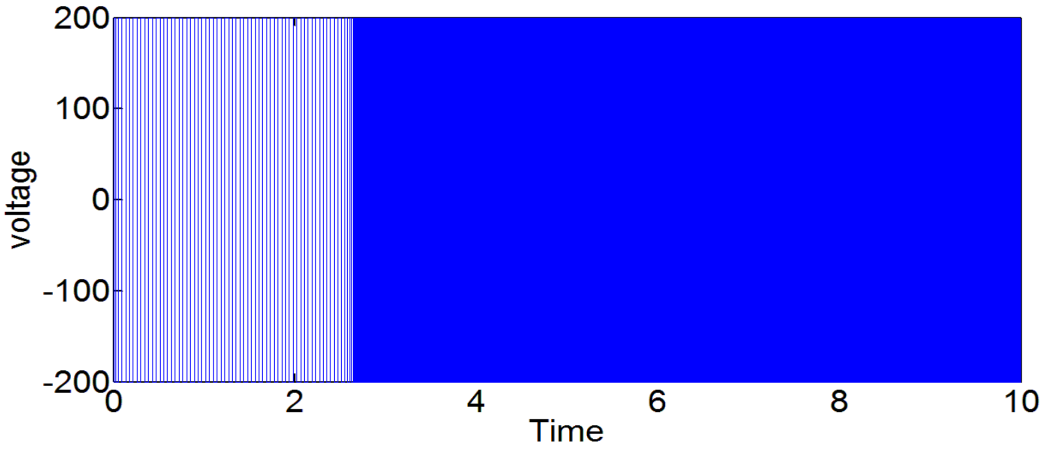

Figure 4. The control input voltage to the piezoelectric

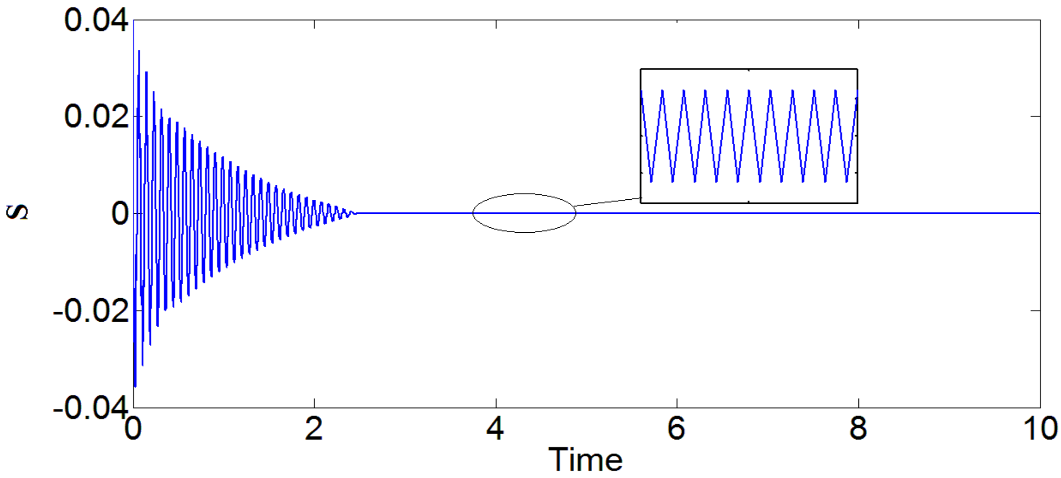

Figure 5. The sliding variable *s*

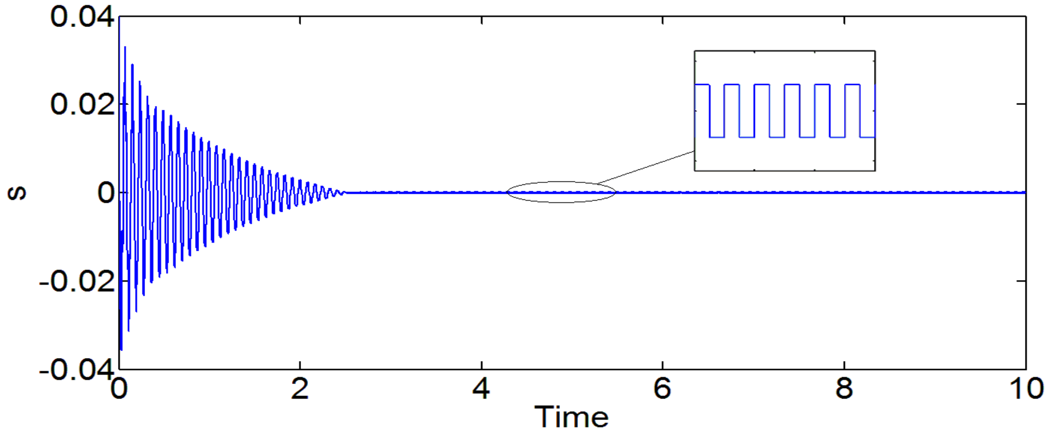

Figure 6. The sliding variable *s*

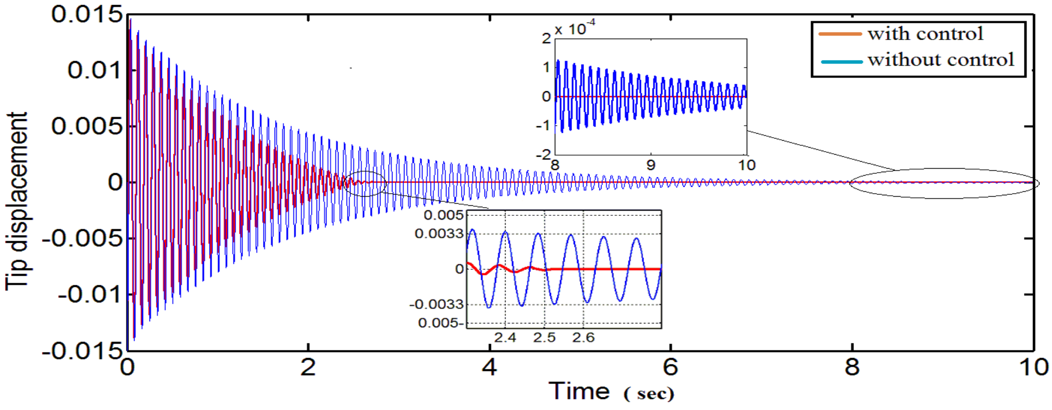

Figure 7. Tip Displacement for open loop and closed loop control system

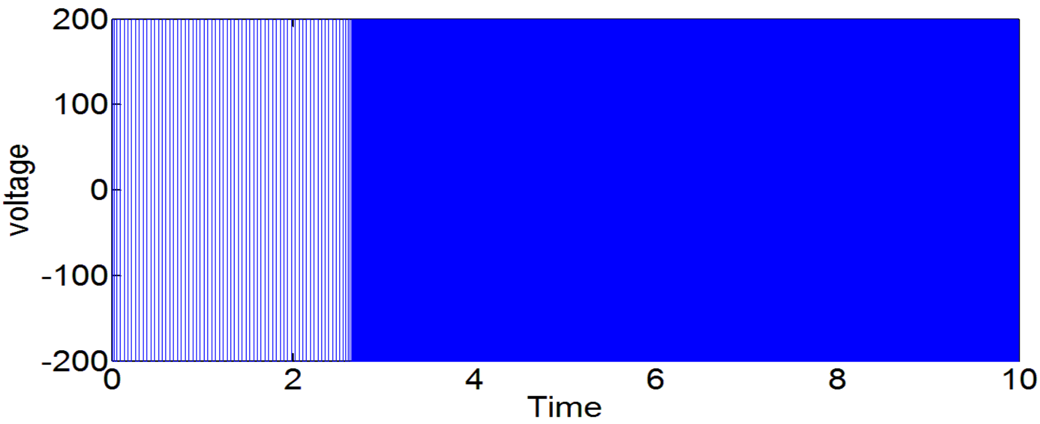

Figure 8. The control input voltage to the piezoelectric

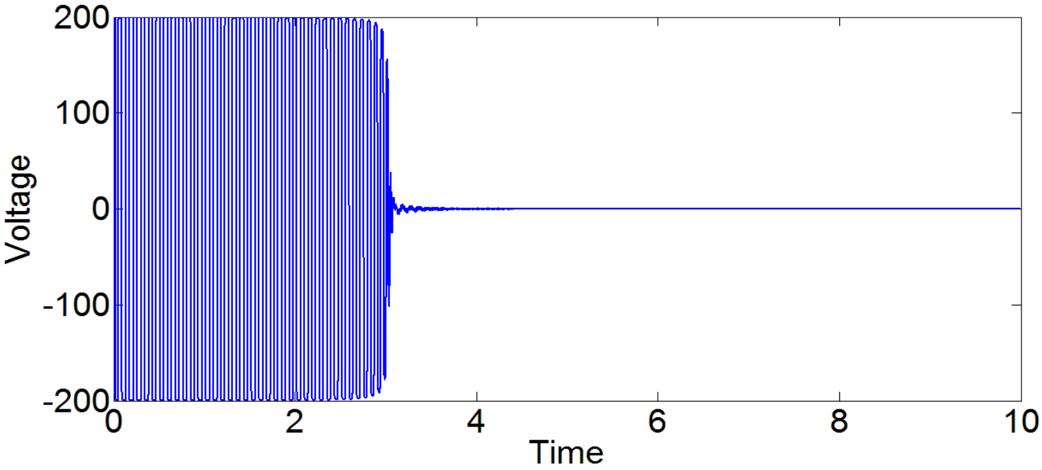

Figure 9. Control input voltage to the piezoelectric by using approximate function

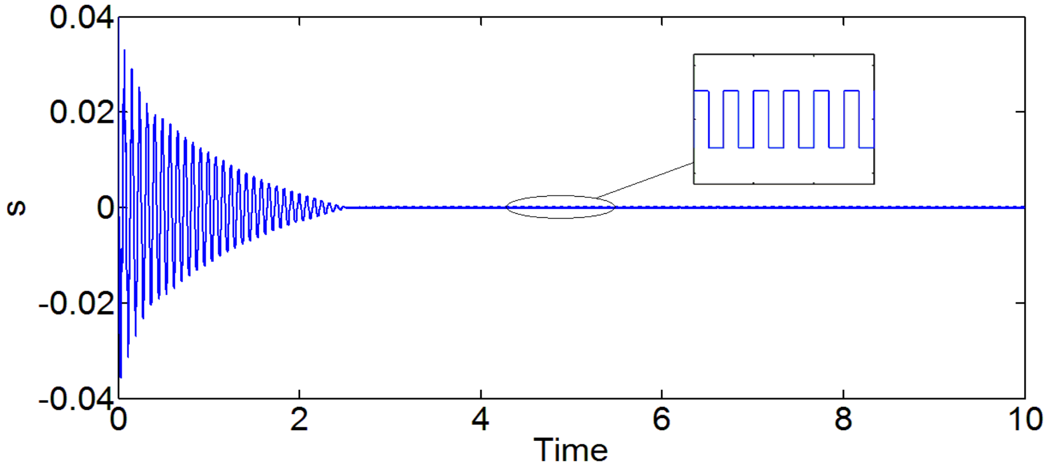

Figure 10. The sliding variable s using approximate function

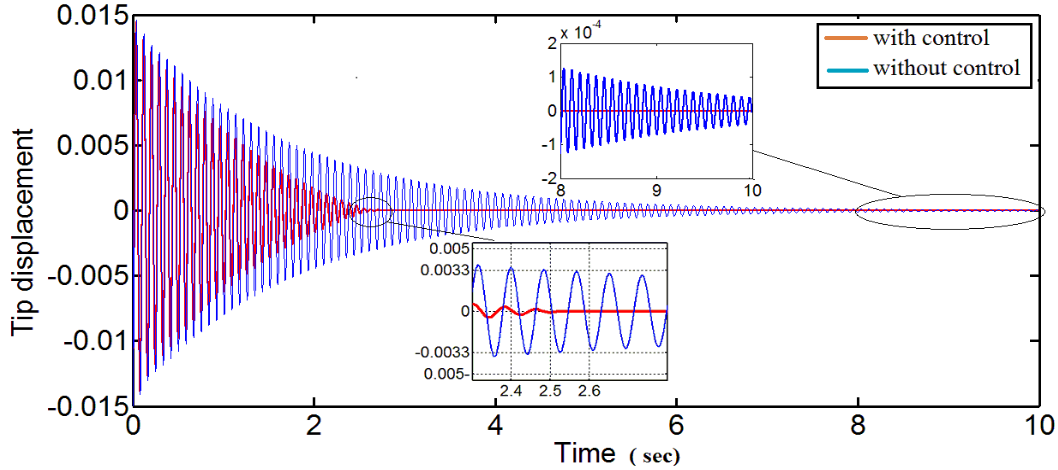

Figure 11. Tip Displacement for open loop and closed loop control system using approximate function

Table 1. The specification for the flexible cantilever beam and piezoelectric

Physical Specification	Cantilever Beam **(st-st)**	Piezoelectric
Length	L=276 mm	l_a =46 mm
Width	b =33 mm	b= 33 mm
Thickness	t_b =1 mm	t_a = 0.762 mm
Young modulus	E_b =193.06 Gpa	E_{p} = 68 Gpa
Density	ρ_b =8030 Kg/m^3	ρ_p = 7700 Kg/m^3
Damping coefficients	α = 0.8 & β = 6.8E-5	

Table 2. Natural frequency results of the system

Natural Frequency	**MATLAB** (Hz)	**ANSYS** (Hz)	**Error%**
f_1	11.878	11.421	3.125
f_2	61.376	61.148	0.372
f_3	181.06	180.1	0.558
f_4	153.5	151.3	1.45

Table 3. Singular value of grammians matrix

$\Sigma =$	$diag\{\,0.0011404 \quad 0.0011399 \quad 0.000698 \quad 0.0006932 \quad 0.00058469 \quad 0.00057315 \quad 0.00040318 \quad 0.00037605 \quad 0.00034589 \quad 0.00032743 \quad 0.00018763 \quad 9.8742e-05 \quad 6.1004e-05 \quad 5.7566e-05 \quad \dots\dots\}$
Selected singular values for model reduction	$\sigma_{(1)} = dig\{0.0011404 \quad 0.0011399 \quad 0.000698\}$

Table 4. System eigenvalues and controlled system eigenvalues

System Eigenvalues	Controlled System Eigenvalues
-96730 + 0i	-96757 + 0i
-84999 + 0i	-85330 + 0i
-21374 +13107i	-20079 + 14749i
-21374 - 13107i	-20079 - 14749i
-11184 + 14277i	-10038 + 17969i
-11184 - 14277i	-10038 - 17969i
-17782 + 0i	-17721 + 0i
-17342 + 0i	-17338 + 0i
-6491.8 + 12198i	-6289.6 + 11276i
-6491.8 - 12198i	-6289.6 - 11276i
-3092.9 + 9021.6i	-4558.6 + 7464.2i
-3092.9 - 9021.6i	-4558.6 - 7464.2i
-1122.7 + 5634.6i	-1898.7 + 5931.3i
-1122.7 - 5634.6i	-1898.7 - 5931.3i
-482.27 + 3733.7i	-285.41 + 3354.9i
-482.27 - 3733.7i	-285.41 - 3354.9i
-190.95 + 2359.6i	-135.03 + 1341.8i
-190.95 - 2359.6i	-135.03 - 1341.8i
-44.402 + 1136.8i	-3.3486 + 1148.7i
-44.402 - 1136.8i	-3.3486 - 1148.7i
-5.4563 + 385.6i	-14.623 + 386.09i
-5.4563 - 385.6i	-14.623 - 386.09i
-0.58936 + 74.626i	1.056e-09 + 0i
-0.58936 - 74.626i	-43.536 + 0i

Permeability Prediction for Nahr-Umr Reservoir / Subba field by Using FZI Method

Sameera M. Hamd- Allah
Assistant professor
Department of Petroleum Engineering
College of Engineering
University of Baghdad
Email: sameerahamdulla@yahoo.com

Basim Mohammed Noor
Consultant
Ministry of Oil
Department of Reservoir Field Development
Email: basimmnk@yahoo.com

Ahmed Radhe Watten
Department of Petroleum Engineering
College of Engineering
University of Baghdad
Email:ahmedeng_1990@yahoo.com

ABSTRACT

The permeability determination in the reservoirs that are anisotropic and heterogeneous is a complicated problem due to the limited number of wells that contain core samples and well test data. This paper presents hydraulic flow units and flow zone indicator for predicting permeability of rock mass from core for Nahr-Umr reservoir/ Subba field. The Permeability measurement is better found in the laboratory work on the cored rock that taken from the formation. Nahr-Umr Formation is the main lower cretaceous sandstone reservoir in southern of Iraq. This formation is made up mainly of sandstone. Nahr-Umr formation was deposited on a gradually rising basin floor. The digenesis of Nahr-Umr sediments is very important due to its direct relation to the porosity and permeability.

In this study permeability has been predicated by using the flow zone indicator methods. This method attempts to identify the flow zone indicator in un-cored wells using log records. Once the flow zone indicator is calculated from the core data, a relationship between this FZI value and the well logs can be obtained.

Three relationships have been found for Nahr-Umr reservoir/Subba field by FZI method.

By plotting the permeability of the core versus the permeability that is predicted by FZI method the parameter R^2 was found (0.905) which is very good for predict the permeability.

Key words: permeability, FZI

حساب النفاذيه لمكمن نهر عمر / حقل صبه باستخدام طريقة FZI

سميرة محمد حمد الله
استاذ مساعد
جامعة بغداد/كلية الهندسة/قسم هندسة النفط

باسم محمد نور
خبير
دائرة المكامن وتطوير الحقول/وزارة النفط

احمد راضي وطن
جامعة بغداد/كلية الهندسة/قسم هندسة النفط

الخلاصة

ان حساب النفاذيه في المكامن غير المتجانسه هي مسألة صعبه وذلك لان عينات اللباب وبيانات فحص الابار تكون قليله ومحدوده لعدد معين من الابار. في هذا البحث يتم استعراض (hydraulic flow units) و (flow zone indicator) لاستخدامها في حساب نفاذيه الصخور من خلال عينات اللباب الماخوذه من مكمن نهر عمر في حقل صبه. افضل نفاذيه هي النفاذيه المحسوبه في المختبر من عينات اللباب الماخوذه من الحقل. تكوين نهر عمر هو المكمن الرئيسي الاسفل في جنوب العراق وهو مكمن طباشيري. تكوين نهر عمر يتكون بصوره رأيسيه من حجر الرمل. تكوين نهر عمر ترسب بصوره تدريجيه في حوض نهري صاعد. تشخيص رواسب تكوين نهر عمر هي عمليه مهمه جدا وذلك لما للرواسب من تاثير مباشر على مساميه ونفاذيه المكمن.

في هذا البحث تم حساب النفاذيه لمكمن نهر عمر في حقل صبه باستخدام طريقة (Flow zone indicator) . هذه الطريقه تحاول حساب قيمه (Flow zone indicator) في الابار التي ليس بها عينات اللباب باستخدام المجسات. بعد حساب (Flow zone indicator) من بيانات اللباب المتوفره يتم ايجاد علاقه بين هذه القيمه المحسوبه (Flow zone indicator) ومجسات الابار .ثلاثه علاقات وجدت لمكمن نهر عمر/حقل صبه باستخدام طريقه FZI

بواسطه رسم نفاذيه اللباب ضد النفاذيه المستحصله بطريقه FZI فان المتغير R^2 قد وجد (0.905) حيث يتعبر قيمه جيدة لايجاد النفاذيه بطريقه FZI

الكلمات الرئيسيه : النفاذية , FZI

1. INTRODUCTION

One of the most important rock parameters for the evaluation of hydrocarbon reservoirs is permeability. Permeability was controlled by the size of the connecting passage between pores. Recovery of hydrocarbons from the reservoir is an important process in petroleum engineering and estimating permeability can aid in determining how much hydrocarbons can be produced from a reservoir.

Pasternak, 2009 stated that there is more one method to determine the permeability and porosity that are composed much of the technical literature in the industry of oil. There was no defined equation between the values of porosity and permeability. In many cases the relationship between porosity and permeability was qualitatively and in any way was not direct or indirect quantitatively. At all it was possible to find very high value of porosity without founding any permeability, as in the cases of pumice stones (where the permeability effective was approach to zero), clay and shale. The reverse might be true where the permeability was high and the porosity was low, like in micro fractured carbonate reservoirs. In spite of this fundamental lack of corresponding between the two properties, there were often can be find a good correlations between the porosity and permeability within one formation.

Tiab, and Donaldson, 2004 gave that the reservoir rock nature may contain oil dictated that the fluids quantities that were trapped within the pores of these rocks. The porosity may be defined as a measure of the void space of rock, and the permeability was the ability measurement of the rock to transmit fluid. Knowledge of the porosity and permeability was essentially before the questions concern the types of fluid, amount of fluid, rate of fluid flowing, and fluid recovery estimate could be answered.

2. FLOW UNITS

Bear, 1972, stated that the flow unit may be as the representative of the elementary volume of the total reservoir rock which the geologically and petro physical properties of the rock volume are the same.

Hear et al., 1984, defined the flow unit as a reservoir zone that was laterally and vertically continuous, and has similar permeability, porosity, and bedding characteristic.

Ebank, 1987, defined the hydraulic flowing units as portions of the reservoir which the geologically and petro physical properties that affects the flow of fluids were consistence and predictably different from the properties of other reservoir rocks volume.

Gunter, et al., 1997, showed that the flow units as continuous stratigraphic intervals of similar reservoir process that honor the geological frameworks and maintain the characteristically of the rock types. The hydraulic flow unit concept of hydraulic may be used to find the permeability.

3. DEVELOPMENT OF FLOW UNIT CONCEPT.

Amaefule, et al., 1993, considered the mean hydraulic radius role is in defining hydraulic flow units and correlation permeability from cores data. Their approach was essential based on the modified Kozeny-Carmen equation:

$$k = \left(\frac{1}{2\tau^2 \times S_{gv}{}^2}\right) \times \left(\frac{\emptyset_{eff}{}^3}{(1-\emptyset_{eff})^2}\right) \tag{1}$$

The **Amaefule et al,**defined the mean hydraulic radius as follows:

$$rmh = \frac{Cross\ sectional\ Area}{Wetted\ perimeter} = \frac{r}{2} \tag{2}$$

Tiab, and Donaldson, 2004, considered the concept of subgrouping reservoir volume into the flowing unit, suggested that the term $2\tau^2$ in Eq. (1), which is classical referred to as Kozeny constant, is actually “variable constant”. That means that Kozeny constant may vary for different hydraulics units, but is constant for a specific unit. Based on that, **Tiab, and Donaldson, 2004,** introduced the “variable constant” k_τ referred to as the effective zoning factor:

$$k = \left(\frac{1}{k_\tau \times S_{gv}{}^2}\right) \times \frac{\emptyset_{eff}{}^3}{(1-\emptyset_{eff}{}^2)} \tag{3}$$

Tiab, and Donaldson, (2004) proposed to estimate the effective zoning factor:

$$k_\tau = F_s \times \tau^2 \tag{4}$$

Carmen, 1937, simulated a porous medium as a bundle of capillary tubes. They combined Darcy’s law for flow in a porous medium and Poiseuille’s law for flow in tubes. A tortuosity factor was also included, because for a realistic model of porous media the connected pore structure is not straight capillary tubes. **Carmen, 1937,** suggested the following relationship between porosity and permeability:

$$k = \frac{r^2 \times \varphi_{eff}}{8\tau^2} = \frac{\varphi_{eff}}{2\tau^2} \times \left(\frac{r}{2}\right)^2 = \frac{\varphi_{eff} \times r_{mh}{}^2}{2\tau^2} \tag{5}$$

Al –Ajmi, and Holditch, 2000, showed that the mean hydraulic radius can be related to the specific surface area per unit grain volume S_{gv}, and the effective porosity φ_{eff}, by the following equation:

$$S_{gv} = \frac{1}{r_{mh}} \times \left(\frac{\varphi_{eff}}{1-\varphi_{eff}}\right) \tag{6}$$

Combining Eqs. (5) and (6), gives the generalized Kozeny-Carmen equation:

$$k = \frac{{\varphi_{eff}}^3}{(1-\varphi_{eff})^2} \times \frac{1}{F_s \times \tau^2 \times {S_{gv}}^2} \tag{7}$$

The term ($F_s\times\tau^2$) is known as the Kozeny constant, which is usually between 5 and 100 in most reservoir rocks. The term ($F_s\times\tau^2\times S_{gv}^2$) a function of geological characteristics of porous media and varies with changes in pore geometry. The determination of the ($F_s\times\tau^2\times S_{gv}^2$) group is the focal point of the Hydraulic Flow Unit (HFU) classification technique.

4. IDENTIFICATION OF FLOW ZONE INDICATOR (FZI) AND RESERVOIR QUALITY INDEX (RQI)

Taslimi, 2008 showed that flow zone indicator depends on geological characteristics of the material and various pore geometry of a rock mass; hence, it is a good parameter for determining HFU. Flow zone indicator is a function of reservoir quality index and void ratio.

Amaefule, et al., 1993, addressed the variability of Kozeny's constant by dividing Eq.(1) by the effective porosity φ_{eff}, and taking the logarithm:"

$$\sqrt{\frac{k}{\varphi_{eff}}} = \frac{1}{0.0314} \times \left(\frac{\varphi_{eff}}{1-\varphi_{eff}}\right) \times \frac{1}{\tau\, S_{gv}\sqrt{F_s}} \tag{8}$$

Where, the constant 0.0314 is the permeability conversion factor from μm^2- md.

Al –Ajmi, and Holditch, 2000, defined the flow zone indictor FZI (μm) as:

$$FZI = \frac{1}{\tau\, S_{gv}\sqrt{F_s}} \tag{9}$$

Reservoir quality index RQI (μm) as:

$$RQI = 0.0314\sqrt{\frac{K}{\varphi_{eff}}} \tag{10}$$

And normalized porosity φ_z (fraction) as:

$$\varphi_z = \frac{\varphi_{eff}}{1 - \varphi_{eff}} \tag{11}$$

Substituting Eq. (9) and Eq. (10) in Eq. (8) gives the following equation:

$$RQI = FZI \times \varphi_z \tag{12}$$

Taking the logarithm of both sides of Eq. (12) yields:

$$\log RQI = \log FZI \times \log \varphi_z \tag{13}$$

Al –Ajmi, and Holditch, 2000, considered that in a Log-Log plot of RQI versus φ_z all the samples with similar FZI values lie on a straight line with a slope of one; and data samples with the same FZI values, but significantly different from the preceding one, will lie on another, parallel, unit-slope lines; and so on **Perez, 2003** samples that lie on the same straight line have similar pore throat attributes, and thereby constitute a unique HFU. Each line represents a HFU and the intercept of this line with φ_z=1is the mean FZI value for that HFU. Each flow unit is characterized by FZI. **Amaefule, et al.,1993,** determined the basis of HFU classification is to identify groups of data that form unit-slope straight lines on a Log-Log plot of RQI versus φ_z, as shown in **Fig.1**.

5. FZI CORRELATION WITH WELL LOGS DATA

FZI is then correlated with certain combinations of logging tool responses to predict permeability values in cored and un-cored intervals of wells. This method attempts to identify the flow zone indicator in un-cored wells using log records. Once the flow zone indicator is calculated from the core data, a relationship between this FZI value and the well logs can be obtained, **Pablo, 2008**.

Eqs. (10) through (12) are used to compute the functions for preparing a log-log plot of RQI versus φ_z for each reservoir unit of all the wells. The data that have similar FZI values fall on a straight line (of the same slope); and all the data on the same straight line can be considered to have similar pore throat attributes (the same hydraulic unit) governing the flow. The permeability can be computed for those points on the same straight line (with same FZI) where core permeability plotted versus core porosity as shown in **Fig.2**:

Using the Eq. (14) to calculate the permeability in the un-cored wells:

$$K = 1014 \times FZI^2 \times \frac{{\varphi_{eff}}^3}{(1 - \varphi_{eff})^2} \tag{14}$$

The cross plot of the logarithm of permeability versus porosity data obtained from core analyses is shown in **Fig.1**. The cross plot of the logarithm of the reservoir quality index (RQI) versus the logarithm of the normalized porosity (Øz) for various values of the Flow Zone Indicator (FZI) are shown in Figure **Fig.2**. The cross plots of the K-predicated by FZI and K-core versus depth for each well are shown in **Figs .3** to **7**. A good agreement between the k-predicted and k-core values along most depth intervals of the units may be noticed from these figures. By plotting the permeability of the core versus the permeability that is predicted by FZI method for the cored wells the parameter R^2 was found (0.905) as in **Fig.8** and this value is considered good to find the values of permeability for Subba field /Nahr-Umr reservoir.

5. CONCLUSIONS

- FZI method is very accurate method in estimating permeability in un-cored well. Good agreement has been obtained between core permeability and calculated permeability by FZI method.
- FZI method gave three groups for Nahr-Umr reservoir, each group represent type of rocks, each type have the similar porosity and similar properties which can be used to divide the reservoir.

REFERENCES

- Bear, J. 1972, *Dynamics of Fluids in Porous Media*. Elsevier, New York.
- Carmen, P.C. 1937, *Fluid Flow through Granular Beds*, Trans. AICHE, V.15.
- Djebbar Tiab, and Erle C. Donaldson, 2004, *Petrophysics; Theory and Practice of Measuring Reservoir Rock and Fluid Transport Properties*, 2nd edition, Gulf Professional Publishing, Elsevier, Inc.
- Ebanks, W. J., 1987, "*The Flow Unit Concept-An Integrated Approach to Reservoir Description for Engineering Projects*", Am. Assoc. Geol. Annual Convention.
- Elena Pasternak, 2009, *Porosity–Permeability Relationship,* Allan Hancock College.
- Fahad A. Al-Ajmi, Stephen A. Holditch, 2000, *Permeability Estimation using Hydraulic Flow Units in a Central Arabia Reservoir,* Saudi Aramco-Schlumberger, SPE.
- Gunter, G. W., Finneran, J. M., Hartman, D. J. and Miller, J. D., 1997, *Early Determination of Reservoir Flow Units Using an Integrated Petrophysical Method,* SPE 38679. SPE Annual Technical Conference and Exhibition, San Antonio, TX.

- Hear, C. L., Ebanks, W. J., Tye, R. S. and Ranganatha, V., 1984, *Geological Factors Influencing Reservoir Performance of the Hartzog Draw Field, Wyoming*, J. of Petrol. Tech, Aug.

- Hector H. Perez, Akhil Datta –Gupta, 2003, *The Role of Electrofacies, Lithfacies, and Hydraulic Flow Units in Permeability Predictions from Well Logs: A Comparative Analysis Using Classification Trees*, Texas AandM U. and S. Mishra, SPE.

- Jude O. Amaefule, Mehmet Altunbay, Djebbar Tiab, David G. Kersey and Dare K. Keelan, 1993, *Enhanced Reservoir Description: Using Core and Log Data to Identify Hydraulic (Flow) Units and Predict permeability in Uncored Intervals/ Wells*, SPE, Houston, Texas.

- Watten, A. R., 2015, *Simulation Of Surfactant Flooding/Nahr-Umr Rerservoir / Subba field*, M.Sc. thesis, Petroleum Engineering Department, University of Baghdad.

- Lacentre E. Pablo and Carrica M. Pablo, 2008, *A Method to Estimate Permeability on Uncored Wells: The Method, Based on Cores and Log Data, Has Been Shown to Outperform Standard-Regression Techniques, as Well as The Hydraulic-Flow-Unit Approach*, Cengage Learning.

- Taslimi, M. Bohloli, B. Kazemzad E., and Kamali, M.R. 2008, *Determining Rock Mass Permeability in a Carbonate Reservoir, Southern Iran Using Hydraulic Flow Units and Intelligent Systems*, School of Geology, College of Science, University of Tehran, Research Institute of Petroleum Technology, N.I.O.C., Tehran, IRAN, 2nd IASME / WSEAS International Conference on Geology and Seismology (GES '08), Cambridge, UK

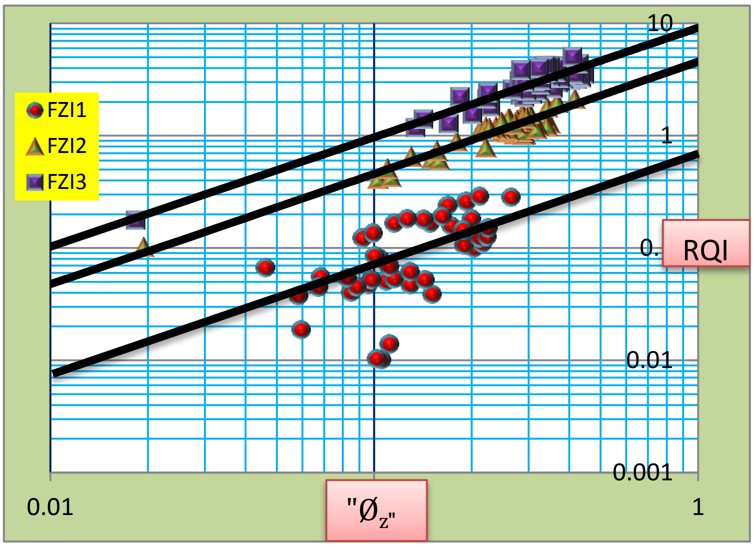

Figure1. Reservoir quality index (RQI) versus the normalized porosity (Øz) for Nahr-Umr formation**. Watten, 2015.**

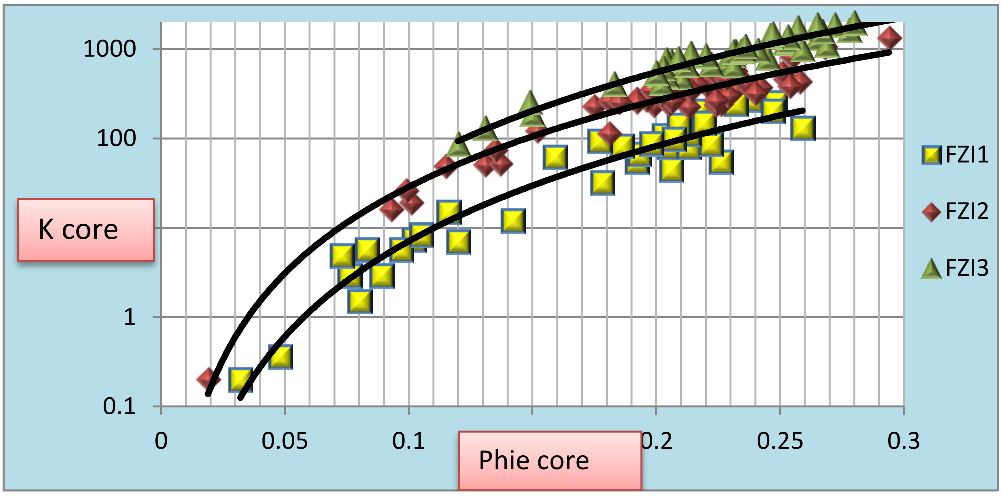

Figure 2. Core permeability versus core porosity for Nahr-Umr formation**. Watten, 2015.**

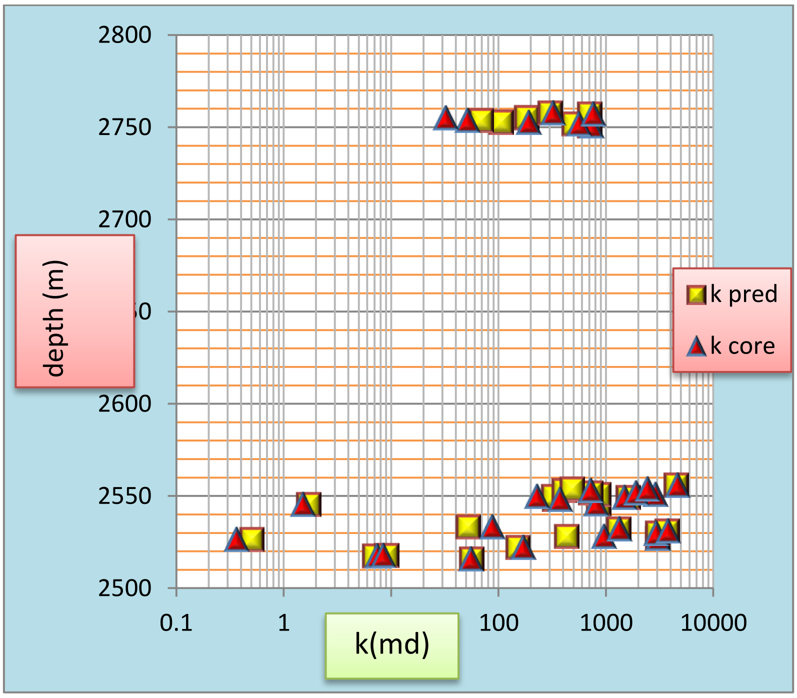

Figure 3. K- Predicted from FZI and K-Core versus depth for Nahr-Umr formation (well su-4). **Watten, 2015.**

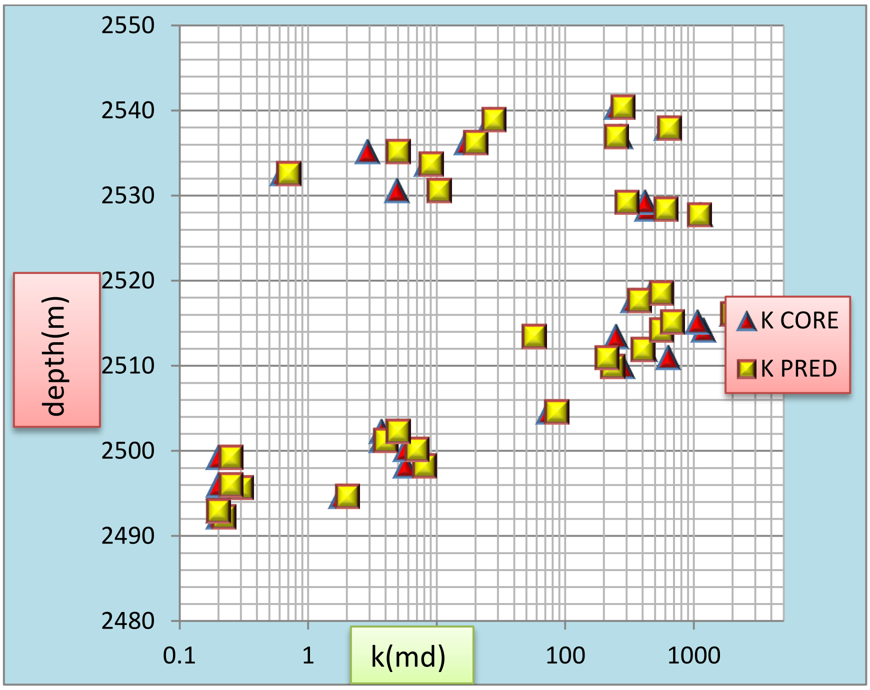

Figure 4. K- Predicted from FZI and K-core versus depth for Nahr-Umr formation (well su-5). **Watten, 2015.**

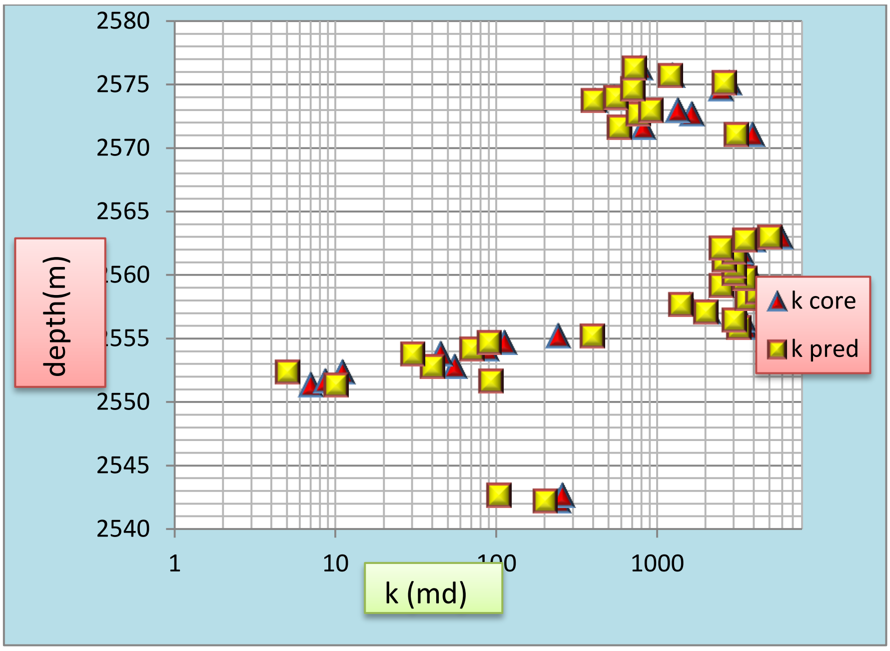

Figure 5. K- Predicted from FZI and K-Core versus depth for Nahr-Umr formation (well su-7). **Watten, 2015.**

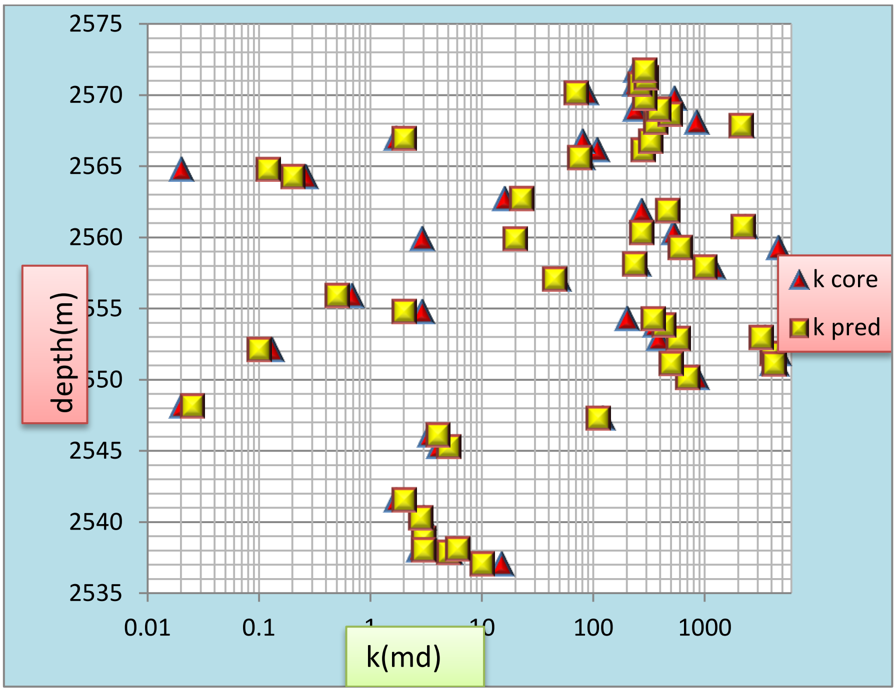

Figure 6. K- Predicted from FZI and K-core versus depth for Nahr-Umr formation (well su-9). **Watten, 2015.**

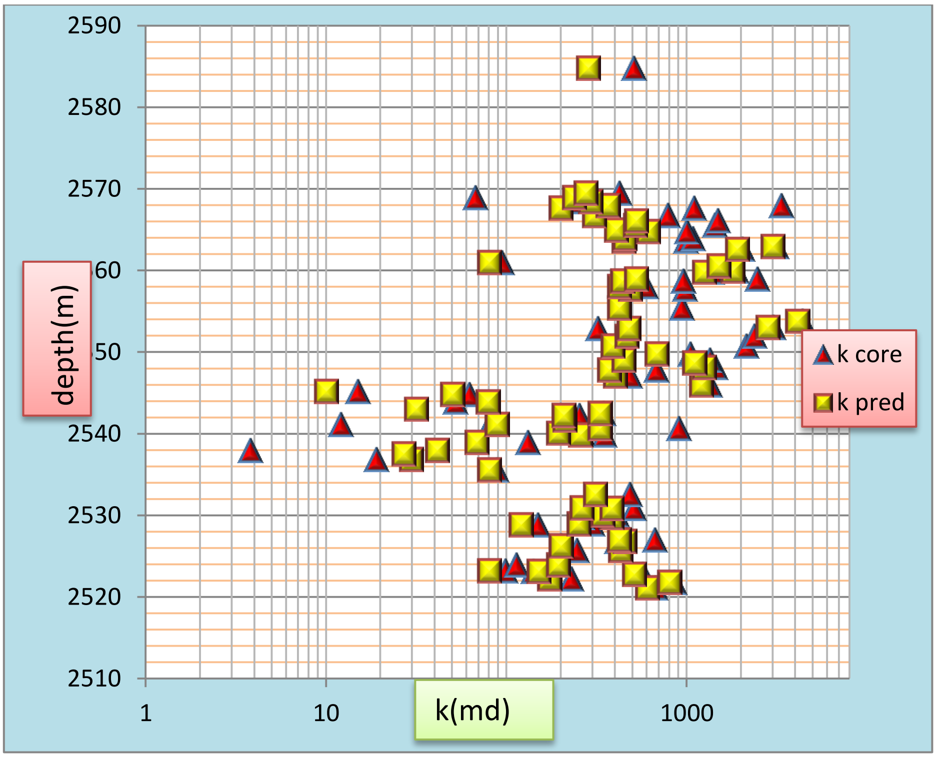

Figure 7. K- Predicted from FZI and K-core versus depth for Nahr-Umr formation (well su-14). **Watten, 2015.**

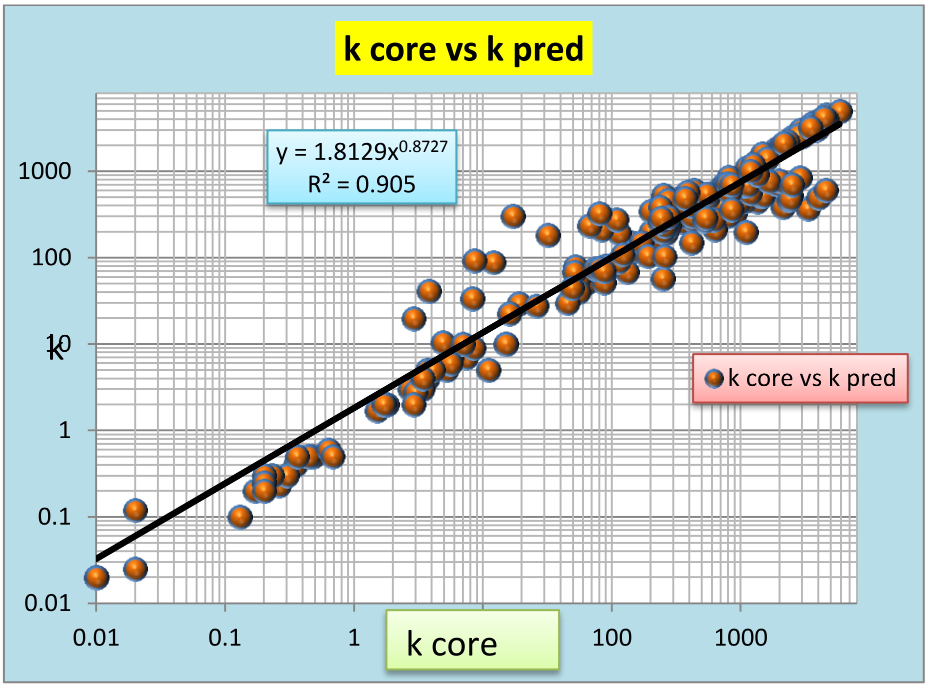

Figure 8: K- Predicted by FZI and K-core.

Table.1 Regression formulas with their correlation coefficient (R^2) by FZI method.

FZI	Formula	R2
FZI =1	$K=24483 *\phi eff^{3.5415}$	0.9437
FZI =2	$K=46612 *\phi eff^{3.211}$	0.9545
FZI =3	$K=14789 *\phi eff^{3.4757}$	0.9391

Symbol	Description	Unit
Fs	effective pore throat shape factor	(---)
K	permeability	md
K_τ	function of pore-pore throat size and geometries, tortuosity and cementation	(---)
r	pore throat radius	µm
rah	mean hydraulic radius	µm

S_{gv}	surface area of grains exposed to fluid per unit volume of solid material	cm2/cm3

NOMENCLATURE

Greek Symbols		
φ_{eff}	Effective porosity	fraction
φz	Normalized porosity	fraction
τ	Tortuosity	(---)

Abbreviations	
FZI	Flow Zone Indicator
HFU	Hydraulic Flow Unit
RQI	Reservoir Quality Index

Correction Factor for Methods of Installation of Piles Group in Sandy Iraqi Soils

Assist.Prof.Dr A'amal Abdul Ghani Al-Saidi
Civil Engineering Department, College of Engineering, University of Baghdad
dr_aamal@yahoo.com

ABSTRACT

Many problems are facing the installation of piles group in laboratory testing and the errors in results of load and settlement are measured experimentally may be happened due to select inadequate method of installation of piles group. There are three main methods of installation in-flight, pre-jacking and hammering methods. In order to find the correction factor between these methods the laboratory model tests were conducted on small-scale models. The parameters studied were the methods of installation (in-flight, pre-jacking and hammering method), the number of piles and in sandy soil in loose state. The results of experimental work show that the increase in the number of piles value led to increase in load carrying capacity of piled raft and decrease in settlement value for three methods of installation. The response of increases load capacity for hammering method is the same value of pre-jacking method at the number of piles less than (N=2), while when the number of piles are beyond (N=3 to 9). The load capacity of hammering method is more than pre-jacking method and the correction factor of method of installation depend on the type of method of installation and the piles number. The increase in carrying capacity by hammering method is due to mobilize the dynamic soil structure interaction (soil-pile and pile-pile interaction) and the change in properties for surrounding soil for loose state of sand is more effective than static soil structure interaction mobilize by pre-jacking method. The correction factor of increase in load capacity and the correction factor of the percentage of settlement reduction for pre-jacking and hammering methods are compared with in-flight method of installation are changed with the number of piles and these values are increased with increasing the number of piles.

Keywords: methods of installation; number of piles; correction factor ; experimental work.

معامل التصحيح لطرق انشاء مجموعة الركائز في الترب الرملية العراقية

الاستاذ المساعد الدكتور امال عبد الغني السعيدي
قسم المدني / كليه الهندسه / جامعه بغداد

الخلاصة

العديد من المشاكل تواجه انشاء مجموعة الركائز في الفحوص المختبرية والاخطاء الحاصلة في نتائج الاحمال والهبوط المقاسة مختبريا قد تحصل نتيجة اختيار الطريقة غير الملائمة في انشاء مجموعة الركائز . هنالك ثلاث طرق رئيسية لانشاء مجموعة الركائز (in-flight , pre-jacking and hammering method) ولاجل الحصول على معامل التصحيح بين هذه الطرق اجريت مجموعة فحوصات لموديلات مختبرية مصغرة . العوامل التي تمت دراستها طريقة انشاء الركائز وعدد الركائز في تربة رملية مفككة .
نتائج الفحوصات المختبرية بينت ان استجابة الزيادة في قابلية التحمل لكلا الطريقتين (pre-jacking and hammering method) هي ذاتها لحد (N=2) ولكن عندما تزداد عدد الركائز من (3 - 9) فان الزيادة في قابلية التحمل لطريقة (hammering method)اكثر من طريقة (pre-jacking) كما ان معامل التصحيح يعتمد على طريقة انشاء الركائز وعددها . الزيادة في قابلية التحمل لطريقة (hammering method) نتيجة تحفيز التفاعل الديناميكي بين الركيزة و التربة (تفاعل تربة-ركيزة و ركيزة- ركيزة) والتغير في خواص التربة الرملية المجاورة في حالتها المفككة هي اكثر فعالية من التفاعل الستاتيكي بين الركيزة والتربة لطريقة (pre-jacking) .
كما ان معامل التصحيح للزيادة في قابلية التحمل ونقصان نسبة الهبوط لكلا الطريقتين(pre-jacking and hammering method) ومقارنتها مع طريقة(in-flight) يتغير مع عدد الركائز ويزداد بزيادتها .

الكلمات الرئيسيه :- طرق الانشاء،عدد الركائز،معامل التصحيح،عمل مختبري .

1. INTRODUCTION

Piled raft is a composite geotechnical foundation system consisting of piles, raft and soil and the behavior of piled raft governed by different interactions (pile-pile, pile-raft and soil-pile-raft). A geotechnical assessment for the design of such a foundation system therefore needs to consider not only the bearing capacity of the pile elements and the raft elements, but their combined capacity and interaction under serviceability loading **Katzenbach et al., 1998**. However, usually three methods are used to install pile model in sand. These methods are listed below, **Linggang, 2006.**
1) In-Flight Pile Installation
2) Pre jacking Method
3) Hammering Method
And these methods governed by mobilize the soil-structure interaction, such as for jacking method the static soil structure interaction will be mobilized while dynamic soil structure interaction mobilize for hammering method. **Katzenbach et al. 1998 and 2000** illustrated that the piled raft foundation indicates a new understanding of soil – structure interaction under static loads as shown in **Fig.1**. The contribution of the rafts as well as the piles is taken into consideration to satisfy the proof of the ultimate load capacity and the serviceability of a piled raft as an overall system.
Giretti 2009 performed a series of centrifuge tests on models of rigid circular piled rafts in loose saturated sand employing both non displacement and displacement piles. The main aim of the tests of the effects the soil–pile (S–P) interaction is mainly governed by the pile installation procedure that is adopted; these procedures range from non-displacement to displacement methods.
In this paper, in order to determine the correction factor for methods of installation of piles group in sand, experimental work were carried out and the parameters studied are:

1- Method of installation (in-flight , pre-jacking and hammering method)
2- The number of piles (N)
3- Diameter of piles is Dp=11.30mm, spacing between piles 3Dp and relative density of sand is 30%.

2. EEXPERIMENTAL WORK:

A series of model loading tests were conducted inside a steel box of dimensions (600X600X700mm) depth, made of steel plate of 3mm thickness, stiffened with 3 lines of 25mm angle sections, provided with 280 *220mm hatch for sand refilling as shown in Plate (1). The base was stiffened with additional 3 mm steel plates and 25 mm steel angle frame and stiffeners, in order to prevent concentration of the load exerted from the piston on a small area.

The internal faces of the box were covered with polyethylene sheets in order to reduce the slight friction which might be developed between the box surface and soil. Scaling laws were followed in the design of the model to eliminate the model stress error and boundary effects.

The square aluminum raft model was a 120mm in dimension and thickness (t_r=15mm). The aluminum model of piles employed in the tests (d_p=11.30mm), where dp is the pile diameter.

2.1. Static Loading Measurement: A conventional compression machine with digital control system was used to apply the axial loading on footing model. The load on the footing was measured using proving ring of 3KN capacity. The settlement of pile raft model was measured by two dial gauges (0.001mm, division) fixed on the edges of the footing by two magnetic holders as shown in Plate (2). The installation of piles group by in-flight system method as shown in Plate (3) to control the installation of piled raft system and prevent the inclination and eccentricity of the model, the center of piled raft model must coincide with the center of the sand container and the center of the loading system, the pre-jacking method of installation of piles group in soil by using the compression machine can be noticed in Plate (4). Plate (5) shows the installation of piles group by hammering method by using known weights ranges from (0.5 to 1kg)

2.2. Soil Used

2.2.1 Sand properties:

Poorly graded sand was used in the tests. The sand was placed in the test box at unit weight of approximately15.3 kN/m^3 (relative density=30%). The properties of sand are given in **Table (1)**.

2.2.2 Mechanical properties of sand

The mechanical properties of used sand that have been extracted from the results of tests using triaxial test (UU test) and direct shear test are listed in **Table 1.**

2.3 Mechanical Properties of Aluminum Used

The aluminum specimen used to model raft and piles were tested in accordance to the **ASTM** (**B557–06**) specifications. Yield strength **(**fy**)**, tensile strength (fu), elongation (e) and Poisson's ratio (*v*). The results mechanical properties of aluminum used under tensile test are listed in **Table (2).**

3. RESULTS AND DISCUSION

Figs. 2 to 7 show the measured load-settlement curves for piled raft at (N=1, 2,3,4,6 and 9), s=3dp, tr=15mm and Dr =30% (where N is the piles number, s: spacing between piles, tr: raft thickness and Dr: relative density of sand). In general the results show increasing the number of piles value led to increase in load carrying capacity of piled raft and decrease in settlement value for three methods of installation.

Fig. 8 shows the computed maximum load and maximum settlement versus the increased in the number of piles. It is clear that the maximum load carried by piled raft increase from (0.35 to 0.82), (0.38 to 1.49) and (0.38 to 1.83 kN) and the maximum settlement decreased from (6 to 1.3), (4.2 to 0.7) and (4.2 to 0.5mm) with increasing the number of piles from (N= 1 to 9) for in-flight, pre-jacking and hammering methods, respectively.

Fig. 9 shows the computed increased in load carrying capacity is equal to {load $_{\text{(pre-jack or hammering method)}}$ / load $_{\text{in-flight method}}$} versus the increase in the number of piles for pre-jacking and hammering methods. The response of increased load capacity for hammering method is the same value of pre-jacking method at the number of piles less than (N=2), while when the number of piles beyond (N=3 to 9) it is clear that the load capacity will be increased from (1.42 to 2.23) for hammering method and (1.355 to 1.82) for pre-jacking method, in other words the correction factor of method of installation depends on the type of method of installation and the piles number. For hammering method it is clear that the increase in carrying capacity more than pre-jacking method because the dynamic soil structure interaction mobilized by hammering method (soil-pile and pile-pile interaction) and the change in properties for surrounding soil for loose state of sand is more effective than static soil structure interaction mobilize by pre-jacking method.

The correction factor of increase in load capacity for pre-jacking and hammering methods are compared with in-flight method is defined by equations below:

Log(Load)=0.227 Log(N)+0.073…(pre-jacking)

Log(Load)=0.334 Log(N)+0.043…(hammering)

Where (N is the piles number)

Fig. 10 shows the computed percentage of settlement reduction (Sr%) is equal to {1-(Settlement $_{\text{pre-jacking or hammering methods}}$ / Settlement $_{\text{in-flight method}}$)} for pre-jacking and hammering methods versus the increase in the number of piles. This figure shows the percentage of settlement reduction increases from (30 to 46%) and (30 to 62%) with increasing the number of piles (N=1 to 9) for pre-jacking and hammering methods, it is clear from the results above that the hammering method is more effective in settlement reduction compared with the pre-jacking method especially when the number of piles are beyond (N=2).

The correction factor of the percentage of settlement reduction (Sr%) for pre-jacking and hammering methods are compared with in-flight method of installation is illustrated below:

Log(Sr%)=0.168Log(N) + 3.476 … (pre-jacking)

Log(Sr%)=0.28Log(N) + 3.43 …..(hammering)

CONCLUSIONS

1- The increase in the number of piles value led to increase in load carrying capacity of piled raft and decrease in settlement value for three methods of installation.
2- The response of increased load capacity for hammering method is the same value of pre-jacking method at the number of piles less than (N=2), while when the number of piles are beyond (N=3 to 9). The load capacity of hammering method is more than pre-jacking method.
3-The correction factor of method of installation depends on the type of method of installation and the piles number.
4-The increase in load carrying capacity by hammering method is due to mobilize the dynamic soil structure interaction (soil-pile and pile-pile interaction) and the change in properties for surrounding soil for loose state of sand is more effective than static soil structure interaction mobilized by pre-jacking method.
5-The correction factor of increase in load capacity and the correction factor of the percentage of settlement reduction (Sr%) for pre-jacking and hammering methods are compared with in-flight method of installation are changed with the number of piles and these values are increased with increasing the number of piles.

REFRENCES

- ASTM (B557 – 06) Standard *Test Methods for Tension Testing Wrought and Cast Aluminum- and Magnesium-Alloy Products*".

- ASTM D422-2001, *Standard Test Method for Particle Size-Analysis of Soils.*

- ASTM D4253-2000, *Standard Test Method for Maximum Index Density and Unit Weight of Soils Using a Vibratory Table*.

- ASTM D4254-2000, *Standard Test Method for Minimum Index Density and Unit Weight of Soils and Calculation of Relative Density*.

- ASTM D854-2005, *Standard Test Method for Specific Gravity of Soil Solids by Water Pycnometer*.

- Daniela Giretti 2009. *Modeling of Piled Raft Foundations in Sand* Ph. D. Thesis, University of degli Studi di Ferrara..

- Katzenbach, R., Arslan, U., Moormann, C. and Reul, O. 1998, *Piled Raft Foundation – Interaction Between Piles and Raft*, Darmstadt Geotechnics, Darmstadt Univ. of Technology, No. 4, pp. 279-296.

- Katzenbach, R., Arslan U. and Moormann, C. 2000, *Piled Raft Foundations in Germany* Chapter 13 in Design Applications of Raft Foundations, J. A. Hemsley (ed.), Thomas Telford Ltd., London, U.K, pp. 323.

- Linggang, K. 2006, *Behaviour of Piles Group Subjected to Torsion, Ph.D.* Thesis Science and Technology University, Hong Kong.

Table 1. Properties for Sand Used.

Property		Values
Specific Gravity, Gs		2.65
Dry Unit Weight (γ_d) of Sand	Maximum unit weight, γ_{dmax}	17.9kN/m^3
	Minimum unit weight, γ_{dmin}	14.4 kN/m^3
Void Ratio(e) of Sand	Maximum void ratio (e_{max})	0.81
	Minimum void ratio (e_{min})	0.45
Dry Unit Weight Used (γ_d)	Loose state, γ_{dused}	15.3
Void Ratio Used (e)	Loose state (e_{used})	0.73
Friction Angle (Ø°)	Loose state	28.81°
Poissons Ratio (v)	Loose state	0.30
Modulus of Deformation (E_s, kN/m^2)	Loose state	10000

Table 2. Mechanical Properties of the Used Aluminum Alloy.

Property	**Value**
Modulus of Elasticity (GPa)	70
Minimum % of Elongation (e)	10
Assume Poisson's Ratio (*v*)	0.33

Plate 1. The sand container of used.

Plate 2. Arrangement of the Proving Ring and Dial Gauge During Loading.

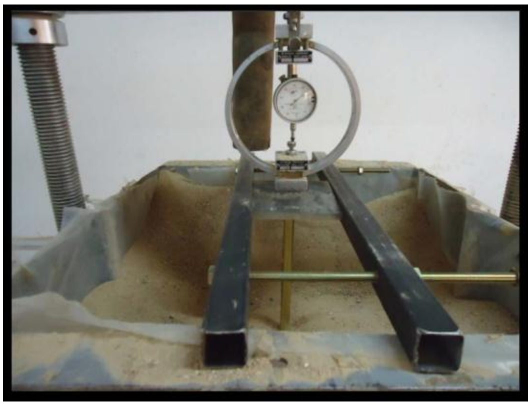

Plate 3. In-Flight Method of Pile Installation System.

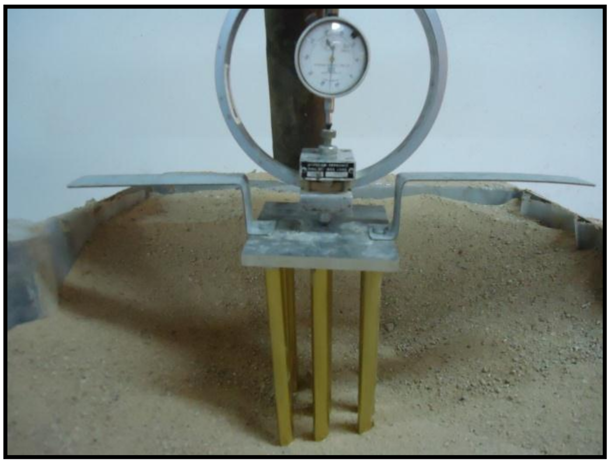

Plate 4. Pre-Jacking Method of Piles Installation System.

Plate 5. Hammering Method of Piles Installation System.

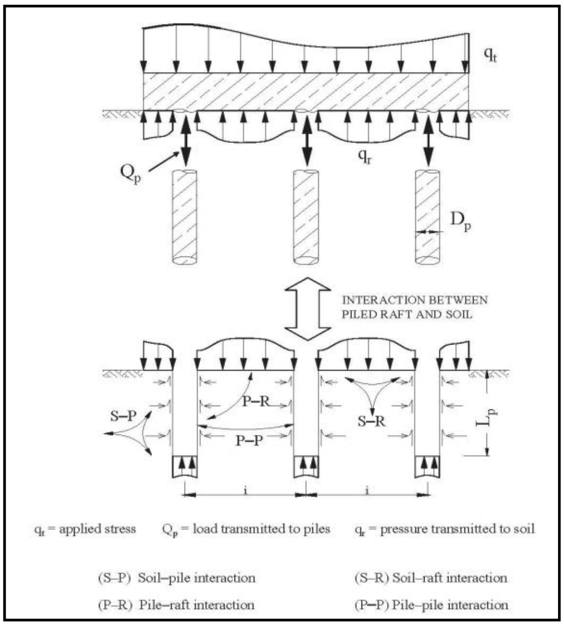

Figure 1. Static Soil-Structure-Interaction of Piled Rafts (**after Katzenbach al., 1998**).

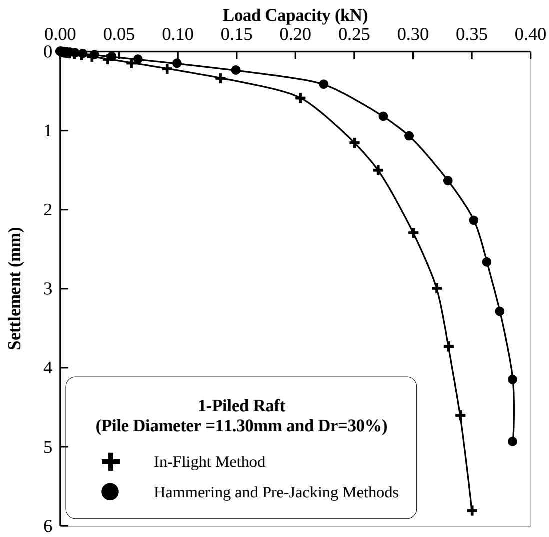

Figure 2. Load –Settlement curves for 1-Piled Raft.

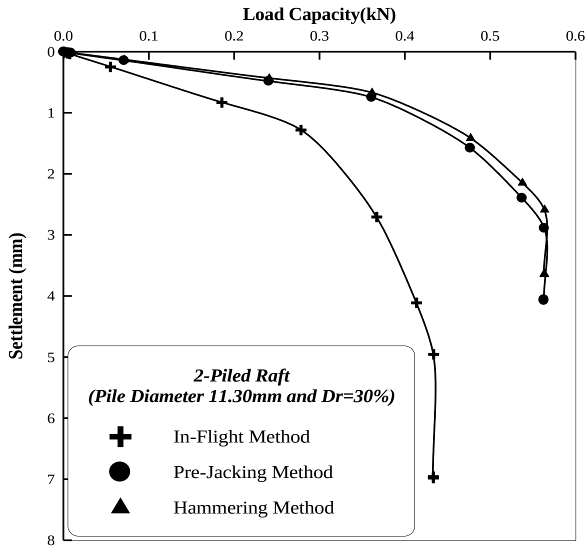

Figure 3. Load –Settlement curves for 2-Piled Raft.

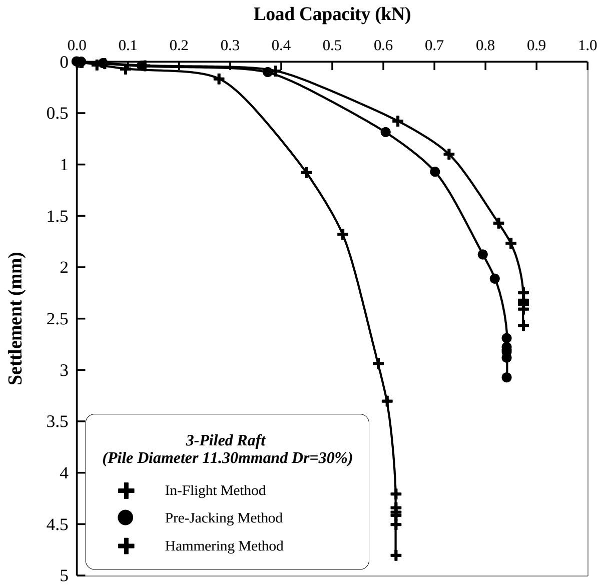

Figure 4. Load –Settlement curves for 3-Piled Raft.

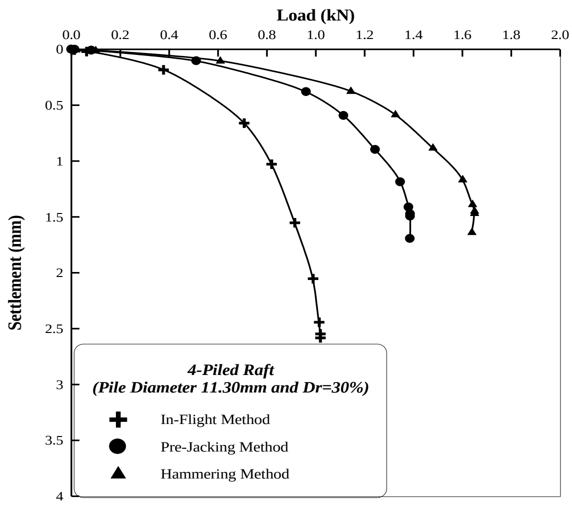

Figure 5. Load –Settlement curves for 4-Piled Raft.

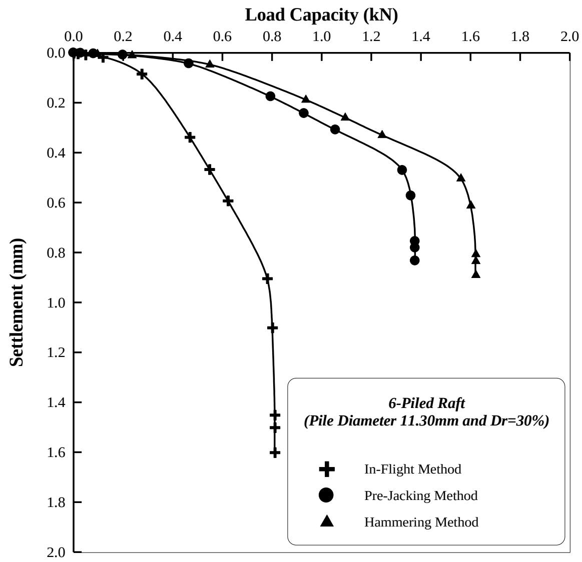

Figure 6. Load –Settlement curves for 6-Piled Raft.

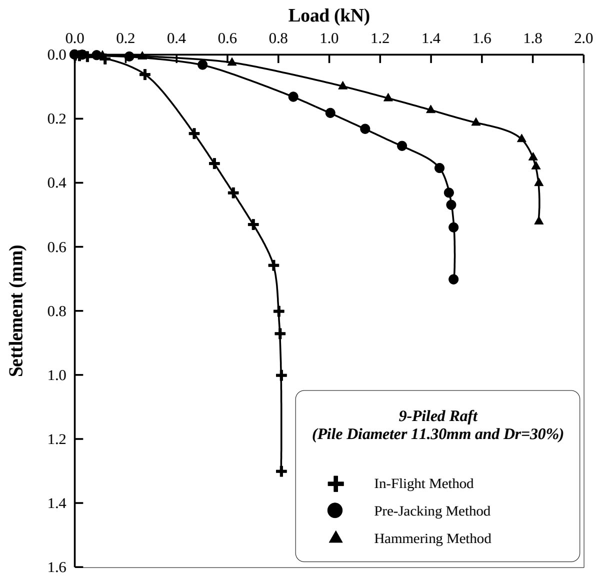

Figure 7. Load –Settlement curves for 9-Piled Raft.

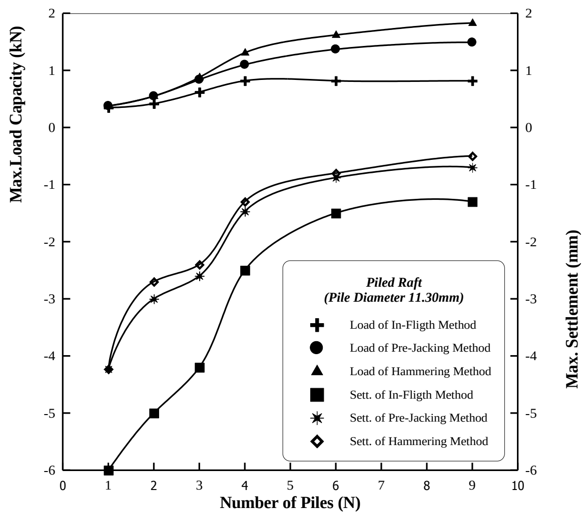

Figure 8. Max. Load and Max. Settlement Versus The Number of Piles.

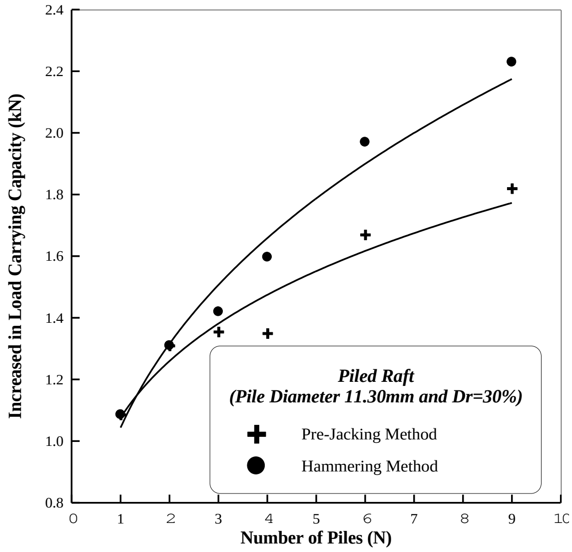

Figure 9. Increased in Load Capacity versus the Number of piles

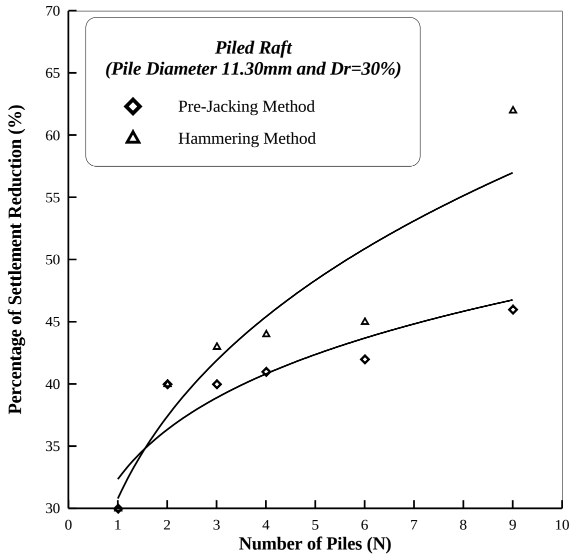

Figure 10. Percentage of Settlement Reduction Versus The Number of Piles.

Improvement of Traffic Movement for Roads Network in Al-Kadhimiya City Center

Dr. Mohammed Qadir Ismael
Assistant Professor
College of Engineering – University of Baghdad
drmohammedalbayati@gmail.com

Ali Jasim Mohammed
M.Sc., Transportation Eng.
College of Engineering – University of Baghdad
alij.itas@yahoo.com

ABSTRACT

Numerous regions in the city of Baghdad experience the congestion and traffic problems. Due to the religious and economic significance, Al-Kadhimiya city (inside the metropolitan range of Baghdad) was chosen as study area. The data gathering stage was separated into two branches: the questionnaire method which is utilized to estimate the traffic volumes for the chosen roads and field data collection method which included video recording and manual counting for the volumes entering the selected signal intersections. The stage of analysis and evaluation for the seventeen urban roads, one highway, and three intersections was performed by HCS-2000 software.The presented work plots a system for assessing the level of service for roads network within the study region. Moreover, several improvement alternatives were proposed to overcome the traffic movement operations issues. This work shows that traffic facilities currently undergoing serious degradation causing a traffic jam. Therefore, the implementation of some remedial action is necessary to improve the level of service for these facilities.

Key words: Kadhimiya, traffic, level of service, improvement, network.

تحسين الحركة المرورية لشبكة الطرق في مركز مدينة الكاظمية

د. محمد قادر اسماعيل
أستاذ مساعد
كلية الهندسة – جامعة بغداد

علي جاسم محمد
ماجستير هندسة مواصلات
كلية الهندسة – جامعة بغداد

الخلاصة

تعاني العديد من المناطق في مدينة بغداد من الاختناقات والمشاكل المرورية. نظرا للاهمية الدينية والاقتصادية تم اختيار مدينة الكاظمية (داخل حدود امانة بغداد) كمنطقة دراسة. تم تقسيم مرحلة تجميع المعلومات الى مرحلتين : طريقة الاستبانة والتي استخدمت لتقدير الحجومات المرورية للطرق المختارة وطريقة تجميع البيانات الموقعي وتتضمن التسجيل الفديوي والعد اليدوي للحجوم الداخلة للتقاطعات المختارة. مرحلة التحليل والتقييم لسبعة عشرطريق حضري، طريق سريع واحد وثلاث تقاطعات تم اجراؤها باستخدام برنامج HCS-2000. يرسم العمل المقدم نظاما لتقييم مستوى الخدمة لشبكة الطرق ضمن منطقة الدراسة.علاوة على ذلك اقترحت عدة بدائل للتحسين للتغلب على مشاكل عمليات الحركة المرورية. يبين هذا العمل ان المنشآت المرورية المختارة حاليا تمر بفترة تراجع خطير مؤدية الى حالات توقف تام ولذلك فمن الظروري تطبيق بعض خطوات المعالجة لتحسين مستوى الخدمة لهذه المرافق.

الكلمات الرئيسة : الكاظمية , مرور , مستوى الخدمة , تحسين , شبكة .

1. INTRODUCTION

It is gloabaly recognazied that transportation system is a principal component of the economic, social, cultural and political structure of our society. In recent years, significant changes in both of emphasis and scope of urban transportation planning have occurred. Traffic engineering plays a vital role in reducing the time of journeys, reducing accidents and increasing safety, reducing traffic congestion, increasing the speed of the vehicle, and obtaining information for the geometrical design of various roads components. The ultimate form of intersection control is the traffic signal due to its alternate ability to assign right-of-way to a specific movement, it can substantially reduce the number and nature of intersection conflicts as no other form of control can, **McShane, 2004**. The signalized intersection is generally representing the capacity constraint on any network of streets and is the most complex location in the traffic system. Therefore, the analysis of these locations must consider a wide variety of prevailing conditions, including geometric of the intersection, turning movements, relative approach volumes, traffic composition, and the details of intersection signalization, **Edwards, 1992**.

2. DELAY AT SIGNALIZED INTERSECTIONS

The delay is one of the most important Measures of Effectiveness (MOEs) in traffic studies. It represents the direct cost of fuel consumption and the indirect cost of time loss to the motorist, **Sadegh and Radwan, 1988**. **Webster**, **1958**, presented the results of his research conducted at the road research laboratory in London. The research was focused on vehicle delay at fixed traffic signals and optimum sitting of such signal. They used the simulation technique to simulate the behavior of traffic. They assumed that vehicles arrive at the random pattern.

The collected delay values are analyzed and the model below was adopted to represent the simulated data:

$$d = \frac{C(1-\lambda)^2}{2(1-\lambda X)} + \frac{X^2}{2q(1-X)} - 0.65\left[\frac{C}{q^2}\right]^{1/3} . X^{(2+5\lambda)} \tag{1}$$

where:

d= the average delay per vehicle, sec,
C= cycle time, sec,
λ= proportion of the cycle time, which is effectively green for the phase under consideration,
X= the degree of saturation,
q= flow, vehicle per cycle.

3. PREVIOUS STUDIES

Many traffic improvement studies were performed in different locations of Baghdad city. Some of these studies used Highway Capacity Software (HCS-2000) and others used TRANSYT-7F programs to the evaluation process and provide the optimal signal timing data.

The following articles summarize some of these studies:

Amanat Baghdad, (1982), conducted Baghdad Comprehensive Transportation Study (BCTS) with the objective of the evaluation of traffic performance for the selected facilities in Baghdad city.

A roadway network has been recommended that attracts the major traffic movements to the primary road system, enabling public transport to benefit from the improved traffic conditions and restricting the use of local streets to local traffic. The recommended highway network consists of an inner freeway box (ring road 1) around and close to the Central Business District (CBD), an inner orbital route (ring road 2) of expressway standard, a middle orbital route (ring road 3) of freeway standard, a long-term outer orbital (ring road 4) of freeway standard.

Mankhi, 2002, investigated the influence of delay, running speed and the density of passenger in the bus, and the capacity of the route parameters on evaluating the overall routes and network levels of service. The data collection for the work was included two parts; the first was the questionnaire methods while the second was the field data collection. The study shows that each of the selected four individual service characteristics affects the level of service evaluation by different percentage according to their importance to the users.

Khader, 2003, analyzed the traffic pattern in the center of Al-Kadimiya and defined the traffic problems. The video recording was utilized to observe the volume of traffic and pedestrian. Data were abstracted and analyzed using Event, Excel, and STATISTICA programs. Furthermore, the TRAFFICQ program was used to test the proposed engineering design for the network.

Hilal, 2004, developed a computer program for determination of the signal cycle which minimizes the overall vehicle delay at isolated signal controlled intersection.

Al-Zaidy, 2005, studied the influence of socioeconomic factors on trip generation for Al-Hadar District at Al-Dora area at the south of Baghdad City. The study found that the most effective independent variable on trip generation for families are number of worker, number of students, type of vehicle and age group

4. STUDY AREA

Initially, the study area was categorized to include three main cases:

I. Interrupted traffic flow at signalized intersections due to heavy traffic volumes, for this case the following intersections are considered:
   - Boratha Mosque intersection.
   - Al-Shalchiya intersection.
   - Aden intersection.

II. Interrupted traffic flows at the arterial streets. Most of the arterials within the study area were analyzed.

III. Uninterrupted traffic flows at expressway segments. Al-Shemal expressway.

All the three study cases are within the municipality border of Al-Kadhimiya city.

Figs.1 to 4 illustrate the study area, while **Table 1** presents the adopted survey methods and the utilized equipment.

5. PEAK HOUR SELECTION

According to trip purpose, PCU (passenger car unit) travel times fluctuate throughout the day. Considerable differences occur during different periods of the day. Therefore, in video recording it was found often necessary to obtain the most significant periods of the day required to satisfy the study objectives. In this aspect, four periods were identified from (6:00 am to 6:00 pm) to determine the peak period time. According to the recording processes, it has been clarified that the peak period is from 8:00 am to 9:00 am for intersections (Boratha Mosque and Shalchiya), while for Aden-intersection, the peak period was from 2:00 pm to 3:00 pm. **Tables 2** to **4** show the variation of traffic flow for the three intersections. These data are depicted in **Figs 5** to **7**.

6. OPERATION ANALYSIS OF EXISTING TRAFFIC FLOW (INTERSECTIONS)

The most common method to evaluate the performance of any traffic network is to simulate the existing traffic flow patterns along the area under study. **Tables 5** to **7** summarize the analysis of the intersections level of service under existing condition. It is obviously noticed from designated tables that the total delay for the most intersection under consideration is very high and the max (v/c) is greater than (1.0), furthermore, the level of service is (F) for all intersections.

7. ALTERNATIVES FOR IMPROVEMENT OF TRAFFIC PERFORMANCE (INTERSECTIONS)

After studying the performance of all intersections as mentioned previously for the existing condition, and in order to improve the traffic performance in the study area, the following improvement alternatives are introduced:

7.1 Alternative No.1 (Cycle Length Optimization)

To relieve the breakdown condition (level of service F), the optimization process is considered as the first improvement stage. HCS2000-Signals contains a signal timing estimation/optimization module called "SOAP2K". Currently, SOAP2K is capable of performing genetic algorithm optimization of cycle length and phase times. **Table 8** shows the best cycle length selected for each intersection. The selection of the best phasing time for each phase sequence for each approach depends on the traffic volume. **Tables 9** to **11** show the performance evaluation for all intersections under the first alternative. From the output results, it can be noticed that the measure of effectiveness ((v/c) ratio, total delay) are improved for all intersections. Although these improvements occur for all intersections, both of (Boratha Mosque and Al-Shalchiya) intersections still suffer from the high value of total delay time.

7.2 Alternative No.2 (Increasing the Number of Lanes)

This stage includes increasing the number of lanes on specified approaches to isolated intersections in order to increase the capacity of the approaches operating at oversaturation condition, and to provide better level of service. Therefore, one lane was added on approaches for each intersection according to the available area. **Tables 12** to **14** show the performance evaluation for all intersections. From the results obtained from the second improvement alternative, it can be noticed that a huge saving in measures of effectiveness, especially the total delay, is obtained for all intersections.

7.3 Alternative No.3 (Combination of the First Two Alternatives)

The third alternative is a combination of the first two improvements. This alternative includes selecting the best cycle length by timing optimization and increasing the number of lanes on the approaches. **Tables 15** to **17** summarize the results obtained from HCS-2000 program under this alternative. It can be noticed that the total delay is decreased for all intersections. It can also be noticed that the LOS for intersection 3 is upgraded to level C.

7.4 Alternative No.4 (Overpasses Construction)

Alternative No.4 is designed to include the construction of overpasses in the following intersections:

1. The overpass at Boratha Mosque intersection in EB and WB directions.
2. The overpass at Al-Shalchiya intersection in NB and SB directions along 14th July Street.

Consequently, for this alternative the phase sequences for the intersections mentioned above are changed as follows:

1. Boratha Mosque intersection is changed to 3-phase instead of a 4-phase operation.
2. Al-Shalchiya intersection is changed to 2-phase instead of a 3-phase operation.

It is important to note that the implementation of alternative No.3 is required in this stage, which includes selecting the best cycle length by timing optimization and increasing the number of lanes on the approaches.**Table 18** and **Table 19** show the performance evaluation of intersections 1 and 2 under alternative No.4. It can be noticed from these tables that a very high percentage of reduction in total delay at Boratha Mosque, and Al-Shalchiya intersections are obtained, and the LOS for these intersections is upgraded to level C and level B, respectively.

8. EVALUATION OF THE IMPROVEMENT ALTERNATIVES (INTERSECTIONS)

Table 20 summarizes the percent of saving in the measures of effectiveness for the four alternatives in comparison with results obtained from simulation of existing condition. According to Eq. (2).

$$\text{Saving, \%} = \frac{(\text{TD Existing} - \text{TD Alternative})}{\text{TD Existing}} \times 100 \qquad (2)$$

where:

TD = Total Delay for intersection.

Percentages of saving vary from one alternative to another. From **Table 20**, it can be concluded that alternative No.4 has the highest saving and benefit among other alternatives. **Figs. 8** to **10** show the percentage of saving for all intersections.

9. ANALYSIS OF URBAN STREETS WITHIN THE STUDY AREA

In this study, important arterials of the study area are analyzed and computations for LOS are performed by HCS-2000 program. **Table 21** summarizes the analysis of the arterials level of service under current condition.

10. URBAN STREETS LEVEL OF SERVICE UNDER FUTURE CONDITION

The future condition is represented by the annual growth rate of 3% during the next five to ten years. The analysis is carried out to identify the performance of the study area under these conditions.**Table 22** and **Table 23** summarize the results obtained from simulation of the existing condition of the studied area with a growth rate of (3%) in target years (2015) and (2020) respectively.

11. IMPROVEMENT ALTERNATIVES OF TRAFFIC PERFORMANCE (ARTERIALS)

In order to improve the traffic performance in the study area, the following improvement alternatives are introduced.

11.1 Alternative No.1 (Roadway Widening)
This alternative includes increasing the number of lanes which lead to increase the capacity of the arterials and to provide a better arterial level of service.**Table 24** shows the performance evaluation for all arterial streets under the first alternative.

11.2 Alternative No.2 (Modify Signals)
This alternative involves reconfiguring intersection in order to increase (g/C) ratio, where (g) is the duration of effective green for the approach and (C) is the cycle length for the intersections. The gained effect from changing (g/C) ratio on arterials performance is shown in **Table 25**, and it is indicating that high reduction in delay (greater saving) is achieved for all arterial accompanied by upgrading LOS for some arterials.

11.3 Alternative No.3 (Combination of the First Two Alternatives)
The third alternative is a combination of the first two improvements. This alternative includes widening roadway along with increasing (g/C). **Table 26** summarizes the results obtained from analysis operation. By observing this table, it can be noticed that the total delay is decreased for all arterial.

12. EVALUATION OF THE IMPROVEMENT ALTERNATIVE FOR ARTERIALS
Table 27 summarizes the percent of saving in the measures of effectiveness for the three alternatives in comparison with results obtained from simulation of the existing condition of the study area. Percentages of saving vary from one alternative to another. By observing **Table 27**, it can be concluded that Alternative No.3 has the highest saving and benefit among other alternatives. **Fig. 11** shows the percentage of saving for all arterials.

13. INTERSECTIONS AND ARTERIAL LOS UNDER FUTURE CONDITION
The future condition is represented by the annual growth rate of 3% during the next five to ten years and investigated for alternative No.4 in the intersection case. **Tables 28** to **31** summarize the percent of saving in the measures of effectiveness for alternative No.4 in comparison with results obtained from simulation of existing condition of the studied area with growth rate of (3%) in target years (2015) and (2020), respectively .

14. CONCLUSIONS
According to the results of this work, the following conclusions have been drawn:
1. For analyzed signalized intersections:

   a) The cycle time optimizations minimize the total delay in Boratha Mosque, Al-Shalchiya and Aden intersection by (3.5%, 16.1%, 18.45%) respectively. Furthermore, Aden intersection performs adequate LOS by optimizing cycle time only.
   b) Increasing the number of lanes (one lane added to each approach per intersection) will produce a significant saving in all measures of effectiveness, though reducing the existing total delay of Boratha Mosque, Al-Shalchiya and Aden intersection by (73.2%, 43.9%, 33.9%) respectively.

c) Increasing the number of lanes in conjunction with optimizing the cycle time will reduce the total delay by (73.4%, 58.8%, 38.0%) respectively.
d) The overpass construction is the best solution for traffic problem for both (Boratha Mosque Int.) and (Al-Shalchiya Int.) a high percentage of saving in delay will be obtained (34.8%, 16.4%) and LOS will be upgraded to LOS C and B respectively.

2. For analyzed arterial (Based on future condition):

a) Arterial (Al-Rabiaa, Boratha, Al-Damergi, 14 Ramadan, Al-Askareen, Mohammed Al-jwaad, Mohammed Al-Qasim, Al-Smoud, Al-Hasan, Al Tobchi and Al-Farazdak) shows adequate LOS performance in the future condition and no improvement needed for these arterials
b) Roadway widening which is adding one lane for each arterial per direction decreases the delay significantly for all arterials. Arterials (Al-Hamza, Zain Al-Abiden, Ibn Siena and Abid Al-Mohsin Al-Kadimi) will improve their LOS from F to LOS D, E, E, and E respectively.
c) Modifying Signal timing decreases the control delay for arterials. The delay in Arterials (Al-Hassain, Al-Hamza, Mosa Al-Kadhim, Zain Al-Abiden, Ibn Siena and Abid Al-Mohsin Al-Kadimi) will reduce by (19.1%, 30.0%, 23.8%, 31.9%, 22.9%, 51.0%) respectively.
d) Modifying Signal timing in conjunction with Roadway widening will upgrade the LOS for arterials (Al-Hamza, Zain Al-Abiden, Ibn Siena and Abid Al-Mohsin Al-Kadimi) from F to LOS of C, D, E, C, and C respectively.

15. RECOMMENDATION

1. For intersections

a) It is recommended to implement the cycle length optimization for all intersection in the study area.

b) It is recommended to implement the fourth alternative which is constructing overpasses for both (Boratha Mosque Int.) and (Al-Shalchiya Int.).

2. For arterials

a) It is recommend to perform wider questionnaire survey to include a sufficient area to cover on board arterials, through its important to mention that the results for arterials are based on volumes that the questionnaire survey covered only.

b) It is recommended to implement the third alternative which consists of a combination of roadway widening and modifying signal timing.

REFERENCES

- Amanat Baghdad, “Baghdad Comprehensive Transportation Study”, Final report, Kirkpatrick ,S.W., Baghdad, December, 1982.

- Al-Zaidy, M.A, “Influence of Socio-Economic Factor on Trip Generation of a Selected District in Baghdad”, M.Sc. Thesis, University of Baghdad, 2005.

- Edwards, J.D.Jr, “Transprtation Plannin Handbook”, Institute of Transportation Engineering, Prentice-Hall, Inc., New Jersey, 1992.

- Hilal, M.M., “Development of A Computer Aided Design Program for Signalized Intersection”, MSC. Thesis, University of Baghadad, 2004.

- Khader, H.M., “Improving Traffic Network Performance in the Center of Al-Kadimiya City”, M.Sc., Thesis, University of Baghdad, March, 2003.

- Mankhi, F.A., “Evaluation and Improvement of the Performance of a Selected Public Bus Network in Baghdad City”, M.Sc., Thesis, University of Al-Mustansiria, April, 2002.

- McShane, Prassas., and Ross, “Traffic Engineering”, 3rd.edition. Prentice-Hall. New Jersey. U.S R.P.2004.

- Sadegh, A. and Radwan, A.E., “Comparative Assessment of 1985 HCM delay”, Journal of Transportation Engineering, Vol.114,No.2, 1988,P.P 194-195.

- Webster, F.V., “Traffic Signal Setting”, Road Research Loboratory, Technical Report No. 39, London, 1958.

NOMENCLATURE

MOEs= Measures of Effectiveness
d= the average delay per vehicle, sec,
C= cycle time, sec,
λ= proportion of the cycle time, which is effectively green for the phase under consideration,
X= the degree of saturation,
q= flow, vehicle per cycle.
BCTS= Baghdad Comprehensive Transportation Study
CBD= Central Business District
HCS= Highway Capacity Software
PCU= Passenger Car Unit
v/c= Volume/Capacity
LOS= Level of Service
TD = Total Delay for intersection

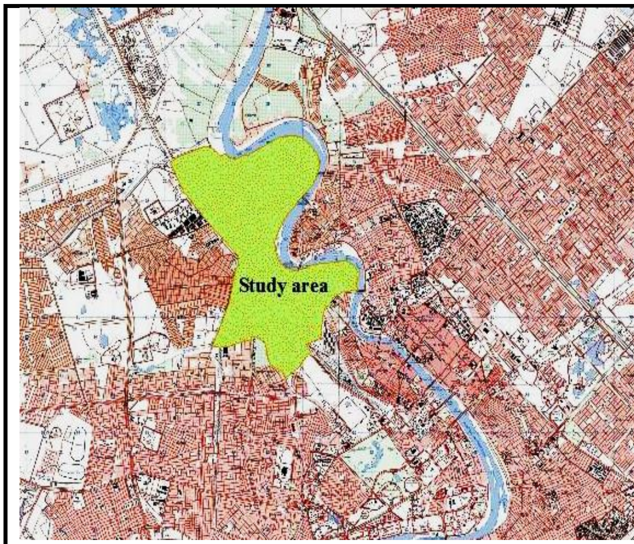

Figure 1. The study area

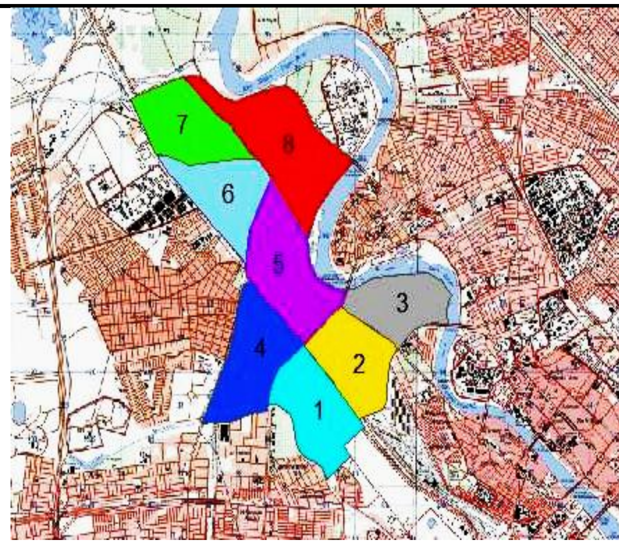

Figure 2. The selected zones

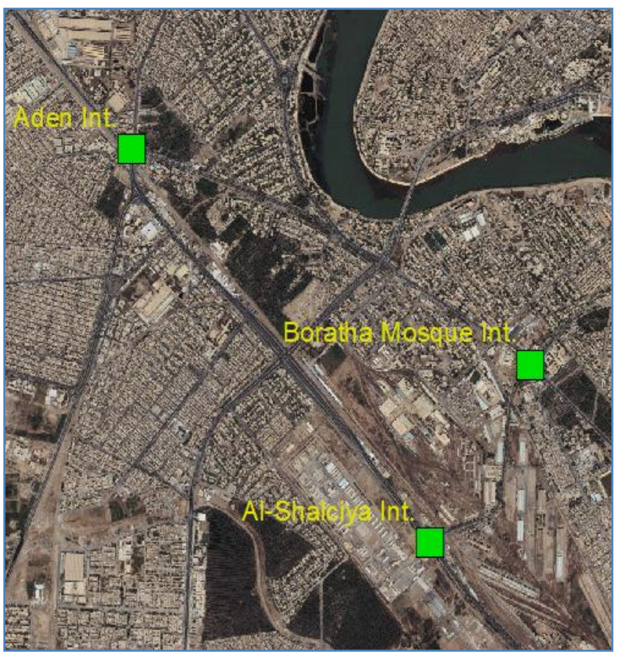

Figure 3. The intersections locations

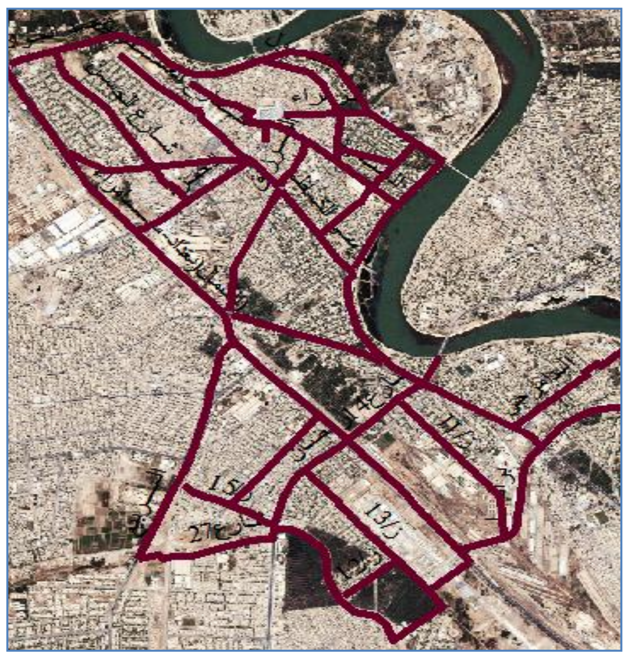

Figure 4. The arterial streets and highway in the study area

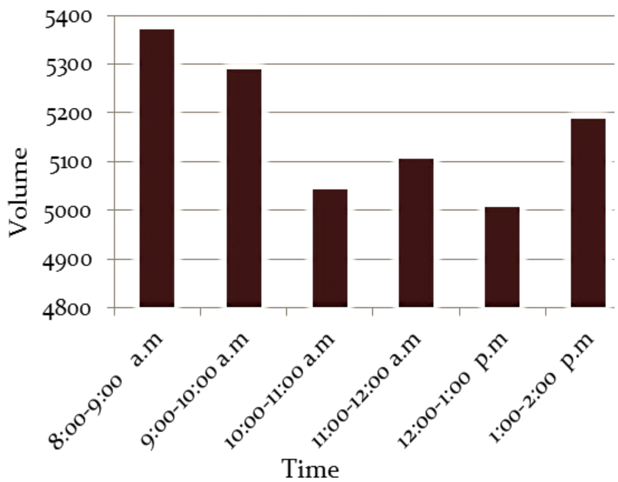

Figure 5. Variation of traffic flow at Boratha Mosque intersection (Int.1)

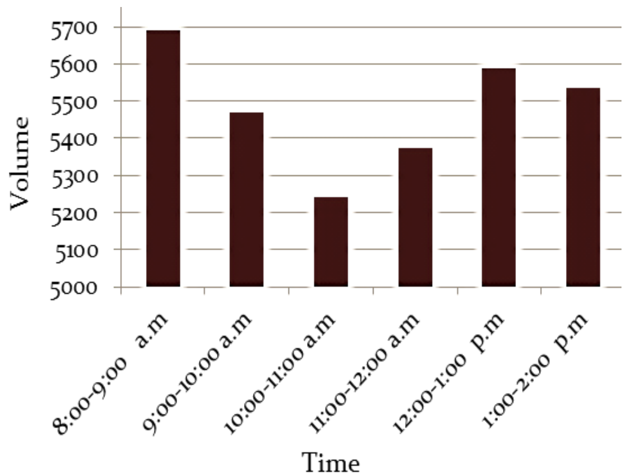

Figure 6. Variation of traffic flow at Al-Shalchiya intersection (Int.2)

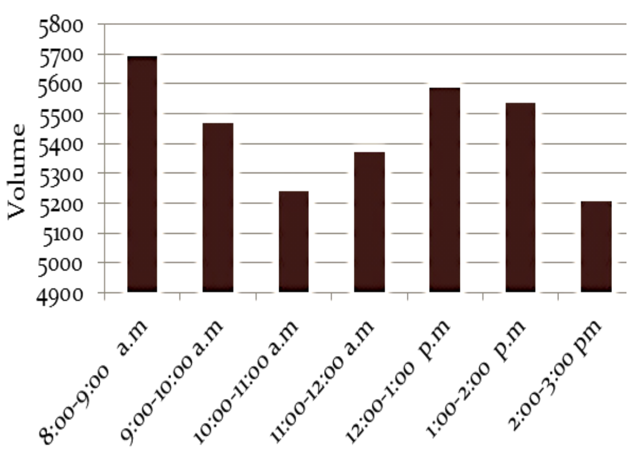

Figure 7. Variation of traffic flow at Aden intersection (Int.3)

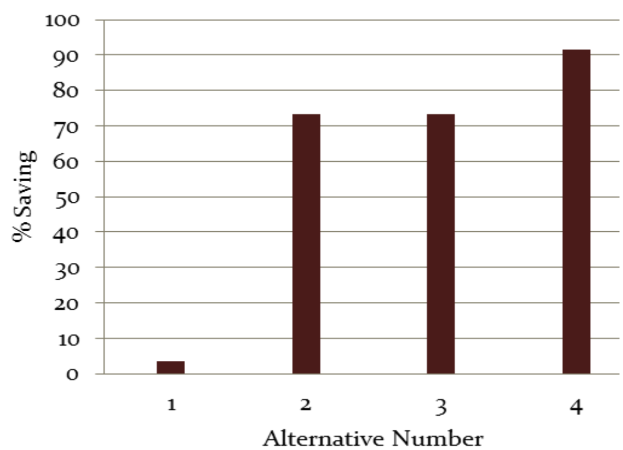

Figure 8. Saving in average delay for Boratha Mosque (Int.1)

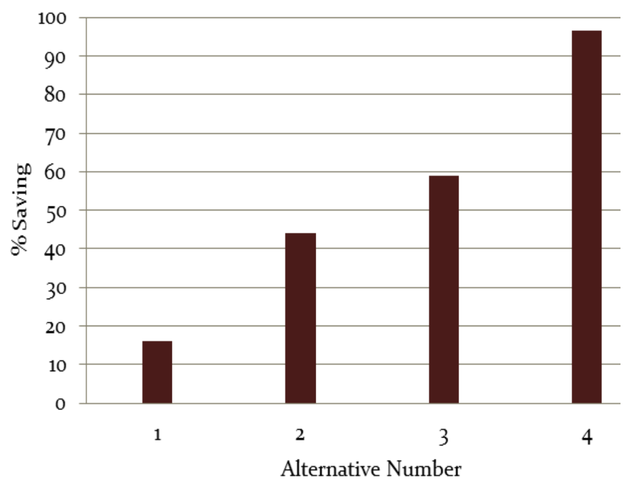

Figure 9. Saving in average delay for Al-Shalchiya (Int.2)

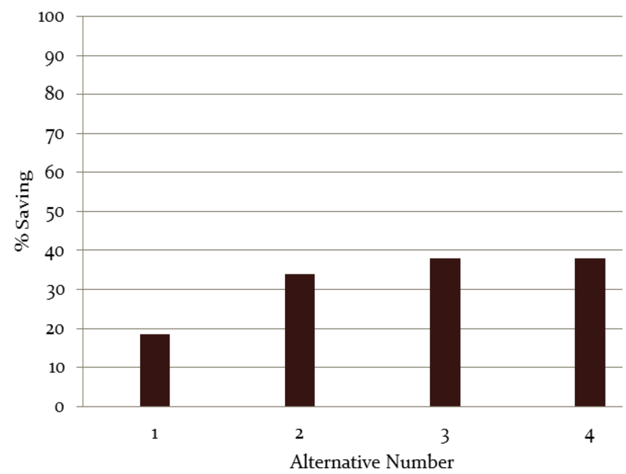

Figure 10. Saving in average delay for Aden (Int.3)

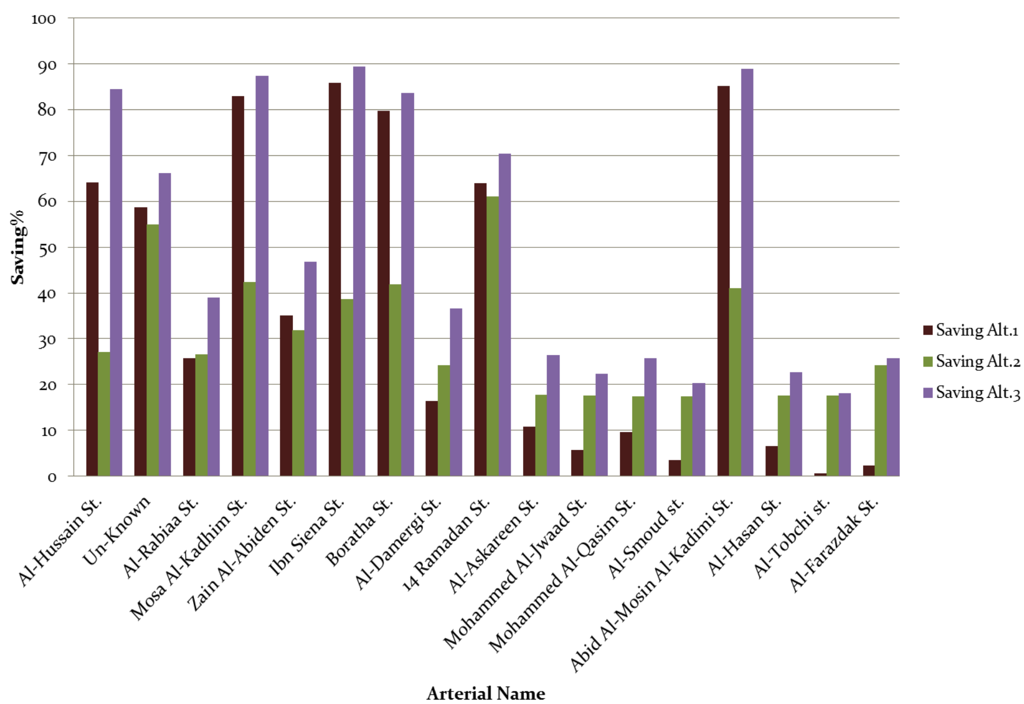

Figure 11. Saving in average delay for arterials under all alternatives

Table 1. Survey methods and equipment

Survey	Method	Equipment and personnel
Traffic volume (for junctions)	Video technique and manual count	Digital video camera and manual count
Traffic volume (for Road network)	Questionnaire	Two trained interviewer groups
Distance	GPS and manual	GIS program with internet connection, Baghdad aerial view digital picture and meters tape

Table 2. Variation of traffic flow at Boratha Mosque intersection (Int.1)

Duration	Volume (vph)
8:00-9:00 am	5371
9:00-10:00 am	5289
10:00-11:00 am	5044
11:00-12:00 am	5107
12:00-1:00 pm	5006
1:00-2:00 pm	5188
2:00-3:00 pm	5041

Table 3. Variation of traffic flow at Al-Shalchiya intersection (Int.2)

Duration	Volume (vph)
8:00-9:00 am	5691
9:00-10:00 am	5468
10:00-11:00 am	5240
11:00-12:00 am	5372
12:00-1:00 pm	5587
1:00-2:00 pm	5535
2:00-3:00 pm	5204

Table 4. Variation of traffic flow at Aden intersection (Int.3)

Duration	Volume (vph)
8:00-9:00 am	4210
9:00-10:00 am	4149
10:00-11:00 am	4056
11:00-12:00 am	4004
12:00-1:00 pm	4144
1:00-2:00 pm	4282
2:00-3:00 pm	4361

Table 5. Performance evaluation of Boratha Mosque intersection (Int.1), current condition

Lane Mov.		Vol. (vph)	c (vph)	g/C	v/c	d (sec)	LOS	App. d. (sec)	App. LOS	Int. d (sec)	Int. LOS
EB	L	271	280	0.22	1.08	120.1	F	138.6	F	408.9	F
	Th	928	863	0.22	1.19	143.9	F				
WB	L	608	273	0.21	2.32	650.3	F	388.7	F		
	Th	514	546	0.21	0.98	79.1	E				
NB	L	561	248	0.17	2.60	779.5	F	551.1	F		
	Th	725	488	0.17	1.71	374.3	F				
SB	L	653	333	0.26	2.18	583.4	F	496.9	F		
	Th	1120	660	0.26	1.88	446.4	F				

Table 6. Performance evaluation of Al-Shalchiya intersection (Int.2), current condition

Lane Mov.		Vol. (vph)	c (vph)	g/C	v/c	d (sec)	LOS	App. d. (sec)	App. LOS	Int. d (sec)	Int. LOS
EB		-	-	-	-	-	-	-	-	461.1	F
WB	L	932	1023	0.27	1.01	57.8	E	57.8	E		
	Th	-	-	-	-	-	-				
NB	L	-	-	-	-	-	-	372.8	F		
	Th	2771	1632	0.33	1.77	372.8	F				
SB	L	1908	772	0.32	2.69	787.6	F	787.6	F		
	Th	-	-	-	-	-	-				

Table 7. Performance evaluation of Aden intersection (Int.3), current condition

Lane Mov.		Vol. (vph)	c (vph)	g/C	v/c	d (sec)	LOS	App. d. (sec)	App. LOS	Int. d (sec)	Int. LOS
EB	L	185	670	0.19	0.28	40.2	D	39.7	D	90.2	F
	Th	197	951	0.19	0.21	39.2	D				
WB	L	263	902	0.2	0.21	39.4	D	57.8	E		
	Th	702	702	0.2	1	79.5	E				
NB	L	1533	1256	0.26	1.22	148.6	F	372.8	F		
	Th	529	1816	0.26	0.29	33.9	C				
SB	L	-	-	-	-	-	-	787.6	E		
	Th	615	705	0.2	0.87	58.1	E				

Table 8. The existing and the best cycle length selected with total delay for intersections

Intersections	The Existing Cycle Length (sec)	The Existing Total Delay (sec/veh)	The Best Cycle Length Selected (sec)	Total Delay after Timing Optimization (sec/veh)
1	115	408.9	120	394.6
2	73	461.9	90	387.6
3	114.0	90.2	83	29.6

Table 9. Performance evaluation of Boratha Mosque intersection (Int.1), alternative (1)

Lane	Mov.	Vol. (vph)	c (vph)	g/C	v/c	d (sec)	LOS	App. d. (sec)	App. LOS	Int. d (sec)	Int. LOS
EB	**L**	271	226	0.17	1.33	225.9	F	263.7	F	394.6	F
	Th	928	695	0.17	1.48	274.7	F				
WB	**L**	608	259	0.2	2.44	709.5	F	429	F		
	Th	514	517	0.2	1.03	97	F				
NB	**L**	561	355	0.25	1.82	423.6	F	266.6	F		
	Th	725	699	0.25	1.19	145.1	F				
SB	**L**	653	312	0.24	2.33	652.4	F	558.6	F		
	Th	1120	620	0.24	2.01	503.9	F				

Table 10. Performance evaluation of Al-Shalchiya intersection (Int.2), alternative (1)

Lane	Mov.	Vol. (vph)	c (vph)	g/C	v/c	d (sec)	LOS	App. d. (sec)	App. LOS	Int. d (sec)	Int. LOS
EB		-	-	-	-	-	-	-	-	387.6	F
WB	**L**	932	540	0.14	1.92	458.7	F	458.7	F		
	Th	-	-	-	-	-	-				
NB	**L**	-	-	-	-	-	-	210.7	F		
	Th	2771	2057	0.41	1.4	210.7	F				
SB	**L**	1908	918	0.37	2.26	598.3	F	598.3	F		
	Th	-	-	-	-	-	-				

Table 11. Performance evaluation of Aden intersection (Int.3), alternative (1)

Lane Mov.		Vol. (vph)	c (vph)	g/C	v/c	d (sec)	LOS	App. d. (sec)	App. LOS	Int. d (sec)	Int. LOS
EB	L	185	427	0.12	0.43	36.9	D	13.7	B	29.6	C
	Th	197	606	0.12	0.33	34.7	C				
WB	L	263	953	0.21	0.28	28	C	46.2	D		
	Th	702	742	0.21	0.95	54.4	D				
NB	L	1533	1760	0.37	0.87	39.6	C	25.5	C		
	Th	529	2544	0.37	0.21	18.1	B				
SB	L	-	-	-	-	-	-	41.9	D		
	Th	615	694	0.2	0.89	47.8	D				

Table 12. Performance evaluation of Boratha Mosque intersection (Int.1), alternative (2)

Lane Mov.		Vol. (vph)	c (vph)	g/C	v/c	d (sec)	LOS	App. d. (sec)	App. LOS	Int. d (sec)	Int. LOS
EB	L	271	437	0.17	0.69	53.1	D	99.7	F	109.7	F
	Th	928	926	0.17	1.11	113.3	F				
WB	L	608	479	0.19	1.32	205.4	F	134.9	F		
	Th	514	710	0.19	0.75	51.4	D				
NB	L	561	546	0.2	1.18	145.4	F	114.9	F		
	Th	725	795	0.2	1.05	91.3	F				
SB	L	653	742	0.3	0.98	68.1	E	97.5	F		
	Th	1120	1091	0.3	1.14	114.7	F				

Table 13. Performance evaluation of Al-Shalchiya intersection (Int.2), alternative (2)

Lane Mov.		Vol. (vph)	c (vph)	g/C	v/c	d (sec)	LOS	App. d. (sec)	App. LOS	Int. d (sec)	Int. LOS
EB		-	-	-	-	-	-	-	-	259.1	F
WB	L	932	1365	0.27	0.76	28.3	C	28.3	C		
	Th	-	-	-	-	-	-				
NB	L	-	-	-	-	-	-	214.1	F		
	Th	2771	2040	0.33	1.41	214.1	F				
SB	L	1908	1087	0.32	1.91	437.1	F	437.1	F		
	Th	-	-	-	-	-	-				

Table 14. Performance evaluation of Aden intersection (Int.3), alternative (2)

Lane Mov.		Vol. (vph)	c (vph)	g/C	v/c	d (sec)	LOS	App. d. (sec)	App. LOS	Int. d (sec)	Int. LOS
EB	L	185	553	0.11	0.33	37.6	D	14.4	B	24.0	C
	Th	197	560	0.11	0.35	37.7	D				
WB	L	263	1016	0.23	0.26	28.5	C	31.2	C		
	Th	702	1131	0.23	0.62	33.2	C				
NB	L	1533	2170	0.34	0.71	27.1	C	23.8	C		
	Th	529	2353	0.34	0.22	20.9	C				
SB	L	-	-	-	-	-	-	27.8	C		
	Th	615	1136	0.23	0.54	31.8	C				

Table 15. Performance evaluation of Boratha Mosque intersection (Int.1), alternative (3)

Lane Mov.		Vol. (vph)	c (vph)	g/C	v/c	d (sec)	LOS	App. d. (sec)	App. LOS	Int. d (sec)	Int. LOS
EB	L	271	444	0.18	0.68	54.2	D	96.5	F	108.7	F
	Th	928	940	0.18	1.1	108.8	F				
WB	L	608	470	0.19	1.35	218.6	F	143.4	F		
	Th	514	696	0.19	0.77	54.4	D				
NB	L	561	549	0.2	1.17	144.7	F	114.8	F		
	Th	725	799	0.2	1.04	91.6	F				
SB	L	653	757	0.31	0.96	65	E	91.8	F		
	Th	1120	1112	0.31	1.12	107.5	F				

Table 16. Performance evaluation of Al-Shalchiya intersection (Int.2), alternative (3)

Lane Mov.		Vol. (vph)	c (vph)	g/C	v/c	d (sec)	LOS	App. d. (sec)	App. LOS	Int. d (sec)	Int. LOS
EB		-	-	-	-	-	-	-	-	190.4	F
WB	L	932	735	0.15	1.41	226.5	F	226.5	F		
	Th	-	-	-	-	-	-				
NB	L	-	-	-	-	-	-	102.1	F		
	Th	2771	2482	0.4	1.16	102.1	F				
SB	L	1908	1302	0.38	1.59	295.4	F	295.4	F		
	Th	-	-	-	-	-	-				

Table 17. Performance evaluation of Aden intersection (Int.3), alternative (3)

Lane Mov.		Vol. (vph)	c (vph)	g/C	v/c	d (sec)	LOS	App. d. (sec)	App. LOS	Int. d (sec)	Int. LOS
EB	L	185	596	0.12	0.31	35.4	D	13.6	B	22.5	C
	Th	197	603	0.12	0.33	35.5	D				
WB	L	263	994	0.22	0.26	28	C	30.7	C		
	Th	702	1107	0.22	0.63	32.7	C				
NB	L	1533	2531	0.4	0.61	21.4	C	18.9	B		
	Th	529	2744	0.4	0.19	16.9	B				
SB	L	-	-	-	-	-	-	35.2	D		
	Th	615	817	0.16	0.75	40.3	D				

Table 18. Performance evaluation of Boratha Mosque intersection (Int.1), alternative (4)

Lane Mov.		Vol. (vph)	c (vph)	g/C	v/c	d (sec)	LOS	App. d. (sec)	App. LOS	Int. d (sec)	Int. LOS
EB	L	271	812	0.23	0.37	25.6	C	25.6	C	34.8	C
	Th	-	-	-	-	-	-				
WB	L	608	824	0.23	0.77	33.8	C	33.8	C		
	Th	-	-	-	-	-	-				
NB	L	561	679	0.25	0.93	49.1	D	41.4	D		
	Th	725	989	0.25	0.84	35.6	D				
SB	L	653	901	0.36	0.81	29.1	C	31.7	C		
	Th	1120	1368	0.36	0.91	33.2	C				

Table 19. Performance evaluation of Al-Shalchiya intersection (Int.2), alternative (4)

Lane Mov.		Vol. (vph)	c (vph)	g/C	v/c	d (sec)	LOS	App. d. (sec)	App. LOS	Int. d (sec)	Int. LOS
EB		-	-	-	-	-	-	-	-	16.4	B
WB	L	932	1219	0.24	0.85	24.4	C	24.4	C		
	Th	-	-	-	-	-	-				
NB		-	-	-	-	-	-	-	-		
SB	L	1908	2312	0.67	0.9	12.4	B	12.4	B		
	Th	-	-	-	-	-	-				

Table 20. Comparisons between all improvements and existing conditions

		Int. 1	Int. 2	Int. 3
Existing Condition	**T. D (sec/veh)**	408.9	461.9	90.2
	Int. LOS	F	F	F
Alternative (1)	**T. D (sec/veh)**	394.6	387.6	29.6
	Int. LOS	F	F	C
	Saving %	3.5	16	67
Alternative (2)	**T. D (sec/veh)**	109.7	259.1	24.0
	Int. LOS	F	F	C
	Saving %	73.2	44	73.3
Alternative (3)	**T. D (sec/veh)**	108.7	190.4	22.5
	Int. LOS	F	F	C
	Saving %	73.4	59	75.1
Alternative (4)	**T. D (sec/veh)**	34.8	16.4	22.5
	Int. LOS	C	B	C
	Saving %	91.5	96.5	75.1

Table 21. Performance of arterials under existing conditions

Arterial Name	Volume	Number of lanes	Presence of median	Section Length (Km)	LOS
Al-Hussain St.	5399	6	No	1.302	F
Al-Hamza	3955	6	Yes	1.169	D
Al-Rabiaa St.	4935	8	Yes	2.284	C
Mosa Al-Kadhim St.	4673	6	Yes	3.538	E
Zain Al-Abiden St.	3520	6	No	1.204	E
Ibn Siena St.	3219	4	Yes	1.512	F
Boratha St.	4611	6	Yes	2.269	E
Al-Damergi St.	1454	4	No	1.227	B
14 Ramadan St.	5416	8	Yes	2.206	D
Al-Askareen St.	2277	6	Yes	1.896	C
Mohammed Al-Jwaad St.	2130	8	Yes	4.273	B
Mohammed Al-Qasim St.	3390	8	Yes	1.344	C
Al-Smoud st.	862	6	Yes	2.268	C
Abid Al-Mohsin Al-Kadimi St.	3711	4	No	1.291	F
Al-Hasan St.	2327	8	Yes	1.845	C
Al-Tobchi st.	108	6	Yes	1.127	D
Al-Farazdak St.	75	2	No	0.502	D

Table 22. Future performance of arterial, target year (2015) & r = 3%.

Arterial Name	Volume	Number of lanes	Presence of median	Section Length (Km)	LOS
Al-Hussain St.	6263	6	N	1.302	F
Al-Hamza	4587	6	Yes	1.169	E
Al-Rabiaa St.	5725	8	Yes	2.284	D
Mosa Al-Kadhim St.	5421	6	Yes	3.538	F
Zain Al-Abiden St.	4083	6	N	1.204	F
Ibn Siena St.	3734	4	Yes	1.512	F
Boratha St.	5349	6	Yes	2.269	E
Al-Damergi St.	1686	4	No	1.227	B
14 Ramadan St.	6282	8	Yes	2.206	D
Al-Askareen St.	2641	6	Yes	1.896	C
Mohammed Al-Jwaad St.	2471	8	Yes	4.273	B
Mohammed Al-Qasim St.	3932	8	Yes	1.344	D
Al-Smoud st.	1000	6	Yes	2.268	C
Abid Al-Mohsin Al-Kadimi St.	4304	4	No	1.291	F
Al-Hasan St.	2699	8	Yes	1.845	C
Al-Tobchi st.	125	6	Yes	1.127	D
Al-Farazdak St.	87	2	No	0.502	D

Table 23. Future performance of arterial, target year (2020) & r = 3%.

Arterial Name	Volume	Number of lanes	Presence of median	Section Length (Km)	LOS
Al-Hussain St.	7235	6	N	1.302	F
Al-Hamza	5299	6	Yes	1.169	F
Al-Rabiaa St.	6613	8	Yes	2.284	D
Mosa Al-Kadhim St.	6262	6	Yes	3.538	F
Zain Al-Abiden St.	4717	6	N	1.204	F
Ibn Siena St.	4314	4	Yes	1.512	F
Boratha St.	6179	6	Yes	2.269	E
Al-Damergi St.	1948	4	No	1.227	C
14 Ramadan St.	7257	8	Yes	2.206	E
Al-Askareen St.	3051	6	Yes	1.896	C
Mohammed Al-Jwaad St.	2855	8	Yes	4.273	B
Mohammed Al-Qasim St.	4542	8	Yes	1.344	D
Al-Smoud st.	1155	6	Yes	2.268	C
Abid Al-Mohsin Al-Kadimi St.	4972	4	No	1.291	F
Al-Hasan St.	3118	8	Yes	1.845	C
Al-Tobchi st.	145	6	Yes	1.127	D
Al-Farazdak St.	101	2	No	0.502	E

Table 24. Arterials LOS and controlling delay, alternative (1)

Arterial Name	LOS	Control Delay
Al-Hussain St.	D	98.0
Al-Hamza	C	25.1
Al-Rabiaa St.	B	24.8
Mosa Al-Kadhim St.	B	24.5
Zain Al-Abiden St.	E	24.3
Ibn Siena St.	C	23.1
Boratha St.	B	28.4
Al-Damergi St.	B	16.2
14 Ramadan St.	B	26.5
Al-Askareen St.	C	19.6
Mohammed Al-Jwaad St.	B	18.2
Mohammed Al-Qasim St.	C	20.7
Al-Smoud st.	C	16.6
Abid Al-Mohsin Al-Kadimi St.	C	22.4
Al-Hasan St.	C	18.5
Al-Tobchi st.	D	15.3
Al-Farazdak St.	D	12.9

Table 25. Arterials LOS and controlling delay, alternative (2)

Arterial Name	LOS	Control Delay
Al-Hussain St.	F	199.0
Al-Hamza	C	27.4
Al-Rabiaa St.	B	24.5
Mosa Al-Kadhim St.	D	82.5
Zain Al-Abiden St.	E	25.5
Ibn Siena St.	E	99.7
Boratha St.	D	81.3
Al-Damergi St.	B	14.7
14 Ramadan St.	B	28.6
Al-Askareen St.	B	18.1
Mohammed Al-Jwaad St.	B	15.9
Mohammed Al-Qasim St.	C	18.9
Al-Smoud st.	C	14.2
Abid Al-Mohsin Al-Kadimi St.	C	88.4
Al-Hasan St.	B	16.3
Al-Tobchi st.	D	12.7
Al-Farazdak St.	C	10.0

Table 26. Arterials LOS and controlling delay, alternative (3)

Arterial Name	LOS	Control Delay
Al-Hussain St.	C	42.4
Al-Hamza	B	20.6
Al-Rabiaa St.	B	20.4
Mosa Al-Kadhim St.	B	18.2
Zain Al-Abiden St.	D	19.9
Ibn Siena St.	B	17.3
Boratha St.	B	23.0
Al-Damergi St.	B	12.3
14 Ramadan St.	B	21.7
Al-Askareen St.	B	16.2
Mohammed Al-Jwaad St.	B	15.0
Mohammed Al-Qasim St.	C	17.0
Al-Smoud st.	C	13.7
Abid Al-Mohsin Al-Kadimi St.	C	16.8
Al-Hasan St.	B	15.3
Al-Tobchi st.	D	12.6
Al-Farazdak St.	C	9.8

Table 27. Comparisons between all improvements and existing conditions

Arterial Name	Existing Condition		Alternative 1			Alternative 2			Alternative 3		
	LOS	C.D.	LOS	C. D.	Saving%	LOS	C. D.	Saving%	LOS	C. D.	Saving%
Al-Hussain St.	F	272.8	D	98.0	64.1	F	199.0	27.1	C	42.4	84.5
Al-Hamza	D	60.8	C	25.1	58.7	C	27.4	54.9	B	20.6	66.1
Al-Rabiaa St.	C	33.4	B	24.8	25.7	B	24.5	26.6	B	20.4	38.9
Mosa Al-Kadhim St.	E	143.2	B	24.5	82.9	D	82.5	42.4	B	18.2	87.3
Zain Al-Abiden St.	E	37.4	E	24.3	35.0	E	25.5	31.8	D	19.9	46.8
Ibn Siena St.	F	162.4	C	23.1	85.8	E	99.7	38.6	B	17.3	89.3
Boratha St.	E	139.9	B	28.4	79.7	D	81.3	41.9	B	23.0	83.6
Al-Damergi	B	19.4	B	16.2	16.5	B	14.7	24.2	B	12.3	36.6
14Ramadan	D	73.4	B	26.5	63.9	B	28.6	61.0	B	21.7	70.4
AlAskareen St.	C	22.0	C	19.6	10.9	B	18.1	17.7	B	16.2	26.4
Mohammed Al-Jwaad	B	19.3	B	18.2	5.7	B	15.9	17.6	B	15.0	22.3
Mohammed Al-Qasim	C	22.9	C	20.7	9.6	C	18.9	17.5	C	17.0	25.8
Al-Smoud	C	17.2	C	16.6	3.5	C	14.2	17.4	C	13.7	20.3
Abid Al-Mohsin Al-Kadimi St.	F	150.0	C	22.4	85.1	C	88.4	41.1	C	16.8	88.8
Al-Hasan St.	C	19.8	C	18.5	6.6	B	16.3	17.7	B	15.3	22.7
Al-Tobchi st.	D	15.4	D	15.3	0.6	D	12.7	17.5	D	12.6	18.2
Al-Farazdak	D	13.2	D	12.9	2.3	C	10.0	24.2	C	9.8	25.8

Table 28. Comparative analysis of MOEs between the existing condition and the alternative no.4 at all intersections, target year (2015) & r = 3%.

	EXISTING CONDITION		ALTERNATIVE (4)		SAVING%
INTERSECTIONS	T.D (sec/veh)	LOS	T.D (sec/veh)	LOS	
1	408.9	F	54.9	D	86.6
2	461.9	F	38.7	D	91.6
3	60.0	E	21.3	C	64.0

Table 29. Comparative analysis of MOEs between the existing condition and the alternative no.4 at all intersections, target year (2020) & r = 3%.

INTERSECTIONS	EXISTING CONDITION		ALTERNATIVE (4)		SAVING%
	T.D (sec/veh)	LOS	T.D (sec/veh)	LOS	
1	408.9	F	103.9	F	74.6
2	461.9	F	98.7	F	78.6
3	98	F	32.3	C	67

Table 30. Comparisons between all improvements and existing conditions, target year (2015) & r = 3%

Arterial Name	Existing Condition		Alternative 1			Alternative 2			Alternative 3		
	LOS	C.D.	LOS	C. D.	Saving%	LOS	C. D.	Saving%	LOS	C. D.	Saving%
Al-Hussain St.	F	384.6	F	181.7	52.8	F	299.6	22.1	E	117.0	69.6
Al-Hamza	E	137.1	C	28.2	79.4	D	78.9	42.5	B	22.9	83.3
Al-Rabiaa St.	D	101.4	B	27.8	72.6	C	47.2	53.5	B	22.6	77.7
Mosa Al-Kadhim St.	F	234.1	D	69.2	70.4	F	164.1	29.9	B	22.9	90.2
Zain Al-Abiden St.	F	102.6	E	26.9	73.8	F	52.4	48.9	D	22.0	78.6
Ibn Siena St.	F	256.2	C	32.4	87.4	F	184.1	28.1	C	19.9	92.2
Boratha St.	E	225.5	C	67.4	70.1	E	162.2	28.1	B	27.5	87.8
Al-Damergi	B	21.2	B	17.0	19.8	B	16.0	24.5	B	12.9	39.2
14Ramadan	D	152.1	C	39.0	74.4	D	92.3	39.3	B	24.6	83.8
AlAskareen St.	C	23.7	C	20.6	13.1	C	19.5	17.7	B	17.1	27.8
Mohammed Al-Jwaad	B	20.1	B	18.8	6.5	B	16.6	17.4	B	15.5	22.9
Mohammed Al-Qasim	D	25.0	C	21.9	12.4	C	20.5	18.0	C	18.1	27.6
Al-Smoud	C	17.6	C	16.8	4.5	C	14.5	17.6	C	13.9	21.0
Abid Al-Mohsin Al-Kadimi St.	F	409.3	C	27.3	93.3	F	171.0	58.2	C	19.1	95.3
Al-Hasan St.	C	20.8	C	15.3	26.4	B	17.1	17.8	B	15.9	23.6
Al-Tobchi st.	D	15.4	D	15.3	0.6	D	12.7	17.5	D	12.7	17.5
Al-Farazdak	D	13.3	D	12.9	3.0	C	10.1	24.1	C	9.8	26.3

Table 31. Comparisons between all improvements and existing conditions, target year (2020) & r = 3%

Arterial Name	Existing Condition		Alternative 1			Alternative 2			Alternative 3		
	LOS	C.D.	LOS	C. D.	Saving%	LOS	C. D.	Saving%	LOS	C. D.	Saving%
Al-Hussain St.	F	510.7	F	276.2	45.9	F	413.0	19.1	F	202.0	60.4
Al-Hamza	F	223.8	D	62.8	71.9	F	156.6	30.0	C	26.9	88.0
Al-Rabiaa St.	D	182.4	C	62.0	66.0	E	119.4	34.5	B	26.4	85.5
Mosa Al-Kadhim St.	F	336.5	F	145.9	56.6	F	256.4	23.8	D	84.9	74.8
Zain Al-Abiden St.	F	184.3	E	38.5	79.1	F	125.5	31.9	E	25.0	86.4
Ibn Siena St.	F	362.4	E	99.5	72.5	F	279.4	22.9	C	43.9	87.9
Boratha St.	E	284.8	E	142.8	49.9	F	253.1	11.1	D	83.9	70.5
Al-Damergi	C	27.5	B	17.9	34.9	B	17.7	35.6	B	13.6	50.5
14Ramadan	E	241.2	E	108.7	54.9	E	172.3	28.6	C	53.4	77.9
AlAskareen St.	C	26.0	C	21.8	16.2	C	21.3	18.1	B	18.0	30.8
Mohammed Al-Jwaad	B	21.2	B	19.5	8.0	B	17.5	17.5	B	16.1	24.1
Mohammed Al-Qasim	D	27.9	D	23.6	15.4	C	22.7	18.6	C	19.4	30.5
Al-Smoud	C	18.0	C	17.1	5.0	C	14.9	17.2	C	14.1	21.7
Abid Al-Mohsin Al-Kadimi St.	F	539.1	E	88.5	83.6	F	264.3	51.0	C	34.4	93.6
Al-Hasan St.	C	22.0	C	20.1	8.6	C	18.1	17.7	B	16.6	24.5
Al-Tobchi st.	D	15.4	D	15.3	0.6	D	12.8	16.9	D	12.7	17.5
Al-Farazdak	E	13.4	D	13.0	3.0	C	10.2	23.9	C	9.8	26.9

Fire Flame Influence on the Behavior of reinforced Concrete Beams Affected by Repeated Load

Dr.Shatha Dheyaa Mohammed
Lecturer
College of Engineering- University of Baghdad
Email:Shathadhia@yahoo.com

Dr. Nada Mahdi Fawzi
Professor
College of Engineering- University of Baghdad
Email: naljalawi@yahoo.com

ABSTRACT

The influence and hazard of fire flame are one of the most important parameters that affecting the durability and strength of structural members. This research studied the influence of fire flame on the behavior of reinforced concrete beams affected by repeated load. Nine self- compacted reinforced concrete beams were castellated, all have the same geometric layout (0.15x0.15x1.00) m, reinforcement details and compressive strength (50 Mpa).

To estimate the effect of fire flame disaster, four temperatures were adopted (200, 300, 400 and 500) ^{o}C and two method of cooling were used (graduated and sudden). In the first cooling method, graduated, the tested beams were leaved to cool in air while in the second method, sudden, water splash was used to reduce the temperature. Eight of the tested beams were divided in to four groups, each were burned to one of the adopted temperature for about half an hour and cooled by the adopted cooling methods (one by sudden cooling and the other by graduated cooling). After burning and cooling the beams were tested under the effect of repeated load (loading – unloading) for five cycle and then up to failure.

As a compared with the non- burned beam, the results indicated that the ultimate load capacity of the tested beams were reduced by (16, 23, 54 and 71)% after being burned to (200, 300, 400 and 500) ^{o}C , respectively, for a case of sudden cooling and by (8, 14, 36 and 64)% , respectively, for a case of graduated cooling. It was also found that the effect of sudden cooling was greater than that in a case of graduated cooling.

Regarding the failure mode, there was a different between the non-burred beam and the other ones even that all of them had the same geometric layout, compressive strength and reinforcement details. The failure mode for all burned beams was combined shear- flexure failure which was belong to the reduction in the compressive strength of the concrete due to the effect of the temperature rising , while the failure mode of the non-burned beam was flexure failure which was compatible with the preliminary design. It was also detected that the residual deflection proportion directly with the temperature, as the temperature increase to (200, 300, 400 and 500) ^{o}C the residual deflection compared with the non-burned beam increased by (32, 48, 326 and 358)% for a case of sudden cooling and by (13, 29, 303 and 332)% for a case of graduated cooling. Another effect was appear represented by the method of cooling, the results showed that the sudden cooling had more effect on the residual deflection than the graduated cooling by (15-6)% approximately. To vanish the residual deflection, numbers of cycle (loading-unloading) were required. It was found that this number increase as the temperature of burning increased and it's also larger in a case of sudden cooling.

Key words: concrete beam, self- compacted, fire flame, repeated load.

تأثيراللهب على سلوك العتبات الخرسانية المسلحة الخاضعة لتاثير الاحمال الدورية

د. شذى ضياء محمد
مدرس
كلية الهندسة - جامعة بغداد

د.ندى مهدي فوزي
استاذ
كلية الهندسة - جامعة بغداد

الخلاصة

يعتبر تاثير ومخاطر لهب النيران من اكثر العوامل المؤثرة على ديمومة ومقاومة العناصر الإنشائية . يدرس هذا البحث تأثير لهب النيران على تصرف العتبات الخرسانية المسلحة الخاضعة لتأثير الأحمال الدورية. إشتمل برنامج البحث صب تسعة من العتبات الخرسانية المسلحة باستخدام خرسانة ذاتية الرص بمقاومة انضغاط (50 Mpa) جميعها تتطابق في الابعاد الهندسية (0.15x0.15x1.00) م وتفاصيل التسليح.

لتخمين تاثير مخاطر لهب النيران تم إعتماد اربع درجات حرارة مختلفة هي على التوالي (200, 300, 400 and 500) درجة سيليزية كما تم إعتماد طريقتين للتبريد ، التبريد التدريجي والفجائي. في الطريقة الاولى للتبريد (التدريجي) يترك النموذج بعد حرقه في الهواء الطلق ليبرد اما في الطريقة الثانية (التبريد المفاجئ) فيستخدم الماء للتبريد إذ يرش النموذج بكمية كافية من الماء لتبريده. قسمت ثماني من النماذج المستخدمة الى اربعة مجاميع كل مجموعة تم حرقها الى واحدة من درجات الحرارة المعتمدة في البحث ولمدة نصف ساعة وتم تبريد نموذجي كل مجموعة بواحدة من طرق التبريد المعتمدة (التبريد التدريجي او الفجائي). بعد إتمام عملية الحرق والتبريد تم فحص النماذج تحت تاثير الاحمال الدورية ولخمس دورات ومن ثم الى مرحلة الفشل.

مقارنة مع النموذج غير المحروق، بينت النتائج إنخفاض قيمة الحمل الأقصى للنماذج المفحوصة بمعدل %(71 , 54 ,23 ,16) لدرجات الحرق المعتمدة (500 , 400 ,300 ,200) على التوالي لحالة التبريد الفجائي و بمعدل %(64 , 36 ,14 ,8) لحالة التبريد التدريجي. كما بينت النتائج بان تأثير التبريد الفجائي أكبر من تأثير التبريد الفجائي وان هذا التباين بين الطريقتين يقل بزيادة درجة حرارة الحرق.

فيما يخص طور الفشل، كان هناك إختلاف بين النموذج غير المحروق وبقية النماذج المحروقة بالرغم من تطابق الأبعاد الهندسية ، مقاومة الإنضغاط وتفاصيل التسليح لجميع النماذج المفحوصة. بالنسبة للنماذج المحروقة . كان طور الفشل في جميع النماذج المحروقة مركبا (قص – انحناء) نتيجة لإنخفاض مقاومة الانضغاط في الخرسانة بفعل تاثير حرارة الحرق في حين كان طور الفشل في النموذج غير المحروق (انحناء) وهو ما صمم عليه النموذج. فيما يتعلق بالاحمال الدورية تبين بان الهطول المتبقي يتناسب طرديا مع درجة حرارة الحرق كما تبين تأثر مقدار الهطول المتبقي بطريقة التبريد فللتبريد الفجائي تاثير اكبر على مقدار الهطول المتبقي بنسبة تتراح بين %(6-15) تقريبا.

الكلمات الرئيسية: العتبات الخرسانية، خرسانة ذاتية الرص، اللهب ، الاحمال الدورية.

1. INTRODUCTION

Exposure to high temperatures resulting from the fires is one of the common things in concrete and steel buildings. In such case, concrete composition will suffer from self-deterioration due to the difference in the thermal expansion of its components. Fletcher et al 2007, stated that, the free water evaporates when concrete heated, and above 100 ^{o}C, approximately, there will be a releasing of water that chemically bonds in the hydrated calcium silicate. In some cases, the surface layer of concrete specimen is not able to resist the pressure of the water and steam, and spalling occurs. Shrinkage of the hydrated cement paste will accurse due to the released water if the concrete dose not spall, while both the reinforcing bars and the coarse aggregate will subject to thermal expansion. Consequently, stresses will develop in the composite material and form micro cracks through the matrix. Above approximately 400 ^{o}C the crystals calcium hydroxide begin decomposing into calcium oxide and water process reaching its highest intensity at above 535 ^{o}C.

Venkatesh, K. 2014, indicated that the compressive strength of the concrete decrease slightly up to 400 ^{o}C, then it decreased rapidly when it reached about 600 ^{o}C then it began to diminish continuously as temperature increased more and more till approximately disappeared at 1000 ^{o}C.
Many theoretical researches or finite element models have been conducted to study the behavior of different structural elements exposed to high temperature, **Obaidat and Haddad 2016, Lakhani et. al. 2014, Neno et. al. 2013**, but a very little experimental works were carried out to investigate the behavior of burred beams under the effect of repeated load, therefore an experimental program was performed to find the behavior, ultimate load and the residual deflection of self-compacted concrete beams subjected to fire flame under the effect of repeated load.

2. EXPERIMENTAL PROGRAM:

Three stages were included in the program of the experimental work. In the first stage, nine beams were castled and cured using self-compacted concrete of (50 Mpa) compressive strength and mix proportion as illustrated in **Table 1,** the properties of the consuming materials were illustrated in **Table 2** up to **Table 10.** All the tested beams had the same geometric layout and reinforcement details (0.15x0.15) m as cross section and (1.00) m total length, **Fig. 1**.
Burning the beams was the second stage of the experimental program, eight of the tested beams were divided into four groups each were burned to one of the adopted temperature (200, 300, 400 and 500) ^{o}C using a steel furnace that manufactured by 3mm thick plate bents like two L-shape with a capacity of two specimens, **Fig. 2**. The clear space around the beam was 500mm height by 400mm width and 2600mm length. These dimensions provide enough space around the beam to reach the fire flame from the sources and to ensure that the flame are not concentrated on a limited area but distributed on a wide area of the beam bottom and sides. Fire sources were designed as a network of methane burners nozzles, the nozzles were allocated, four in each side of the furnace. Two thermocouples were used, one for each beam, to monitoring the temperature. The rate of temperature increasing was adopted to be the same for all burning possess (3-5^{o}C /min), approximately, and after reaching the adopted temperature of 200, 300, 400 and 500 ^{o}C, the beams kept at the same temperature for half an hour. During the burning process time-deflection was measured by a dial gauge of 0.01 mm sensitivity placed at the mid-top point, **Fig. 2**.Then after the burned beams of a cetin group were cooled by the adopted methods (one gradually by leaving at lab temperature and the other suddenly by using water splash). The last stage was the repeated loading test. Each beams was tested under the effect of repeated load for five cycle then after up to failure. The adopted peak load of each cycle was (2500 kN), approximately.

3. RESULTS AND DISCUSSION

Results discussion considered two main items. The first focus on the output data of the burning stage. In this stage, cracks were generated on all beam surfaces with an intensity increased with the increasing of burning temperature, **Fig. 4** up to **Fig. 11**. For an individual beam the generated cracks were more distributed in the bottom surface (tension zone) due to the deflected shape produced by increasing the temperature and these cracks were mostly extended towered the side surfaces of the beam **Fig. 4** up to **Fig. 11**.There was also an increasing in the maximum crack width with the increasing of the fire temperature to reach 0.45 mm in a case of 500 ^{o}C and sudden cooling, **Table 11.** The results of this stage also improve the effect of the cooling method on the intensity of the generated cracks. Sudden cooling had more effect to generate cracks due to the variation in the rate of temperature rising and rate of temperature reducing (sudden cooling) which had a damage effect on the bond between concrete composite materials. Another phenomena was appeared in this stage this is the spalling of the concrete surfaces, all the beams that burned up to 400 ^{o}C and greater in addition to the beam that burned up to 300 ^{o}C with sudden cooling were spalled, **Fig.6** up to **Fig. 11**. This is usually belong to the rapid varying in the interior temperature caused by sudden cooling and/or high burning temperature that expand the consuming materials of the concrete (sand and gravel) and steel reinforcement, **DeHaan, John D, 2006, NFPA 921, 2004, Lentini, John J.,2006.**

During this stage, middle deflection of the tested beams was recorded versus the measured temperature. The trend of the deflection-temperature curves, **Fig. 12**, showed the compatibility between the curves in a case of individual temperature (same temperature and different method of cooling) and between cases of different temperature. This improve the control of the temperature rising rate that adopted in the test.

Repeated-load test was the second stage to be discussed. The results of this stage improved the effect of both temperature rise and method of cooling on the ultimate load capacity of the burned beams. Regarding the burning temperature, there was indirect proportion with the ultimate load capacity, increasing the temperature to (200, 300, 400 and 500) ^{o}C produced a reduction in ultimate load capacity by (16, 23, 54 and 71)% in a case of sudden cooling and by (8, 14, 36 and 64)% in a case of graduate cooling. While the effect of cooling method demonstrate that sudden cooling had more influence on the reduction of ultimate load capacity.

Even that the preliminary design of all the tested beams was checked to be flexure failure, the failure mode of all the burned beams was combined shear-flexure mode with different degree of participation between shear and flexure failure. As the burning temperature increase the percentage of shear failure increase and shear cracks began to generate in earlier stage of loading, **Fig. 13**. This is belong to the decrease in the compressive strength of concrete due to the breakdown of interfacial bond which is caused by the incompatible volume change between the concrete components during heating and cooling , **Georgali, B. and Tsakiridis, P. 2005, Koksal, et. al. 2011**.

Regarding the residual deflection, there was a variation in the behavior of the tested beams during the repeated-load. It was detected that the increasing in the burning temperature cause an increasing in the residual deflection by (32, 48, 326 and 358)% as the temperature increase to (200, 300, 400 and 500) ^{o}C for a case of sudden cooling and by (13, 29, 303 and 332)% for a case of graduated cooling and number of cycle that required to vanish the residual deflection.

4. CONCLUSIONS:

1. As a compared with the non- burred specimen, the results indicated that the ultimate load capacity of the tested specimens were reduced by (16, 23, 54 and 71)% after being burned to (200, 300, 400 and 500) ^{o}C , respectively, for a case of sudden cooling and by (8, 14, 36 and 64)% , respectively.
2. The effect of sudden cooling on the ultimate load capacity was greater than of that in a case of graduated cooling and this variance was reduced as the temperature increased.
3. There was a different in the failure mode between the non-burred specimen and the other ones even that all of them had the same geometric layout, compressive strength and reinforcement details. The failure mode for all burred specimens was combined shear- flexural failure which is belong to the reduction in the compressive strength of the concrete due to the effect of the

temperature, while the failure mode of the non-burred specimen was flexural failure which was compatible with the design.

4. It was detected that the residual deflection proportion directly with the temperature, as the temperature increase to (200, 300, 400 and 500) ^{o}C the residual deflection compared with the non-burned beam will be increased by (32, 48, 326 and 358)% for a case of sudden cooling and by (13, 29, 303 and 332)% for a case of graduated cooling.
5. Method of cooling affected the residual deflection. The result showed that the sudden cooling had more effect on the residual deflection than the graduated by (15-6)%, approximately.
6. After burning, cracks were performed on the concrete surface of the beams especially in tension zone (bottom surface), and these cracks increase in length, width and depth as the fire flame temperature increase.
7. Method of cooling had an effect on the intensity and width of the generated cracks, the sudden
8. The required number of cycles to vanish the residual deflection proportion directly with the fire temperature and sudden cooling method.

REFERENCES

- DeHaan, John D., 2006., *Kirk's Fire Investigation*, 6th Edition. pp 258-261.

- Fletcher, L.A., Stephen W. J., Torero, R. O., and Asif U., 2007, *Behaviour of Concrete*
    - *Structures in Fire*, Thermal Science, Vol. 11, No. 2, pp37-52.

- Georgali, B. and Taskiridis, P.E, 2005, *Microstructure of Fire-Damaged Concrete. A case study*, Cement and Concrete Composites, www. Elsevier.com, 27, pp 255-259.

- Hitesh, L., Tarvinder, S., Akanshu, S., Reddy, G.R. and Singh, R.K. ,2014 ,*Prediction of post Fire load deflection response of RC flexural members using simplistic numerical approach*, Structural Engineering and Mechanics, An Int'l Journal Vol. 50 , No. 6.

- Koksal, F. Gencel, O., Brostow, W. and Hagg Lobland H.E., 2011, *Effect of High Temperature on Mechanical and Physical Properties of Light-weight Cement Based Refractory Including Expanded Vermiculite*, Material Research Innovations, Vol. 16, No. 1 , pp 7-13.

- Lentini, John J.,*2006, Scientific Protocols for Fire Investigation, pp 453-459*

- NFPA 921, 2004, *Guide To Fire and Explosion Investigations*. 6th Edition. Section 6.6.

- Neno, T., Alen, H. and Ivica, B., 2013, *The behaviour of structures under Fire – numerical model with experimental verification* , An Int'l Journal ,Vol. 15, No. 3.

- Venkatesh, K., 2014, *Properties of Concrete at Elevated Temperature*, Hindawi Publishing Corporation , ISRN Civil Engineering, 15 pages, Vol. 2014, Article ID 468510, http// dx.doi.org/10.1155/2014/468510 .

- Yasmeen T. Obaidat and Rami H. H., 2016, *Prediction of residual mechanical behavior of heat-exposed LWAC short column: a NLFE model* ,Structural Engineering and Mechanics, An Int'l Journal Vol. 57 ,No. 2.

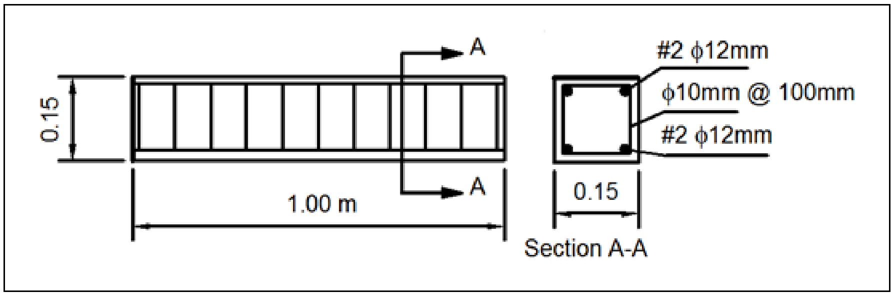

Figure 2. Steel finance setup.

Figure 3. Test Setup.

Figure 1. Geometric layout and reinforcement details of the tested beams.

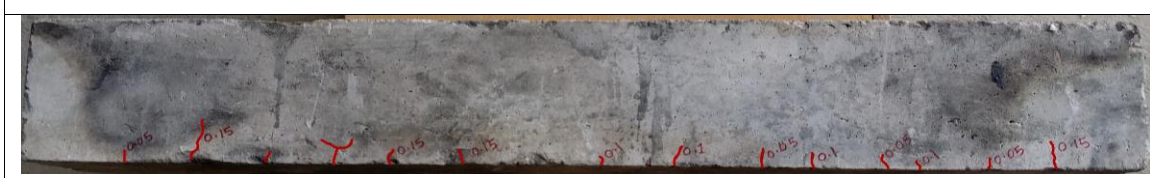

S.V 1

S.V.2

B.V.

Figure 4. Surface of specimen T200S after fire test.

S.V. 1

S.V.2

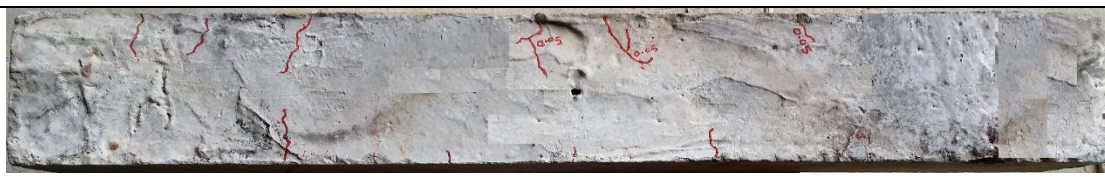

B.V.

Figure 5. Surface of specimen T200G after fire test.

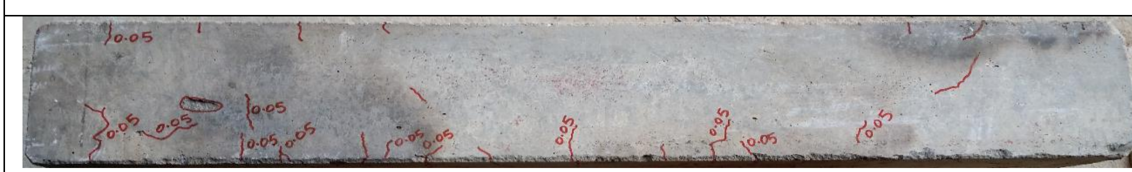

S.V. 1

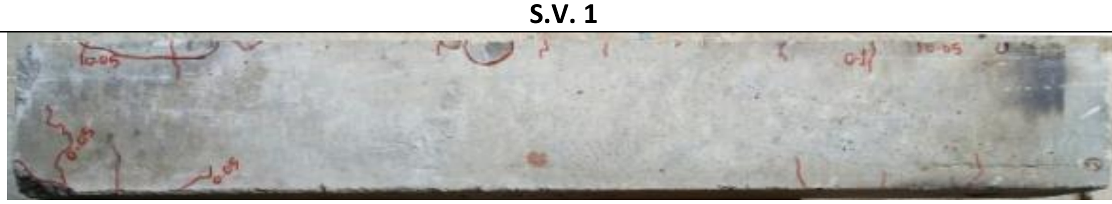

S.V.2

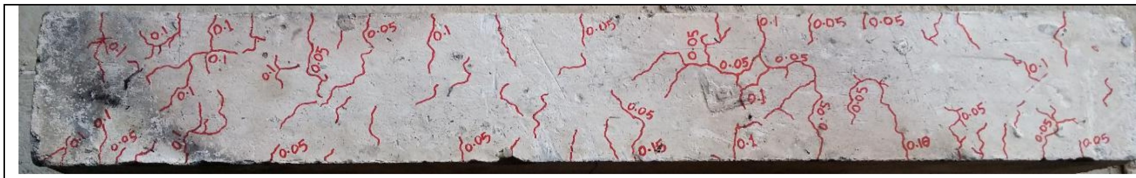

B.V.

Figure 6. Surface of specimen T300S after fire test.

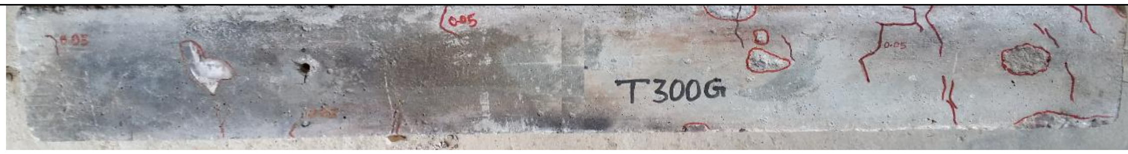

S.V. 1

S.V.2

B.V.

Figure 7. Surface of specimen T300G after fire test.

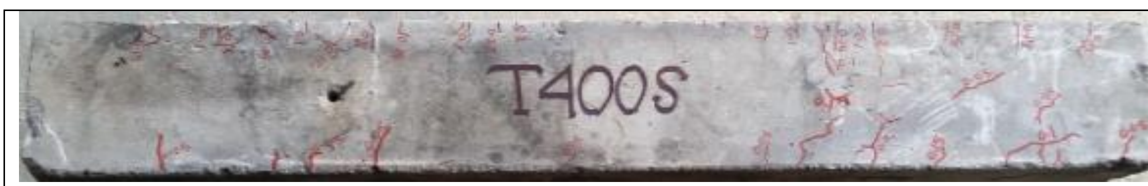

S.V. 1

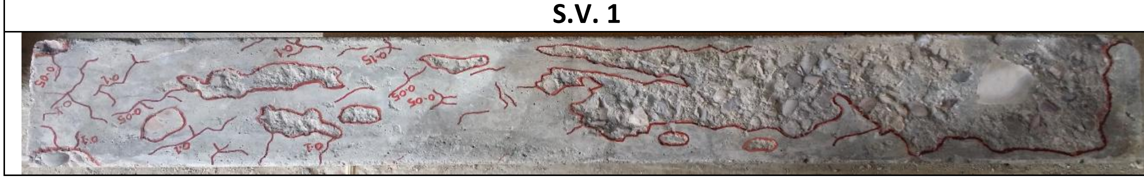

S.V.2

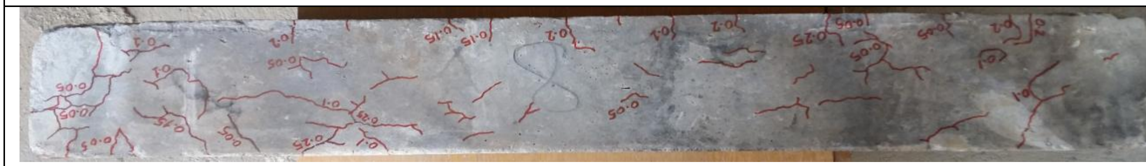

B.V.

Figure 8. Surface of specimen T400S after fire test.

S.V. 1

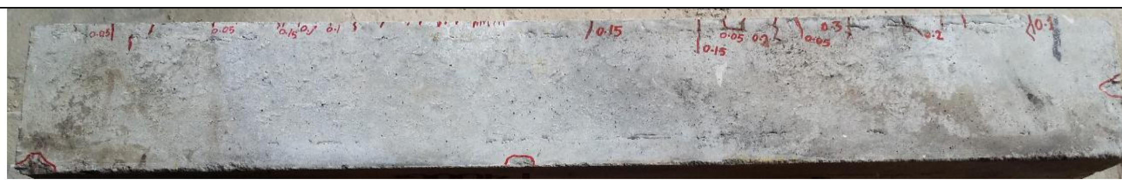

S.V.2

B.V.

Figure 9. Surface of specimen T400G after fire test.

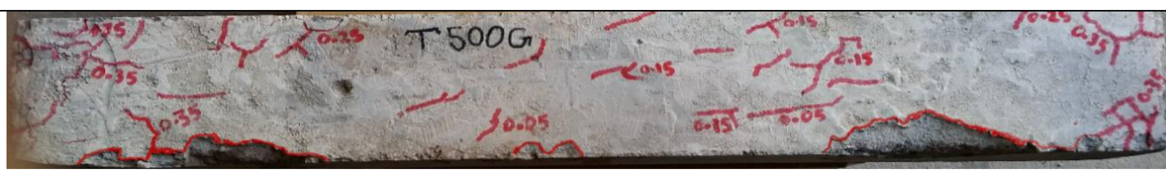

S.V. 1

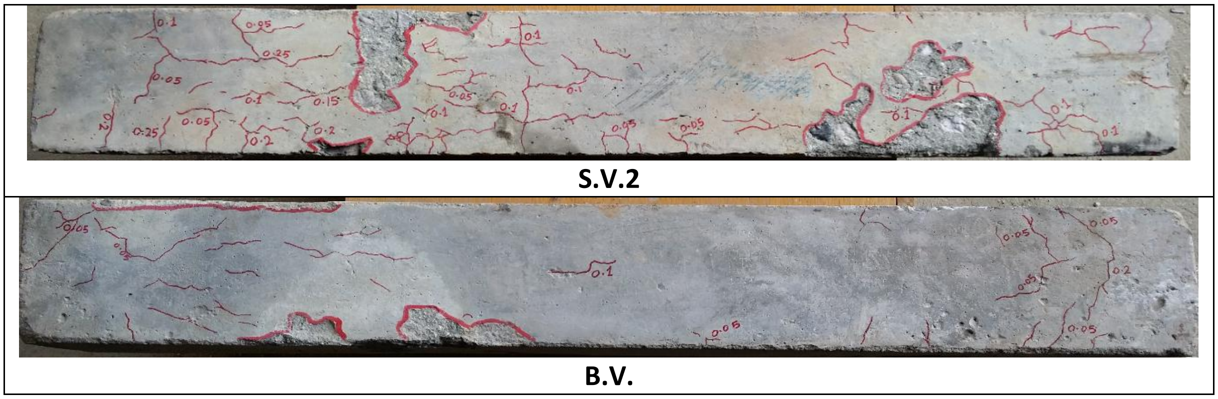

Figure 10. Surface of specimen T500G after fire test.

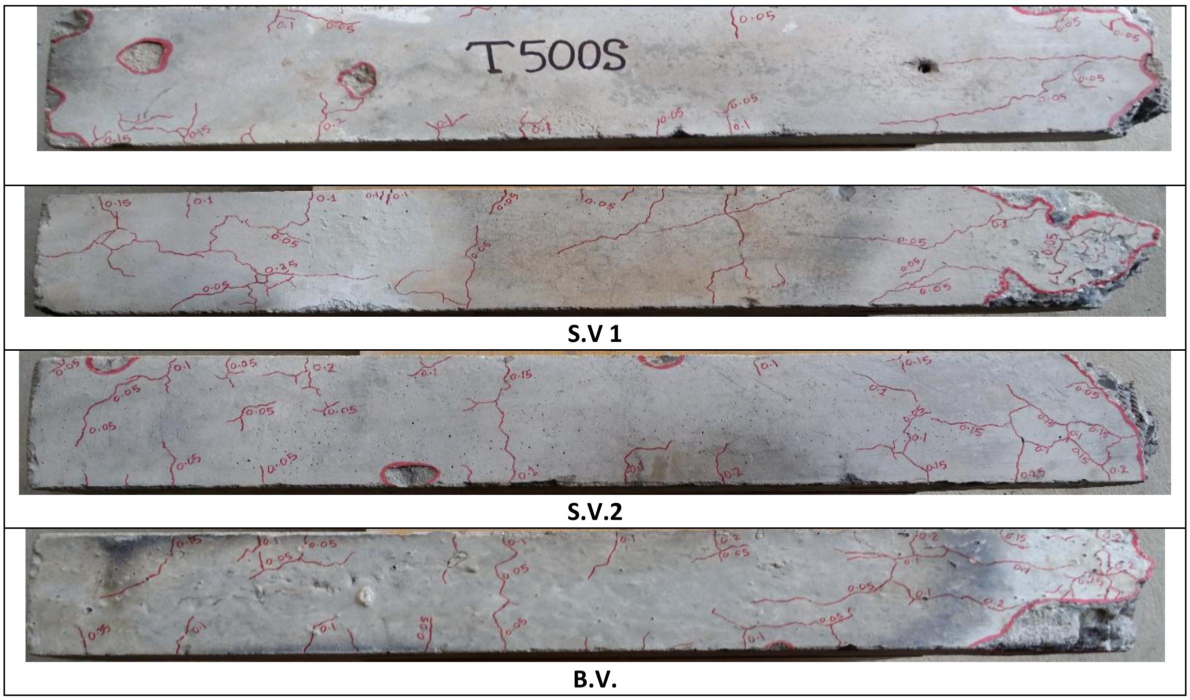

Figure 11. Surface of specimen T500S after fire test.

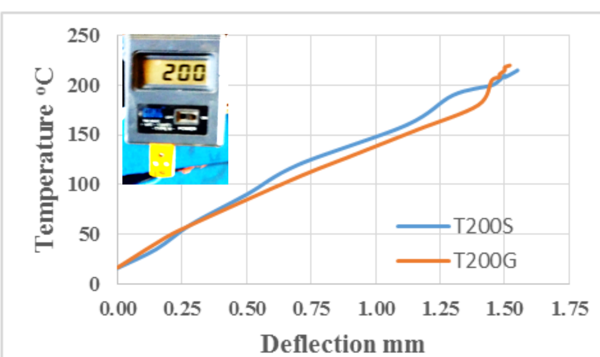

(a) Temperature = 200 °C

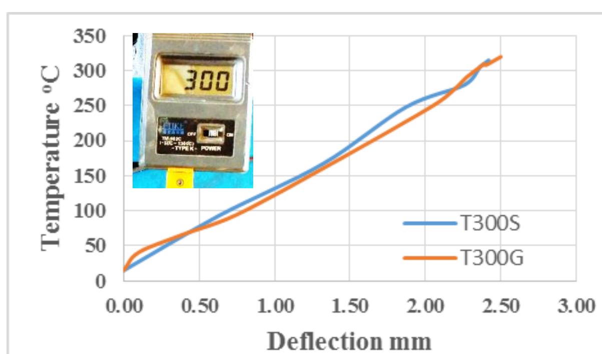

(b) Temperature = 300 °C

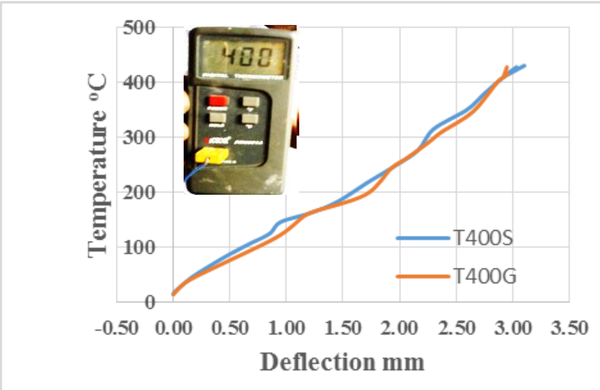

(c) Temperature = 400 ^{o}C

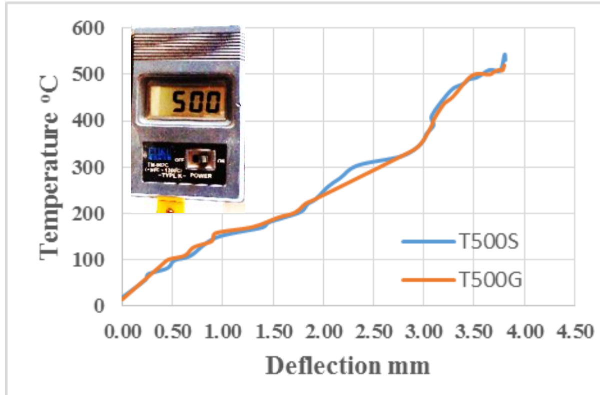

(d) Temperature = 500 ^{o}C

Figure 12. Deflection – temperature curves at burning test.

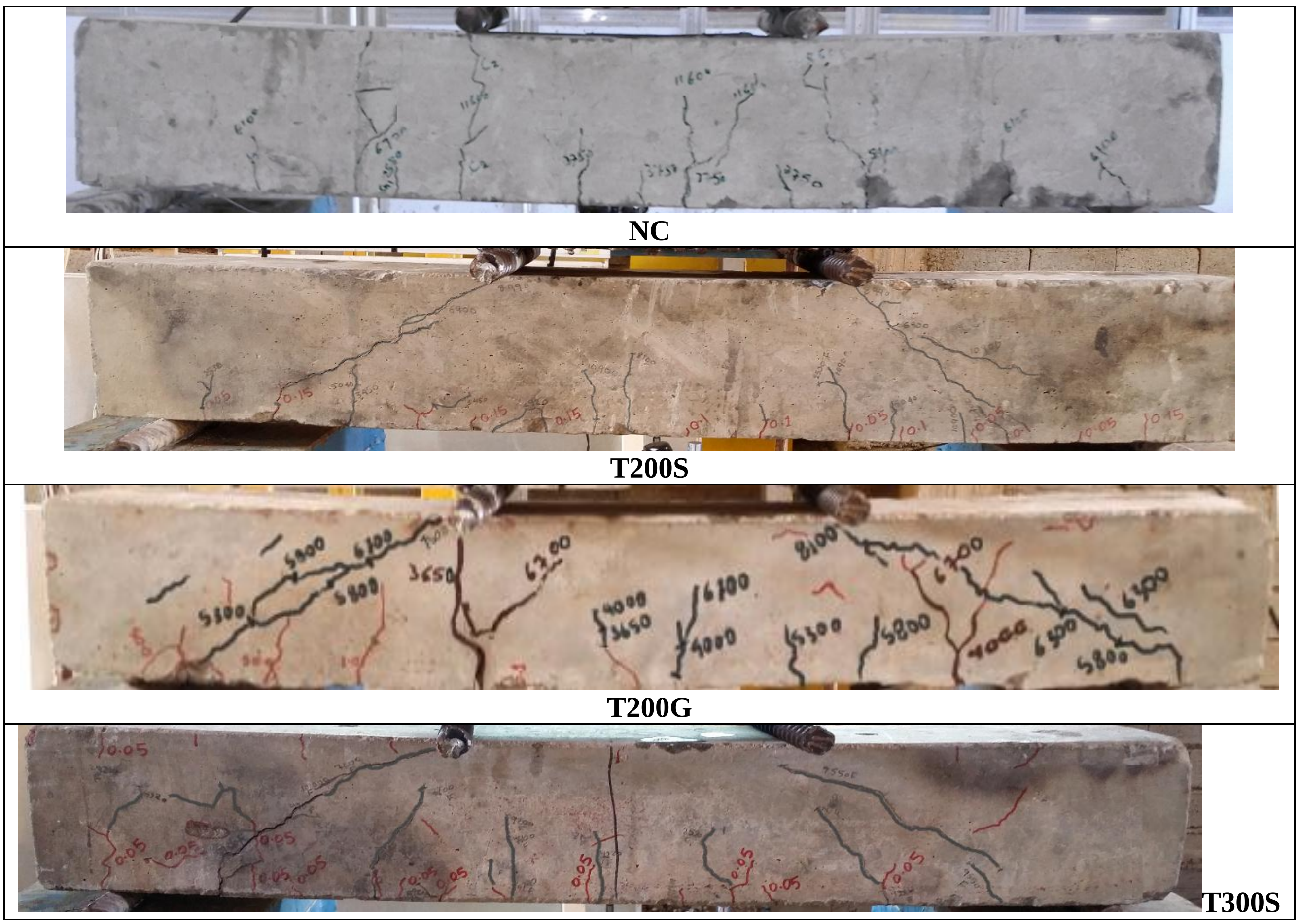

T300G

T400S

Figure 13. Crack pattern of specimens after repeated – load test.

T400G

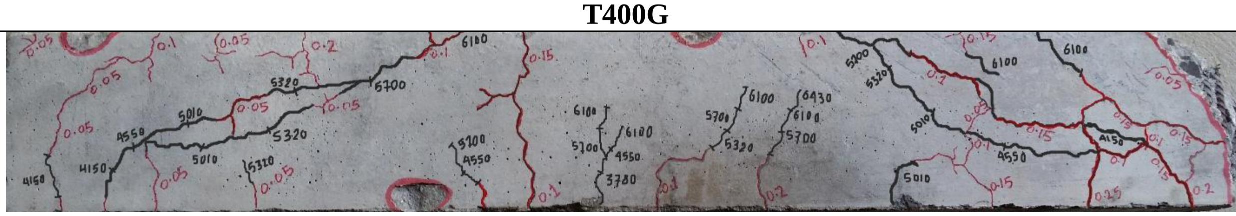

T500S

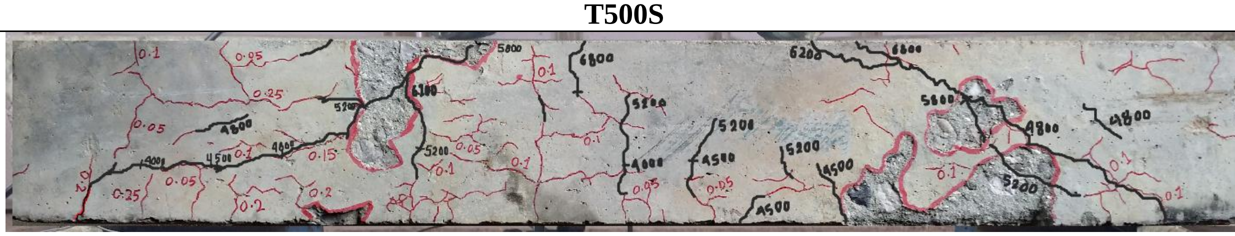

T500G

Figure 13. Crack pattern of specimens after repeated – load test (Continue).

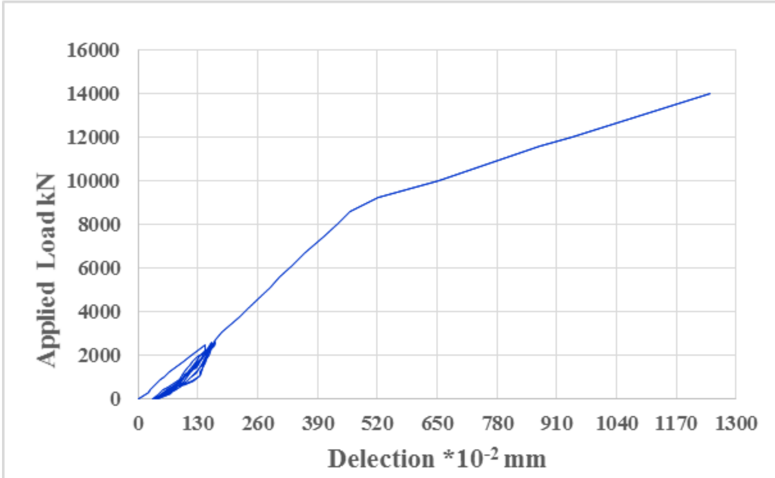

Figure 14. Load- central deflection of specimen WOF tested under repeated load

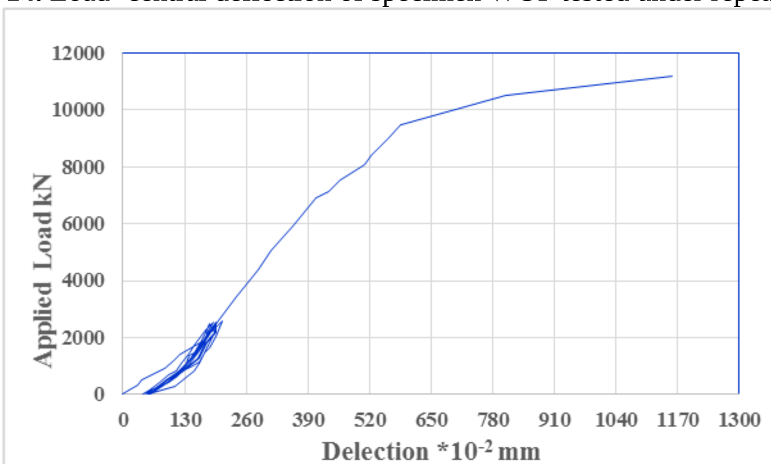

Figure 15. Load- central deflection of specimen T200S tested under repeated load.

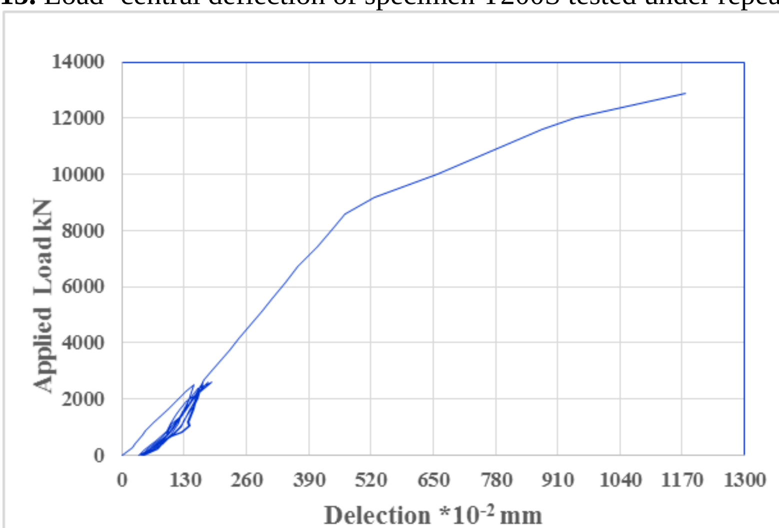

Figure 16. Load- central deflection of specimen T200G tested under repeated load

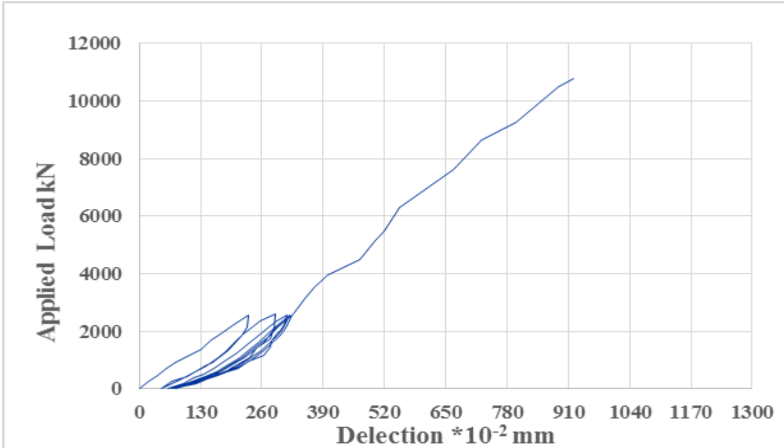

Figure 17. Load- central deflection of specimen T300S tested under repeated load

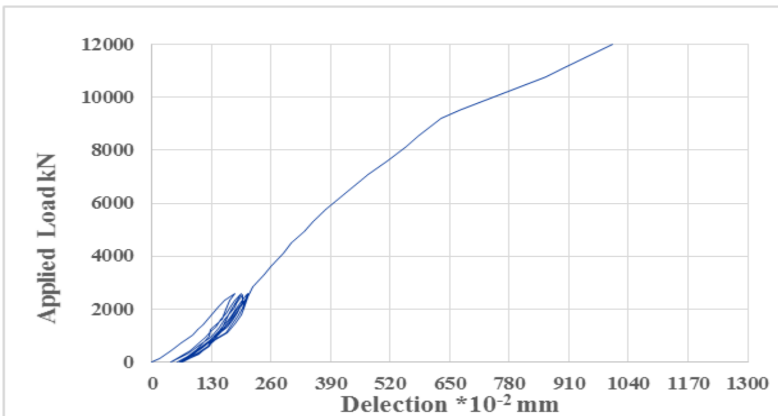

Figure 18. Load- central deflection of specimen T300G tested under repeated load

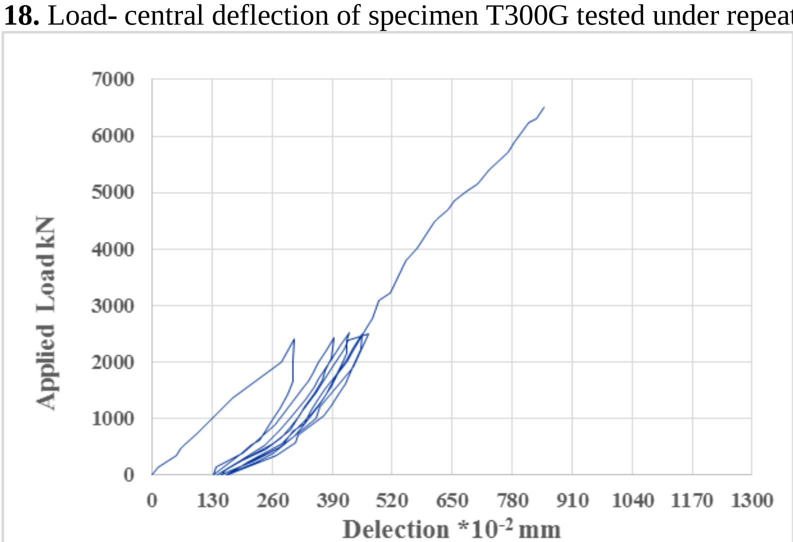

Figure 19. Load- central deflection of specimen T400S tested under repeated load

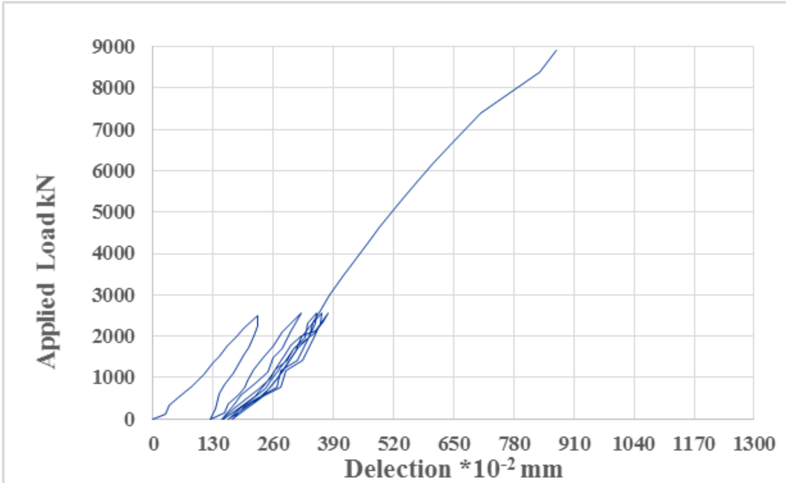

Figure 20. Load- central deflection of specimen T400G tested under repeated load

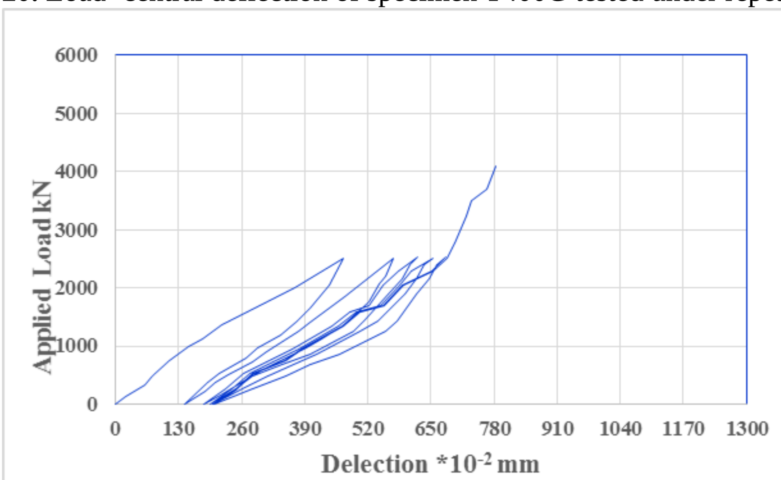

Figure 21. Load- central deflection of specimen T500S tested under repeated load

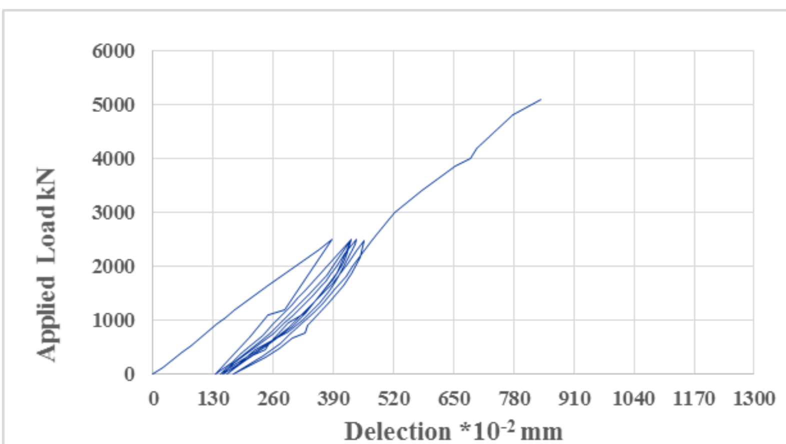

Figure 22. Load- central deflection of specimen T500G tested under repeated load

Table 1. Details of the adopted mix .

Mix Ratio (by weight)	w/c	Mix Proportion (kg/m^3)				SP*	SF**
		Water	Cement	Sand	Gravel		
1:2.35:2.59	0.29	163.3	563	750	883	2.4	3%

*lt /100 kg of cement (Max limit is 2.7).
** Replacement by weight of cement.

Table 2. Chemical composition of cement.*

No.	Compound Composition	Chemical Composition	% Weight	Iraqi Specification No. 5 / 1993
1	Silica	SiO_2	20.28	---
2	Alumina	Al_2O_3	5.00	---
3	Iron Oxide	Fe_2O_3	3.44	---
4	Lime	CaO	63.80	---
5	Magnesia	MgO	2.33	5 (max)
6	Sulfate	SO_3	2.4	2.8 (max)
7	Insoluble residue	I.R	1.27	1.5 (max)
8	Loss on ignition	L.O.I	3.00	4.0 (max)
9	Tricalcium aluminates	C_3A	0.58	---
10	Lime saturation factor	L.S.F	0.93	0.66 – 1.02
11	Tricalcium alumina ferrite	C_4AF	Not available	---
12	Tricalcium silicate	C_3S	Not available	---
13	Dicalcium silicate	C_2S	Not available	---
14		Fe_2O_3- Al_2O_3	Not available	---

*All the test were conducted by the National Center of Laboratories and Researches (Baghdad).

Table 3. Physical properties of cement.*

No.	Physical Properties	Test Result	Iraqi Specification No. 5 / 1993
1	Specific surface area (Blaine Method) m^2/kg	392	230 (min)
2	Setting time (Yicale's Method) Initial time setting : (hour: mint) Final time setting : (hour: mint)	 2:25 3:50	 00:45 (min) 10:00 (max)
3	Autoclave Expansion %	0.08	0.80 (max)
4	Compressive Strength, Mpa 7 days 28 days	 21.41 27.81	 15.00 (min)\ 23.00 (min)

*All the test were conducted by the National Center of Laboratories and Researches (Baghdad).

Table 4. Physical properties of the fine aggregate.*

No.	Physical Properties	Test Result	Iraqi Specification No. 45 / 1993
1	Specific gravity	2.63	---
2	Sulfate contained %	0.22	0.5 (max)
3	Absorption	0.50	---

*All the test were conducted by the National Center of Laboratories and Researches (Baghdad).

Table 5. Grading of the fine aggregate.

Sieve size (mm)	% Passing by Weight	Limit of Iraqi Specification No. 45 / 1993			
		Zone 1	Zone 2	Zone 3	Zone 4
10	100	100	100	100	100
4.75	100	90-100	90-100	90-100	95-100
2.36	91.8	60-95	75-100	85-100	95-100
1.18	76.5	60-90	55-90	75-10	90-100
0.60	51	30-70	35-59	60-79	80-100
0.30	12.2	5-34	8-30	12-40	15-50
0.15	2.7	5-20	0-10	0-10	0-15
$75x10^{-3}$	2.66	5 max			

Table 6. Grading of the coarse aggregate.

Sieve Size (mm)	% Passing by Weight	Limit of Iraqi Specification No. 45 / 1993
37.5	100	100
19	97.1	95-100
9.5	51.4	30-60
4.75	6.8	0-10

Table 7. Physical properties of the coarse aggregate.*

No.	Physical Properties	Test Result	Iraqi Specification No. 45 / 1993
1	Specific gravity	2.63	---
2	Sulfate contained %	0.04	0.1 (max)
3	Absorption	0.7	---

*All the test were conducted by the National Center of Laboratories and Researches (Baghdad).

Table 8. Chemical composition of silica fume.*

No.	Compound Composition	Chemical Composition	% Weight
1	Silica	SiO_2	92.03
2	Alumina	Al_2O_3	0.18
3	Lime	CaO	0.70
4	Iron Oxide	Fe_2O_3	1.10
5	Magnesia	MgO	2.10
6	Sulfate	SO_3	0.85
7	Loss on ignition	L.O.I	3.78

*All the test were conducted by the S. C. Geological Survey and Mining.

Table 9. Chemical requirements of SF according to ASTM C1240-03.

Chemical Composition	Test Result	Limit of ASTM C 1240-03
Silica (SiO_2), min	92.03	85.00
Loss on ignition (L.O.I) , max	3.78	6.00

Table 10. Technical description of GLENIUM51*.

Form	Viscous liquid
Color	Light brown
Relative density	1.1
PH	6.6
Viscosity	128 +/- 30 CPS
Transport	Not classified as dangerous
Labelling	No hazard label required

*Data sheet of the Manuscript.

Table 11. Details of the tested beams.

Beam Sample	Temp. ^oC	Cooling	Ultimate load kN	Residual deflection mm	Max. crack width after burning mm	Max. burning deflection mm
NC	-----	-----	14000	0.31	-----	------
T200S	200	Sudden	11700	0.41	0.25	1.55
T200G	200	Graduated	12900	0.35	0.10	1.52
T300S	300	Sudden	10800	0.46	0.30	2.42
T300G	300	Graduated	12000	0.40	0.20	2.5
T400S	400	Sudden	6500	1.32	0.40	3.05
T400G	400	Graduated	8900	1.25	0.35	2.95
T500S	500	Sudden	4100	1.42	0.45	3.81
T500G	500	Graduated	5100	1.34	0.35	3.80

احتساب مؤشر كثافة النقل من بعض مؤشرات الانتاجية لخطوط سكك الحديد بأستخدام الشبكات العصبية

سوسن رشيد محمد
استاذ مساعد
جامعة بغداد/ كلية الهندسة

عباس محمد برهان
مدرس
جامعة بغداد/ كلية الهندسة

احمد محمد علي هادي
مدرس
الجامعة المستنصرية/ كلية الهندسة

الخلاصة

تقيَّم كفاءة الاداء لخطوط سكك الحديد من خلال مجموعة من المؤشرات والمعايير اهمها: كثافة النقل، انتاجية المنتسب، انتاجية عربة المسافرين، انتاجية عربة الشحن، وانتاجية القاطرات. وتتضمن هذه الدراسة محاولة لاحتساب اهم هذه المؤشرات وهو مؤشر كثافة النقل من خلال مؤشرات الانتاجية الاربع وذلك باستخدام تقنية الشبكات العصبية الاصطناعية. وقد تم في هذه الدراسة استخدام برنامجين للشبكات العصبية هما (Simulnet) و (Neuframe)، فقد تم اعتماد نتائج البرنامج الثاني. اظهرت نتائج تدريب واختبار الشبكة العصبية على البيانات المستخدمة في الدراسة والتي استحصلت من شبكة المعلومات الدولية (الانترنيت)، بأن نسبة الخطأ في عملية التدريب والاختبار كانت حوالي (10%) وان نتائج استعلام الشبكة قد اعطت نتائج بدقة مقبولة احصائياً بحيث انها كانت افضل من النتائج المستحصلة من معادلة الانحدار الخطي المتعدد لنفس البيانات.

الكلمات الرئيسية: مؤشرات، خطوط سكك، مؤشر كثافة النقل، الشبكات العصبية

Calculating the Transport Density Index from Some of the Productivity Indicators for Railway Lines by Using Neural Networks

Sawsan Rasheed Mohamed
Assistant Professor
Engineering College
Baghdad University
Email: Sawsan_2@yahoo.com

Abbas Mohammed Burhan
Instructor
Engineering College
Baghdad University
Email: abbas_alshemosi@yahoo

Ahmed Mohammed Ali Hadi
Instructor
Engineering College
Al-Mustansirya University
Email:ahmad.ubaidl.research@gmail

ABSTRACT

The efficiency evaluation of the railway lines performance is done through a set of indicators and criteria, the most important are transport density, the productivity of enrollee, passenger vehicle production, the productivity of freight wagon, and the productivity of locomotives. This study includes an attempt to calculate the most important of these indicators which transport density index from productivity during the four indicators, using artificial neural network technology. Two neural networks software are used in this study, (Simulnet) and (Neuframe), the results of second program has been adopted. Training results and test to the neural network data used in the study, which are obtained from the international information network has showed that the error rate in the training and the testing process was about (10%) and that the results of the network query has given the results of acceptable accuracy statistically so that it was better than results obtained from multiple linear regression equation for the same data.

Key Words: Indicators, Railway Lines, Transport Density Index, Neural Networks

الشبكات العصبية الاصطناعية (Artificial Neural Networks - ANN):

الشبكات العصبية هي ادوات تحليلية يمكن من خلالها تحليل البيانات بطريقة تحاكي عمل الشبكة العصبية البشرية، للوصول الى النموذج الرياضي الذي يربط بين مجموعة من المتغيرات المصنفة الى متغيرات مستقلة وتابعة، وذلك من خلال احتساب نسب وزنية للمتغيرات المستقلة بحيث تعطي اقل نسبة خطأ ممكنة في تقدير المتغيرات التابعة **(Rzempoluck, 1998)**.

شكل رقم (1) مخطط توضيحي لعمل الخلية العصبية (العصبون Neuron) حيث تدخل الايعازات من خلال المشابك العصبية (Synapses) w_1 الى w_{12} ويقوم جسم الخلية بتجميع المدخلات الموزونة التي يؤلف مجموعها ($\sum_i w_i x_j$) وعندما يكون هذا المجموع كبيراً بما فيه الكفاية يولد نبضة تسري خلال محور الخلية (Axon) تسري الى الخلايا التالية. عملية اطلاق النبضة العصبية يمكن وصفها بمرور المجموع الموزون خلال دالة الانتقال غير الخطية $f(\sum_i w_i x_j)$ المصاحبة لعمل محور الخلية. الخلايا العصبية الحقيقية تتحمل عدد من المدخلات قد يصل الى 10,000 مدخل ويمكنها اخراج اكثر من مُخرج واحد.

آلية عمل الشبكة العصبية:

تتألف الشبكة العصبية بصورة عامة من m من عقد الادخال (X_1 to X_m) ومن n من العقد المخفية (H_1 to H_n) ومن p من عقد الاخراج (Y_1 to Y_p) كما موضح في **شكل رقم (2)**. الاشارة الخارجة المنبثقة من كل عقدة يعبر عنها بـ (قيمة التفعيل Activation Value) لتلك العقدة، فعقدة الادخال X_i تولد قيمة تفعيل يرمز لها x_i، والعقدة المخفية H_j تولد قيمة تفعيل يرمز لها h_j، وعدة الاخراج Y_k تولد قيمة تفعيل يرمز لها y_k. فعلى سبيل المثال فإن قيمة التفعيل لعقدة الادخال X_1 ترسل الى العقدة المخفية H_1 بعد ضربها بالمقدار 0.5 (بحسب المثال المبين في الشكل رقم 2) ويمثل هذا المقدار الوزن الرابط بين العقدتين X_1 و H_1، وهذا يعني ان مُخرج العقدة X_1 يُضرب بالوزن 0.5 قبل ان يتم تقديمه الى العقدة H_1. وقيمة التفعيل للعقدة المخفية H_1 ترسل الى عقدة الاخراج Y_1 بعد ضربها بالمقدار 1.3 (بحسب نفس المثال) والذي يمثل الوزن الرابط بين العقدتين H_1 و Y_1، وهذا يعني ان مُخرج العقدة H_1 يُضرب بالوزن 1.3 قبل ان يتم تقديمه للعقدة Y_1 (**Rzempoluck, 1998**).

تتألف الشبكة العصبية من ثلاث طبقات، تتألف الطبقة الاولى فيه من عقد الادخال التي تستلم المدخلات المتمثلة بقيم المتغيرات المستقلة من نماذج التدريب، بينما تتألف الطبقة الثانية من العقد المخفية التي تتضمن بعد عملية التدريب الخصائص التي قامت الشبكة بتمييزها من نماذج التدريب، اما الطبقة الثالثة فتتألف من عقد الإخراج التي تعطي القيم التقديرية للمخرج المتوقع لكل نموذج تدريب. اوزان الشبكة تتغير تباعاً مع تعلم الشبكة للعلاقة المضمّنة في قيم نماذج التدريب. كل عقدة مخفية تستلم المدخلات من كل عقد الادخال X_i بعد ان توزن كل قيمة مدخلة بقيمة الوزن الخاصة بها w_{ij} ويتم جمع هذه المدخلات الموزونة في العقدة المخفية، وبذلك فإن العقدة المخفية H_j تستلم القيمة المدخلة المساوية الى ($\sum_i w_{ij} x_i$) وتقوم بتوليد القيمة المخرجة المساوية الى ($h_j = f(\sum_i w_{ij} x_i)$) حيث ان:

h_j هي القيمة المخرجة من العقدة H_j

x_i هي الاشارة المولدة من عقدة الادخال X_i

w_{ij} هي الاوزان الرابطة بين عقد الادخال (X_1 to X_m) وبين العقدة المخفية H_j

f هي دالة التفعيل للعقدة H_j

إن وجود العقد المخفية هو الذي يعطي الشبكات العصبية قدرتها على نمذجة اي دالة تربط بين المتغيرات المستقلة والمتغيرات التابعة. والخاصية الموجودة في العقد المخفية التي تعطيها هذه القدرة هي دالة التفعيل، وعادة ما تكون هذه الدالة ممثلة بعلاقة غير خطية كما في الدالة اللوجستية (Logistic Function) الآتية:

$$f(x) = 2 / (1 + e^{(-g\,x)}) - 1 \qquad [-1, 1]$$

أو كما في الدالة الاسية (Sigmoid Function) الآتية:

$$f(x) = 1 / (1 + e^{(-g\,x)}) \qquad [0, 1]$$

حيث ان : g هو معامل الكسب (Gain Factor) الذي يحدد مدى السرعة التي تصل فيها الدالة الى قيمتها الغائية (Limiting Value). ويبين الشكل رقم (3) شكل الدالة اللوجستية عندما ($g=1$).

شكل رقم (3) الدالة اللوجستية $f(x)$ تمثل دالة نموذجية لدوال الانتقال غير الخطي المستعملة في مستوى العقد المخفية في الشبكات العصبية، قيمة الدالة تقترب من (-1) كلما تكبر قيم x في الاتجاه السالب، وتقترب من ($+1$) كلما تكبر قيم x في الاتجاه الموجب.

يمكن ان يمثل المحور الافقي في هذا الشكل القيم المدخلة الى العقد المخفية، هذه القيم المدخلة تمثل المجموع الوزني للاشارات القادمة من عقد الادخال X_i. اما المحور العمودي في الشكل فيمثل المخرجات المقابلة لتلك المدخلات والتي سيتم اخراجها من العقد المخفية H_j. وبنفس الطريقة ستستلم كل عقدة من عقد الإخراج Y_k الاشارات الخارجة من العقد المخفية بعد ان يتم وزنها بالاوزان الرابطة بين العقد المخفية وعقد الاخراج والتي يبلغ مقدارها ($\sum_j w_{jk} H_j$) وبدورها تقوم عقدة الإخراج بإعطاء القيمة ($y_k = f(\sum_j w_{jk} h_j)$) حيث ان:

y_k هي القيمة المخرجة من العقدة Y_k

h_j هي الاشارة المولدة من عقدة الادخال H_j

w_{jk} هي الاوزان الرابطة بين العقد المخفية (H_1 to H_n) وبين عقدة الإخراج Y_k

f هي دالة التفعيل التي يمكن ان تكون غير خطية مثل الدالة المذكورة اعلاه، او ان تكون دالة خطية بواحدة من الصيغتين الآتيتين:

1) $f(x) = g\,x \;;\; -1/g \le x \le 1/g$ [1]

2) $f(x) = -1 \;;\; x < 1/g$ [2]

$f(x) = 1 \;;\; x > 1/g$

حيث ان g هو معامل الكسب المذكور اعلاه.

والذي يحدد كون دالة التفعيل لعقد الإخراج خطية او غير خطية هو نوع التدريب المقدم للشبكة.

وبدمج المعادلتين المبينتين اعلاه لـ (h_j) و (y_k) يمكن تمثيل النموذج الرياضي لشبكة عصبية ذات مستوى واحد من العقد المخفية بالنموذج الآتي:

$$y_k = f(\textstyle\sum_j w_{jk}\, f(\sum_i w_{ij}\, x_i)) \qquad [3]$$

آلية احتساب الاوزان:

تتلخص آلية عمل الشبكة باسلوب التولد العكسي (Back-Propagation) اثناء عملية التدريب، حيث انها تعطي قيم اولية للاوزان تخصصها للمتغيرات المستقلة الداخلة ومنها تحصل على المخرجات المتمثلة بالطبقة الاولى من العقد المخفية، هذه

المخرجات تصبح بدورها مدخلات لتحصيل الطبقة التالية حتى يتم الوصول الى مستوى المخرجات النهائية وهذا المسار يسمى (Forward Pass)، ثم تبدأ مرحلة الرجوع بحساب الفروقات بين قيم المخرجات المحتسبة وبين قيم المخرجات المستهدفة المعطاة ضمن نماذج التدريب، وتحسب القيمة النسبية لمشتقة الخطأ الجزئية لكل عقدة مقارنة الى الخطأ الكلي، ثم تعديل الاوزان لكل عقدة بموجب هذه النسب إذ كلما كانت القيمة النسبية للخطأ اكبر كان نسبة التعديل في الوزن اكبر، ثم السير رجوعاً من طبقة المخرجات الى طبقة العقد المخفية ثم الى طبقة المدخلات (Back Pass)، وهكذا تستمر عملية السير الامامي والخلفي حتى الوصول الى اقل نسبة خطأ ممكنة **(Tofan، 2009)**.

يوضح **الشكل رقم (4)** شبكة متعددة الطبقات ذات الانتشار الراجع للخطأ، في هذه الشبكة ينتشر التفعيل بالاتجاه الامامي خلال الشبكة من المدخلات الى المخرجات. وبالتوافق مع ذلك تنتشر قيم الاخطاء خلال الشبكة في الاتجاه المعاكس من المخرجات رجوعاً الى المدخلات.

مراحل تشغيل الشبكة العصبية:

يتضمن العمل بالشبكة العصبية ثلاث مراحل (Stages or Phases) **(Tofan، 2009)** **(Rzempoluck، 1998)**:

الاولى: هي مرحلة التعليم أو التدريب (Training or Learning Phase) والهدف منها تعليم الشبكة للوصول الى افضل تقدير للاوزان التي ستستعمل في حسابات الشبكة، وذلك من خلال تزويد الشبكة بعدد كاف من نماذج التدريب المشتملة على المتغيرات المستقلة (الداخلة) والمتغيرات التابعة (المستهدفة).

والثانية: هي مرحلة الاختبار او الفحص (Testing or Validation Phase) وهي مرحلة متصلة بمرحلة التدريب وفيها تظهر مقدرة الشبكة على تقدير قيم للمتغيرات التابعة ومقارنتها مع القيم المستهدفة لمجموعة اخرى من النماذج.

والثالثة: هي مرحلة التطبيق او الاستخدام (Running Phase) وفيها يتم استخدام الشبكة للتنبؤ بقيم المتغيرات التابعة استناداً الى مجموعة من مدخلات المتغيرات المستقلة، مع عدم وجود ما يقابلها من قيم المتغيرات التابعة قبل تشغيل الشبكة. في هذه المرحلة يكون المطلوب من الشبكة تطبيق النموذج الرياضي الذي توصلت اليه من خلال مرحلة التدريب. مستوى جودة التنبؤ في هذه المرحلة يعتمد على عدة عوامل منها:

- عدد نماذج التدريب بالنسبة الى عدد المتغيرات المستقلة.
- عدد نماذج التدريب بالنسبة الى عدد الاوزان في الشبكة.
- عدد العقد المخفية.
- عدد المستويات المخفية.

معايير تقييم كفاءة أداء شبكات السكك الحديد

مما لا شك فيه أن تحقيق الجدوى الاقتصادية والمالية من خلال الاستثمار الفعال لقطاع النقل بالسكك الحديد وإيجاد الصيغ العملية المتطورة الكفيلة بتحسين أداء هذا المرفق الحيوي والهام قد أصبح الهدف الرئيسي للجهات المشرفة على إدارة هذا القطاع.

وهناك عدد من المعايير أو المؤشرات الهامة المستخدمة لتقييم اداء شبكات السكك الحديد لدى شبكات السكك العالمية والاتحاد الدولي للسكك الحديد والبنك الدولي للإنشاء والتعمير، وتمتاز هذه المؤشرات بأنها تغطي كافة جوانب نشاط أي شبكة سكك حديد من حيث قياس فعاليتها في تحقيق أهدافها والاستخدام الأمثل لوسائل الإنتاج والموارد المتاحة بالإضافة إلى قياس كفاءة أداء خدمة القطارات بالقياس إلى المساحة والسكان وبالمقارنة مع الشبكات الأخرى**(كاظم, 2005)**.

مؤشر كثافة النقل لخط السكة (Traffic Density or Traffic Intensity)

يعتبر هذا المؤشر المعيار الأهم في قياس كفاءة الأداء الإنتاجية لأي خط من خطوط سكك الحديد وهو يمثل كثافة حركة النقل بالمركبات السككية لكل كيلومتر من الخطوط أي بعبارة أخرى هو حاصل قسمة إجمالي العدد السنوي من المسافرين وأطنان البضائع المنقول لمسافة (1 كم) على الطول الكلي لخطوط الشبكة ويقاس بـ(وحدة نقل.كم/ كم خطوط) والمعادلة رقم (4) تمثل طريقة احتساب المؤشر **(كاظم, 2005)**.

$$\text{مؤشر كثافة النقل لخط السكة} = \frac{\text{اجمالي الوحدات المنقولة لكل مسافة كيلومتر واحد}}{\text{طول الخط أو الشبكة}} \qquad [4]$$

إجمالي الوحدات المنقولة لكل مسافة كيلومتر واحد = إجمالي [عدد المسافرين المنقولين لكل كيلومتر واحد (مسافر.كم) + وزن البضائع المنقولة لكل مسافة كيلومتر واحد (طن.كم)].

إن شركات السكك التي تستخدم خطوطها بشكل مكثف هي الشركات التي تحقق أفضل النتائج الاقتصادية للاستثمار السككي الذي تشكل كلفة خطوط السكك الجزء الأعظم منه وبمبالغ ضخمة لا يمكن استردادها إلا بالتشغيل المكثف للخطوط ولفترة طويلة. وهذا لا يتم إلا من خلال التطوير المستمر للخطوط ولأنظمة التشغيل والصيانة والتسوق فضلا عن القرارات الأولية المتعلقة بإنشاء الخطوط وفق دراسات الجدوى الاقتصادية والفنية، حيث تحرص شركات السكك العالمية –بالتركيز خلال مرحلة التصاميم عند تنفيذ المشاريع الجديدة– على إقرار مستوى جودة مرتفع للمواصفات التصميمية لخطوط السكك مع تفضيل أن تكون مزدوجة ومكهربة مما يساعد على جعلها ضمن فئة متقدمة نوعيا وفق الاتحاد الدولي للسكك الحديد والتي تمتاز بارتفاع المستوى النوعي للخدمات المقدمة كالسرعة ودقة المواعيد وانتظام السير وغيرها مما يؤدي بالنتيجة إلى زيادة استيعاب الخط للمزيد من القطارات ومن ثم زيادة كثافة النقل وبعبارة أخرى زيادة إنتاجية الخط**(كاظم, 2005)**.

مؤشر الكفاءة الإنتاجية للقاطرة (Locomotive Productivity):

وهو من المؤشرات الأكثر سهولة وملائمة لقياس كفاءة أداء إدارة سككية معينة ويحسب عادة من حاصل قسمة إجمالي العدد السنوي من المسافرين وأطنان البضائع المنقولة لمسافة (1 كم) على عدد القاطرات الموجودة لدى الشركة السككية ويقاس المؤشر بـ(وحدة نقل.كم/ القاطرة) وتوضح المعادلة رقم (5) طريقة احتساب المؤشر**(كاظم, 2005)**.

$$\text{مؤشر إنتاجية القاطرة} = \frac{\text{إجمالي الوحدات المنقولة لكل مسافة كم واحد}}{\text{إجمالي عدد القاطرات الموجودة}} \qquad [5]$$

وإذا ما علمنا بأن القطارات والمركبات السككية المحركة هي المعدات الأكثر تكلفة التي تمتلكها شركات السكك فأن القدرة على انتاج أكبر عدد ممكن من (وحدات النقل.كم) سنويا للقاطرة الواحدة تعتبر من أهم العوامل المؤثرة في نوع النتائج المالية للشركات السككية. وهذا يتطلب الاستمرار في تطوير أنظمة التشغيل والصيانة وانتظام أعمال الصيانة وتطور الخطوط مما يساعد على تقليل فترة دورة القاطرة وبالتالي يؤدي الى رفع انتاجية القاطرة.

مؤشر الكفاءة الإنتاجية لعربة المسافرين (Coach Productivity):

تركز الكثير من دول العالم –المتقدمة منها والنامية– على تقديم خدمة نقل المسافرين بواسطة السكك الحديدية باعتبارها خدمة ضرورية ولازمة، ومن المطلوب رعايتها من قبل الدولة لأسباب عديدة منها اجتماعية واقتصادية وبيئة وسياحية. وتحرص الكثير من شركات السكك العالمية في مرحلة التصاميم على إقرار درجة جودة معينة للمواصفات التصميمية للخطوط والأنظمة التشغيلية والوحدات والمحركة والمتحركة والذي ينتج عنه ارتفاع مستوى الخدمات المقدمة للمسافرين من حيث السرعة والرفاهية وانتظام المواعيد والأمان والموثوقية وتوفير التكاليف وغير ذلك مما ينعكس إيجابا في زيادة الطلب على النقل. ومن الإجراءات التي تؤدي إلى زيادة إقبال الزبائن على خدمة نقل المسافرين في السكك هي تلك التي تشتمل على التحسين المستمر لعربات المسافرين وتنفيذ مشاريع تطوير البنية التحتية لرفع سرعة القطارات وتطوير المحطات وغير ذلك، وهذه الاجراءات ستؤدي بدورها الى زيادة إنتاجية شبكة السكك من خلال زيادة الكفاءة الإنتاجية لعربة المسافرين والتي هي عبارة عن حاصل قسمة العدد السنوي للمسافرين المنقولين لمسافة (1 كم) على عدد عربات المسافرين الموجودة لدى الشركة ويقاس المؤشر بـ(مسافر.كم/ عربة) وتوضح المعادلة رقم (6) طريقة احتساب هذا المؤشر(**Olievschi, 2009**).

$$\text{مؤشر إنتاجية عربة المسافر} = \frac{\text{إجمالي المسافرين المنقولين لكل مسافة كم واحد}}{\text{إجمالي عدد عربات المسافرين الموجودة}} \qquad [6]$$

مؤشر الكفاءة الإنتاجية لشاحنة البضائع (Wagon Productivity):

توظف معظم شركات السكك الحديد رأسمالا في شاحنات البضائع اكبر مما توظفه في قاطرات البضائع ففي الدول النامية يخصص معدل (54) شاحنة بضائع لكل قطار بضائع وهذا يستوجب مبالغة ضخمة. وتعاني الكثير من شركات السكك العالمية من طول دورة الشاحنة لعدة أسباب منها سوء نظام التشغيل حيث تبرز مشاكل سوء الاستخدام والتحميل باتجاه واحد والعودة فارغة بالإضافة إلى الزمن الميت حيث تنظر الشاحنات من أجل المغادرة والتصنيف والتعليق والتفريغ أو الفصل في ساحات الفرز والبضائع. وبالتالي كلما طالت المدة كلما طالت دورة الشاحنة مما يؤثر سلبا في الإنتاجية. ويتطلب هذا الأمر تحسين أنظمة الصيانة والتشغيل وخصوصا في ساحت الفرز باستخدام أنظمة المحاكاة بالحاسوب حيث ثبت من تجارب الكثير من الشركات السككية انخفاض الفترة التي تستغرقها الشاحنات في ساحات الفرز إلى النصف عند استخدام هذه الأنظمة مما أدى الى تحسين كفاءة إنتاجية الشاحنة بشكل كبير. وتمثل انتاجية الشاحنة حاصل قسمة العدد السنوي لأطنان البضائع المنقولة لمسافة (1 كم) مقسومة على عدد الشاحنات الموجودة لدى الشركة، ويقاس هذا المؤشر بـ(طن.كم/ شاحنة). ولذلك تركز الكثير من شركات السكك في دراسات الجدوى الاقتصادية على توفر مصادر لتحقيق الطلب على نقل البضائع ضمن وحول مسار مشروع خط السكك الحديد كوجود المصانع والمرافئ البحرية والجوية والتجمعات التجارية والحقول الزراعية والمناجم ونحوها، بالإضافة إلى التنسيق مع أنماط النقل الأخرى لغرض العمل بمبدأ النقل المتعدد الأنماط. وتوضح المعادلة رقم (7) طريقة احتساب هذا المؤشر(**كاظم, 2005**) (**Olievschi, 2009**).

$$\text{مؤشر إنتاجية شاحنة البضائع} = \frac{\text{إجمالي وزن البضائع المنقولة لكل مسافة (1كم)}}{\text{إجمالي عدد شاحنات البضائع الموجودة}} \qquad [7]$$

مؤشر الكفاءة الإنتاجية للمنتسب (Employee Productivity):

تسعى مختلف الوحدات الاقتصادية سواء كانت تنتج سلع أم خدمات إلى زيادة معدلات أدائها من خلال رفع مستويات إنتاجية عناصر الإنتاج فيها، وبالنظر لأهمية العنصر البشري في تلك الوحدات فإنها تحرص على قياس إنتاجية العاملين فيها لسببين أساسين:

- تأثير إنتاجية العنصر البشري على إنتاجية بقية عناصر الإنتاج (كالمكائن والمعدات ورأس المال).
- ارتفاع كلفة هذا العنصر في العملية الإنتاجية (تكاليف الأجور والرواتب والسكن والضمان الإجتماعي وغيرها).

والمقصود بإنتاجية المنتسبين أو العاملين هو (معدل الإنتاج المتحقق للمنتسب الواحد خلال مدة زمنية معينة) وبالنظر لتعدد الخدمات التي تقدمها شركات ومنشأة السكك (نقل البضائع، نقل المسافرين) فهنالك اختلاف في المعايير التي تقيس إنتاجية كل من هذه الخدمات. ومن المؤشرات المستخدمة في هذا المجال:

- مؤشر إنتاجية المنتسب بدلالة معدل إجمالي وحدات النقل المنقولة لمسافة (1 كم) لكل منتسب.
- مؤشر إنتاجية المنتسب بدلالة معدل كيلومترات طول خط سكة الحديد لكل منتسب.
- مؤشر إنتاجية المنتسب بدلالة معدل كيلومترات سير القطارات لكل منتسب.
- مؤشر إنتاجية المنتسب بدلالة معدل الإيرادات المتحققة للشركة لكل منتسب.
- مؤشر إنتاجية المنتسب بدلالة معدل عدد المسافرين لكل منتسب.
- مؤشر إنتاجية المنتسب بدلالة معدل الكيلومترات السفرية لكل منتسب.
- مؤشر إنتاجية المنتسب بدلالة عدد الأطنان لكل منتسب.
- مؤشر إنتاجية المنتسب بدلالة معدل الكيلومترات الطنية لكل منتسب.

إن المؤشرات السائدة والمستخدمة عالميا لقياس إنتاجية المنتسبين هما المؤشران الأول والرابع وذلك لشموليتها لكل أوجه النشاط الذي تقوم به الشركة السككية بالإضافة إلى إن المؤشر الرابع (إنتاجية المنتسب من الإيرادات) يعكس مشكلة متزايدة عالميا بسبب إرتفاع كلفة المنتسبين (الأجور والرواتب والضمان الاجتماعي والسكن وغيرها) حيث تبلغ هذه الكلفة في كل من بلجيكا وفرنسا والسعودية على التوالي 55%، 34%، 35% من التكاليف الكلية، وإن المعدل العالمي هو (42%) مما يؤدي الى عجز إيرادات بعض الشركات عن سداد كلف المنتسبين ولذلك فأن الكثير من شركات السكك العالمية تتلقى مساعدات حكومية متزايدة فهي تبلغ في نفس الدول المذكورة أعلاه لعام 1998 على سبيل المثال 12%، 16%، 29%، على التوالي من الإيرادات الكلية. وتوضح المعادلتين (8) و(9) طريقة احتساب هذين المؤشرين**(كاظم, 2005) (Olievschi, 2009)**.

$$\text{مؤشر انتاجية المنتسب} = \frac{\text{إجمالي الوحدات المنقولة لمسافة كم واحد}}{\text{إجمالي عدد المنتسبين}} \quad [8]$$

$$\text{مؤشر انتاجية اجر المنتسب} = \frac{\text{إجمالي إيرادات نقل البضائع والمسافرين}}{\text{إجمالي أجور المنتسبين}} \quad [9]$$

وسنختار المؤشر الاول فقط في هذه الدراسة لعدم توفر بيانات كافية حول انتاجية اجر المنتسب ضمن البيانات التي تم الحصول عليها.

المؤشرات المذكورة أعلاه هي التي ستكون محور هذه الدراسة، وهناك عدد آخر من مؤشرات قياس اداء السكك الحديد لم يتم تناولها في هذا البحث بسبب عدم توفر بيانات كافية لقيم هذه المؤشرات في خطوط سكك الحديد التي شملتها الدراسة، ومن المفيد الاشارة اليها، منها:

1. مؤشر جاهزية القاطرات.
2. مؤشر معدل طول المسافة لرحلة المسافر.
3. مؤشر معدل مسافة نقل (1 طن) من البضائع للرحلة الواحدة.
4. مؤشر نسبة معدل تعريفة نقل المسافرين إلى معدل تعريفة نقل البضائع.
5. مؤشر الكفاءة النوعية.

البيانات المستعملة في هذه الدراسة:

تم الحصول على البيانات المستعملة في هذه الدراسة من ملفات متاحة على موقع الانترنيت المعنون (WORLD BANK'S RAILWAY DATABASE) والذي يتضمن قواعد بيانات السكك الحديد العالمية (Railway Data-Base RDB) حيث تمكن الباحث من الحصول على قاعدتي بيانات للعامين 2001 و 2007.

في البداية تم اختيار قاعدة بيانات 2007 وتم تصفية الخلايا الفارغة فيها فتبين ان حجم البيانات المتبقية لا يفي بمتطلبات الدراسة. ولمعالجة هذه الحالة تم دمج بيانات قاعدة عام 2001 مع بيانات قاعدة عام 2007 ثم ازالة البيانات المكررة من القاعدة الناتجة فتم الحصول على 200 نموذج تضمنت العديد من الخلايا الفارغة لبعض المتغيرات، وقام الباحث باملاء بعض الخلايا الفارغة الخاصة بالمتغير التابع موضوع الدراسة (معيار كثافة النقل) من خلال احتسابها مستعيناً بالبيانات الاولية الموجودة ضمن قاعدتي البيانات وباستعمال القوانين المبينة أعلاه. وبذلك تم ملء العديد من الخلايا الفارغة بحيث اصبح الحجم النهائي للبيانات كافياً لاجراء الاختبار البحثي، وتم في النهاية الحصول على 129 نموذجاً، تضمنت بعضها قيماً شاذة بشكل واضح تقع على مسافة اكثر من 3 انحرافات معيارية عن الوسط الحسابي لباقي القيم، فتم استبعادها لينتهي حجم البيانات الى 108 سجل بيانات لـ 77 دولة وللفترة الزمنية المحصورة بين 1990 الى 2005. قواعد البيانات المذكورة تم تطويرها من قبل (Water and Urban Development Department) بدءاً من عام 1987 بهدف توفير البيانات الكافية للمدراء للاستفادة منها في مجال تطوير النقل بالسكك الحديد (**Thompson and Fraser, 1993**).

احتساب مؤشر كثافة النقل من بعض مؤشرات الانتاجية لخطوط سكك الحديد:

بعد ان تم بيان مقدمة عن الشبكات العصبية الاصطناعية وعن اهم مؤشرات الانتاجية والاداء لخطوط سكك الحديد، وبعد ان تم بيان مصادر المعلومات لهذه المؤشرات، تتلخص العمليات الحسابية في هذه الدراسة بالخطوات الآتية:

1) تدريب واختبار واستعلام الشبكات العصبية باسلوب التولد العكسي (Back-Propagation Network) لتحديد اوزان مؤشرات الانتاجية الاربع (انتاجية المنتسبين- انتاجية عربات المسافرين- انتاجية شاحنات النقل- انتاجية القاطرات) في سبيل تقدير كثافة النقل لخطوط سكك الحديد من هذه المؤشرات، وذلك عن طريق اعتبار المؤشرات الاربع كعقد ادخال في الشبكة العصبية ومؤشر كثافة النقل كعقدة اخراج من تلك الشبكة.

2) استخدام نفس البيانات التي تم تدريب الشبكة العصبية بها في الخطوة السابقة لاستنباط معادلة خطية من خلال تقنية الانحدار الخطي المتعدد، تربط بين المؤشرات الاربع كمتغيرات مستقلة وبين كثافة النقل كمتغير تابع.
3) مقارنة نواتج (50) سجل من سجلات البيانات المستخدمة في عمليتي الاختبار والاستعلام في الشبكة العصبية مع القيم المتوفرة في قاعدة البيانات الاساسية المستخدمة في هذه الدراسة، وذلك باستخدام اسلوب اختبارات المعنوية للفرق بين وسطي عينتين من نفس المجتمع الاحصائي باسلوب المشاهدات المزدوجة. ثم اجراء نفس الاختبار للمقارنة بين نتائج معادلة الانحدار الخطي المتعدد وبين القيم المتوفرة في قاعدة البيانات الاساسية.
4) مقارنة نتائج الاختبارين الاحصائيين لمعرفة مدى كفاءة الشبكات العصبية في تقدير قيم المتغير التابع بالمقارنة مع اسلوب الانحدار الخطي المتعدد.
5) اجراء تحليل حساسية كثافة النقل للمؤشرات الاربع التي تمثل متغيرات الادخال، واستنتاج النموذج الرياضي للشبكة العصبية الاصطناعية.

الخطوة الاولى: حساب كثافة النقل باستخدام الشبكة العصبية الاصطناعية

تتضمن هذه الخطوة تكوين الشبكة العصبية الاصطناعية واحتساب كثافة النقل من مؤشرات الانتاجية الاربع باستخدام هذه الشبكة. ولتحقيق هذه الغاية تم استخدام برنامجين من برامج الشبكات العصبية، هما برنامج (Simulnet 3.08) وبرنامج (Neuframe 4).

البرنامج الاول (Simulnet) (اصدار سنة 1997) قديم نسبياً ويعطي نتائج متباينة بشكل كبير بين محاولة واخرى لنفس البيانات وقد تم الحصول على خصائص الشبكة العصبية باستخدام هذا البرنامج مع واحدة من افضل مخرجاتها التي تم الحصول عليها بعد محاولات عديدة للبرنامج وباستخدام مختلف الخيارات المتاحة فيه. وقد حدد البرنامج عدد العقد المخفية بعقدة واحدة في طبقة مخفية واحدة، ولم تتحسن النتائج عند قيام الباحث بزيادة عدد العقد المخفية.

وبالنظر لعدم استقرار نتائج برنامج (Simulnet) فقد تم اعتماد البرنامج الثاني (Neuframe 4) (اصدار سنة 2000) لكونه اكثر استقراراً ويعطي نتائج متقاربة جداً في التشغيلات المختلفة لنفس الشبكة. يبين **الجدول رقم (1)** خلاصة نتائج الشبكة باستخدام هذا البرنامج. وعند استعلام الشبكة العصبية عن نتائج العينات الخمسين الاولى من عينات الاختبار كانت النتائج كما هي مبينة في **الجدول رقم (2)**.

الخطوة الثانية: حساب كثافة النقل باستخدام الانحدار الخطي المتعدد

تتضمن هذه الخطوة تطبيق الانحدار الخطي المتعدد (Multiple Linear Regression) على بيانات التدريب المدخلة الى الشبكة العصبية لاستنباط معادلة خطية، وذلك باستخدام دالة (Linest) المضمنة في برنامج (MS Excel) فكانت المعادلة رقم(10) الناتجة هي:

$$\text{شدة النقل (Traffic Density)} = m_1 X_1 + m_2 X_2 + m_3 X_3 + m_4 X_4 \qquad [10]$$

حيث أن:

X_4, X_3, X_2, X_1 : هي مؤشرات انتاجية المنتسب، انتاجية عربة المسافرين، انتاجية شاحنة البضائع، وانتاجية القاطرة على التوالي.

m_4, m_3, m_2, m_1 : هي ثوابت المعادلة الخطية الناتجة من حساب الانحدار الخطي المتعدد.

ويبين **الجدول رقم (3)** قيم ثوابت المعادلة وقيمة معامل الحساب (Coefficient of Determination (r^2)) للمعادلة الناتجة من عملية الانحدار الخطي المتعدد لمدخلات التدريب. ويلاحظ في هذا الجدول ان قيمة معامل الحساب تقترب من (1.0) فهي تشير بذلك الى تقارب جيد بين البيانات الاصلية وبين نتائج معادلة الانحدار الخطي. وعند استخراج معادلة الانحدار تم

اعتبار الحد المطلق في المعادلة (b) صفراً وذلك لأن اعتباره قيمة غير صفرية يؤدي الى خفض قيمة معامل الايجاد، ومن المنطقي ان لا تكون هناك كثافة للنقل عندما تكون مؤشرات الانتاجية الاربع كلها اصفاراً.

الخطوة الثالثة: مقارنة مخرجات طريقتي احتساب كثافة النقل

تتضمن هذه الخطوة مقارنة مخرجات الشبكة العصبية ومخرجات معادلة الانحدار الخطي المتعدد مع البيانات الاصلية كل على حدة باستخدام تقنية اختبارات المعنوية للفرق بين وسطين حسابيين لعينتين من نفس المجتمع (المشاهدات المزدوجة)، وتتلخص خطوات كل من هاتين المقارنتين بما يأتي:

- فرضية العدم والفرضية البديلة: $H_o: f_d = 0$; $H_1: f_d \neq 0$
- مستوى معنوية الخطأ (α): $\alpha = 0.05$
- مؤشر الاختبار ((Test Statistic (z) يحسب باستخدام المعادلة رقم (11):

$$z = \frac{\bar{x}}{S/\sqrt{n}} \qquad [11]$$

$n = 50$

فينتج ان مقدار مؤشر الاختبار للمقارنتين هو : $z_1 = 1.7713$; $z_2 = 4.5476$

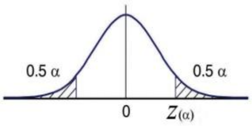

- القيمة الجدولية لـ $(z_{\alpha=0.05}) = 1.96$
- ينتج من المقارنتين ان: $z_1 < z_{\alpha=0.05}$; $z_2 > z_{\alpha=0.05}$

ويبين **الجدول رقم (4)** نتائج المقارنتين الاحصائيتين وحسابات الفروق بين المشاهدات المزدوجة.

الخطوة الرابعة: مناقشة نتائج المقارنة

تبين من النتائج المبينة في **الجدول رقم (4)** ان الفرق بين الوسطين الحسابيين لكثافة النقل حسب البيانات الاصلية وكثافة النقل بحسب مخرجات استعلام الشبكة العصبية الاصطناعية هو فرق غير معنوي ضمن مستوى معنوية (0.05)، بخلاف الفرق بين الوسطين الحسابيين لكثافة النقل حسب البيانات الاصلية وكثافة النقل بحسب مخرجات معادلة الانحدار الخطي المتعدد، فعلى الرغم من ان مستوى الانحدار كان جيداً بحسب قيمة معامل الايجاد (r^2) الا ان الفرق بين الوسطين الحسابيين بينهما يمثل فرقاً معنوياً، مما يشير الى ان تقدير كثافة النقل لخطوط سكك الحديد باستخدام مؤشرات الانتاجية الاربع يكون باستخدام الشبكات العصبية افضل منه باستخدام الانحدار الخطي المتعدد.

الخطوة الخامسة: اجراء تحليل الحساسية واستنتاج النموذج الرياضي للشبكة

أ) تحليل الحساسية:

لبيان مدى حساسية كثافة النقل لكل متغير من المتغيرات الداخلة سيتم فيما يأتي اجراء تحليل الحساسية بحسب الطريقة الآتية والمبينة في المصدر **(Tofan, 2009)**:

1) لكل عقدة مخفية (j) نحسب ناتج الضرب (P_{ij}) حيث ان (i) تمثل رقم عقدة الادخال و (j) تمثل رقم العقدة المخفية، وذلك بضرب القيمة المطلقة للوزن الرابط بين عقدة الادخال والعقدة المخفية × القيمة المطلقة للوزن الرابط بين نفس العقدة المخفية وعقدة الاخراج.
2) لكل عقدة مخفية (j) نقسم قيم (P_{ij}) لكل عقدة ادخال على مجموع قيم (P_{ij}) لتلك العقدة المخفية والذي يساوي ($\sum P_{ij}$) لتحصيل القيمة (Q_{ij}).

3) لكل عقدة ادخال (i) نجمع قيم (Q_{ij}) الخاصة بها لكل قيم (j) لنحصل على (S_i)، ثم نجمع قيم (S_i) لتحصيل القيمة ($\sum S_i$).

4) نقسم كل قيمة من قيم (S_i) على المجموع ($\sum S_i$) لتحصيل نسبة تأثير كل متغير ادخال على القيمة المخرجة من الشبكة.

ويبين **الجدول رقم (5)** نتائج هذا التحليل.

يلاحظ هنا عند مقارنة تحليل الحساسية الناتج مع تحليل الحساسية الناتج ضمن مخرجات برنامج (Simulnet) ان انتاجية القاطرة هي العامل الاكثر تأثيراً على كثافة النقل وبفرق واضح عن بقية العوامل في كلا التحليلين، ويختلف التحليلان في مدى حساسية كثافة النقل لتغير العوامل الثلاث الاخرى.

ب) استنتاج النموذج الرياضي للشبكة العصبية:

يمكن تمثيل حسابات الشبكة العصبية بالنموذج الرياضي المشتمل على المعادلات الآتية (انظر **الجدول رقم 6** لترتيب قيم الاوزان):

Input Scaling of $(x_i) = (x_i - x_{min}) / (x_{max} - x_{min})$ [12]

Hidden Layer Model : $h_j = \Phi(\sum_i w_{ij}\, x_i)$ [13]

Output Layer Model : $y_k = \Phi(\sum_j w_{jk}\, h_j) = \Phi(\sum_j w_{jk}\, \Phi(\sum_i w_{ij}\, x_i))$ [14]

where the sigmoid function is : $\Phi(t) = 1 / (1 + e^{(-g\, t)})$

المعادلة رقم (12) تحول قيم المدخلات الى قيم مناسبة لحسابات الشبكة عن طريق تحويلها الى قيم نسبية، وبعد انتهاء الحسابات يُعاد تحويل قيم المخرجات بعملية معكوسة لاستحصال القيم الرقمية الصحيحة للمخرجات، وبذلك يكون عمل هذه المعادلة هو نفس عمل وحدة التحويل (Encoder) في برنامج (Neuframe).

مجاميع حاصل ضرب الاوزان × متغيرات الادخال يتم تعويضها في دالة التفعيل الأسية، حيث ان:

$T_j = \sum_i w_{ij}\, x_i$ (Summation includes w_{oj})

$t_k = \sum_j w_{jk}\, h_j = \sum_j w_{jk}\, \Phi(t_j)$ (Summation includes w_{ok})

ومع افتراض ان قيمة (g) تساوي 1.0، وبالاستناد الى **جدول رقم (6)**:

$$t_{j=1} = -\,0.180214505 + 0.686261652 x_1 + 0.046266174\, x_2 - 0.526911164\, x_3 + 1.463035512\, x_4$$

$$t_{j=2} = 0.635897702 - 1.360412268\, x_1 - 0.245728395\, x_2 - 0.908420545\, x_3 - 2.04127738\, x_4$$

$$t_{j=3} = 0.379851428 + 0.105046876 x_1 - 0.072760153\, x_2 - 0.160273296\, x_3 - 1.948132277\, x_4$$

ينتج من ذلك:

$$h_1 = \Phi(\, t_{j=1}) = 1 / (1 + e^{(-t\, j1)})$$

$$h_2 = \Phi(\, t_{j=2}) = 1 / (1 + e^{(-t\, j2)})$$

$$h_3 = \Phi(\, t_{j=2}) = 1 / (1 + e^{(-t\, j3)})$$

ثم:

$$t_{k=1} = -\,0.069630097 + 2.273622393\, h_1 - 3.029695331\, h_2 - 2.257864264\, h_3$$

ومنه تحسب قيم مخرجات الشبكة:

$$y_1 = \Phi(\, t_{k=1}) = 1 / (1 + e^{(-t\, k1)})$$

ويبين **الجدول رقم (6)** قطعة برنامج حاسوبي بلغة (C^+) تم استخراجه باستخدام برنامج (Neuframe) من الشبكة العصبية الناتجة من هذه الدراسة.

المناقشة والاستنتاجات:

بينت الدراسة بان انتاجية القاطرة هي العامل الاكثر تأثيراً على كثافة النقل وبفرق واضح عن بقية العوامل في كلا التحليلين، ويختلف التحليلان في مدى حساسية كثافة النقل لتغير العوامل الثلاث الاخرى.

تبين من النتائج المبينة في الجدول رقم (4) ان الفرق بين الوسطين الحسابيين لكثافة النقل حسب البيانات الاصلية وكثافة النقل بحسب مخرجات استعلام الشبكة العصبية الاصطناعية هو فرق غير معنوي ضمن مستوى معنوية (0.05)، بخلاف الفرق بين الوسطين الحسابيين لكثافة النقل حسب البيانات الاصلية وكثافة النقل بحسب مخرجات معادلة الانحدار الخطي المتعدد، فعلى الرغم من ان مستوى الانحدار كان جيداً بحسب قيمة معامل الايجاد (r^2) الا ان الفرق بين الوسطين الحسابيين بينهما يمثل فرقاً معنوياً، مما يشير الى ان تقدير كثافة النقل لخطوط سكك الحديد باستخدام مؤشرات الانتاجية الاربع يكون باستخدام الشبكات العصبية افضل منه باستخدام الانحدار الخطي المتعدد.

بينت الدرسة ايضا أن الشبكات العصبية قادرة على نمذجة العلاقات المعقدة بين ظروف العمل والإنتاجية من عملية وتحقيق دقة مقبولة في التقدير.

مصادر الدراسة:

- Olievschi, V. N., 2009, *South East European Railways Reform-The World Bank Involvement*, The World Bank, Brussels (A study available as a pdf file from Internet).
- Rzempoluck, E. J., 1998, *Neural Network Data Analysis Using Simulent*, Springer-Verlag New York Inc.
- Thompson, L. S. and Fraser, J. M., 1993, *World Bank's Railway Database*, Transportation, Water and Urban Development, The World Bank, http://siteresources.worldbank.org/INTTRANSPORT/Resources/336291-1119275973157/td-rw6.pdf.
- Tofan, A. S., 2009, *Neural Networks for Estimating the Ceramic Productivity of Walls and Floors*, M.Sc. Thesis submitted to the College of Engineering – Baghdad University.
- The World Bank, 2007, *World Bank's Railway Data Base*, from internet, siteresources.**worldbank**.org/EXT**RAILWAYS**/.../**railways_database**_2007.xls.
-
- كاظم، علي جبار، 2005، *نظام تقويم كفاءة الاداء ومتابعة اعمال السكك الحديد العراقية*، اطروحة دكتوراه– ادارة مشاريع، الجامعة التكنولوجية.

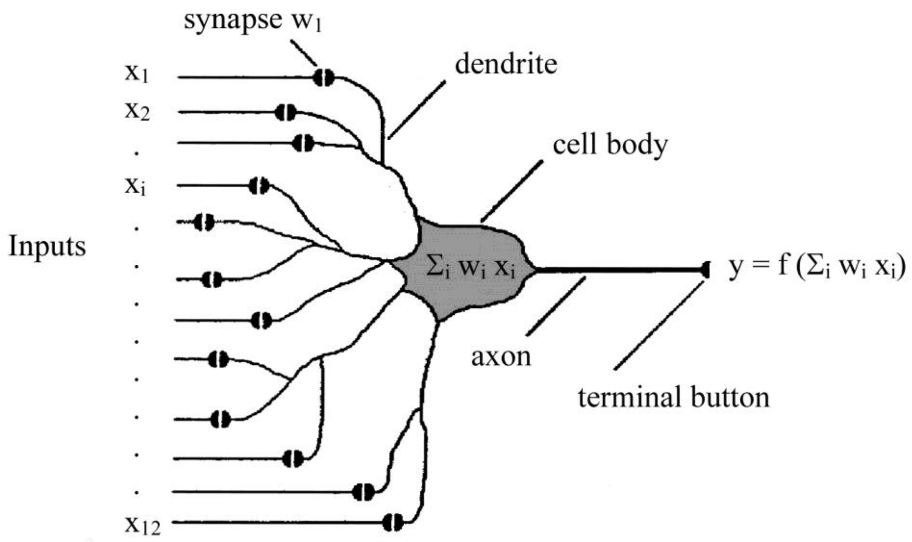

شكل رقم 1

مخطط عمل الخلية العصبية.

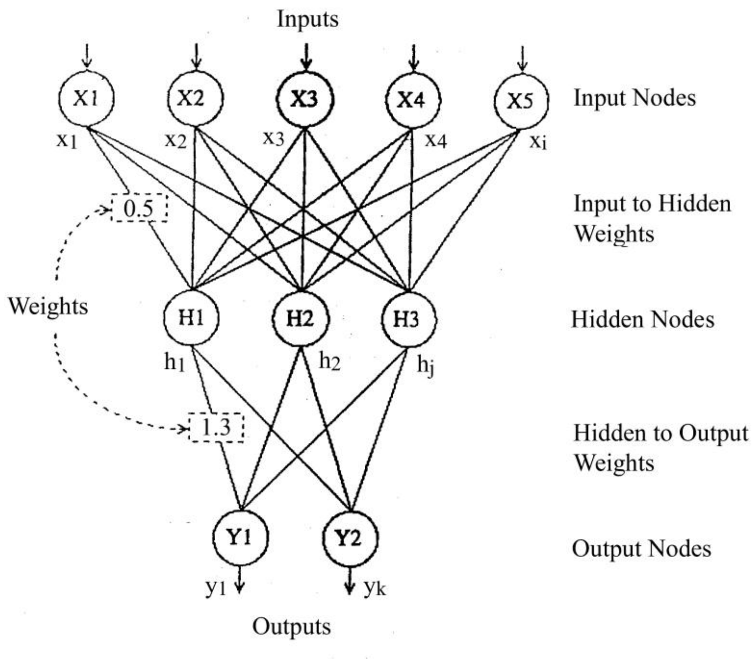

شكل رقم 2. طبقات الشبكة العصبية.

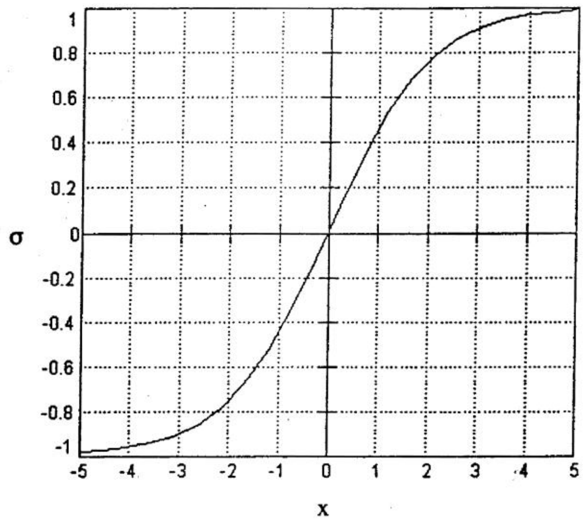

شكل رقم 3. شكل الدالة اللوجستية.

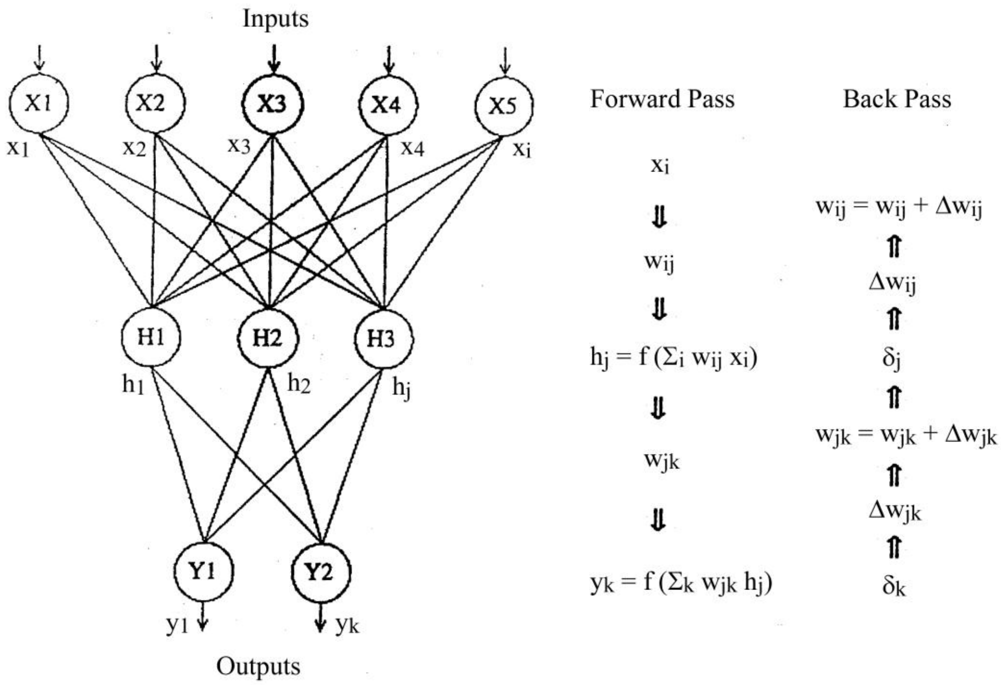

شكل رقم 4. الشبكة متعددة الطبقات ذات الانتشار الراجع للخطأ.

جدول 1. خلاصة نتائج الشبكة العصبية الناتجة من استخدام برنامج (Neuframe 4).

Back Propagation Network
The network has 3 layers.
Layer 1 has 4 Linear nodes.
Layer 2 has 3 Sigmoid nodes.
Layer 3 has 1 Sigmoid nodes.

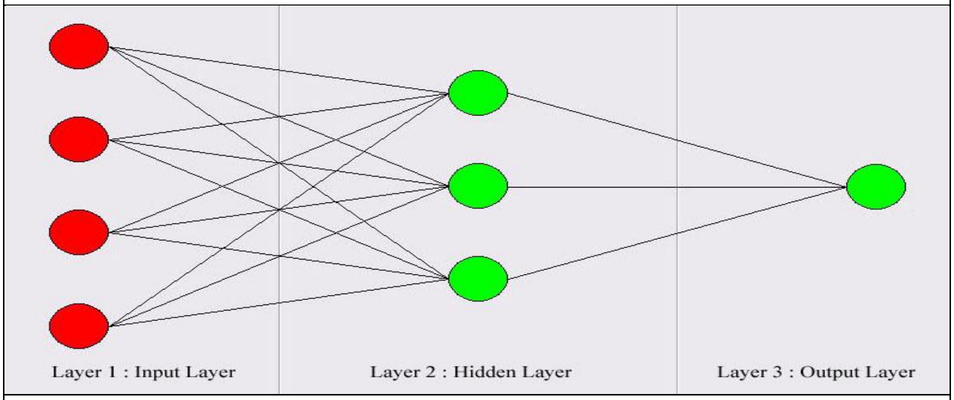

Training Error = 0.101831
Test Error = 0.105764

Weights:

Layer 2		
Node 1	Bias is	-0.180214505
Node 1	Weight from 1 is	0.686261652
Node 1	Weight from 2 is	0.046266174
Node 1	Weight from 3 is	-0.526911164
Node 1	Weight from 4 is	1.463035512
Node 2	Bias is	0.635897702
Node 2	Weight from 1 is	-1.360412268
Node 2	Weight from 2 is	-0.245728395
Node 2	Weight from 3 is	-0.908420545
Node 2	Weight from 4 is	-2.04127738
Node 3	Bias is	0.379851428
Node 3	Weight from 1 is	0.105046876
Node 3	Weight from 2 is	-0.072760153
Node 3	Weight from 3 is	-0.160273296
Node 3	Weight from 4 is	-1.948132277
Layer 3		
Node 1	Bias is	-0.069630097
Node 1	Weight from 1 is	2.273622393
Node 1	Weight from 2 is	-3.029695331
Node 1	Weight from 3 is	-2.257864264

جدول 2. نتائج استعلام الشبكة العصبية الاصطناعية عن قيم مؤشر كثافة النقل.

Input				Traffic Density (Data-Base Value) (Test Target)	Network Query Output
Employee Prod.	Coach Prod.	Wagon Prod.	Locomotive Prod.		
610.39	9634.74	443.29	41109.55	3973.7	4456.35
2209.93	7128.52	963.67	49960.4	4245.69	5666.38
378.91	1981.09	327.21	22170.21	1085.98	2232.91
1729.38	4408.72	1795.31	37391.89	3077.86	4725.12
547.46	3057.99	318.32	18925.38	3881.3	2045.56
668.77	3945.62	455.02	20101.61	4084.75	2309.16
99.09	1259.26	173.4	7156.57	517.15	743.7
260.86	1263.16	298.41	12013.16	693.24	1214.34
126.07	787.89	156.18	6137.63	757.33	674.3
215.17	666.67	347.54	10400	892.7	1066.56
471.8	4686.51	317.78	23590	1415.12	2507.95
322	4533.33	556.89	21000	658.04	2243.4
609.54	4392.52	694.09	31097.08	3485.58	3466.72
957.63	7902.12	1037.15	44753.77	4670.16	4963.98
581.33	429.2	664.78	22602	474.43	2477.89
688.45	5162.1	1065.45	57860.84	6367.17	5648.37
847.2	1313.95	461.73	10925.77	996.81	1484.66
336.95	13150.84	229.83	49408.78	3754.33	5014.57
272.6	1461.68	308.31	10918.29	369.64	1140.98
112.02	4258.62	4.38	10232.33	505.36	980.65
400.23	2308.04	577.55	18954.06	3566.77	2035.07
486.92	1908.57	604.52	16855.52	3187.57	1885.05
520.64	2622.05	542.99	19932.62	2313.54	2197.64
678.37	2421.58	744.09	37883.12	2054.95	4107.14
268.1	1178.77	122.88	8279.8	2484.25	877.97
990.63	6775.86	578.64	28303.57	1553.92	3442.59
339.33	1045.45	491.39	17551.72	561.81	1800.61
853.28	5301.37	715.26	29677.52	4119.2	3498.88
3404.85	225.18	1164.64	41841.27	5468.07	5441.53
857.01	3928.12	620.01	28796.69	2103.07	3347.93
1708.53	3794.3	672.12	36502.24	2253.04	4503.3
189.11	2842.61	43.49	25572.76	2270.97	2368.73
68.31	227.27	164.7	7008.7	147.13	698.31
1219.78	4053.44	1289.4	33733.49	2188.21	4162.22
1423.71	12495.59	1799.73	35258.91	1904.63	4595.74
865	3171	796	13535.35	7440	1891.15
173.21	2783.78	550.65	17744.44	586.81	1792.54
225.7	3435.16	293.86	12679.78	606.72	1302.98
311.02	4050	349.04	17313.33	698.12	1793.84
548.54	6517.79	359.54	37202.76	3170.38	3974.01
555.68	2876.29	529.59	19459.77	1521.22	2174.84

336.84	4312.98	478.53	19354.75	1656.65	2057.17
455.42	4452.7	563.78	26580.04	1622.86	2882.85
383.6	5630.97	865.02	18591.6	2476.29	2185.54
191.48	2871.89	124.6	7313.75	126.95	813.17
671.82	377.3	185.04	15604.59	114.32	1681.41
116.57	3201.51	288.99	10251.99	1364.76	1048.28
169.37	4267.79	588.54	23320.87	2802.7	2384.02
447.06	3670.14	228.71	15567.88	3765.57	1656.99
59.63	613.72	77.09	4062.37	521.56	499.64

جدول 3. نتائج احتساب معادلة الانحدار الخطي المتعدد.

m_1	2.033614876
m_2	-0.002930185
m_3	-0.251881432
m_4	0.096333869
r^2	0.841594808

جدول 4. نتائج المقارنة الاحصائية باستخدام اختبار معنوية الفرق بين الاوساط الحسابية من نفس المجتمع من خلال المشاهدات المزدوجة.

Traffic Density	Network Query Output	Regression Output	Network Query Output – Traffic Density	Regression Output – Traffic Density
3973.7	4456.35	5061.65	482.65	1087.95
4245.69	5666.38	9043.41	1420.69	4797.72
1085.98	2232.91	2818.08	1146.93	1732.1
3077.86	4725.12	6653.87	1647.26	3576.01
3881.3	2045.56	2847.34	-1835.74	-1033.96
4084.75	2309.16	3170.31	-1775.59	-914.44
517.15	743.7	843.56	226.55	326.41
693.24	1214.34	1608.9	521.1	915.66
757.33	674.3	805.99	-83.03	48.66
892.7	1066.56	1349.95	173.86	457.25
1415.12	2507.95	3138.2	1092.83	1723.08
658.04	2243.4	2524.28	1585.36	1866.24
3485.58	3466.72	4047.57	-18.86	561.99
4670.16	4963.98	5974.36	293.82	1304.2
474.43	2477.89	3190.84	2003.46	2716.41
6367.17	5648.37	6690.51	-718.8	323.34
996.81	1484.66	2655.25	487.85	1658.44
3754.33	5014.57	5348.54	1260.24	1594.21
369.64	1140.98	1524.22	771.34	1154.58
505.36	980.65	1199.94	475.29	694.58
3566.77	2035.07	2487.59	-1531.7	-1079.18
3187.57	1885.05	2456.11	-1302.52	-731.46
2313.54	2197.64	2834.52	-115.9	520.98
2054.95	4107.14	4834.45	2052.19	2779.5

2484.25	877.97	1308.43	-1606.28	-1175.82
1553.92	3442.59	4575.55	1888.67	3021.63
561.81	1800.61	2254.06	1238.8	1692.25
4119.2	3498.88	4398.5	-620.32	279.3
5468.07	5441.53	10660.87	-26.54	5192.8
2103.07	3347.93	4349.25	1244.86	2246.18
2253.04	4503.3	6810.48	2250.26	4557.44
2270.97	2368.73	2828.82	97.76	557.85
147.13	698.31	771.94	551.18	624.81
2188.21	4162.22	5393.59	1974.01	3205.38
1904.63	4595.74	5801.97	2691.11	3897.34
7440	1891.15	2853.2	-5548.85	-4586.8
586.81	1792.54	1914.78	1205.73	1327.97
606.72	1302.98	1596.4	696.26	989.68
698.12	1793.84	2200.57	1095.72	1502.45
3170.38	3974.01	4589.75	803.63	1419.37
1521.22	2174.84	2862.85	653.62	1341.63
1656.65	2057.17	2416.35	400.52	759.7
1622.86	2882.85	3331.65	1259.99	1708.79
2476.29	2185.54	2336.71	-290.75	-139.58
126.95	813.17	1054.16	686.22	927.21
114.32	1681.41	2821.76	1567.09	2707.44
1364.76	1048.28	1142.5	-316.48	-222.26
2802.7	2384.02	2430.28	-418.68	-372.42
3765.57	1656.99	2340.5	-2108.58	-1425.07
521.56	499.64	491.39	-21.92	-30.17
		Mean	352.1262	1121.7474
		Std. Deviation	1405.66453	1744.217182
		z (Test Statistic)	1.771338883	4.547571264
		Decision	$z_1 < 1.96 \rightarrow$ difference is not significant	$z_2 > 1.96 \rightarrow$ difference is significant

جدول 5. تحليل الحساسية للمتغيرات الداخلة في حساب كثافة النقل.

Input Nodes (i)	Absolute Weights (from input to hidden)	Hidden Nodes (j)	Absolute Weights (from hidden to output)	Output Node (k)	P_{ij}		$Q_{ij} = P_{ij} / \sum_i P_{ij}$
1	0.686261652	1	2.273622393	1		1.56029986	0.252072756
2	0.046266174					0.105191808	0.016994162
3	0.526911164					1.197997023	0.193541267
4	1.463035512					3.326390302	0.537391814
					$\sum_i P_{ij}$	**6.189878992**	
1	1.360412268	2	3.029695331			4.121634695	0.298608531
2	0.245728395					0.744482171	0.053937028
3	0.908420545					2.752237483	0.199397000
4	2.041277380					6.184448547	0.448057441
					$\sum_i P_{ij}$	**13.8028029**	
1	0.105046876	3	2.257864264			0.237181587	0.045947991
2	0.072760153					0.16428255	0.031825629
3	0.160273296					0.361875347	0.070104283
4	1.948132277					4.39861825	0.852122097
					$\sum_i P_{ij}$	**5.161957735**	

Input Variables	$S_i = \sum_j Q_{ij}$	R.I % = $(S_i / \sum S_i) * 100\%$
Employee Productivity	0.5966293	19.89%
Coach Productivity	0.1027568	3.43%
Wagon Productivity	0.4630425	15.43%
Locomotive Productivity	1.8375714	61.25%

جدول 6. معاملات النموذج الرياضي للشبكة العصبية.

Hidden Layer Nodes	W_{ij} (Weight from node i in the input layer to the node j in the hidden layer)				Hidden Layer Bias W_{oj}
	i = 1	i = 2	i = 3	i = 4	
j = 1	0.686261652	0.046266174	-0.526911164	1.463035512	-0.180214505
j = 2	-1.360412268	-0.245728395	-0.908420545	-2.04127738	0.635897702
j = 3	0.105046876	-0.072760153	-0.160273296	-1.948132277	0.379851428

Output Layer Nodes	W_{jk} (Weight from node j in the hidden layer to the node k in the output layer)			Output Layer Bias W_{ok}
	j = 1	j = 2	j = 3	
k = 1	2.273622393	-3.029695331	-2.257864264	-0.069630097

ENGINEERING

College of Engineering University of Baghdad No.9 Vol. 22 September 2016

List of Contents

English Section:

ISSN 1726 - 4073

Journal of Engineering

A Scientific Refereed Journal
Published by
College of Engineering
University of Baghdad

September
2016

Number 9
Volume 22

ISSN 1726 - 4073

مجلة الهندسة

مجلة علمية محكمة تصدرها

كلية الهندسة ـ جامعة بغداد

أيلول

2016

العدد 9

المجلد 22

قائمة المحتويات

القسم العربي: